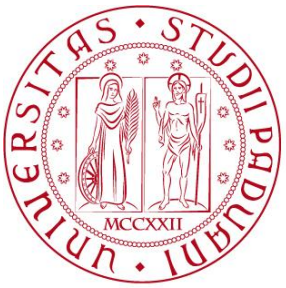

UNIVERSITÀ
DEGLI STUDI
DI PADOVA

Sede Amministrativa: Università degli Studi di Padova
Dipartimento di Tecnica e Gestione dei Sistemi Industriali

Scuola di Dottorato di Ricerca in Ingegneria Meccatronica e dell'Innovazione Meccanica del Prodotto

Indirizzo di Meccatronica

Ciclo XXX

Impedance-Based Stability Analysis in Smart Grids with Large Penetration of Renewable Energy

Direttore della Scuola: Ch.mo Prof. Roberto Caracciolo
Coordinatore di Indirizzo: Ch.mo Prof. Roberto Caracciolo
Supervisore: Ch.mo Prof. Paolo Mattavelli

Dottorando: Francesco Cavazzana

Contents

Abbreviations

AC Alternate Current

AVR Automatic Voltage Regulator

BESS Battery Energy Storage System

CCI Current Controlled Inverter

DC Direct Current

DER Distributed energy resource

DPWM Digital Pulse Width Modulation

GINC Generalized Inverse Nyquist Criterion

GNC Generalized Nyquist Criterion

IMU Impedance Measurement Unit

MIMO Multi-input multi-output

PCS Power Controlled Source

PLL Phase-locked Loop

PV Photovoltaic

PWM Pulse Width Modulation

SISO Single-input single-output

WG Wind Generation

VCI Voltage Controlled Inverter

VSI Voltage Source Inverter

List of Figures

List of Tables

Abstract

The wide diffusion of distributed energy resources (DERs) has led to a scenario where the penetration of renewables is very high and can significantly affect the grid stability. The increasing complexity of these systems requires a suitable stability approach: the impedance-based analysis has one of its main advantages in the possibility to characterize the components separately, e.g. source and load, and to estimate the stability at a certain interface applying the Nyquist criterion to the impedance ratio. This method has been widely used in DC systems, to investigate the converters interactions and anticipating the stability of the final scenario also in case of multiple paralleled converters, often using criteria to limit the interactions and guarantee a stable configuration. Then, the method has been extended to three-phase system, where the multi-input multi-output configuration needs the generalized Nyquist criterion (GNC) for the stability assessment.

The first case presented in this work is a grid-connected large photovoltaic (PV) farm, where the inverter control is provided in *abc*-frame, and considering a balanced and symmetrical system the equivalent single-phase inverter is used in this analysis. The stability is addressed according to the aforementioned impedance-based approach, including also the equivalent generator contributions. The *impedance multiplication effect* is here formalized also for the case of different parallel inverters. The influence of the line impedance and of the power rating of the inverter are considered. The outcome of the study is an approach featuring both accurate stability analysis, as in multi-input multi-output based approaches, and modularity, as in impedance-based approaches. Moreover, the grid sensitivity

is investigated for the case of multiple paralleled inverters, in order to analyze how it changes with an increasing number of connections.

Recently, the interest on the hybrid-grids with diesel generators and battery energy storage systems (BESSs) are gaining higher attention because nearly one in five people in the world live without access to electricity. This off-grid solution is then able to provide a continuous generation and also integrate the renewables in the same system. The second part focuses on the modeling of a three-phase hybrid-grid, where the diesel generator is controlled in isochronous mode, and the inverters interfacing the BESSs are droop-controlled with an additional external loop to provide the exact tracking of the power references when the generator is connected. The experimental results of a system with a 400kVA diesel generator and up to 300kVA coming from the BESSs are included. The analysis has led to the full reproduction of the interaction between the diesel generator and an increasing number of connected inverters, where the total inertia of the system changes. However, in literature there is no stability analysis accurate enough to analyze such a complex system and predict instabilities. The modularity of the impedance-based stability analysis can then provide a subdivision of this complexity, and so represents a suitable approach. In this work, the output impedance of a droop-controlled inverter is determined, in order to characterize this element widely used in off-grid applications. After determining the operating point, the analytical model of the output impedance is derived in both controller and system frame, including the effect of the decoupling impedance and the inverter inner dynamics. Finally, this work presents a mathematical tool to convert impedance between different dq-frames. The application of this conversion tool to the aforementioned droop-controlled inverter case will be provided, in order to prove the correctness of the transformation.

Acknowledgments

First of all, I want to thank my supervisor Prof. Paolo Mattavelli for his invaluable support during these three years. He taught me how patience, method and hard work can be powerful allies to carry on research projects. He has been very understanding during the hard times I had during my Ph.D. and I will benefit of his advices in my future personal life and professional career.

I would like to thank my colleagues Andrea Petucco, Luca Dalla Santa, Dr. Riccardo Sgarbossa, Dr. Fabio Tinazzi, Davide Biadene, Ludovico Ortobmina and Aram Khodamoradi for their collaboration during these years and especially for their friendship and the nice times we had together.

Special thanks go to Dr. Tommaso Caldognetto, whose collaboration has been very important during all the three years, and whose friendship has been a certainty from when we shared University courses.

I want to thank Prof. Dushan Boroyevich and Prof. Rolando Burgos, who hosted me at the Center for Power Electronic Systems (CPES) at Virgina Tech. That experience has been very important, and it will positively affect my personal and professional life.
Many thanks to all the Ph.D. Students and Visiting Scholars at CPES, who have been very welcoming, collaborative and with who I shared great moments.
I want to remember in particular Benjamin Cheong and Guo Xu, with whom I shared very funny lunches and intense moments.
Special thanks to Teresa Shaw for her perfect welcome and help during all my period at CPES: she has been very important for my experience.

Special thanks also to Lauren Shutt, for being so supportive and for her friendship. She showed me that USA is not only work and she made me feel home during all my staying.

I would like to thank my dear friends for their patience and support during all these years. They have been very encouraging and helpful, even in the toughest times.

Finally, endless thanks to my parents Mariagrazia and Livio, my sisters Chiara Marta Elisa and Lucia, my brother Giovanni, my brothers-in-law, my niece and my nephews. They helped me a lot with all the nice moments we had together. Without their support I couldn't have accomplished this intense three-year journey.

Padova, January 2018
Francesco Cavazzana

Chapter 1

Introduction

1.1 Overview

The extensive diffusion of renewable energy sources (RESs) has increased the interest on renewables. According to [1], renewable power generating capacity saw its largest annual increase ever in 2015, with an estimated 147GW of renewable capacity added, covering about 23.7% of the global electricity production. Different renewable energies are indicated in Fig. 1.1, where most of the market share is held by wind (WG), 3.7%, and solar photovoltaic (PV) generation, 1.2%, after hydropower 16.6% (the five BRICS countries are Brazil, the Russia, India, China and South Africa). WG and PV both saw record additions for the second consecutive year, together making up about 77% of all renewable power capacity added in 2015. China is the biggest WG producer, while PV generation is more uniformly distributed in these main countries.

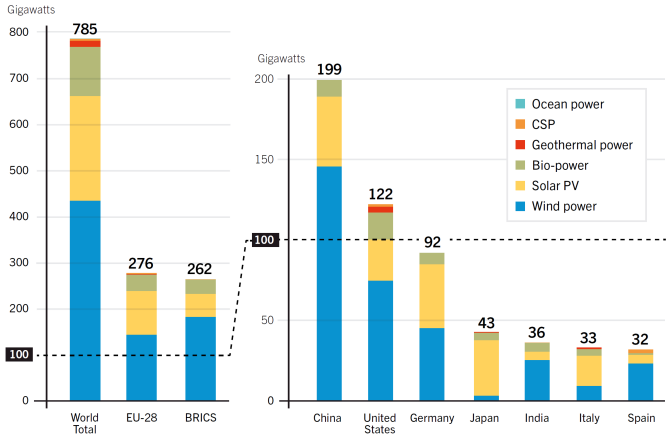

FIGURE 1.1: Renewable Power Capacities in World, EU-28, BRICS and Top Seven Countries, End-2015 [1].

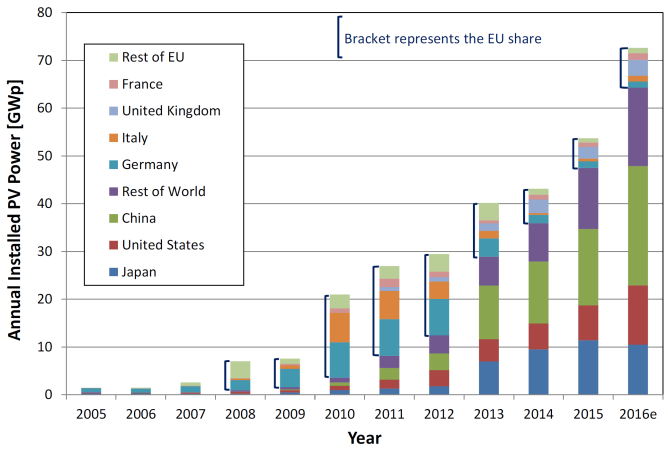

(A) Annual installations

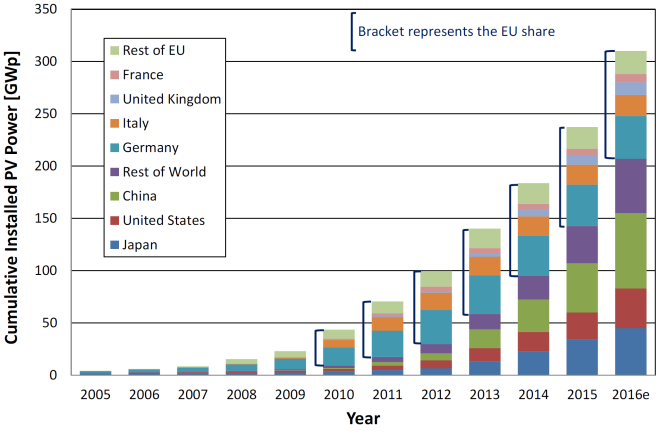

(B) Cumulative installations

FIGURE 1.2: Annual and Cumulative PV system installations from 2005 to 2016 [2].

As stated in [2], Europe installed around 7GW in 2016, less than United States installations, while China installed more than 20GW, as shown in Fig. 1.2a. These new installations are added to the existing ones in the cumulative graph in Fig. 1.2b. The trend confirms PV market is gaining higher attention in the renewable energy environment.

The wide diffusion of PV panels leads to the installation of the interface converters, i.e. inverters, to convert the DC voltage given by the solar panel to the AC voltage of the grid. Therefore, these massive and capillary new installations of the interface converters bring the chance to improve stability and power quality of the whole main grid, providing redundancy to the system. However, the interface converter dynamics have also the potential of causing instabilities, especially when the system complexity becomes difficult to manage and analyze.

Nearly one in five (18%) people in the world live without access to electricity, many of them living in locations that are beyond the reach of the current grid

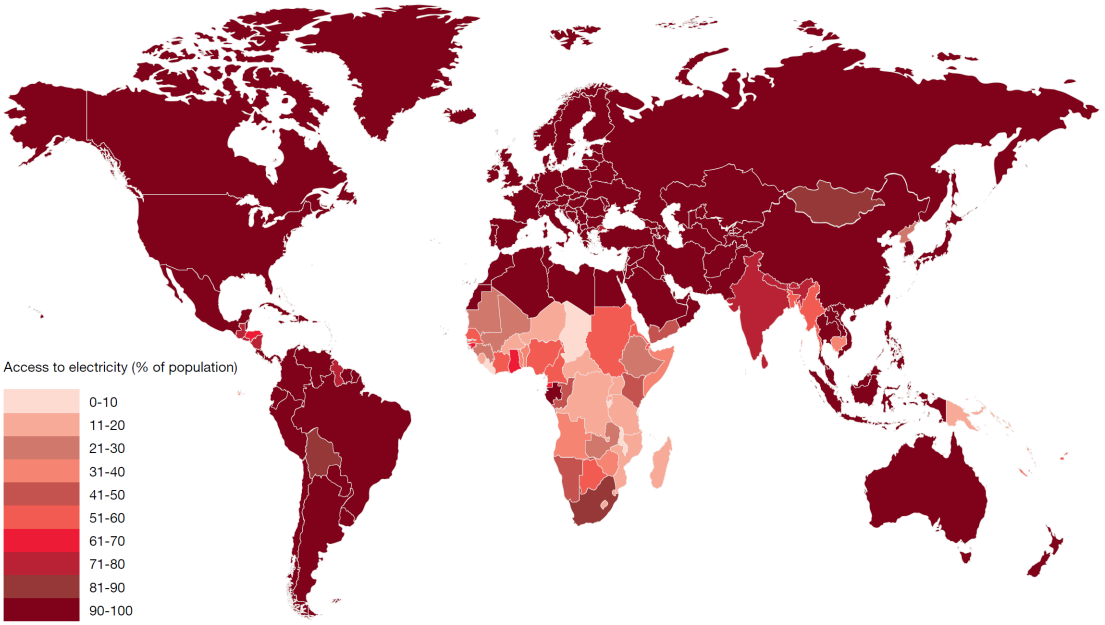

FIGURE 1.3: Access to electricity around the world [3]. Source: World Bank Data

system. Ninety-five percent of these 1.2 billion people are in sub-Saharan Africa and developing countries in Asia. In both Asia and Africa, electrification rates are lowest in rural areas although, in sub-Saharan Africa in particular, urban areas also contain a considerable number of those without electricity [3]. Fossil fuel supplied mini-grids are well established in many locations as off-grid solutions: Philippines count more than 100 operating isolated diesel grids and Mali has around 200 small diesel mini-grids. Increasingly, these diesel installations are being supplemented with renewable technologies to create hybrid mini-grids [3]. The typical solution for a mini-grid adopts diesel generators (DGs), used to guarantee a continuous operation, and different kind of DERs, interfaced to the grid with appropriate converters.

Moreover, energy storage is a crucial tool for enabling an effective integration of renewables, unlocking the benefits of local generation and a clean, resilient energy supply. This technology continues to prove its value to grid operators around the world who must manage the variable generation of PV and WG energy [4]. Hence, the battery energy storage systems (BESSs) find their main purpose in storing the energy *surplus* produced during daytime and releasing it during night, when needed.

1.2 Impedance-Based Stability Analysis

One of the earliest instability issues was found in aircraft DC power system in 1950's [5,6]. In the 1960's, the the US Navy installed a large number of line voltage regulators (LVRs) at the Aircraft Electric Service Stations to eliminate voltage losses due to cable length. The LVRs were intended to provide regulated voltage between $\pm 0.5\%$ but, upon energization the system reached a sustained oscillation, i.e. limit cycle. This phenomenon was solved decreasing the number of LVRs and decreasing the regulation bandwidths [7]. passing through automotive [8], ship [9–11] and space station [12–14] fields.

The stability analysis of power systems is often performed using eigenvalues, extracted from the matrix A coming from the canonical state-space model representation of the examined system [15, 16]. This approach requires all the system information, e.g. converter topologies, circuit parameters, control strategies. This huge amount of data is not easy to be computed and the system model has to be derived every time. Moreover, the knowledge of all the proprietary information from different component vendors is not feasible, impeding a proper modeling of the system [15].

Another method to study the stability of a system is through the loop gain analysis [15,17–21]. The control design is performed off-line, meeting the predetermined stability specifications. Moreover, some techniques allow the on-line measurement and an autotuning procedure, in order to correct the control coefficients when new blocks are connected to the system.

However, the two aforementioned stability approaches can not be used when some subsystems information are missing. Therefore, a "black box" approach is preferred, since no information of the subsystems are needed.

In this context, the impedance-based stability analysis finds its strength. This approach was firstly successfully introduced by Middlebrook in 1976 and used in DC-DC converters [22] for a long time, where the stability at each interface is determined using the measured impedances and Nyquist stability criterion. The main advantage lies on the possibility to know all the effects due to the inner characteristics, from the physical components to the control parameters: all these information are intrinsically modeled by the output impedance [15]. Hence, the source-load impedance ratio is determined and stability criteria can be applied, and creating the forbidden regions it is then possible to ensure that the system meets the predetermined specifications [23–27], beside the more conservative small-gain

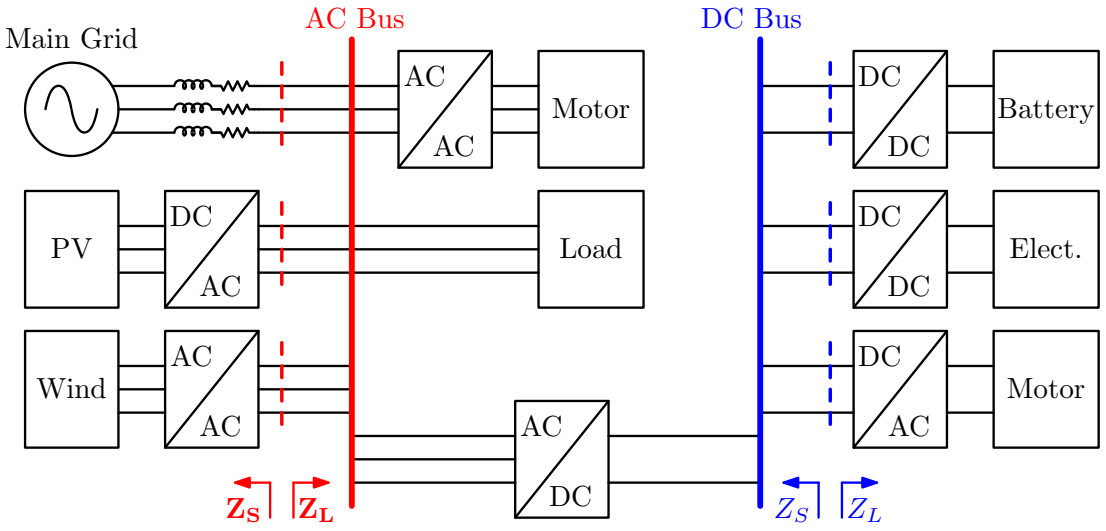

FIGURE 1.4: Generic grid with AC and DC bus [15].

criterion [22]. One of the advantages of the impedance-based approach is modularity, since the system does not need to be re-formulated when a new component is added, and the stability analysis is performed looking only at the impedance ratio. This method has been widely used in various DC systems, such as more electric aircraft [28] or shipboard [9–11, 29], and in AC systems, such as for single phase [30] and three-phase converters [27], e.g. grid-tied inverters [15, 31].

In Fig. 1.4 a generic system with AC and DC buses is shown. The grid includes different sources, such as PV and wind generations, and loads, such as motors or batteries. The stability can be evaluated thanks to the impedance ratio at the interfaces. As can be seen, the impedances in the AC side are indicated in bold as matrices, i.e. $\mathbf{Z_S}$ and $\mathbf{Z_L}$, while the DC impedances are 1×1 transfer functions, i.e. Z_S and Z_L.

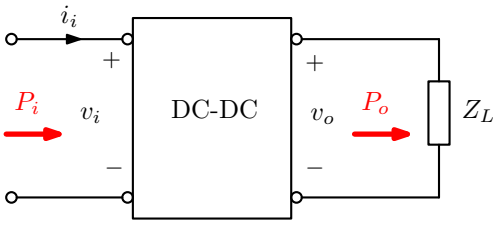

(A) DC-DC converter without input filter

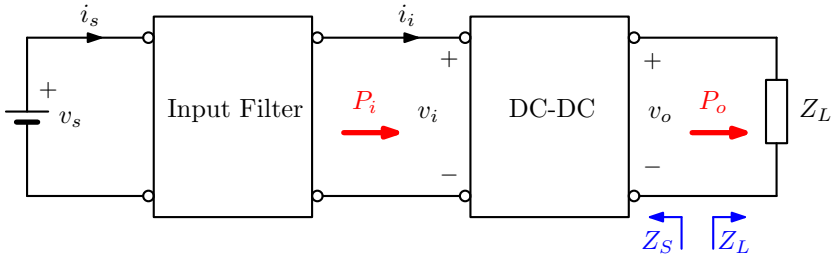

(B) DC-DC converter with input filter

FIGURE 1.5: DC-DC converter without and with input filter.

1.2.1 Impedance-based stability analysis in DC systems

In DC systems, high regulation bandwidth and high efficiency $\eta \simeq 1$ make the converters input impedance act the as a negative incremental resistance [27]. The input and output powers in Fig. 1.5a can be related as:

$$P_i = v_{dc} i_{dc} = \eta P_o \simeq P_o = const. \tag{1.1}$$

assuming that the inner voltage control keeps $v_o = const.$, and the derivative can be expressed as

$$dP_i = d(v_i i_i) = dv_i i_i + v_i di_i = 0 \tag{1.2}$$

Therefore, the input negative resistance is calculated as:

$$R_i = \frac{dv_i}{di_i} = -\frac{v_i}{i_i} \tag{1.3}$$

Moreover, considering that $i_i = P_i / v_i$:

$$R_i = \frac{dv_i}{di_i} = -\frac{v_i^2}{P_i} \tag{1.4}$$

This negative input resistance may cause negatively damped oscillations [27]. Therefore, stability has to be addressed when an input filter is added, as in Fig. 1.5b. This analysis can be done starting from the Thèvenin equivalent in

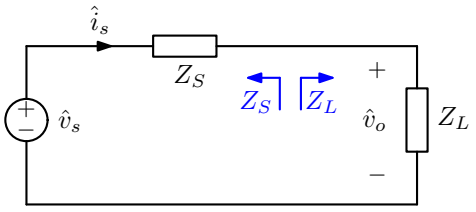

FIGURE 1.6: Thèvenin model of the DC-DC converter with input filter.

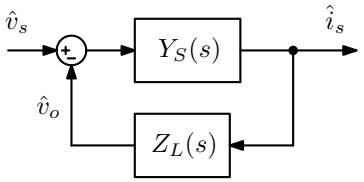

FIGURE 1.7: SISO feedback system associated to Fig. 1.6.

Fig. 1.6, where the input filter and the converter impedances are collected in Z_S. Therefore, the stability can be evaluated, in the interface between the load and the DC-DC converter output, thanks to the Nyquist stability criteria applied to the minor loop gain $L = Z_S/Z_L$.

The theorem is here presented, as stated in [32]:

Theorem 1. Let the feedback system shown in Fig. 1.7 have no open-loop uncontrollable and/or unobservable modes whose corresponding characteristic frequencies lie in the right-half plane (RHP). Then this configuration will be closed-loop stable if and only if the graph of $Z_S(j\omega)Y_L(j\omega)$, for $-\infty < \omega < \infty$, encircles the point $-1 + j0$ as many times anticlockwise as $Z_S(s)Y_L(s)$ has right-half plane (RHP) poles.

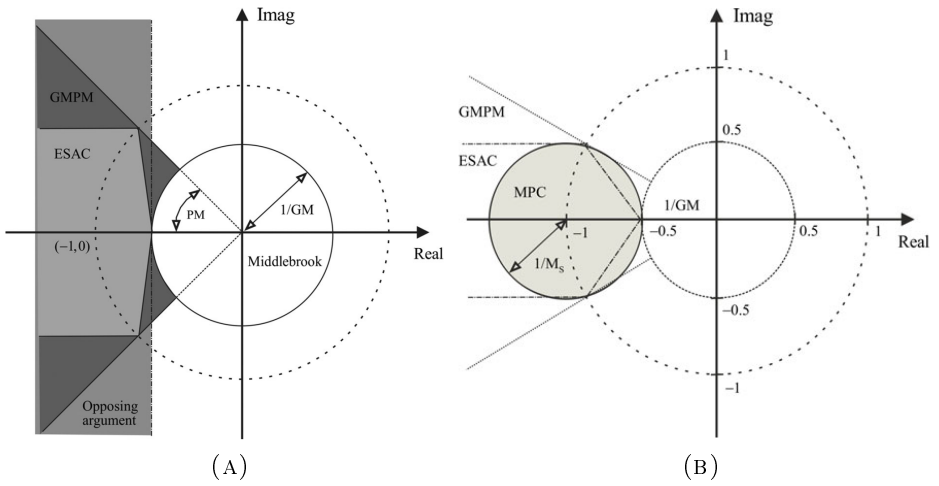

FIGURE 1.8: Forbidden regions in the complex plane for the loop gain [26].

As mentioned above, the forbidden regions for the loop gain in the complex plane can help to define the system stability. The main proposed criteria are here indicated, from the most restrictive to the less restrictive, valid when no right half plane poles (RHPs) are included in L. From Fig. 1.8 can be seen the forbidden regions proposed in literature:

- Middlebrook [22,33] proposed a conservative specification, which imposes the minor loop gain L to stay within the unitary circle (or a circle with smaller radius). This requirement allows to not encircle the instability point $-1+j\cdot 0$ and ensures a stable system. However, this restrictive condition leads to the need of bulky input filters and can not always be easy to implement [15];

- Ref. [25] proposed the so called "opposing argument" forbidden region, which ensures the minor loop gain not to encircle the instability point, and allows to the loop gain to move in almost half of the plane;

- Ref. [23] gives probably one of the most used criterion, which draws the forbidden region according to the gain margin (GM) and the phase margin (PM) specifications, ensuring the desired stability level for the system;

- Ref. [24] presents the one of the less restrictive forbidden regions, which are intended to guarantee a good distance from the instability point and to avoid its encirclement. The shape of the forbidden region is rectangular;

- Ref. [34] presents the less restrictive forbidden region, which allows to have a system with the desired level of stability. The loop gain does not go inside the forbidden region and the Nyquist criterion is satisfied.

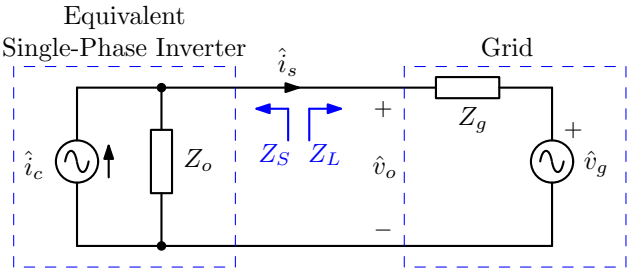

(A) Equivalent Single-Phase Inverter Impedance-Based Analysis as in [30]

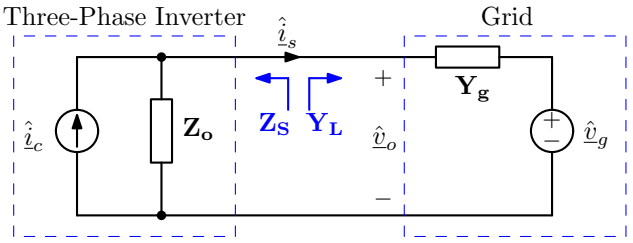

(B) Three-Phase Inverter Impedance-Based Analysis in *dq*-domain as in [31]

FIGURE 1.9: Small-signal representation of an inverter-grid system [30].

1.2.2 Impedance-based stability analysis in AC systems

The impedance-based approach can be performed in AC systems both considering the *abc*-frame and *dq*-frame.

For single-phase inverters, it is possible to consider the approach presented in [30], where the stability of a grid-connected inverter is considered. This work performs the stability analysis of the inverter, considered as a current-controlled source, through the source-load impedance ratio as shown in Fig. 1.9a. The expression for the output voltage $v_o(s)$ is derived superimposing the effects of the inverter current generator $i_c(s)$ and of the grid voltage generator $v_g(s)$:

$$v_o(s) = i_c(s) \cdot \frac{Z_o(s)}{1 + Z_o(s)/Z_g(s)} - v_g(s) \cdot \frac{1}{1 + Z_o(s)/Z_g(s)} \tag{1.5}$$

From this formulation, it is clear that the loop gain can be associated to the impedance ratio of the system $L(s) = Z_o(s)/Z_g(s) = Z_S(s)/Z_L(s)$, and the analysis can be conducted as previously done for DC systems.

For three-phase inverter, the main distinction for the impedance-based analysis is given by the control frame. When the control is implemented in *abc*-frame, under the assumptions of balanced system and symmetrical loads, it is possible to consider the equivalent single-phase inverter. This assumption enables the

possibility to analyze three-phase converters with the approach described in [30]. On the other hand, when the control is implemented in the synchronous reference dq-frame, it is not possible to derive the equivalent single-phase inverter, due to the Park's transformation and the consequent cross-coupling terms between d-axis and q-axis, as in Fig. 1.9b. Under the condition of a balanced three-phase AC system, the impedances result in 2×2 matrices:

$$\mathbf{Z_S}(s) = \begin{bmatrix} Z_{Sdd}(s) & Z_{Sdq}(s) \\ Z_{Sqd}(s) & Z_{Sqq}(s) \end{bmatrix} \quad , \quad \mathbf{Z_L}(s) = \begin{bmatrix} Z_{Ldd}(s) & Z_{Ldq}(s) \\ Z_{Lqd}(s) & Z_{Lqq}(s) \end{bmatrix} \tag{1.6}$$

Assuming that $\mathbf{Z_S} = \mathbf{Z_o}$ and $\mathbf{Z_L} = \mathbf{Z_g}$ and defining that $\mathbf{Y_S} = \mathbf{Z_S}^{-1}$ and $\mathbf{Y_L} = \mathbf{Z_L}^{-1}$, one can write:

$$\hat{\underline{i}}_s = \mathbf{Y_L} \cdot [\mathbf{Y_S} + \mathbf{Y_L}]^{-1} \cdot \hat{\underline{i}}_c - [\mathbf{Z_S} + \mathbf{Z_L}]^{-1} \cdot \hat{\underline{v}}_g \tag{1.7}$$

which can be put in the form:

$$\hat{\underline{i}}_s = [\mathbf{I} + \mathbf{Z_S} \cdot \mathbf{Y_L}]^{-1} \cdot \mathbf{Z_S} \cdot \mathbf{Y_L} \cdot \hat{\underline{i}}_c - [\mathbf{I} + \mathbf{Z_S} \cdot \mathbf{Y_L}]^{-1} \cdot \mathbf{Y_L} \cdot \hat{\underline{v}}_g \tag{1.8}$$

The impedance ratio can be noticed from the previous expression:

$$\mathbf{L}(s) = \mathbf{Z_S}(s) \cdot \mathbf{Y_L}(s) = \begin{bmatrix} Z_{Sdd}(s) & Z_{Sdq}(s) \\ Z_{Sqd}(s) & Z_{Sqq}(s) \end{bmatrix} \cdot \begin{bmatrix} Y_{Ldd}(s) & Y_{Ldq}(s) \\ Y_{Lqd}(s) & Y_{Lqq}(s) \end{bmatrix} \tag{1.9}$$

and the stability is assessed according to the generalized Nyquist criterion (GNC). The latter was proposed by MacFarlane and Postlethwaite [35] in the 1970s as an extension of the Nyquist stability, developed for scalar functions, to a generalized stability criterion which addresses matrix transfer function [27]. In [36] the criterion applied to the inverse of the loop gain is presented.

Let $\{\lambda_1(s), \lambda_2(s), \ldots, \lambda_m(s)\}$ be the set of frequency-dependent eigenvalues of $\mathbf{L}(s)$, which can be defined from

$$\mathbf{L}(s) = \begin{bmatrix} Z_{Sdd}(s)Y_{Ldd}(s) + Z_{Sdq}(s)Y_{Lqd}(s) & Z_{Sdd}(s)Y_{Ldq}(s) + Z_{Sdq}(s)Y_{Lqq}(s) \\ Z_{Sqd}(s)Y_{Ldd}(s) + Z_{Sqq}(s)Y_{Lqd}(s) & Z_{Sqd}(s)Y_{Ldq}(s) + Z_{Sqq}(s)Y_{Lqq}(s) \end{bmatrix} \tag{1.10}$$

and

$$\mathbf{C}(s) \cdot \mathbf{L}(s) \cdot \mathbf{C}^{-1}(s) = \begin{bmatrix} \lambda_1(s) & 0 \\ 0 & \lambda_2(s) \end{bmatrix} \tag{1.11}$$

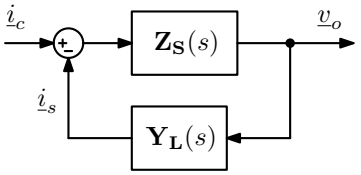

FIGURE 1.10: MIMO feedback system associated to Fig. 1.9b.

Theorem 2. Let the multivariable feedback system have no open-loop uncontrollable and/or unobservable modes whose corresponding characteristic frequencies lie in the right-half plane (RHP). Then this configuration will be closed-loop stable if and only if the net sum of anti-clockwise encirclements of the critical point $-1+j\cdot 0$ by the set of characteristic loci (reciprocal of each of the $\{\lambda_1(s), \lambda_2(s), \ldots, \lambda_m(s)\}$ in the complex plane) of the return ratio $\mathbf{L}(s) = \mathbf{Z_S}(s)\cdot\mathbf{Y_L}(s)$ is equal to the total number of right-half plane poles of $\mathbf{Z_S}(s)$ and $\mathbf{Y_L}(s)$.

In some cases the generalized Nyquist will close through infinity and interpretation may become difficult. In these cases, the generalized inverter Nyquist may yield easier interpretation [27]. The generalized inverter Nyquist theorem [36] may be stated as follows:

Theorem 3. Let the multivariable feedback system shown in Fig. 1.10 have no open-loop uncontrollable and/or unobservable modes whose corresponding characteristic frequencies lie in the right-half plane (RHP). Then this configuration will be closed-loop stable if and only if the net sum of anti-clockwise encirclements of the critical point $-1+j\cdot 0$ by the set of *inverse* characteristic loci of the return ratio $\mathbf{L}(s) = \mathbf{Z_S}(s)\cdot\mathbf{Y_L}(s)$ is equal to the total number of right-half plane poles of $\mathbf{Z_S}(s)$ and $\mathbf{Y_L}(s)$.

The generalized Nyquist theorem necessitates knowledge of the zeros of the return ratio $\mathbf{L}(s)$, which may require extra effort. However, if the return ratio $\mathbf{L}(s)$ is square and nonsingular, then its zeros and poles are the poles and zeros, respectively, of its inverse $\mathbf{L}^{-1}(s)$ [27].

1.3 Purpose of the thesis

The purpose of this work is to apply the impedance-based stability analysis to some cases of interest. The presence of significant skin effect or proximity effect of the cable connection that create an impedance not easily described by lumped circuit model. The approach described on the thesis can be applied to any kind

of impedance. This analysis will be done in the equivalent single-phase system, where an *abc*-frame control has been implemented, and in the *dq*-frame, where the generalized Nyquist criterion (GNC) will be used to investigate the stability.

Firstly, impedance-based stability analysis will be performed for a large PV farm, considering the existing results present in literature and presenting a complete approach.

Secondly, a hybrid-grid is modeled and simulated. A literature review of hybrid-grids with diesel generators is presented, completed with the modeling and the comparison with experimental data of a 400kVA generator with droop-controlled inverters, used as interface for a storage system. In particular, this case presents some oscillations due to poor stability margins.

In order to provide the possibility to perform the analysis of the aforementioned hybrid-grid, which has not been performed yet, the output impedance of the droop-controlled inverter is analyzed, starting from the control of the inverter in *dq*-frame. Moreover, a mathematical tool for the conversion of the impedance between different *dq*-frames is then presented.

Chapter 2

Grid-Connected Stability Analysis

2.1 Introduction

Power generation from renewables is continuously increasing due to new connections to the grid of both small scale distributed generators and medium to large scale renewable power plants. In the latter case renewable sources are typically connected to a point of common coupling (PCC) with the grid by using a large number of relatively small converter modules, for scalability and reliability reasons. Fig. 2.1 shows the example of a photovoltaic (PV) farm. In such system architectures the parallel connected converters interact with each others and with the grid, increasing the harmonic current distortion at inverters output [37] and, potentially leading to instability issues [38,39] as the number of inverters increases.

The stability of single inverters connected to the grid is widely discussed in the literature. The effect of the different control aspects are specifically analyzed, for what concerns current control parameters, disturbance rejection by grid voltage feedforward, passive or active damping [40, 41]. The effect of grid synchronization via phase-locked loops (PLLs) [42, 43] on inverter output impedance is also documented in the literature; in [44, 45] it is shown, in particular, a negligible effect of PLLs when looking at dynamics above the grid frequency.

While the reported studies allow to design robust controllers for converters considered individually, when many inverters are connected in parallel additional interactions arise, which call for specific system-level stability analysis approaches that should feature *i*) accuracy, to take into account all the dynamics relevant to stability study, *ii*) scalability, to easily scale the modeling and the analysis to systems having an arbitrary number of converters, and *iii*) flexibility, to allow the

description of systems composed of converters of even different kinds (e.g., having different parameters, line connections or power ratings). Relevant approaches have been recently proposed in [46–54]. The method described in [46] approaches stability analysis by classifying system poles as *internal* (i.e., those associated to the single inverters) and *external* (i.e., those due to the interaction between the converters and the grid), therefore introducing two kinds of stability, namely, internal (related to internal poles) and external (related to external poles). An equivalent inverter model representing the parallel of n identical inverters is also proposed, giving an important result in terms of external stability, namely, that each inverter module perceives a higher applied impedance due to the presence of the other inverters connected in parallel, effect herein referred to as *impedance multiplication*. In [47] a similar study is proposed, also introducing the concepts of interactive current, associated with the interactions between inverters, disregarding the grid impedance, and of common current, related to the interaction with the grid impedance; the physical meaning of the internal poles is attributed to the interactive current.

In [55] the interaction between active impedances, due to the inverters, and the passive impedances is discussed in the case of a wind farm. Such interaction occurs also in PV farms, as in [48, 49], where the analysis of the sensitivity of inverters current quality with respect to the value of grid impedances due to parallel operation is presented.

The analysis in [46, 47] has the advantage of giving an accurate description of the system, but becomes difficult to use when the inverters are not equal and lacks in modularity, because the addition of different inverters requires a reformulation of the system description. On the other hand, impedance-based approaches [22, 30, 56, 57] can overcome these disadvantages, as shown in [38, 58, 59], but do not give all the stability contributions, notably, the internal stability is missing.

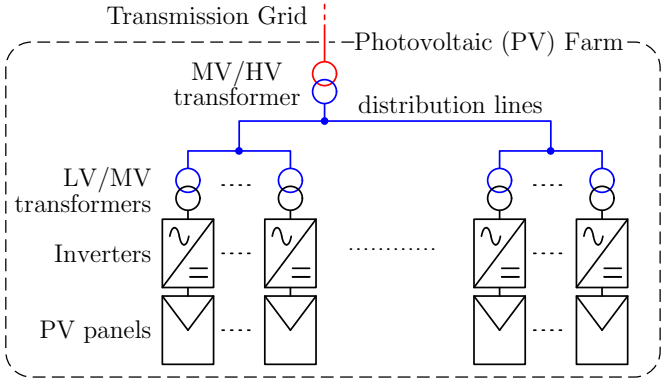

FIGURE 2.1: Typical architecture of a large photovoltaic plant.

This chapter aims at giving a stability study of a PV plant with parallel inverters, possibly having different parameters, considering also the grid contribution and combining both the completeness of the multi-input multi-output (MIMO) approaches and the modularity of impedance-based analyses in a unifying framework. Moreover, the impedance multiplication effect occurring in the equivalent inverter case [46] is revised with the source/load impedance approach, which allows to focus specifically on the external stability. An extension of this effect to the case of parallel connected inverters with different parameters is presented, allowing to evaluate the current loop gain and the grid sensitivity considering the impedance perceived by the inverters, providing in this way a valuable tool for the design of inverter controllers. Finally, the equivalent inverter is also used to analyze the influence of the grid voltage on the currents injected by the PV inverters, herein referred to as *grid sensitivity*.

This chapter is organized as follows. Sect. 2.2 presents a generic PV plant using the Norton equivalent generator and then combining the inverters in a MIMO system. Extending [49,60], the grid voltage effect on the inverters output current is included in the analysis. The equivalent single inverter is then described, applying the impedance multiplication effect also to the general case with parallel inverters with different parameters. Sec. 2.3 presents an example of application of the described methodology to the case of inverters with different parameters. Sec. 2.4 presents the simulation and the experimental results for the stability analysis, where an external instability is replicated in laboratory. Finally, the analysis on the grid sensitivity is also verified by simulation and experimental results. Sec. 2.5 concludes this chapter.

2.2 Theoretical Analysis

A typical photovoltaic plant consists of parallel three-phase inverter modules. Assuming a symmetrical and balanced three-phase system, it is possible to consider the equivalent single-phase inverter [46]. Hence, the system under investigation in Fig. 2.2 describes a PV farm with n-paralleled grid-connected current-controlled inverters, where the PCC with voltage v_{PCC} is indicated. The grid is modeled as an equivalent Thèvenin generator, where v_g is the grid voltage and $Z_g = R_g + sL_g$ is the grid impedance.

In this section the j-th inverter module (for $j = 1, \ldots, n$) is equipped with an internal current control where the error is processed by a controller G_{cj}, which drives the digital pulse width modulator (DPWM) G_{dpwmj}. By considering the

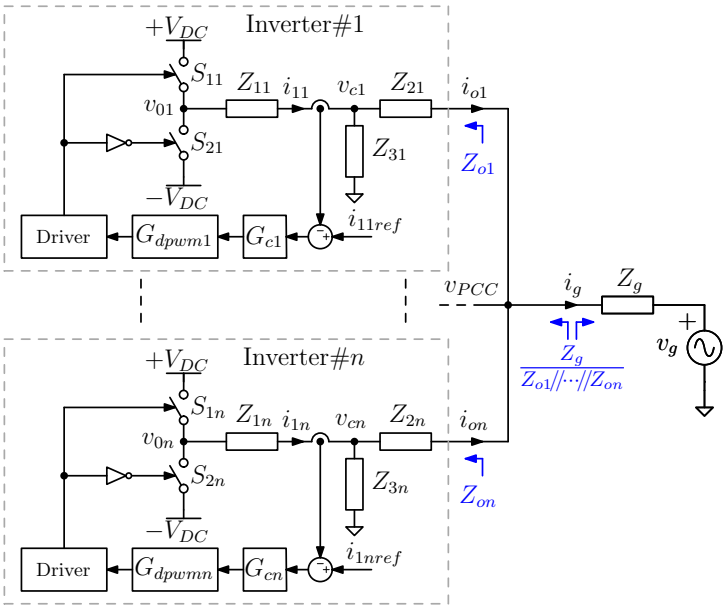

FIGURE 2.2: The photovoltaic (PV) plant with n current-controlled inverters connected in parallel. The grid voltage contribution is considered.

linearized average model of a grid connected voltage source inverter [61], these contributions can be collected in the term:

$$PI'_j = G_{cj} \cdot G_{dpwmj} \cdot V_{DC} \tag{2.1}$$

where the gain V_{DC} (i.e., the bus voltage) results from the average model of the inverter. The current references i_{1jref} are given by phase-locked loops (PLLs), whose effect in the frequency range that is herein of interest can be neglected; the same holds for slow power systems dynamics [62]. The voltage v_{0j} imposed by each inverter leg is then filtered by the LCL network Z_{1j}, Z_{2j}, and Z_{3j}, where:

$$Z_{1j} = R_{1j} + sL_{1j} \quad , \quad Z_{2j} = R_{2j} + sL_{2j} \quad , \quad Z_{3j} = R_{3j} + 1/(sC_{3j}) \tag{2.2}$$

Equivalently, each converter module can be represented by the Norton equivalent circuit, namely, by an independent equivalent current generator i_{sj} with a parallel output impedance Z_{oj} (for $j = 1, \ldots, n$) [60], as shown in Fig. 2.4a, whose expressions are derived in Sec. 2.2.1. Finally, in Sec. 2.2.2 all the inverters are connected at the PCC, in order to analyze the stability of the whole plant.

2.2.1 Equivalent Model of a Single Inverter

Norton equivalent models of the parallel connected inverters can be used for stability analysis. The short circuit current and the output impedance of the equivalent

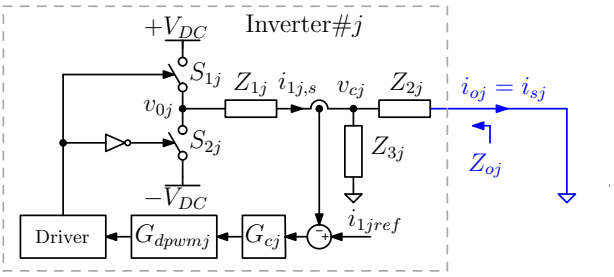

(A) Electrical scheme

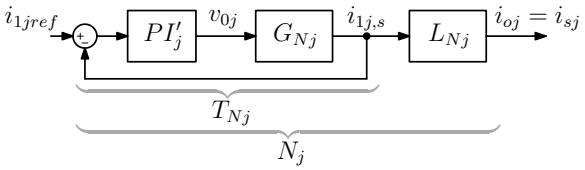

(B) Block scheme

FIGURE 2.3: Inverter for the determination of the short-circuit current transfer function and the output impedance.

model of the generic j-th inverter are derived as follows.

2.2.1.1 Short circuit current i_{sj}

Referring to Fig. 2.3a, it is possible to calculate the transfer function of the inverter short-circuit current. To this end, let us determine the admittance G_{Nj} from the voltage v_{oj} to the current on the inverter side inductance $i_{1j,s}$, when the output is short-circuited, and the current partition L_{Nj} from the inverter side inductance to the output:

$$G_{Nj} = \frac{i_{1j,s}}{v_{oj}} = \frac{Z_{2j} + Z_{3j}}{Z_{1j} \cdot (Z_{2j} + Z_{3j}) + Z_{2j} \cdot Z_{3j}} \tag{2.3}$$

$$L_{Nj} = \frac{i_{sj}}{i_{1j,s}} = \frac{Z_{3j}}{Z_{2j} + Z_{3j}} \tag{2.4}$$

By referring to the block diagram in Fig. 2.3b, the loop transfer function can be expressed as:

$$T_{Nj} = \frac{i_{1j,s}}{i_{1jref}} = \frac{PI'_j \cdot G_{Nj}}{1 + PI'_j \cdot G_{Nj}} \tag{2.5}$$

and the total transfer function from the reference current i_{1jref} to the short-circuit output current i_{sj} is given by:

$$N_j = \frac{i_{sj}}{i_{1jref}} = \frac{PI'_j \cdot G_{Nj}}{1 + PI'_j \cdot G_{Nj}} \cdot L_{Nj} \tag{2.6}$$

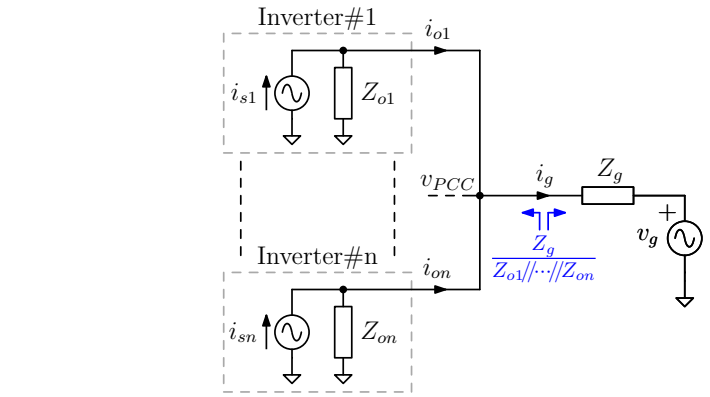

(A) Electrical scheme

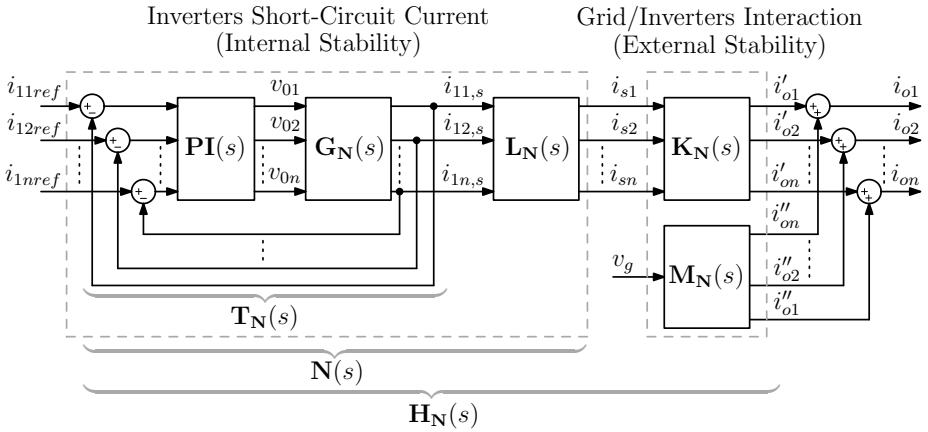

(B) Block scheme

FIGURE 2.4: The photovoltaic (PV) plant with n current-controlled inverters connected in parallel modeled as Norton equivalent generators. The stability contributions are highlighted and the grid voltage contribution in the output currents is considered.

2.2.1.2 Output impedance Z_o

Similarly, by referring to Fig. 2.2, the output impedance Z_O can be expressed as:

$$Z_{oj} = Z_{2j} + Z_{1j,CL} // Z_{3j} \tag{2.7}$$

where $Z_{1j,CL} = Z_{1j} \cdot \left(1 + PI'_j / Z_{1j}\right)$ is the closed loop impedance.

2.2.2 Modeling of the Whole Plant

In Fig. 2.4a, n-inverters modeled with the Norton equivalent generator derived in Sec. 2.2.1.1 are connected in parallel. The resulting system can be represented as a MIMO system, as shown in Fig. 2.4b. The block scheme is divided in two parts:

- the first part consists of n single-input single-output (SISO) systems combined together using all diagonal matrices $\mathbf{PI}(s)$, $\mathbf{G_N}(s)$, $\mathbf{L_N}(s)$ and the resulting $\mathbf{N}(s)$;
- the second part consists of two non-diagonal matrices $\mathbf{K_N}(s)$ and $\mathbf{M_N}(s)$, which represent, respectively, the output current contributions from the inverters and from the grid.

Before going into the PV plant analysis, the most important vectors (with dimension $n \times 1$) are defined next:

- $\mathbf{i_{1nref}} = [i_{11ref}, \ldots, i_{1nref}]^T$: inverters current references;
- $\mathbf{v_{0n}} = [v_{01}, \ldots, v_{0n}]^T$: voltages impressed by inverters bridges of switches;
- $\mathbf{i_{1n,s}} = [i_{11,s}, \ldots, i_{1n,s}]^T$: controlled inverters currents in short-circuit condition;
- $\mathbf{i_{sn}} = [i_{s1}, \ldots, i_{sn}]^T$: inverters output current in short-circuit condition;
- $\mathbf{i'_{on}} = [i'_{o1}, \ldots, i'_{on}]^T$: inverter contributions to the output currents;
- $\mathbf{i''_{on}} = [i''_{o1}, \ldots, i''_{on}]^T$: grid contributions to the output currents;
- $\mathbf{i_{on}} = [i_{o1}, \ldots, i_{on}]^T$: total output currents.

All the matrices defined hereafter have dimension $n \times n$.

2.2.2.1 Internal Stability

The matrix $\mathbf{N}(s)$ (see Fig. 2.4b) collects all the terms to obtain the output short-circuit currents:

$$\mathbf{i_{sn}} = \mathbf{T_N}(s) \cdot \mathbf{L_N}(s) \cdot \mathbf{i_{1nref}} = \mathbf{N}(s) \cdot \mathbf{i_{1nref}} \tag{2.8}$$

where the transfer function matrix $\mathbf{T_N}(s)$ is given by

$$\mathbf{T_N}(s) = [\mathbf{I} + \mathbf{G_N}(s) \cdot \mathbf{PI}(s)]^{-1} \cdot \mathbf{G_N}(s) \cdot \mathbf{PI}(s) \tag{2.9}$$

The terms of the matrices $\mathbf{G_N}(s) = \text{diag}\{G_{N1}, \ldots, G_{Nn}\}$, $\mathbf{L_N}(s) = \text{diag}\{L_{N1}, \ldots, L_{Nn}\}$, $\mathbf{T_N}(s) = \text{diag}\{T_{N1}, \ldots, T_{Nn}\}$ and $\mathbf{N}(s) = \text{diag}\{N_1, \ldots, N_n\}$ are defined in (2.3), (2.4), (2.5) and (2.6), respectively (for $j = 1, \ldots, n$).

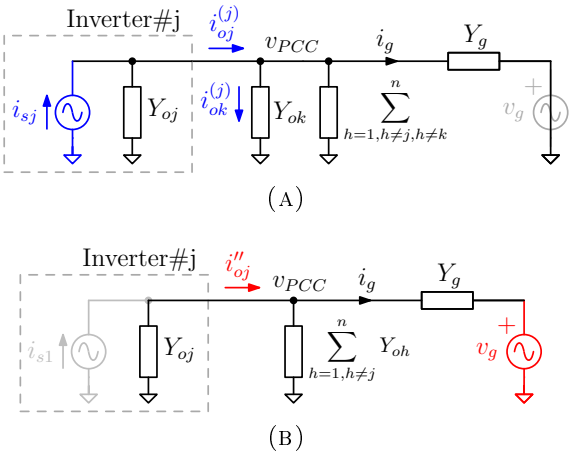

FIGURE 2.5: Electrical scheme for the contribution calculation from (a) the inverters and (b) from the grid.

It is worth observing that all the considered matrices are diagonal: this stems from the fact that there is no coupling between the inverters, due to the short-circuit condition. For this reason the poles of $\mathbf{T_N}(s)$ are related to the stability of the inverters considered individually [46] and are called *internal poles*.

2.2.2.2 External Stability

The output currents are determined by the contributions coming from all the inverters, through the matrix $\mathbf{K_N}(s)$, and the grid voltage, through the matrix $\mathbf{M_N}(s)$ (see Fig. 2.4b). External stability concerns the interaction between the parallel inverters and the grid [46], therefore, as shown in the following of this subsection, the corresponding poles to look at for this stability analysis are common to all the inverters. In the general case of different inverters, the matrix $\mathbf{K_N}(s)$ has all non-equal terms:

$$\mathbf{i'_{on}} = \underbrace{\begin{pmatrix} K_{N11} & K_{N12} & \cdots & K_{N1n} \\ K_{N21} & K_{N22} & \cdots & K_{N2n} \\ \vdots & \vdots & \ddots & \vdots \\ K_{Nn1} & K_{Nn2} & \cdots & K_{Nnn} \end{pmatrix}}_{\mathbf{K_N}(s)} \cdot \mathbf{i_{sn}} \tag{2.10}$$

where, by using the admittances $Y_{oj} = 1/Z_{oj}$ and $Y_g = 1/Z_g$ of the scheme in Fig. 2.5a, it yields:

$$K_{Njj} = \frac{1 + \frac{\sum_{h=1,h\neq j}^{n} Y_{oh}}{Y_g}}{1 + \frac{\sum_{h=1}^{n} Y_{oh}}{Y_g}}, \quad K_{Njk} = \frac{-\frac{Y_{ok}}{Y_g}}{1 + \frac{\sum_{h=1}^{n} Y_{oh}}{Y_g}} \tag{2.11}$$

for $j = 1, \ldots, n$ and $k = 1, \ldots, n$. Notably, the two terms have the same denominator and the stability is determined by the impedance ratio $\sum_{h=1}^{n} Y_{oh}/Y_g = Z_g/(Z_{o1}/\!/\cdots/\!/Z_{on})$, as reported in Fig. 2.4a. Hence, the output currents contributions $\mathbf{i'_{on}}$ due to the inverters can be determined as:

$$\mathbf{i'_{on}} = \mathbf{H_N}(s) \cdot \mathbf{i_{1nref}} \tag{2.12}$$

where $\mathbf{H_N}(s) = \mathbf{N}(s) \cdot \mathbf{K_N}(s)$ and

$$H_{Njj} = N_j \cdot K_{Njj} \quad , \quad H_{Njk} = N_j \cdot K_{Njk} \tag{2.13}$$

for $j = 1, \ldots, n$ and $k = 1, \ldots, n$ and $j \neq k$.

The grid voltage contribution to the inverter output currents, here called *grid sensitivity*, as in [41], according to Fig. 2.4b can be determined as:

$$\mathbf{i''_{on}} = \mathbf{M_N}(s) \cdot v_g \tag{2.14}$$

where $\mathbf{M_N}(s) = [M_{N1}, \ldots, M_{Nn}]^T$ is the vector for the grid sensitivity transfer functions. The term M_{Nj}, for $j = 1, \ldots, n$, can be calculated according to Fig. 2.5b as:

$$M_{Nj} = -\frac{Y_{oj}}{1 + \frac{\sum_{h=1}^{n} Y_{oh}}{Y_g}} \quad . \tag{2.15}$$

The equivalence of the denominators in (2.11) and (2.15) can be noticed. In particular, the two matrices have the same poles so, as depicted in Fig. 2.4b, the external stability can be studied by looking at the poles of $\mathbf{K_N}(s)$ or $\mathbf{M_N}(s)$.

Finally, considering both the inverters and the grid voltage contributions, the total output currents can be calculated as:

$$\mathbf{i_{on}} = \mathbf{i'_{on}} + \mathbf{i''_{on}} = \mathbf{H_N}(s) \cdot \mathbf{i_{1nref}} + \mathbf{M_N}(s) \cdot v_g \tag{2.16}$$

The poles of $\mathbf{K_N}(s)$ and $\mathbf{M_N}(s)$ are called *external poles* and are related to the interaction between the inverters and the grid [46, 47] or equivalently to the impedance ratio [22, 30, 59, 63].

When a new inverter is added to the system:

1. the short-circuit current stability contribution of the new inverter $\mathbf{N}(s)$ is added as a new diagonal term;

2. the terms in the matrices $\mathbf{K}(s)$ and $\mathbf{M}(s)$ change because of the new impedance connected to the system, according to (2.11) and (2.15), respectively.

The main advantage of the modeling presented above, as compared to [46], is the possibility to accurately describe the entire system by a modular approach, also in case of inverters with different parameters connected in parallel. This analysis can be applied also to other systems of parallel converters.

2.2.3 Equal Parallel Inverters

In case of equal inverters connected in parallel, all the short-circuit currents, output impedances, and, consequently, admittances, are equal (i.e., $i_s = i_{sj}$, $Z_o = Z_{oj}$, $Y_o = Y_{oj}$, for $j = 1, \ldots, n$). In this particular condition, because of the equivalence between inverters, the terms (2.6) composing $\mathbf{N}(s)$ become all equal. The matrix $\mathbf{K_N}(s)$ in (2.10) becomes symmetric, with the diagonal and non-diagonal terms K_{Nd} and K_{Nnd}:

$$K_{Nd} = \frac{Z_o + (n-1) \cdot Z_g}{Z_o + n \cdot Z_g}, \quad K_{Nnd} = -\frac{Z_g}{Z_o + n \cdot Z_g} \tag{2.17}$$

Finally, the matrix $\mathbf{M_N}(s)$ in (2.14) has all equal terms

$$M_N = \frac{1}{Z_o + n \cdot Z_g} \quad . \tag{2.18}$$

The matrix $\mathbf{H_N}(s)$ can be easily calculated. The resulting terms can be compared to the analysis in [46], adding an additional matrix to obtain the inverter output currents, as done in [60]: the two analyses give the same results. However, contrarily to the analysis in [46], the main advantage of this approach lies on the possibility to model the inverters independently from each other and finally combine them in the final MIMO system. Moreover, this approach analyzes the internal and external poles separating distinctly the two contributions (i.e., internal and external), as highlighted in Fig. 2.4b.

2.2.4 The Impedance Multiplication Effect

In this section, the impedance multiplication effect is applied for the case of equal and different parallel inverters.

2.2.4.1 Equal Parallel Inverters

As discussed in [46], by connecting n-paralleled equal inverters to Z_g, the impedance perceived by each inverter is $n \cdot Z_g$. Hence, it is possible to establish the stability conditions of n inverters in an equivalent single inverter system with the impedance multiplied by n, as depicted in Fig. 2.6. This is true because the systems of Fig. 2.2 and Fig. 2.4a present at the PCC the same impedance ratio $n \cdot Z_g/Z_o$ of the system of Fig. 2.6. In Fig. 2.6b the terms G_{Neq}, L_{Neq}, T_{Neq}, N_{eq} in the block scheme are equal to the terms in (2.3), (2.4), (2.5), and (2.6), respectively. The remaining terms K_{Neq} and M_{Neq} can be evaluated from K_{Nd} in (2.17) and M_N in (2.18) for $n = 1$ and then substituting Z_g with $n \cdot Z_g$.

Internal Poles Cancellation: As stated in [46], in this equivalent representation the internal stability poles disappear. By the proposed approach the cancellation of these poles can be analytically proven. Indeed, in the following expression of H_{Neq}:

$$\begin{aligned} H_{Neq} &= N_{eq} \cdot K_{Neq} = \\ &= \left(\frac{PI' \cdot Z_3}{Z_2 \cdot Z_3 + (PI' + Z_1) \cdot (Z_2 + Z_3)} \right) \cdot K_{Neq} \end{aligned} \tag{2.19}$$

the internal poles—given by the denominator of N_{eq}—cancel out with the numerator of K_{Neq}. This derivation shows why in impedance-based representations of the equivalent single inverter case do not have any of these internal poles. These poles are those of the minimal realization of the system $\mathbf{H_N}(s)$, which cancel out also in case they are unstable (i.e., lying in the right-half plane) [64]. In case of equal multi-paralleled inverters, where the internal poles affect the overall system stability, the term $(n-1) \cdot Z_g$ in the numerator of K_{Nd} in (2.17) is not null and the cancellation described above does not take place.

2.2.4.2 Different Parallel Inverters

It is possible to apply the impedance multiplication effect in a general case following these steps:

1. consider a generic j-th inverter (for $j = 1, \ldots, n$) and its output impedance as the reference impedance:

$$Z_o^* = Z_{oj} \quad , \qquad Y_o^* = Y_{oj} \tag{2.20}$$

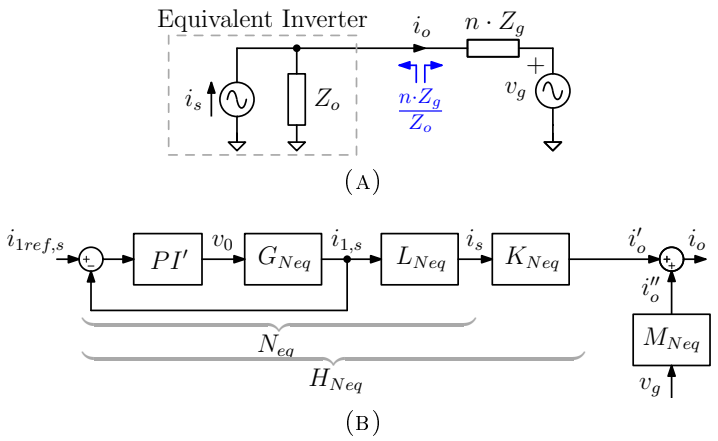

FIGURE 2.6: Equivalent inverter for equal parallel inverters case: (a) electrical scheme and (b) block scheme.

In Fig. 2.7a, $j = 1$ (i.e., $Z_o^* = Z_{o1}$).

2. express all the other $n-1$ inverters output impedances as $Z_{ok} = Z_o^* /\!/ Z_{xk}$ (or $Y_{ok} = Y_o^* + Y_{xk}$), thus:

$$Z_{xk} = \frac{Z_o^* \cdot Z_{ok}}{Z_o^* - Z_{ok}} \quad , \quad Y_{xk} = Y_{ok} - Y_o^* \tag{2.21}$$

for $k = 1, \ldots, n$ and $k \neq j$.

3. since the difference contributions Z_{xk} are in parallel:

$$Z_x = \left(\sum_{k=1, k \neq j}^{n} \frac{1}{Z_{xk}} \right)^{-1} \quad , \quad Y_x = \sum_{k=1, k \neq j}^{n} Y_{xk} \tag{2.22}$$

4. put the resulting Z_x next to the grid impedance Z_g: now all the inverters have the same output impedance. The impedance multiplication effect can be applied to the new grid impedance $\tilde{Z}_g$, in Fig. 2.7a:

$$\tilde{Z}_g = Z_x /\!/ Z_g \quad , \quad \tilde{Y}_g = Y_x + Y_g \quad . \tag{2.23}$$

With this process it is possible to evaluate the impedance perceived by each inverter, due to parallelization, also in case of unequal parallel inverters: the current loop gain and the grid sensitivity can be evaluated as in the case of equal parallel inverters substituting $\tilde{Z}_g$ to Z_g. To be noticed that the short-circuit equivalent generators in Fig.2.6a are different (i.e., the internal poles are different).

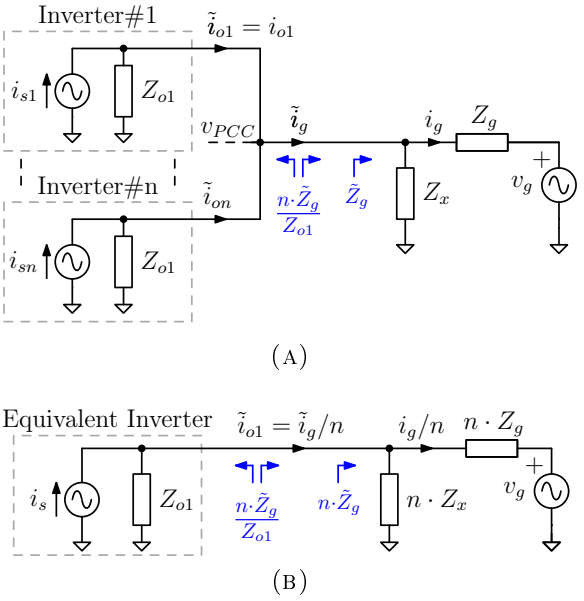

FIGURE 2.7: Application of the impedance multiplication effect for the different parallel inverters case, inverter#1 as reference ($Z_o^* = Z_{o1}$): (a) isolation of the difference contribution ($Z_x = Z_{x2} /\!/ \cdots /\!/ Z_{xn}$) and (b) equivalent inverter with the multiplied impedance.

2.3 Application Example

The theoretical framework presented in Sec. 2.2.4.2 is now applied to an example case composed of two different inverters connected to the PCC by means of interconnection impedances (e.g., cable impedance). The interconnecting impedance for the j-th inverter is indicated as Z_{Cj} and it can be easily taken into account by inclusion in the term Z_{2j} of Fig. 2.2 and, therefore, in the output impedance Z_{oj}. The effect on system stability of the interconnecting impedances and of different inverters power ratings are analyzed, showing, in particular, the effectiveness of the approach in highlighting how the impedance perceived by single inverters change due to parallelization. As shown, increasing inverter power ratings and impedances Z_{Cj} will create a resonance on the multiplied impedance, bringing the system to instability.

Specifically, three configuration cases are considered: *Case I* refers to the basic case of equal parallel inverters, *Case II* considers the effect of connection impedance with different values, *Case III* considers a different power rating for the second inverter. To more clearly show the effectiveness of the developed analysis, a double PI controller in the form:

$$G_c(s) = \left(k_{P1} + \frac{k_{I1}}{s}\right) \cdot \left(k_{P2} + \frac{k_{I2}}{s}\right) \tag{2.24}$$

with a designed crossing frequency of $f_c = 700\,\text{Hz}$ and a phase margin of $\phi_M = 40^o$ is used for G_c in (4.1). For this example of application, an analog implementation with $G_{dpmw} = 1$ is assumed. System parameters are listed in Tab. 2.1.

In the following, the three cases are analyzed, taken inverter#1 as reference converter, as in Fig. 2.7a. Impedance Z_x is then calculated as in (2.22) and the impedance multiplication effect is applied, as in Fig. 2.7b, which finally allows to evaluate the impedance ratio $n \cdot \tilde{Z}_g / Z_{o1}$.

Case I two equal parallel inverters are considered in a stable configuration. The impedances of the lines connecting the inverters to the PCC are considered both equal to pure inductors of value 0.2 mH, while the capacitive behavior of the lines is negligible at the considered frequencies. The grid impedance $Z_g = R_g + sL_g$ is, typically, determined mainly by the LV/HV transformer leakage inductance, referred to the LV side, here $L_g = 3\,\text{mH}$ and $X/R = 8$. The influence of this impedance is further emphasized because of the multiplication effect, especially in case of a large number of inverters, and so it is one of the most crucial parameters of the system. The admittance defined in (2.22) is $Y_x^{(\text{I})} = 0$, because the control, the power rating, and the line impedances are equal. Hence, the impedance perceived by the first inverter is $2\tilde{Z}_g^{(\text{I})} = 2Z_g$ as discussed in Fig. 2.7b for $n = 2$. The reference impedance Z_{o1} and the perceived impedance $2 \cdot Z_g$ can be observed in Fig. 2.8, where a stable intersection is achieved. This is confirmed by the plot of the impedance ratio displayed in Fig. 2.9a, in which the critical point $-1 + j0$ is not encircled.

Case II inverter#2 is now connected through a distribution line ten times longer: $Z_{C1}^{(\text{II})} = 0.2\,\text{mH}$, $Z_{C2}^{(\text{II})} = 2\,\text{mH}$, therefore, $Z_x^{(\text{II})} \neq 0$. The resulting impedance perceived by inverter#1 is then $2\tilde{Z}_g^{(\text{II})} = 2(Z_x^{(\text{II})} \,/\!/\, Z_g)$. As visible in Fig. 2.8, a low-frequency resonance intersecting the reference impedance appears. The correspondent impedance ratio is shown in Fig. 2.9b, which shows that the critical point is encircled in this configuration.

Case III in this case inverter#2 is considered with a power rating five times bigger than in *Case I*: $P_{N2}^{(\text{III})} = 5P_N = 25\,\text{kW}$. Because of this variation $Z_x^{(\text{III})} \neq 0$, and the perceived impedance is $2\tilde{Z}_g^{(\text{III})} = 2(Z_x^{(\text{III})} /\!/ Z_g)$, which is reported in Fig. 2.8. As in *Case II*, a resonance appears in the perceived impedance, causing an unstable intersection with the reference impedance. The resulting impedance ratio is shown in Fig. 2.9c, where the instability point is encircled.

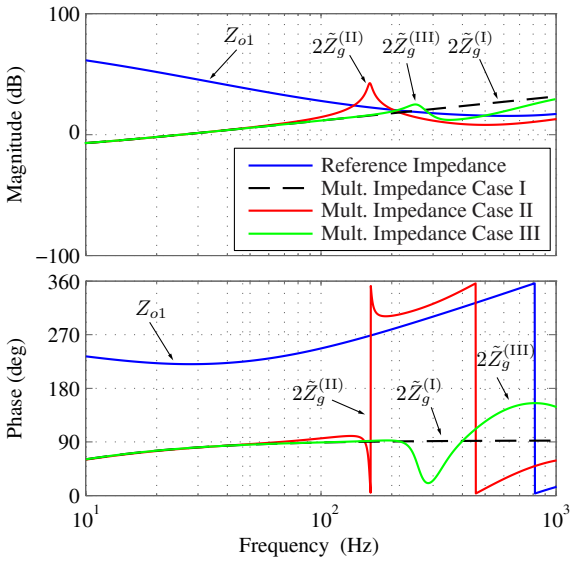

FIGURE 2.8: Bode diagram of the reference inverter impedance and of the perceived grid impedance for impedance ratio analysis in *Case I* two equal parallel inverters, *Case II* equal inverter connected with different cable impedances, *Case III* inverters of different power ratings. System configuration like in Fig. 2.2 with two inverters (i.e., $n = 2$).

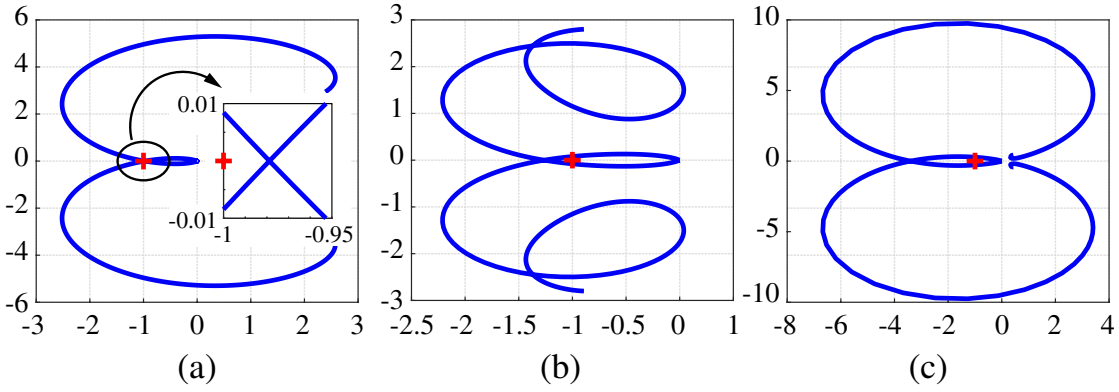

FIGURE 2.9: Nyquist plot of the impedance ratio in: *Case I* two equal parallel inverters, *Case II* equal inverter connected with different cable impedances, *Case III* inverters of different power ratings.

2.4 Experimental Results

This section presents the simulation and experimental results for stability and grid sensitivity analysis. The main experimental setup parameters are reported in Tab. 2.1. The setup consists of three single-phase inverters with LCL output filter controlled by corresponding digital signal processors (DSPs) TI TMS320F2810. The controller described in the following paragraph together with PWM and the synchronization block based on a PLL are implemented in the DSPs. Grid

impedances Z_g are implemented by real, ferrite core inductors with adequate saturation current and size, so that their equivalent series resistances are negligible with respect to the reactance values around and above the grid frequency. The VCI is equipped with additional external capacitances and with a properly designed voltage controller in order to reduce the output impedance Z_{oV} and reach the condition $Z_{oV} \ll Z_g$ in the frequency range of interest. The experimental waveforms of grid voltage and current in case of instability (reported in Fig. 2.12) are acquired as raw data and plotted by Matlab. The disturbances for grid sensitivity measurements are added to the reference of the VCI and the resulting voltages and currents are measured with a sampling frequency of 100 kS/s for an observation window of 1 s. The post-processing is performed by a Matlab script that automatically generates grid sensitivity plots. A corresponding, accurate model of the system has been developed in Matlab/Simulink and the obtained results compared with the theoretical analysis and the experimental measurements.

An external instability case is studied in the following subsections. At first, the open-loop gain T_{OL} of the equivalent inverter case in Fig. 2.10a is analyzed for different values of normalized grid impedance, identifying those values that bring to instability. The unstable case is then evaluated by comparing the results obtained in the two configurations displayed in Fig. 2.10. Finally, the predicted from the theoretical modeling, the simulated, and the measured grid sensitivity for the equivalent inverter case and the three inverters case are reported and discussed.

2.4.1 Stability Analysis

The controller G_c adopted in this experimental validation is the one referred to in Sec. 2.3, with the same crossover frequency and phase margin. On the other hand, a symmetrical, unitary amplitude, triangular carrier modulation is now used, which can be modeled as [61]:

$$G_{dpwmj} = e^{-sT_{sw}/2} \tag{2.25}$$

where T_{sw} is the switching period (see Table 2.1). The current open loop gain results:

$$T_{OL} = PI' \cdot \frac{1}{Z_{1j} + Z_{3j} /\!/ (Z_{2j} + (3Z_g + Z_{oV}))}; \tag{2.26}$$

with PI' defined in (4.1) and Z_{1j}, Z_{2j}, and Z_{3j} defined in (2.2).

Parameter	Symbol	Value	Unit
Nominal power	P_N	5	kW
Nominal voltage	V_N	230	V
Base impedance	Z_{BASE}	10.58	Ω
Frequency PWM	$1/T_{sw}$	12.5	kHz
DC voltage	V_{DC}	400	V
Inverter side inductance	x_{L1}	0.047	p.u.
Grid side inductance	x_{L2}	0.002	p.u.
Capacitor	y_{C3}	0.033	p.u.
Proportional gain	k_{P1}, k_{P2}	0.028, 0.657	–
Integral gain	k_{I1}, k_{I2}	43, 667	–

TABLE 2.1: Test Case Parameters

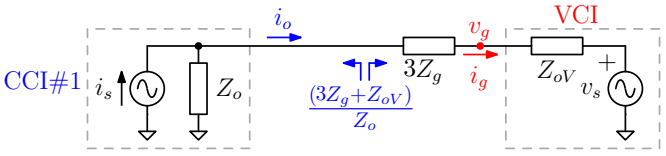

(A) Equivalent inverter case

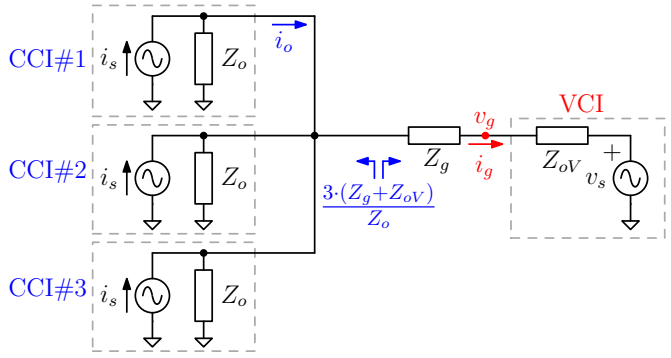

(B) Three paralleled inverters case

FIGURE 2.10: Configurations of the experimental setup ($Z_{oV} \ll Z_g$).

The behavior of T_{OL} for different values of x_L (i.e., the normalized grid inductance L_g with respect to Z_{BASE}) is displayed in Fig. 2.11. By analyzing Fig. 2.11a, it is possibile to notice that the crossing frequency and the phase margin of T_{OL} decrease as the applied inductance increases.

For $x_L = 0.65$ p.u., in correspondence to the T_{OL} crossing frequency the phase margin is negative and the system in Fig. 2.10a becomes unstable; the corresponding time domain waveforms obtained from experimental measurements are reported in Fig. 2.12a (the described unstable control is activated as reported in the figure), causing an unstable mode. The divergence of the current stops because of the saturation of the double PI controller and a waveform superimposed to the fundamental frequency appears on both current and voltage. The same

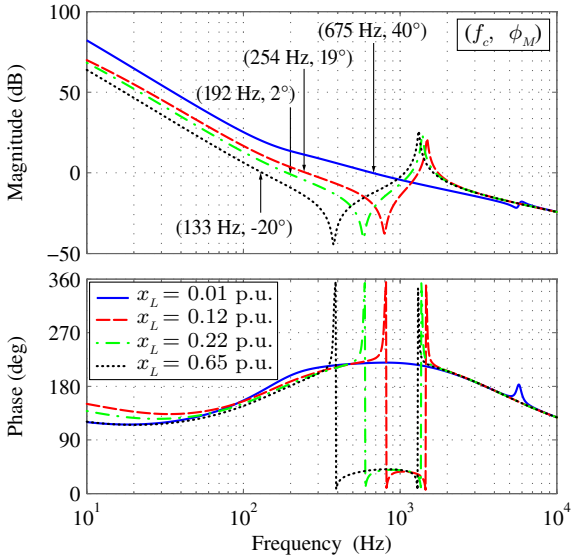

(A) Current Open Loop Gain - Bode diagram

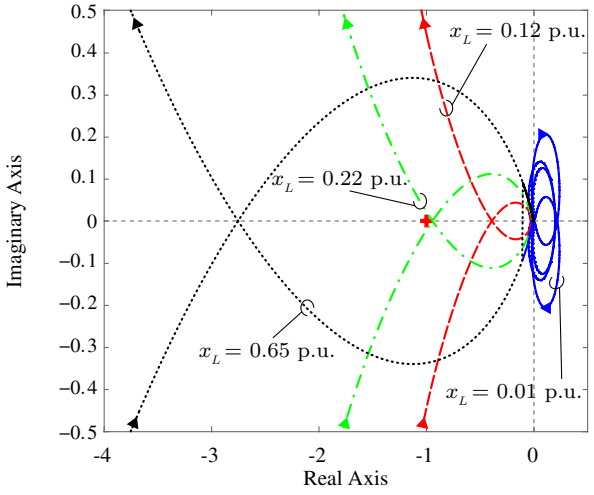

(B) Impedance Ratio - Nyquist diagram

FIGURE 2.11: Stability analysis: (a) Bode diagram of the current open loop gain T_{OL} given by (2.26), (b) corresponding Nyquist diagram of the impedance ratio according to the impedance-based approach.

instability also occurs for $x_L = 0.22\,\text{p.u.} = 0.65\,\text{p.u.}/3$ in the case of Fig. 2.10b, whose time domain waveforms are reported in Fig. 2.12b. Fig. 2.13 reports the spectrum of the measured current waveforms, where an oscillation frequency of 130 Hz, for the equivalent inverter case, and 112 Hz, for the three inverters case, can be observed. The difference between the measured oscillating frequencies is due to the tolerances of the adopted real inductances used in the implementation of the setups.

The x_L values chosen for the unstable case guarantee the same stability conditions in the two test cases depicted in Fig.2.10, where $Z_{oV} \ll Z_g$, and the

impedance ratio is shown in Fig.2.11b for the equivalent inverter case. As can be noticed, when the normalized inductance is $x_L = 0.65\,\text{p.u.}$ the instability point $-1 + j \cdot 0$ is encircled by the curve, and the system described becomes unstable as found from the current open loop gain considerations: this instability can be found from both the MIMO analysis in [46, 47] and the impedance-based analysis [30, 56, 57]. This confirms that the *external poles* are related to the interactions between the inverters and the grid, or equivalently to the impedance ratio of the considered circuit. The internal poles are stable by design.

It is worth remarking that, although the values of x_L seem relatively high as compared to those of a typical weak grid (see, e.g., [65], where a single grid-connected inverter is analyzed), the values used in the test considered herein are realistic; indeed, a very high number of parallel connected inverters causes a particularly high perceived grid impedance.

2.4.2 Grid Sensitivity

The grid sensitivity is studied for different inductances and considering the cases of *i)* three independent inverters and *ii)* one corresponding equivalent inverter, to show the equivalence described in Sect. 2.2.4.

In Fig. 2.14 the analytical model is compared with simulation and experimental results (except for the unstable case). The obtained results show a good match between simulation and experimental behaviors. Notably, Fig. 2.14a and Fig. 2.14b show that by increasing the grid inductance the resonance associated with the instability shown in Fig. 2.12 appears at lower frequencies and with higher magnitudes. Indeed, the black curves show a phase lead in the range of the resonance peak, which indicates the presence of a couple of unstable poles.

The analysis of the grid sensitivity can be used to describe the total harmonic distortion (THD) increase in [41, 48], applying the analysis to the adopted control. The resonance frequencies in Fig. 2.12a are close to the crossing frequencies of the current loop gain and can cause an increase of the THD when the applied impedance changes, that is, when the number of parallel inverters increases. As discussed in [49], a system which guarantees a good stability margin for all the crossing frequencies considered has a lower variation in the THD.

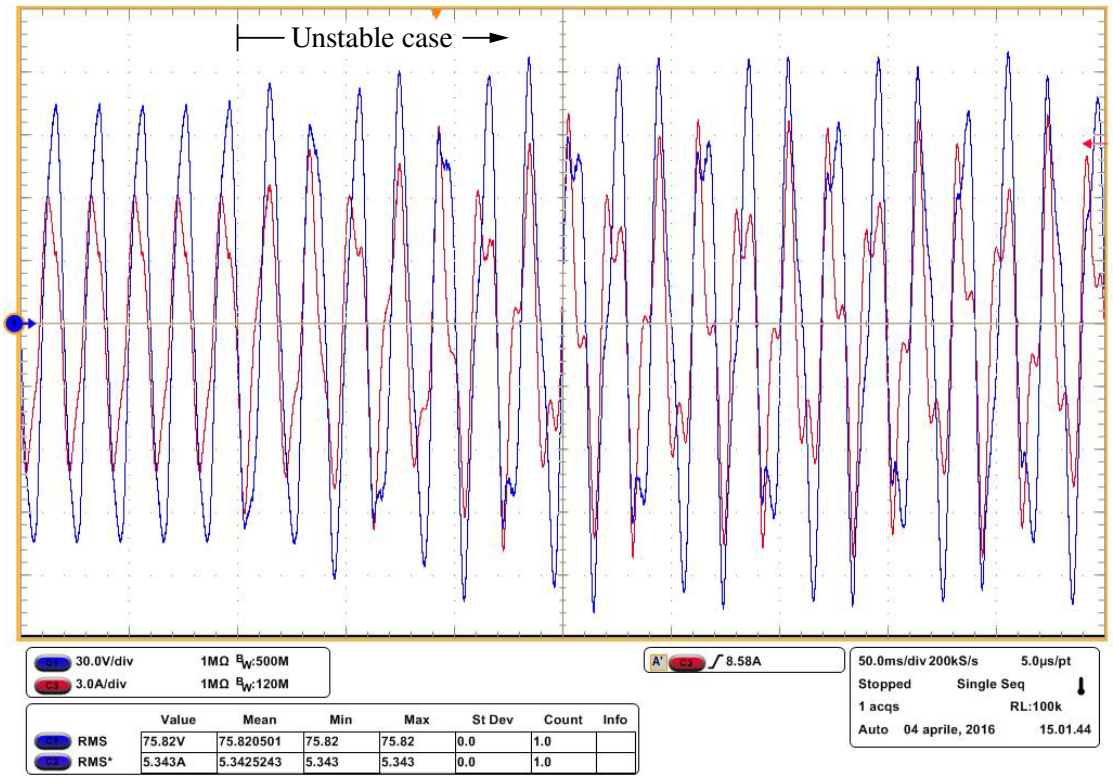

(A) Experimental results for the case in Fig. 2.10a

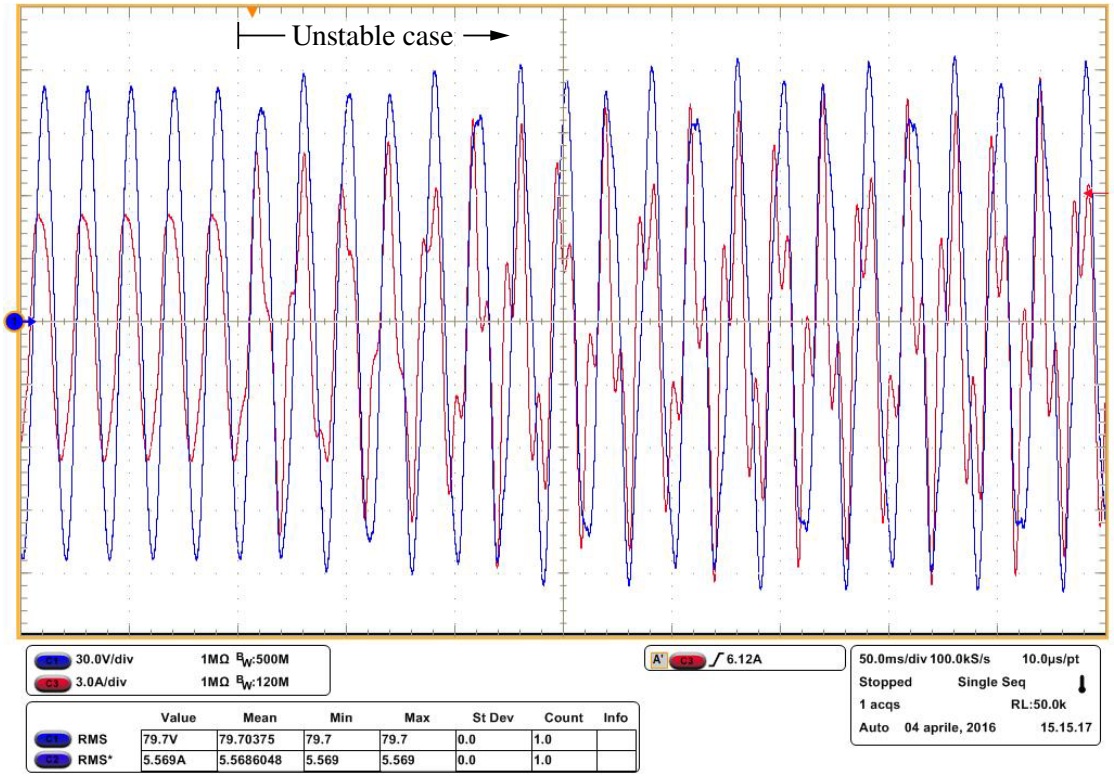

(B) Experimental results for the case in Fig. 2.10b

FIGURE 2.12: Test case for the stability and the grid sensitivity analysis: three CCI in parallel connected to the grid impedance and a VCI that emulates the grid. Blue traces represent voltage v_g, 30 V/div, red traces represent current i_g (3 A/div); the time-scale is 50 ms/div.

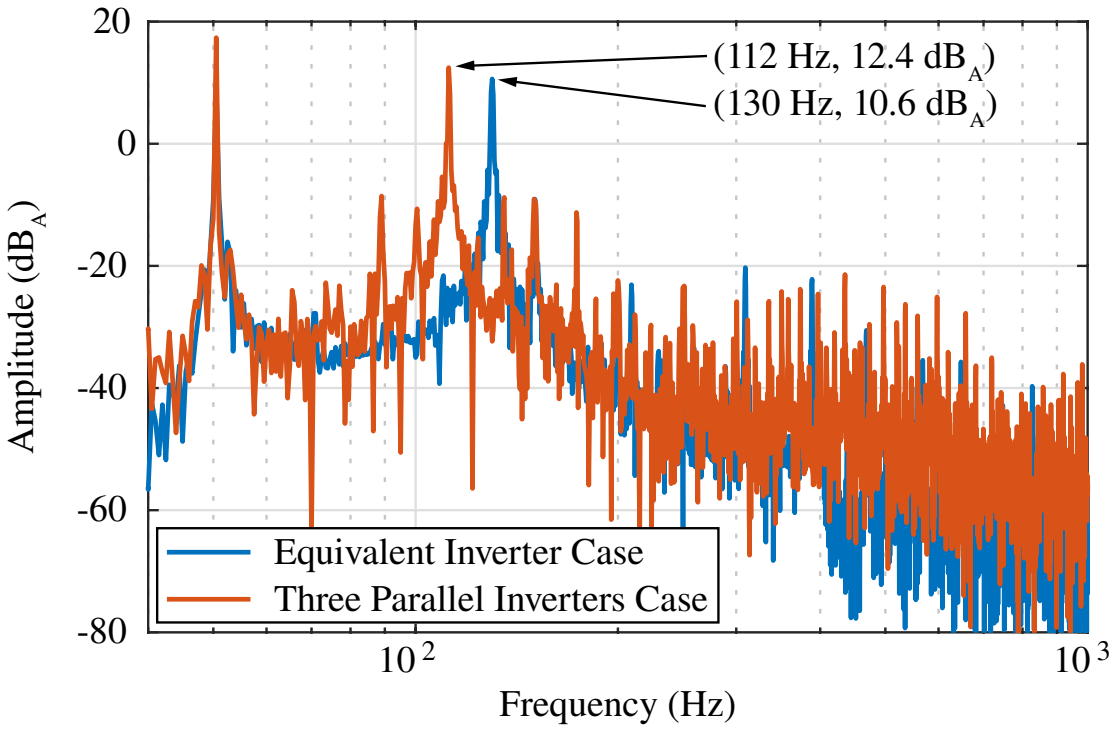

FIGURE 2.13: Frequency spectrum of the experimental results during instability shown in Fig. 2.12a and in Fig. 2.12b.

2.5 Conclusion

This chapter presents a complete modeling of a PV plant, with n-parallel grid-connected inverters. It is shown that existing MIMO approaches give all the stability contributions with a high complexity analysis, while impedance-based approaches have the advantage of being modular, but they do not comprehend all the relevant stability contributions. The stability analysis presented in this work features: *i)* accuracy and *ii)* scalability, as MIMO approaches, and *iii)* flexibility as the conventional impedance-based approach. Moreover, the presented analysis provides a clear explanation and separation of the stability contributions.

The impedance multiplication effect, which can be noticed in the equivalent inverter, is extended to the case of different parallel inverters. The latter is analyzed through simulations results, where the detrimental effects of the parallelization of inverters with a large line impedance or a large power rating are shown from the perspective of the reference inverter. Moreover, an external instability is presented and the grid sensitivity, namely, the influence of the grid voltage on the converter output current, is analyzed in case of multiple equal parallel inverters. Simulation and experimental results are presented for both the stability analysis and the grid sensitivity, using three parallel inverters and the equivalent inverter. Both

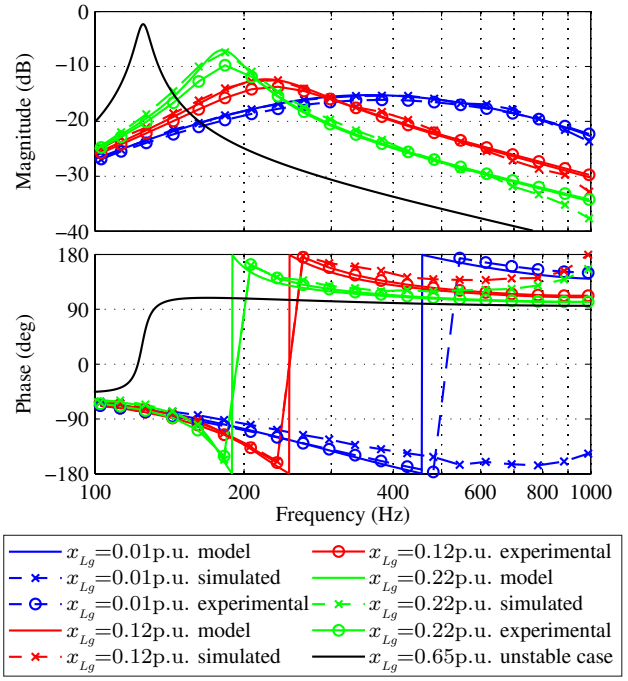

(A) Sensitivities M_{Neq} for the equivalent inverter case in Fig. 2.10a

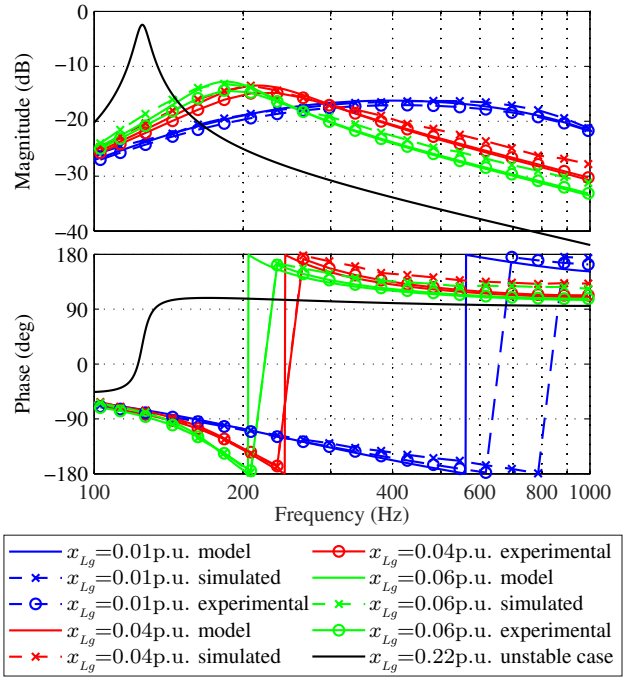

(B) Sensitivities M_N of (2.18) for the parallel inverters case in Fig. 2.10b

FIGURE 2.14: Simulation and experimental sensitivity measures for different values of connected impedances, for the cases in Fig. 2.10a and Fig. 2.10b.

the analyses highlight the need of a suitable controller design, in order to prevent instabilities, to reduce the harmonic distortion and to improve the power quality of the distribution grid.

Chapter 3

Three-Phase DER Modeling

In this chapter the three-phase modeling of a DER is presented. The understanding of the inverter control is crucial for the following chapters, where the simplification of inverter-induced dynamics can significantly reduce the complexity of both the modeling and the analysis. Moreover, the expressions here found are used in Chap. 5.

The first part reports the basic theory for three-phase inverter modeling as in [15, 66, 67]. The switching model is derived in Sec. 3.4 and then the average models in *abc*-frame and *dq*-frame are calculated in Sec. 3.5. Then the state-space model is derived in Sec. 3.6 together with the desired small-signal transfer function matrix needed for the control design.
Secondly, a faster equivalent method to derive the same small-signal transfer function matrix just calculated through state-space representation is presented in Sec. 3.7. The main advantages are of being less complicated and finding correspondences with the equivalent single-phase inverter case, with the only difference that the terms are no longer single-input single-output (SISO) transfer functions but multi-input multi-output (MIMO) transfer function matrices. This results in the presence of 2×2 matrices, whose the product is not commutative and has to be taken into account. All the analytical models of transfer function matrices and output impedances calculated are compared with simulation results.

Finally, the experimental measurements of the output impedance of the VSI is compared with the analytical models in two different cases. The impedance measurement unit (IMU) is introduced, in order to report the basic procedure and issues to measure the output impedance.

The DERs analyzed in this work consist essentially of three-phase voltage source inverters (VSIs), which are used as interfaces in renewable energy applications. In PV applications the conversion from the DC bus to the AC bus is necessary, and the synchronization to the grid is provided through a PLL and only the current controllers are used to deliver power to the grid [15, 31, 45]. The conversion for WG applications is provided through back-to-back converters, which combine a three-phase rectifier and a three-phase inverter sharing the DC voltage impressed on the capacitance, in order to provide an AC/DC-DC/AC conversion and, once again, only current controllers are used to provide power to the grid [68–70].

In islanded grids, especially for battery energy storage systems (BESSs), the power loops of the droop control provide angle and amplitude through the P/f and Q/V laws, which are given as references to a three-phase VSI [71–74].

VSIs are time-varying non-linear systems, while the stability criteria discussed in Chap. 1 are suitable for linear systems: for this reason it is necessary to linearize the model through the small-signal perturbations [15, 75, 76]. The derived small-signal model can subsequently be expressed in the desired reference frame, such as the stationary *abc*- and $\alpha\beta$-frames or the synchronous *dq*-frame. The latter, contrarily to the stationary reference frames, has a constant value operating point, providing a more effective strategy to control the output signals and a better tracking of the references at the fundamental frequency.

The model of the VSI includes a stiff grid V_{dc} connected to a three-phase switching network. The voltages impressed by the switches is then filtered by an LC filter, where the parasitics resistances are considered.

In this work, the VSI is considered in order to analyze the droop-controlled inverter inner dynamics. Typically, the droop-controlled inverter is connected to a resistive-inductive load. The inductive part can be added on purpose or intrinsically due to the cables, and provides the decoupling effect between the active and reactive power loops. For this reason, the VSI will be evaluated in presence of a resistive-inductive load represented by R_L and L_L, respectively.

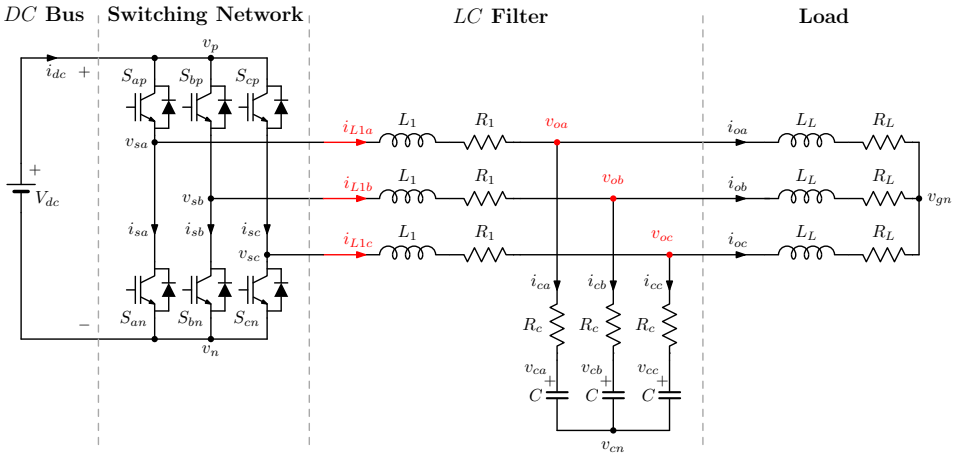

FIGURE 3.1: Three-phase voltage-controlled inverter

3.1 Vectors definition in *abc*-frame

The vectors of the main quantities are here defined in *abc*-frame. The voltage vectors

$$\begin{aligned}
\underline{v}_{sabc} &= [v_{sa}\, v_{sb}\, v_{sc}]^T \\
\underline{v}_{gabc} &= [v_{ga}\, v_{gb}\, v_{gc}]^T \\
\underline{v}_{cabc} &= [v_{ca}\, v_{cb}\, v_{cc}]^T \\
\underline{v}_{oabc} &= [v_{oa}\, v_{ob}\, v_{oc}]^T \\
\underline{v}_{nabc} &= [v_n\, v_n\, v_n]^T \\
\underline{v}_{gnabc} &= [v_{gn}\, v_{gn}\, v_{gn}]^T \\
\underline{v}_{cnabc} &= [v_{cn}\, v_{cn}\, v_{cn}]^T
\end{aligned} \tag{3.1}$$

and the current vectors

$$\begin{aligned}
\underline{i}_{L1abc} &= [i_{L1a}\, i_{L1b}\, i_{L1c}]^T \\
\underline{i}_{L2abc} &= [i_{L2a}\, i_{L2b}\, i_{L2c}]^T \\
\underline{i}_{cabc} &= [i_{ca}\, i_{cb}\, i_{cc}]^T
\end{aligned} \tag{3.2}$$

are defined.

3.2 Switching Network

The VSI consists of a switching network, which model has been developed in [75]. The switches represented in Fig. 3.1 consist of insulated-gate bipolar transistors

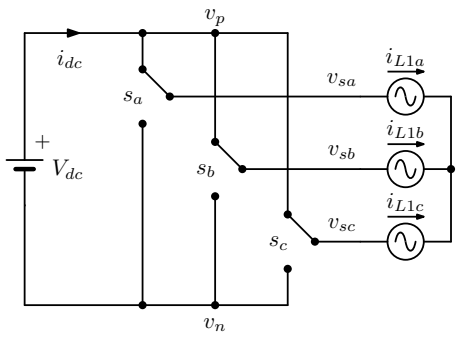

FIGURE 3.2: Three-phase voltage-controlled inverter

(IGBTs), which for the purpose of this analysis can be simplified as ideal switches as reported in Fig. 3.1. The DC source V_{dc} can not be short-circuited by the switches, while a path for the inductor current must always be provided [15]. Hence, the allowed combinations can be represented by the relation:

$$s_{ip} + s_{in} = 1 \qquad i \in \{a, b, c\} \tag{3.3}$$

where only one of the switches in a, b, c legs can be on, while the other has to be off. From this relation, the possible combinations can be analyzed as reported in Tab.3.1. Some important relations can be found:

s_a	s_b	s_c	i_{dc}	v_{sa}	v_{sb}	v_{sc}
0	0	0	0	0	0	0
0	0	1	i_{L1c}	0	0	V_{dc}
0	1	0	i_{L1b}	0	V_{dc}	0
0	1	1	$i_{L1b} + i_{L1c}$	0	V_{dc}	V_{dc}
1	0	0	i_{L1a}	V_{dc}	0	0
1	0	1	$i_{L1a} + i_{L1c}$	V_{dc}	0	V_{dc}
1	1	0	$i_{L1a} + i_{L1b}$	V_{dc}	V_{dc}	0
1	1	1	$i_{L1a} + i_{L1b} + i_{L1c}$	V_{dc}	V_{dc}	V_{dc}

TABLE 3.1: Switches combinations

$$\begin{aligned} i_{dc} &= \begin{bmatrix} s_a & s_b & s_c \end{bmatrix} \cdot \begin{bmatrix} i_{L1a} \\ i_{L1b} \\ i_{L1c} \end{bmatrix} = \underline{s}_{abc}^T \cdot \underline{i}_{L1abc} \\ \underline{v}_{sabc} &= \begin{bmatrix} s_a \\ s_b \\ s_c \end{bmatrix} V_{dc} = \underline{s}_{abc} V_{dc} \end{aligned} \tag{3.4}$$

3.3 *LC* Filter

In this section the voltage and current Kirchhoff laws are applied, in order to describe the LCL filter network with the state-space representation. In Fig.3.2 the three-phase LC filter is represented, where the switching network is represented via voltage sources. Moreover, a resistive-inductive (R_L, L_L) load is considered. In Fig. 3.3b an equivalent representation with vectors is shown, where the nodes and the voltage loops are highlighted.

KCL N_4: in the node N_4 the currents

$$\underline{i}_{L1abc} = \underline{i}_{oabc} + \underline{i}_{cabc} \tag{3.5}$$

where

$$\underline{i}_{cabc} = C\frac{d\underline{v}_{cabc}}{dt} \tag{3.6}$$

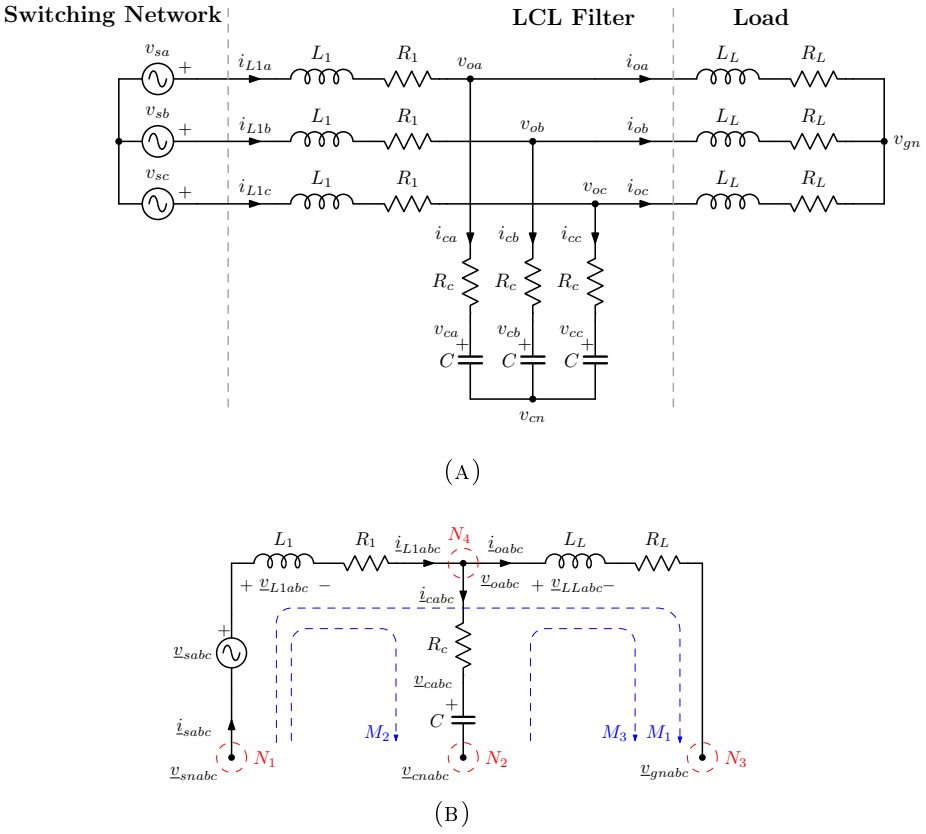

FIGURE 3.3: LC filter of the three-phase voltage source inverter: (a) three-phase representation and (b) equivalent vector representation.

Therefore, the state $\underline{v}_{cabc}$ can be written as follows:

$$\frac{d\underline{v}_{cabc}}{dt} = \frac{1}{C}\underline{i}_{L1abc} - \frac{1}{C}\underline{i}_{oabc} \tag{3.7}$$

KVL M_1: Considering the branches of the inductances L_1 and L_L:

$$\begin{aligned} v_{sa} &= L_1\frac{di_{L1a}}{dt} + R_1 i_{L1a} + L_L\frac{di_{oa}}{dt} + R_L i_{oa} + v_{gn} \\ v_{sb} &= L_1\frac{di_{L1b}}{dt} + R_1 i_{L1b} + L_L\frac{di_{ob}}{dt} + R_L i_{ob} + v_{gn} \\ v_{sc} &= L_1\frac{di_{L1c}}{dt} + R_1 i_{L1c} + L_L\frac{di_{oc}}{dt} + R_L i_{oc} + v_{gn} \end{aligned} \tag{3.8}$$

The three equations can be written in the vector form:

$$\underline{v}_{sabc} = L_1\frac{d\underline{i}_{L1abc}}{dt} + R_1\underline{i}_{L1abc} + L_L\frac{d\underline{i}_{oabc}}{dt} + R_L\underline{i}_{oabc} + \underline{v}_{gnabc} \tag{3.9}$$

The grid neutral voltage v_{gn} can be related to other voltages in the circuit. Summing the three previous equations:

$$\begin{aligned} (v_{sa} + v_{sb} + v_{sc}) = &\dots \\ =&L_1\frac{d}{dt}(i_{L1a} + i_{L1b} + i_{L1c}) + R_1(i_{L1a} + i_{L1b} + i_{L1c}) + \dots \\ &+ L_L\frac{d}{dt}(i_{oa} + i_{ob} + i_{oc}) + R_L(i_{oa} + i_{ob} + i_{oc}) + 3v_{gn} \end{aligned} \tag{3.10}$$

According to KCL, the sums of the currents in the nodes N_1, N_2 and N_3 are equal to zero

$$\begin{aligned} 0 &= i_{L1a} + i_{L1b} + i_{L1c} \\ 0 &= i_{ca} + i_{cb} + i_{cc} \\ 0 &= i_{oa} + i_{ob} + i_{oc} \end{aligned} \tag{3.11}$$

Hence, from the previous equation it is possible to relate the neutral voltage v_{gn} to the source and the grid voltages:

$$v_{gn} = \frac{v_{sa} + v_{sb} + v_{sc}}{3} \tag{3.12}$$

and can be expressed as vector with the expression

$$\underline{v}_{gnabc} = \frac{1}{3}\begin{bmatrix}\sum_{k=a,b,c} v_{sk}\\ \sum_{k=a,b,c} v_{sk}\\ \sum_{k=a,b,c} v_{sk}\end{bmatrix} = \frac{1}{3}\begin{bmatrix}1 & 1 & 1\\ 1 & 1 & 1\\ 1 & 1 & 1\end{bmatrix}\cdot \underline{v}_{sabc} = \frac{V_{dc}}{3}\begin{bmatrix}1 & 1 & 1\\ 1 & 1 & 1\\ 1 & 1 & 1\end{bmatrix}\cdot \underline{s}_{abc} \tag{3.13}$$

where the relation in (3.4) has been used to substitute the term $\underline{v}_{sabc}$.

KVL M_2: Considering the branches of the inductance L_1 and of the capacitor C:

$$\begin{aligned} v_{sa} - L_1\frac{di_{L1a}}{dt} - R_1 i_{L1a} &= R_c i_{ca} + v_{ca} + v_{cn}\\ v_{sb} - L_1\frac{di_{L1b}}{dt} - R_1 i_{L1b} &= R_c i_{cb} + v_{cb} + v_{cn}\\ v_{sc} - L_1\frac{di_{L1c}}{dt} - R_1 i_{L1c} &= R_c i_{cc} + v_{cc} + v_{cn}\end{aligned} \tag{3.14}$$

The previous equations can be vectorized as:

$$\underline{v}_{sabc} - L_1\frac{d\underline{i}_{L1abc}}{dt} - R_1\underline{i}_{L1abc} = R_c C\frac{d\underline{v}_{cabc}}{dt} + \underline{v}_{cabc} + \underline{v}_{cnabc} \tag{3.15}$$

It is necessary to express the capacitors neutral voltage v_{cn} with other quantities already known in the circuit. Summing the three previous equations:

$$\begin{aligned}(v_{sa} + v_{sb} + v_{sc}) - L_1\frac{d}{dt}(i_{L1a} + i_{L1b} + i_{L1c}) - R_1(i_{L1a} + i_{L1b} + i_{L1c}) =\\ = R_c(i_{ca} + i_{cb} + i_{cc}) + (v_{ca} + v_{cb} + v_{cc}) + 3v_{cn}\end{aligned} \tag{3.16}$$

According to KCL, the sum of the currents in the nodes N_1 and N_3 is zero:

$$\begin{aligned} 0 &= i_{L1a} + i_{L1b} + i_{L1c}\\ 0 &= i_{ca} + i_{cb} + i_{cc}\end{aligned} \tag{3.17}$$

it is possible to derive the expression for the neutral point v_{cn} as

$$v_{cn} = \frac{v_{sa} + v_{sb} + v_{sc}}{3} - \frac{v_{ca} + v_{cb} + v_{cc}}{3} \tag{3.18}$$

which can be vectorized as

$$\begin{aligned}\underline{v}_{cnabc} &= \frac{1}{3}\begin{bmatrix}\sum_{k=a,b,c} v_{sk} - \sum_{k=a,b,c} v_{ck} \\ \sum_{k=a,b,c} v_{sk} - \sum_{k=a,b,c} v_{ck} \\ \sum_{k=a,b,c} v_{sk} - \sum_{k=a,b,c} v_{ck}\end{bmatrix} = \\ &= \frac{1}{3}\begin{bmatrix}1 & 1 & 1 \\ 1 & 1 & 1 \\ 1 & 1 & 1\end{bmatrix} \cdot \underline{v}_{sabc} - \frac{1}{3}\begin{bmatrix}1 & 1 & 1 \\ 1 & 1 & 1 \\ 1 & 1 & 1\end{bmatrix} \cdot \underline{v}_{cabc} = \\ &= \frac{V_{dc}}{3}\begin{bmatrix}1 & 1 & 1 \\ 1 & 1 & 1 \\ 1 & 1 & 1\end{bmatrix} \cdot \underline{s}_{abc} - \frac{1}{3}\begin{bmatrix}1 & 1 & 1 \\ 1 & 1 & 1 \\ 1 & 1 & 1\end{bmatrix} \cdot \underline{v}_{cabc}\end{aligned} \tag{3.19}$$

where, once again, the relation in (3.4) has been used to substitute $\underline{v}_{sabc}$.

3.4 Switching Model

In this section, the state-space model of the inverter previously represented is analyzed.

Combining the equations (3.15), (3.9) and (3.7) it is possible to obtain the final expressions for the state-space model:

$$\begin{aligned}\frac{d\underline{i}_{L1abc}}{dt} &= -\frac{R_1 + R_c}{L_1}\underline{i}_{L1abc} + \frac{R_c}{L_1}\underline{i}_{oabc} - \frac{1}{L_1}\underline{v}_{cabc} + \frac{V_{dc}}{L_1}\underline{s}_{abc} - \frac{1}{L_1}\underline{v}_{cnabc} \\ \frac{d\underline{i}_{oabc}}{dt} &= \frac{R_c}{L_L}\underline{i}_{L1abc} - \frac{R_c + R_L}{L_L}\underline{i}_{oabc} + \frac{1}{L_L}\underline{v}_{cabc} + \frac{1}{L_L}(\underline{v}_{cnabc} - \underline{v}_{gnabc}) \\ \frac{d\underline{v}_{cabc}}{dt} &= \frac{1}{C}\underline{i}_{L1abc} - \frac{1}{C}\underline{i}_{oabc}\end{aligned} \tag{3.20}$$

Substituting the expressions of the neutral voltages reported in (3.13) and (3.19) and expanding the matrix expressions:

$$\begin{aligned}\frac{d\underline{i}_{L1abc}}{dt} = &\begin{bmatrix} -\frac{R_1+R_c}{L_1} & 0 & 0 \\ 0 & -\frac{R_1+R_c}{L_1} & 0 \\ 0 & 0 & -\frac{R_1+R_c}{L_1} \end{bmatrix} \cdot \underline{i}_{L1abc} + \dots \\ &+ \begin{bmatrix} \frac{R_c}{L_1} & 0 & 0 \\ 0 & \frac{R_c}{L_1} & 0 \\ 0 & 0 & \frac{R_c}{L_1} \end{bmatrix} \cdot \underline{i}_{oabc} + \dots \\ &+ \frac{1}{3L_1} \begin{bmatrix} -2 & 1 & 1 \\ 1 & -2 & 1 \\ 1 & 1 & -2 \end{bmatrix} \cdot \underline{v}_{cabc} + \frac{V_{dc}}{3L_1} \begin{bmatrix} 2 & -1 & -1 \\ -1 & 2 & -1 \\ -1 & -1 & 2 \end{bmatrix} \cdot \underline{s}_{abc}\end{aligned} \tag{3.21}$$

$$\begin{aligned}\frac{d\underline{i}_{oabc}}{dt} = &\begin{bmatrix} \frac{R_c}{L_L} & 0 & 0 \\ 0 & \frac{R_c}{L_L} & 0 \\ 0 & 0 & \frac{R_c}{L_L} \end{bmatrix} \cdot \underline{i}_{L1abc} + \dots \\ &+ \begin{bmatrix} -\frac{R_c+R_L}{L_L} & 0 & 0 \\ 0 & -\frac{R_c+R_L}{L_L} & 0 \\ 0 & 0 & -\frac{R_c+R_L}{L_L} \end{bmatrix} \cdot \underline{i}_{oabc} + \dots \\ &+ \frac{1}{3L_L} \begin{bmatrix} 2 & -1 & -1 \\ -1 & 2 & -1 \\ -1 & -1 & 2 \end{bmatrix} \cdot \underline{v}_{cabc}\end{aligned} \tag{3.22}$$

$$\frac{d\underline{v}_{cvabc}}{dt} = \begin{bmatrix} \frac{1}{C} & 0 & 0 \\ 0 & \frac{1}{C} & 0 \\ 0 & 0 & \frac{1}{C} \end{bmatrix} \cdot \underline{i}_{L1abc} + \begin{bmatrix} -\frac{1}{C} & 0 & 0 \\ 0 & -\frac{1}{C} & 0 \\ 0 & 0 & -\frac{1}{C} \end{bmatrix} \cdot \underline{i}_{L2abc} \tag{3.23}$$

The previous expressions can be represented by the electrical scheme in Fig. 3.4a. Moreover, it is possible to represent it in a more compact form as in Fig. 3.4b, where

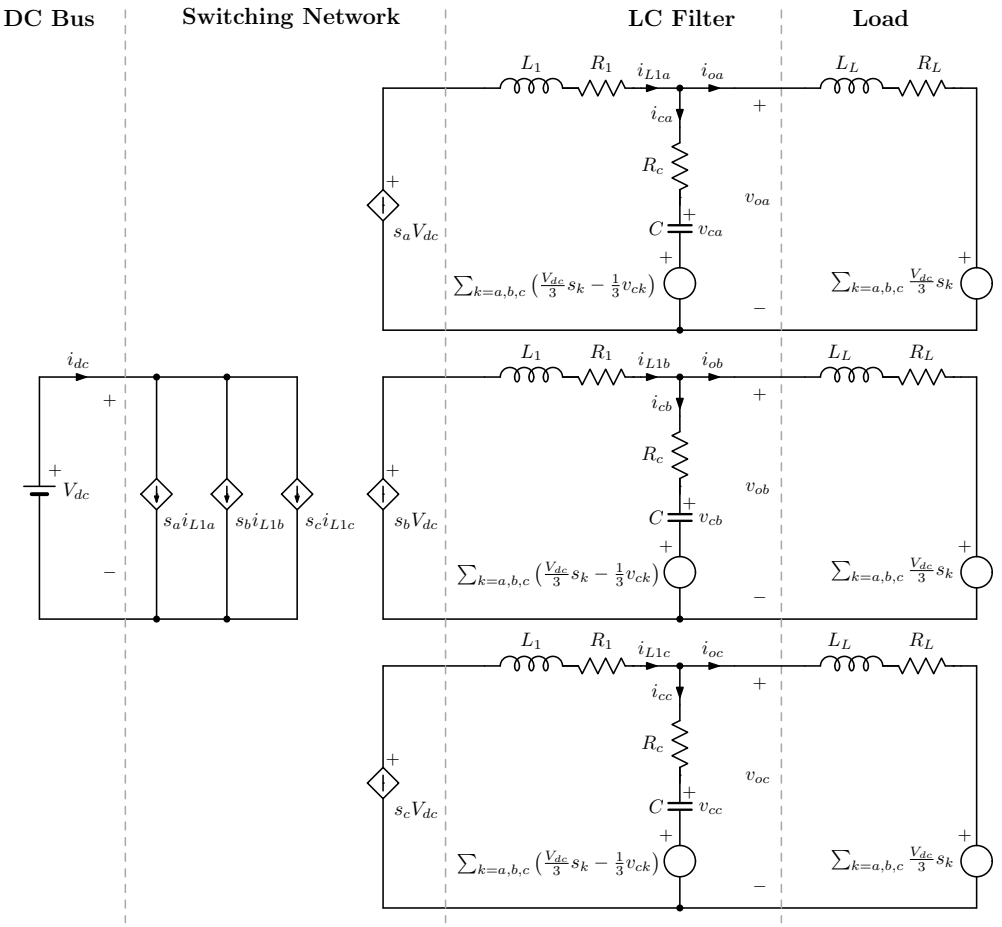

(A) Extended form

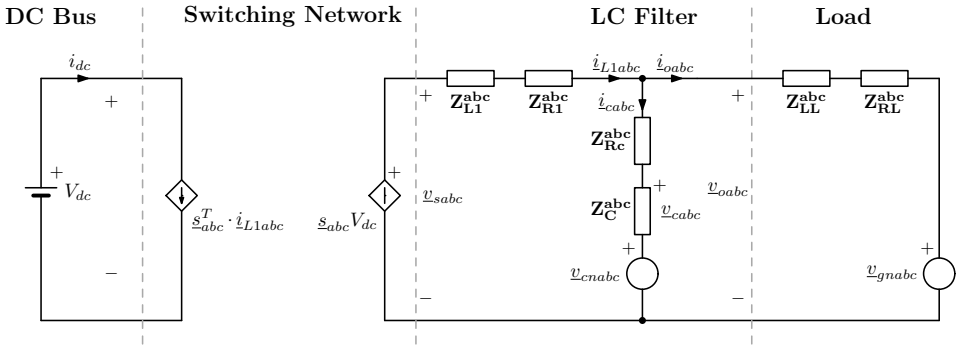

(B) Compact (matricial) form

FIGURE 3.4: Extended and compact form for the electrical scheme in *abc*-frame for the LC voltage source inverter (VSI).

currents and voltages are 3×1 vectors and impedances are 3×3 matrices:

$$\begin{aligned} \mathbf{Z_{L1}^{abc}} &= \begin{bmatrix} sL_1 & 0 & 0 \\ 0 & sL_1 & 0 \\ 0 & 0 & sL_1 \end{bmatrix} \quad , \quad \mathbf{Z_{R1}^{abc}} = \begin{bmatrix} R_1 & 0 & 0 \\ 0 & R_1 & 0 \\ 0 & 0 & R_1 \end{bmatrix} \\ \mathbf{Z_{C1}^{abc}} &= \begin{bmatrix} \frac{1}{sC} & 0 & 0 \\ 0 & \frac{1}{sC} & 0 \\ 0 & 0 & \frac{1}{sC} \end{bmatrix} \quad , \quad \mathbf{Z_{Rc}^{abc}} = \begin{bmatrix} R_c & 0 & 0 \\ 0 & R_c & 0 \\ 0 & 0 & R_c \end{bmatrix} \end{aligned} \tag{3.24}$$

In the switching network one can find the following relations:

$$i_{dc} = \underline{s}_{abc}^T \cdot \underline{i}_{L1abc} \quad , \quad \underline{v}_{sabc} = \underline{s}_{abc} V_{dc} \tag{3.25}$$

3.5 Average Model

The averaging operator is defined as:

$$\overline{x}(t) = \frac{1}{T} \int_{t-T}^{t} x(\tau)\, \mathrm{d}\tau \tag{3.26}$$

where T is the switching period of the PWM modulation.

Applying the operator to the switching quantities:

- switch duty-cycle (can be applied to the other phases):

$$d_{ap} = \overline{s}_{ap}(t) = \frac{1}{T} \int_{t-T}^{t} s_{ap}(\tau)\, \mathrm{d}\tau \tag{3.27}$$

  and

$$\begin{bmatrix} \overline{s}_a \\ \overline{s}_b \\ \overline{s}_c \end{bmatrix} = \underline{\overline{s}}_{abc} = \underline{d}_{abc} = \begin{bmatrix} d_a \\ d_b \\ d_c \end{bmatrix} \tag{3.28}$$

- phase-leg duty-cycle (complementary duty-cycle):

$$d_a = d_{ap} = 1 - d_{an} \tag{3.29}$$

- KVL and KCL:

$$\sum_{k=a,b,c} \overline{v}_k = 0 \quad , \quad \sum_{k=a,b,c} \overline{i}_k = 0 \tag{3.30}$$

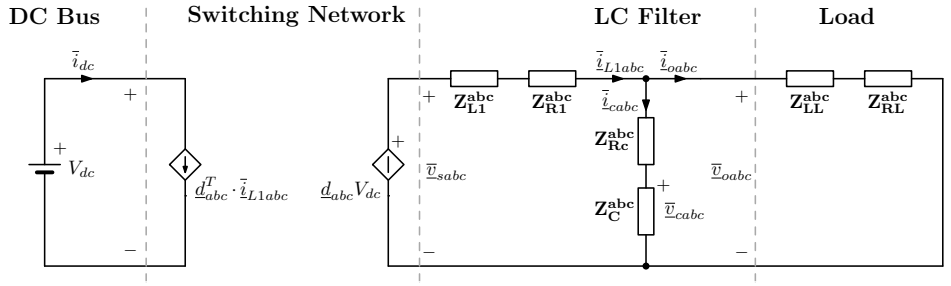

FIGURE 3.5: Average model for the three-phase voltage source inverter (VSI) in *abc*-frame.

- linear components:

$$\bar{v}_R = R\bar{i}_R \quad , \quad \bar{v}_L = L\frac{d\bar{i}_L}{dt} \quad , \quad \bar{i}_C = C\frac{d\bar{v}_C}{dt} \tag{3.31}$$

3.5.1 *abc*-frame

Therefore, substituting $\underline{s}_{abc}$ with $\underline{d}_{abc}$ and removing the neutral point contributions:

$$\begin{aligned}\frac{d\underline{\bar{i}}_{L1abc}}{dt} = &\begin{bmatrix} -\frac{R_1+R_c}{L_1} & 0 & 0 \\ 0 & -\frac{R_1+R_c}{L_1} & 0 \\ 0 & 0 & -\frac{R_1+R_c}{L_1} \end{bmatrix} \cdot \underline{\bar{i}}_{L1abc} + \dots \\ &+ \begin{bmatrix} \frac{R_c}{L_1} & 0 & 0 \\ 0 & \frac{R_c}{L_1} & 0 \\ 0 & 0 & \frac{R_c}{L_1} \end{bmatrix} \cdot \underline{\bar{i}}_{oabc} + \dots \\ &- \frac{1}{L_1}\begin{bmatrix} 1 & 0 & 0 \\ 0 & 1 & 0 \\ 0 & 0 & 1 \end{bmatrix} \cdot \underline{\bar{v}}_{cabc} + \frac{V_{dc}}{L_1}\begin{bmatrix} 1 & 0 & 0 \\ 0 & 1 & 0 \\ 0 & 0 & 1 \end{bmatrix} \cdot \underline{d}_{abc}\end{aligned} \tag{3.32}$$

$$\begin{aligned}\frac{d\underline{\bar{i}}_{oabc}}{dt} = &\begin{bmatrix} \frac{R_c}{L_L} & 0 & 0 \\ 0 & \frac{R_c}{L_L} & 0 \\ 0 & 0 & \frac{R_c}{L_L} \end{bmatrix} \cdot \underline{\bar{i}}_{L1abc} + \dots \\ &+ \begin{bmatrix} -\frac{R_c+R_L}{L_L} & 0 & 0 \\ 0 & -\frac{R_c+R_L}{L_L} & 0 \\ 0 & 0 & -\frac{R_c+R_L}{L_L} \end{bmatrix} \cdot \underline{\bar{i}}_{oabc} + \dots \\ &+ \frac{1}{L_L}\begin{bmatrix} 1 & 0 & 0 \\ 0 & 1 & 0 \\ 0 & 0 & 1 \end{bmatrix} \cdot \underline{\bar{v}}_{cabc}\end{aligned} \tag{3.33}$$

$$\frac{d\overline{\underline{v}}_{cvabc}}{dt} = \begin{bmatrix} \frac{1}{C} & 0 & 0 \\ 0 & \frac{1}{C} & 0 \\ 0 & 0 & \frac{1}{C} \end{bmatrix} \cdot \overline{\underline{i}}_{L1abc} + \begin{bmatrix} -\frac{1}{C} & 0 & 0 \\ 0 & -\frac{1}{C} & 0 \\ 0 & 0 & -\frac{1}{C} \end{bmatrix} \cdot \overline{\underline{i}}_{oabc} \tag{3.34}$$

The resulting electrical scheme is shown in Fig. 3.5, where the switching network becomes:

$$\overline{i}_{dc} = \underline{d}_{abc}^{T} \cdot \overline{\underline{i}}_{L1abc} \quad , \quad \overline{\underline{v}}_{sabc} = \underline{d}_{abc} V_{dc} \tag{3.35}$$

and the neutral voltages are equal to zero.

3.5.2 *dq*-frame transformation

The average model in *abc*-frame can be converted in *dq*-frame using the transformation $\mathbf{T}$ to pass to the synchronous reference frame:

$$\mathbf{T} = \mathbf{T_{dq0/abc}} = \sqrt{\frac{2}{3}} \begin{bmatrix} \cos\omega t & \cos\left(\omega t - \frac{2\pi}{3}\right) & \cos\left(\omega t + \frac{2\pi}{3}\right) \\ -\sin\omega t & -\sin\left(\omega t - \frac{2\pi}{3}\right) & -\sin\left(\omega t + \frac{2\pi}{3}\right) \\ \frac{1}{\sqrt{2}} & \frac{1}{\sqrt{2}} & \frac{1}{\sqrt{2}} \end{bmatrix} \tag{3.36}$$

and the inverse transformation corresponds to the transpose matrix

$$\mathbf{T}^{-1} = \mathbf{T}^{T} = \mathbf{T_{abc/dq0}} = \sqrt{\frac{2}{3}} \begin{bmatrix} \cos\omega t & -\sin\omega t & \frac{1}{\sqrt{2}} \\ \cos\left(\omega t - \frac{2\pi}{3}\right) & -\sin\left(\omega t - \frac{2\pi}{3}\right) & \frac{1}{\sqrt{2}} \\ \cos\left(\omega t + \frac{2\pi}{3}\right) & -\sin\left(\omega t + \frac{2\pi}{3}\right) & \frac{1}{\sqrt{2}} \end{bmatrix} \tag{3.37}$$

The transformations can be performed as:

$$\underline{x}_{dq0} = \mathbf{T} \cdot \underline{x}_{abc} \quad , \qquad \underline{x}_{abc} = \mathbf{T}^{-1} \cdot \underline{x}_{dq0} \tag{3.38}$$

The last expression can be used to substitute the voltage, current and duty-cycle vectors in the average model in *abc*-frame.

$$\begin{aligned}\frac{d\left(\mathbf{T}^{-1}\underline{\bar{i}}_{L1dq0}\right)}{dt} = &\begin{bmatrix} -\frac{R_1+R_c}{L_1} & 0 & 0 \\ 0 & -\frac{R_1+R_c}{L_1} & 0 \\ 0 & 0 & -\frac{R_1+R_c}{L_1} \end{bmatrix} \cdot \left(\mathbf{T}^{-1}\underline{\bar{i}}_{L1dq0}\right) + \dots \\ &+ \begin{bmatrix} \frac{R_c}{L_1} & 0 & 0 \\ 0 & \frac{R_c}{L_1} & 0 \\ 0 & 0 & \frac{R_c}{L_1} \end{bmatrix} \cdot \left(\mathbf{T}^{-1}\underline{\bar{i}}_{odq0}\right) + \dots \\ &- \frac{1}{L_1}\begin{bmatrix} 1 & 0 & 0 \\ 0 & 1 & 0 \\ 0 & 0 & 1 \end{bmatrix} \cdot \left(\mathbf{T}^{-1}\underline{\bar{v}}_{cdq0}\right) + \dots \\ &+ \frac{V_{dc}}{L_1}\begin{bmatrix} 1 & 0 & 0 \\ 0 & 1 & 0 \\ 0 & 0 & 1 \end{bmatrix} \cdot \left(\mathbf{T}^{-1}\underline{\bar{d}}_{dq0}\right)\end{aligned} \tag{3.39}$$

$$\begin{aligned}\frac{d\left(\mathbf{T}^{-1}\underline{\bar{i}}_{odq0}\right)}{dt} = &\begin{bmatrix} \frac{R_c}{L_L} & 0 & 0 \\ 0 & \frac{R_c}{L_L} & 0 \\ 0 & 0 & \frac{R_c}{L_L} \end{bmatrix} \cdot \left(\mathbf{T}^{-1}\underline{\bar{i}}_{L1dq0}\right) + \dots \\ &+ \begin{bmatrix} -\frac{R_c+R_L}{L_L} & 0 & 0 \\ 0 & -\frac{R_c+R_L}{L_L} & 0 \\ 0 & 0 & -\frac{R_c+R_L}{L_L} \end{bmatrix} \cdot \left(\mathbf{T}^{-1}\underline{\bar{i}}_{odq0}\right) + \dots \\ &+ \frac{1}{L_L}\begin{bmatrix} 1 & 0 & 0 \\ 0 & 1 & 0 \\ 0 & 0 & 1 \end{bmatrix} \cdot \left(\mathbf{T}^{-1}\underline{\bar{v}}_{cdq0}\right)\end{aligned} \tag{3.40}$$

$$\frac{d\left(\mathbf{T}^{-1}\underline{\bar{v}}_{cdq0}\right)}{dt} = \begin{bmatrix} \frac{1}{C} & 0 & 0 \\ 0 & \frac{1}{C} & 0 \\ 0 & 0 & \frac{1}{C} \end{bmatrix} \cdot \left(\mathbf{T}^{-1}\underline{\bar{i}}_{L1dq0}\right) + \begin{bmatrix} -\frac{1}{C} & 0 & 0 \\ 0 & -\frac{1}{C} & 0 \\ 0 & 0 & -\frac{1}{C} \end{bmatrix} \cdot \left(\mathbf{T}^{-1}\underline{\bar{i}}_{odq0}\right) \tag{3.41}$$

The transformation $\mathbf{T} = \mathbf{T}(t)$ is time dependent, so it can not be treated as a constant in the derivative:

$$\frac{d\left(\mathbf{T}^{-1}\underline{\bar{i}}_{L1dq0}\right)}{dt} = \mathbf{T}^{-1}\frac{d\underline{\bar{i}}_{L1dq0}}{dt} + \frac{d\mathbf{T}^{-1}}{dt}\underline{\bar{i}}_{L1dq0} \tag{3.42}$$

and

$$\frac{d\left(\mathbf{T}^{-1}\underline{\overline{v}}_{cdq0}\right)}{dt} = \mathbf{T}^{-1}\frac{d\underline{\overline{v}}_{cdq0}}{dt} + \frac{d\mathbf{T}^{-1}}{dt}\underline{\overline{v}}_{cdq0} \tag{3.43}$$

The following expression:

$$\mathbf{T}\frac{d\mathbf{T}^{-1}}{dt} = \begin{bmatrix} 0 & -\omega & 0 \\ \omega & 0 & 0 \\ 0 & 0 & 0 \end{bmatrix} \tag{3.44}$$

can be proved and will be found in the next formulations.

Using these relations, it is possible to rewrite the system as:

$$\begin{aligned} \frac{d\underline{\overline{i}}_{L1dq0}}{dt} = & \begin{bmatrix} -\frac{R_1+R_c}{L_1} & \omega & 0 \\ -\omega & -\frac{R_1+R_c}{L_1} & 0 \\ 0 & 0 & -\frac{R_1+R_c}{L_1} \end{bmatrix} \cdot \underline{\overline{i}}_{L1dq0} + \dots \\ & + \begin{bmatrix} \frac{R_c}{L_1} & 0 & 0 \\ 0 & \frac{R_c}{L_1} & 0 \\ 0 & 0 & \frac{R_c}{L_1} \end{bmatrix} \cdot \underline{\overline{i}}_{odq0} + \dots \\ & - \frac{1}{L_1}\begin{bmatrix} 1 & 0 & 0 \\ 0 & 1 & 0 \\ 0 & 0 & 1 \end{bmatrix} \cdot \underline{\overline{v}}_{cdq0} + \frac{V_{dc}}{L_1}\begin{bmatrix} 1 & 0 & 0 \\ 0 & 1 & 0 \\ 0 & 0 & 1 \end{bmatrix} \cdot \underline{\overline{d}}_{dq0} \end{aligned} \tag{3.45}$$

$$\begin{aligned} \frac{d\underline{\overline{i}}_{odq0}}{dt} = & \begin{bmatrix} \frac{R_c}{L_L} & 0 & 0 \\ 0 & \frac{R_c}{L_L} & 0 \\ 0 & 0 & \frac{R_c}{L_L} \end{bmatrix} \cdot \underline{\overline{i}}_{L1dq0} + \dots \\ & + \begin{bmatrix} -\frac{R_c+R_L}{L_L} & \omega & 0 \\ -\omega & -\frac{R_c+R_L}{L_L} & 0 \\ 0 & 0 & -\frac{R_c+R_L}{L_L} \end{bmatrix} \cdot \underline{\overline{i}}_{odq0} + \dots \\ & + \frac{1}{L_L}\begin{bmatrix} 1 & 0 & 0 \\ 0 & 1 & 0 \\ 0 & 0 & 1 \end{bmatrix} \cdot \underline{\overline{v}}_{cdq0} \end{aligned} \tag{3.46}$$

$$\begin{aligned}\frac{d\overline{v}_{cdq0}}{dt} = &\begin{bmatrix}\frac{1}{C} & 0 & 0\\ 0 & \frac{1}{C} & 0\\ 0 & 0 & \frac{1}{C}\end{bmatrix}\cdot\bar{\underline{i}}_{L1dq0} + \begin{bmatrix}-\frac{1}{C} & 0 & 0\\ 0 & -\frac{1}{C} & 0\\ 0 & 0 & -\frac{1}{C}\end{bmatrix}\cdot\bar{\underline{i}}_{odq0} + \dots\\ &+\begin{bmatrix}0 & \omega & 0\\ -\omega & 0 & 0\\ 0 & 0 & 0\end{bmatrix}\cdot\overline{\underline{v}}_{cdq0}\end{aligned} \tag{3.47}$$

Considering the following relations:

$$\begin{aligned}0 &= \overline{v}_a + \overline{v}_b + \overline{v}_c\\ 0 &= \bar{i}_a + \bar{i}_b + \bar{i}_c\\ 0 &= d_a + d_b + d_c\end{aligned} \tag{3.48}$$

the 0-channel will be omitted, since

$$\begin{aligned}\overline{v}_0 &= 0\\ \bar{i}_0 &= 0\\ d_0 &= 0\end{aligned} \tag{3.49}$$

the system is rewritten hereafter and the final model is represented in Fig. 3.6:

$$\begin{aligned}\frac{d\bar{\underline{i}}_{L1dq}}{dt} = &\begin{bmatrix}-\frac{R_1+R_c}{L_1} & \omega\\ -\omega & -\frac{R_1+R_c}{L_1}\end{bmatrix}\cdot\bar{\underline{i}}_{L1dq} + \begin{bmatrix}\frac{R_c}{L_1} & 0\\ 0 & \frac{R_c}{L_1}\end{bmatrix}\cdot\bar{\underline{i}}_{odq} + \dots\\ &+\begin{bmatrix}-\frac{1}{L_1} & 0\\ 0 & -\frac{1}{L_1}\end{bmatrix}\cdot\overline{\underline{v}}_{cdq} + \begin{bmatrix}\frac{V_{dc}}{L_1} & 0\\ 0 & \frac{V_{dc}}{L_1}\end{bmatrix}\cdot\overline{\underline{d}}_{dq}\end{aligned} \tag{3.50}$$

$$\frac{d\bar{\underline{i}}_{odq}}{dt} = \begin{bmatrix}\frac{R_c}{L_L} & 0\\ 0 & \frac{R_c}{L_L}\end{bmatrix}\cdot\bar{\underline{i}}_{L1dq} + \begin{bmatrix}-\frac{R_c+R_L}{L_L} & \omega\\ -\omega & -\frac{R_c+R_L}{L_L}\end{bmatrix}\cdot\bar{\underline{i}}_{odq} + \begin{bmatrix}\frac{1}{L_L} & 0\\ 0 & \frac{1}{L_L}\end{bmatrix}\cdot\overline{\underline{v}}_{cdq} \tag{3.51}$$

$$\frac{d\overline{\underline{v}}_{cdq}}{dt} = \begin{bmatrix}\frac{1}{C} & 0\\ 0 & \frac{1}{C}\end{bmatrix}\cdot\bar{\underline{i}}_{L1dq} + \begin{bmatrix}-\frac{1}{C} & 0\\ 0 & -\frac{1}{C}\end{bmatrix}\cdot\bar{\underline{i}}_{odq} + \begin{bmatrix}0 & \omega\\ -\omega & 0\end{bmatrix}\cdot\overline{\underline{v}}_{cdq} \tag{3.52}$$

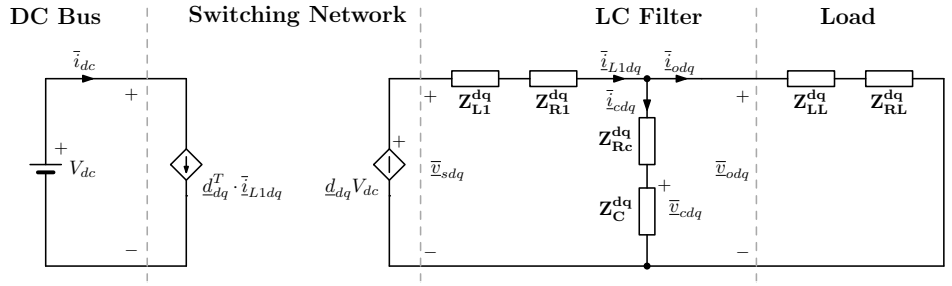

FIGURE 3.6: Average model for the three-phase voltage source inverter (VSI) in *dq*-frame.

3.6 State-Space Model

From the average model previously derived, it is possible to obtain the small-signal model, and then the correspondent state-space representation, of the voltage source inverter with resistive-inductive load.
The state vector and its derivative are defined as:

$$\underline{x} = \begin{bmatrix} \hat{i}_{L1d} \\ \hat{i}_{L1q} \\ \hat{\bar{i}}_{od} \\ \hat{i}_{oq} \\ \hat{v}_{cd} \\ \hat{v}_{cq} \end{bmatrix} \quad , \qquad \underline{\dot{x}} = \frac{d}{dt} \begin{bmatrix} \hat{i}_{L1d} \\ \hat{i}_{L1q} \\ \hat{\bar{i}}_{od} \\ \hat{i}_{oq} \\ \hat{v}_{cd} \\ \hat{v}_{cq} \end{bmatrix} \tag{3.53}$$

The inputs of the system are the duty-cycle:

$$\underline{u} = \begin{bmatrix} \hat{d}_d \\ \hat{d}_q \end{bmatrix} \tag{3.54}$$

The outputs are the inverter side inductance currents:

$$\underline{y} = \begin{bmatrix} \hat{i}_{L1d} \\ \hat{i}_{L1q} \end{bmatrix} \tag{3.55}$$

The system can be therefore described with the state-space representation as:

$$\begin{aligned} \underline{\dot{x}} &= \mathbf{A} \cdot \underline{x} + \mathbf{B} \cdot \underline{u} \\ \underline{y} &= \mathbf{C} \cdot \underline{x} + \mathbf{D} \cdot \underline{u} \end{aligned} \tag{3.56}$$

$$\mathbf{A} = \left[\begin{array}{cc:cc:cc} -\frac{R_1+R_c}{L_1} & \omega & \frac{R_c}{L_1} & 0 & -\frac{1}{L_1} & 0 \\ -\omega & -\frac{R_1+R_c}{L_1} & 0 & \frac{R_c}{L_1} & 0 & -\frac{1}{L_1} \\ \hdashline \frac{R_c}{L_L} & 0 & -\frac{R_c+R_L}{L_L} & \omega & \frac{1}{L_L} & 0 \\ 0 & \frac{R_c}{L_L} & -\omega & -\frac{R_c+R_L}{L_L} & 0 & \frac{1}{L_L} \\ \hdashline \frac{1}{C} & 0 & -\frac{1}{C} & 0 & 0 & \omega \\ 0 & \frac{1}{C} & 0 & -\frac{1}{C} & -\omega & 0 \end{array}\right] \tag{3.57}$$

$$\mathbf{B} = \left[\begin{array}{cc} \frac{V_{dc}}{L_1} & 0 \\ 0 & \frac{V_{dc}}{L_1} \\ \hdashline 0 & 0 \\ 0 & 0 \\ \hdashline 0 & 0 \\ 0 & 0 \end{array}\right] \tag{3.58}$$

$$\mathbf{C} = \left[\begin{array}{cc:cc:cc} 1 & 0 & 0 & 0 & 0 & 0 \\ 0 & 1 & 0 & 0 & 0 & 0 \end{array}\right] \quad , \quad \mathbf{D} = \left[\begin{array}{cc} 0 & 0 \\ 0 & 0 \end{array}\right] \tag{3.59}$$

Using the matrices in (3.57), (3.58) and (3.59), it is possible to determine the

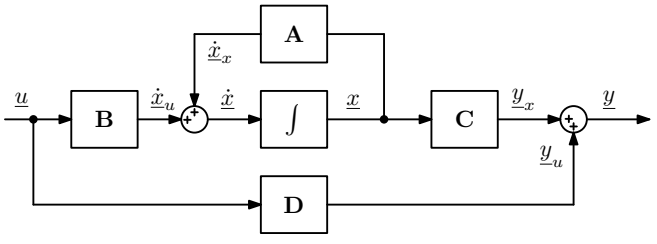

FIGURE 3.7: Generic state-space representation

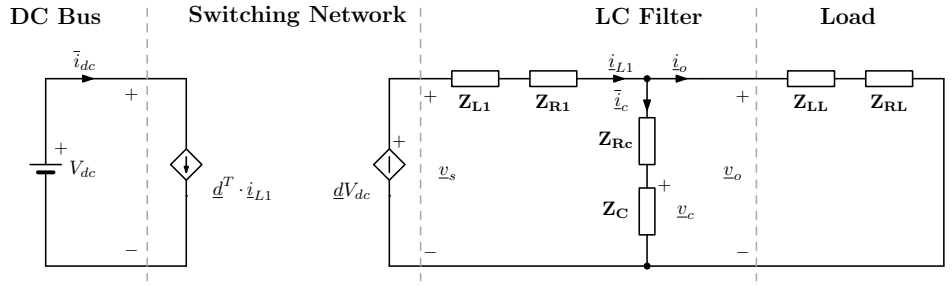

FIGURE 3.8: Average model for the three-phase voltage source inverter (VSI) in dq-frame.

transfer function matrix $\hat{\underline{i}}_{L1} = \mathbf{H_d} \cdot \hat{\underline{d}}$, which represents the core of the current control:

$$\mathbf{H_d} = \mathbf{C}\left(s\mathbf{I} - \mathbf{A}\right)^{-1}\mathbf{B} + \mathbf{D} \tag{3.60}$$

However, the state-space modeling requires a long process to give the desired result and:

- it is not close to the physical concepts of the system under investigation;
- it requires the whole system representation to calculate any transfer-functions;
- it requires major modifications and complete reformulation if the number of states changes.

3.7 Alternative Approach to the State-Space Model

In this section an alternative method to get the desired transfer functions is analyzed. The goals of this additional representation are:

- to have a faster method, compared to the state-space model, to obtain the desired transfer functions;
- to find the correspondences with the physical system;
- to compare the results method with the single-phase inverter modeling.

From Fig. 3.6 it is possible to obtain all the required information, and a simplified notation is expressed in Fig. 3.8. As stated in the beginning of this chapter, the voltages and currents together with the duty-cycle are represented as vectors:

$$\hat{\underline{i}} = \begin{bmatrix} \hat{i}_d \\ \hat{i}_q \end{bmatrix} \quad , \quad \hat{\underline{v}} = \begin{bmatrix} \hat{v}_d \\ \hat{v}_q \end{bmatrix} \quad , \quad \hat{\underline{d}} = \begin{bmatrix} \hat{d}_d \\ \hat{d}_q \end{bmatrix} \tag{3.61}$$

where in this case are 2×1 vector in dq-frame representation.

The impedances are defined as:

$$\begin{aligned} \mathbf{Z_{L1}} &= \begin{bmatrix} sL_1 & -\omega L_1 \\ \omega L_1 & sL_1 \end{bmatrix} \quad , \quad \mathbf{Z_{R1}} = \begin{bmatrix} R_1 & 0 \\ 0 & R_1 \end{bmatrix} \quad , \quad \mathbf{Z_{Rc}} = \begin{bmatrix} R_c & 0 \\ 0 & R_c \end{bmatrix} \\ \mathbf{Y_C} &= \begin{bmatrix} sC & -\omega C \\ \omega C & sC \end{bmatrix} \quad , \quad \mathbf{Z_C} = \frac{1}{C(s^2+\omega^2)} \begin{bmatrix} s & \omega \\ -\omega & s \end{bmatrix} \\ \mathbf{Z_{LL}} &= \begin{bmatrix} sL_L & -\omega L_L \\ \omega L_L & sL_L \end{bmatrix} \quad , \quad \mathbf{Z_{RL}} = \begin{bmatrix} R_L & 0 \\ 0 & R_L \end{bmatrix} \end{aligned} \tag{3.62}$$

and

$$\begin{aligned} \mathbf{Z_{L1}^{par}} &= \mathbf{Z_{L1}} + \mathbf{Z_{R1}} = \begin{bmatrix} R_1 + sL_1 & -\omega L_1 \\ \omega L_1 & R_1 + sL_1 \end{bmatrix} \\ \mathbf{Y_{L1}^{par}} &= (\mathbf{Z_{L1}^{par}})^{-1} = \frac{1}{(R_1 + sL_1)^2 + (\omega L_1)^2} \begin{bmatrix} R_1 + sL_1 & \omega L_1 \\ -\omega L_1 & R_1 + sL_1 \end{bmatrix} \end{aligned}$$

$$\mathbf{Z_C^{par}} = \mathbf{Z_C} + \mathbf{Z_{Rc}} = \frac{1}{C(s^2+\omega^2)} \begin{bmatrix} s + R_c C(s^2+\omega^2) & \omega \\ -\omega & s + R_c C(s^2+\omega^2) \end{bmatrix} \tag{3.63}$$

$$\begin{aligned} \mathbf{Z_L^{tot}} &= \mathbf{Z_{LL}} + \mathbf{Z_{RL}} = \begin{bmatrix} R_L + sL_L & -\omega L_L \\ \omega L_L & R_L + sL_L \end{bmatrix} \\ \mathbf{Y_L^{tot}} &= \left(\mathbf{Z_L^{tot}}\right)^{-1} = \frac{1}{(R_L + sL_L)^2 + (\omega L_L)^2} \begin{bmatrix} R_L + sL_L & \omega L_L \\ -\omega L_L & R_L + sL_L \end{bmatrix} \end{aligned}$$

The data considered are shown in Tab. 3.2.

3.7.1 Direct Control

In the direct control configuration the duty-cycle is the input of the system. After the linearizing process, where the main assumption is that $f_n \ll f_{sw}$, the equivalent circuit can be found in Fig. 3.9a and the correspondent control scheme is depicted in Fig. 3.9b. Two matrices are of interest:

- the transfer function matrix between $\underline{d}$ and $\underline{i}_{L1}$:

$$\hat{\underline{i}}_{L1} = \mathbf{H_d} \cdot \hat{\underline{d}} \tag{3.64}$$

Name	Symbol	Value	Unit
Nominal Power	S_n	2	kW
Nominal Voltage (Line-to-Line)	$V_{n,ll}$	120	V
Nominal Voltage (Line-to-Neutral)	V_n	69.3	V
Nominal Frequency	f_n	60	Hz
Switching Frequency	f_{sw}	20	kHz
Switching Period	T_{sw}	50	µs
Inverter side inductance	L_1	500	μH
ESR	R_1	55	mΩ
Capacitance	C	160	μF
ESR	R_c	100	mΩ
DC Bus Voltage	V_{dc}	200	V

TABLE 3.2: Prototype parameters.

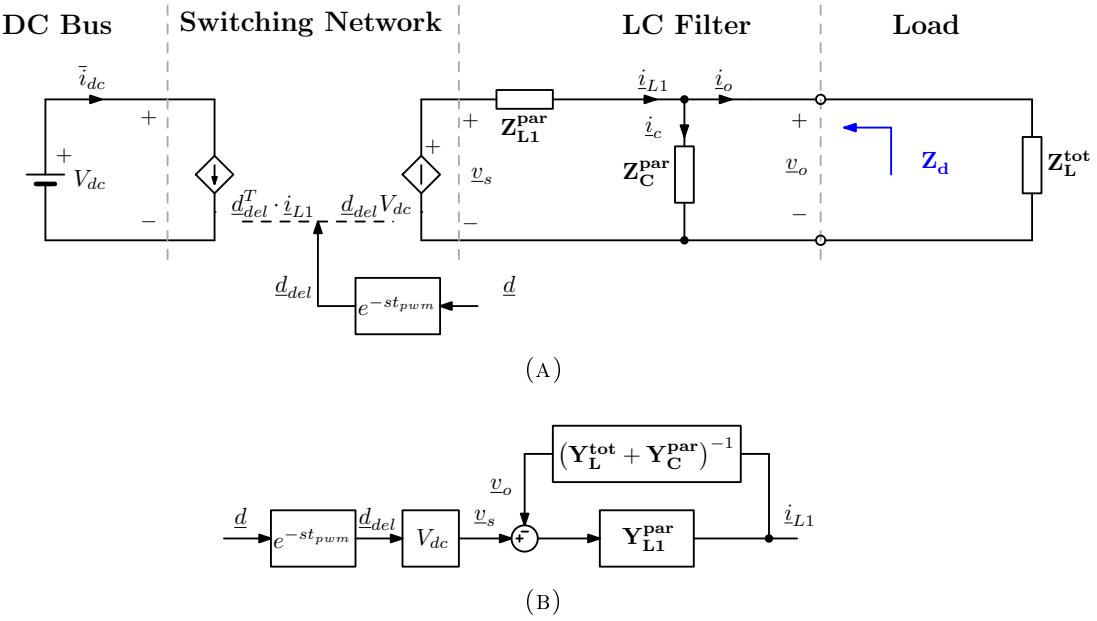

FIGURE 3.9: Direct Control: average model for the three-phase voltage source inverter (VSI) in dq-frame and control scheme.

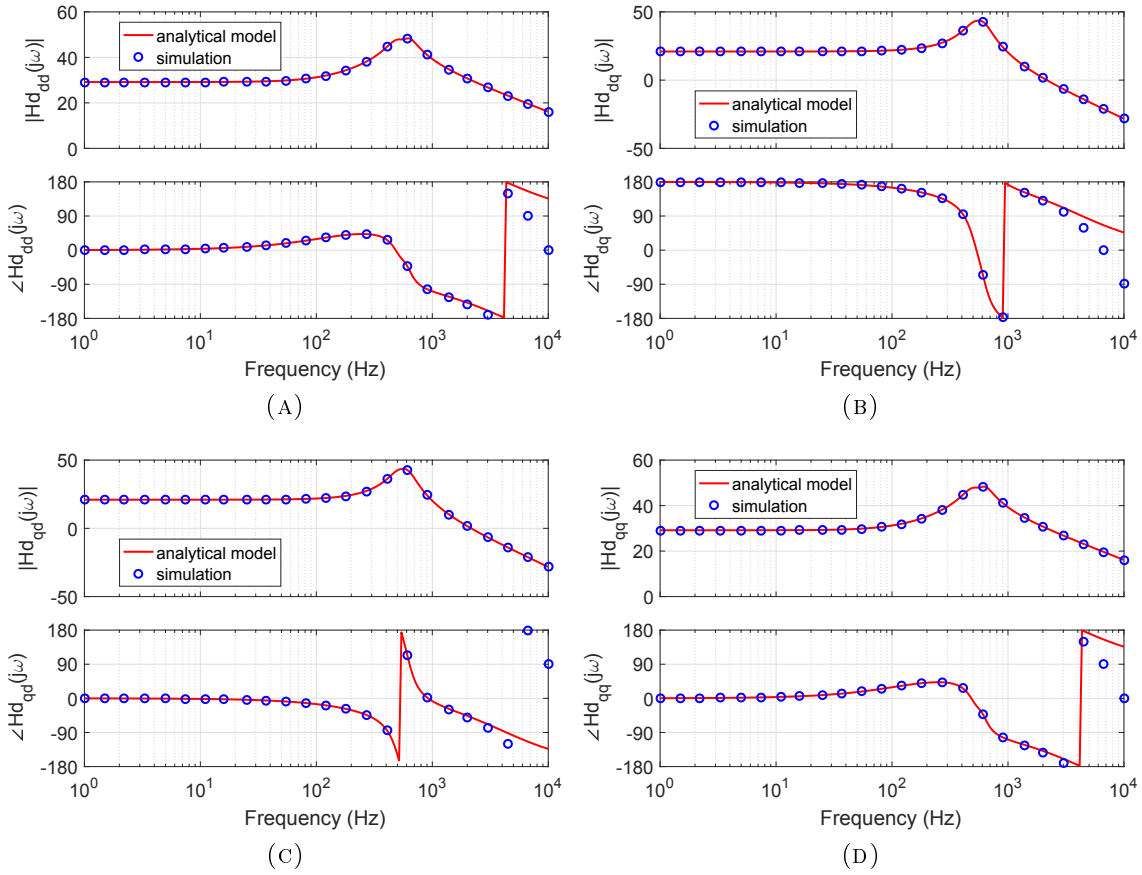

FIGURE 3.10: Direct Control: open loop $\mathbf{H_d}$ ($\underline{d}$ to $\underline{i}_{L1}$) transfer functions in dq-frame.

can be easily calculated considering the block scheme in Fig. 3.9b:

$$\mathbf{H_d} = V_{dc} e^{-st_{pwm}} \left[\mathbf{I} + \mathbf{Y_{L1}^{par}} \cdot \left(\mathbf{Y_L^{tot}} + \mathbf{Y_C^{par}}\right)^{-1}\right]^{-1} \cdot \mathbf{Y_{L1}^{par}} \tag{3.65}$$

The correspondence between analytical model and simulation results can be observed in Fig. 3.10, where a difference in the phase can be noticed due to the Padè approximation of the pulse width modulation delay.

- the output impedance with direct control of the duty-cycle:

$$\mathbf{Z_d} = (\mathbf{Y_{L1}^{par}} + \mathbf{Y_C^{par}})^{-1} \tag{3.66}$$

where

$$\underline{\hat{v}}_o = -\mathbf{Z_d} \cdot \underline{\hat{i}}_o \tag{3.67}$$

since the output currents are defined as outcoming currents.

Therefore, in this condition the output impedance depends only on the LC filter,

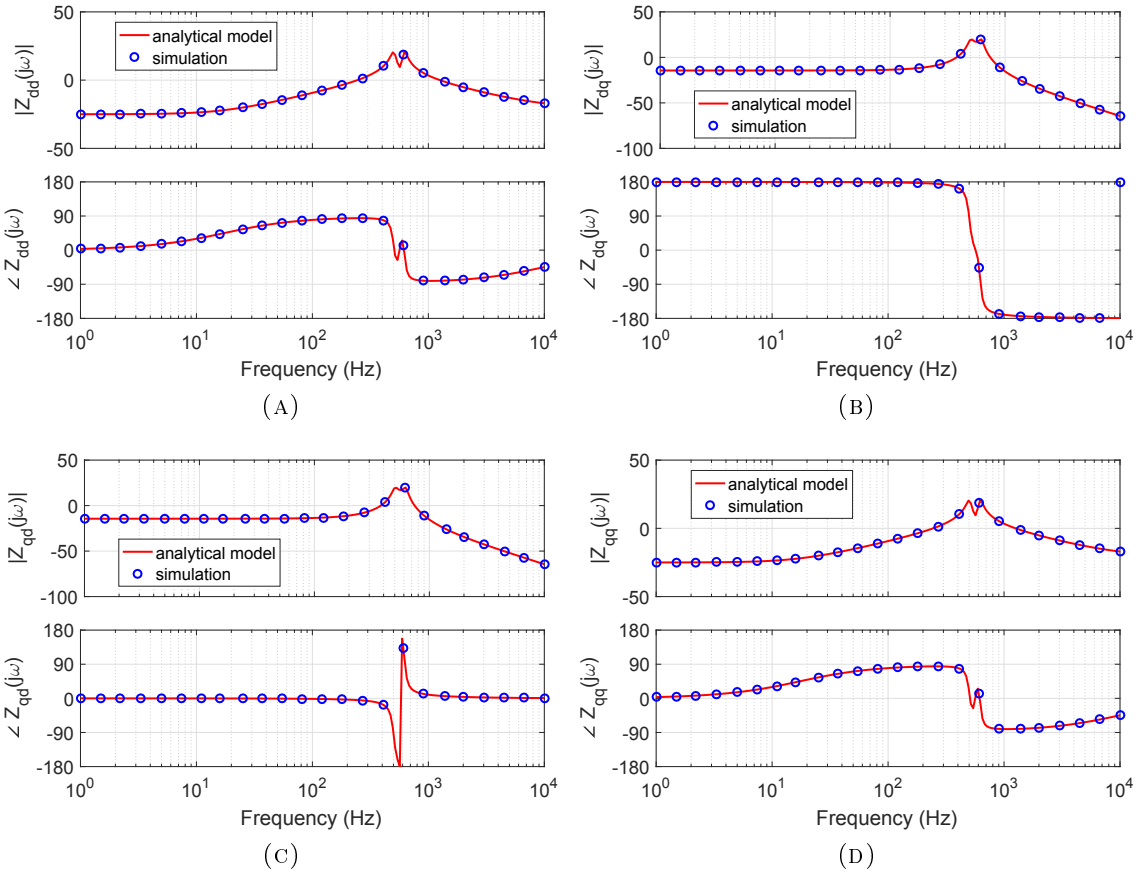

FIGURE 3.11: Direct Control: output impedances $\mathbf{Z_d}$ in dq-frame.

considering all the parasitics involved, and it is equal to the parallel between the inductance and the capacitance.

3.7.2 Current Control

The current controller consists of a proportional controller:

$$\mathbf{R_i}(s) = \begin{bmatrix} k_{pi}e^{-st_{calc}} & 0 \\ 0 & k_{pi}e^{-st_{calc}} \end{bmatrix} \tag{3.68}$$

where the proportional coefficients are equal for both axes and the calculation delay is included and it is equal to the switching period T_{sw}, defined in Tab. 3.2. Therefore: $t_{calc} = T_{sw}$.

The controller acts only on the dd and the qq channels, hence the cross-coupling has to be mitigated. The main goal of this control strategy is to damp the resonance due to the filter and the dq transformation, as can be noticed in Fig. 3.10a and Fig. 3.10d.

Without the integral component, the zero-error tracking of the reference is not guarantee. However, the outer voltage loop will be equipped with a proportional-integral regulator, in order to compensate this steady-state error.

The delay t_{pwm} due to the PWM is modeled with the function $e^{-et_{pwm}}$ is multiplied to the duty-cycle $\underline{d}$, to obtain $\underline{d}_{del}$.

The main transfer functions and the output impedance for the current controlled configuration are determined hereafter:

- the transfer function matrix between $\underline{i}^*_{L1}$ and $\underline{i}_{L1}$:

$$\hat{\underline{i}}_{L1} = \mathbf{H_i} \cdot \hat{\underline{i}}^*_{L1} \tag{3.69}$$

  can be easily determined considering the block scheme in Fig. 3.12b:

$$\mathbf{H_i} = [\mathbf{I} + \mathbf{H_d} \cdot \mathbf{R_i}]^{-1} \cdot \mathbf{H_d} \cdot \mathbf{R_i} \tag{3.70}$$

  The correspondence between analytical model and simulation results can be seen in Fig. 3.13. Once again, the difference becomes consistent at high frequencies, where the delay approximation is no longer acceptable.

- the output impedance can be easily determined considering firstly the effect of the current control on the inverter side inductance

$$\mathbf{Z^{par}_{L1,CC}} = \mathbf{Z^{par}_{L1}} \cdot \left[\mathbf{I} + V_{dc} e^{-st_{pwm}} \mathbf{Y^{par}_{L1}} \cdot \mathbf{R_i}\right] \tag{3.71}$$

  where the impedance is multiplied by the current loop gain. Therefore, the current control acts in the expected way, as in single-phase systems where the impedance is multiplied for $(1 + T_i)$, where T_i is the current open loop gain.

  Hence, the output impedance is determined as the parallel of $\mathbf{Z^{par}_{L1,CC}}$ with the filter capacitor $\mathbf{Z^{par}_{C}}$:

$$\mathbf{Z^{par}_{o,CC}} = \left[\mathbf{Y^{par}_{L1,CC}} + \mathbf{Y^{par}_{C}}\right]^{-1} \tag{3.72}$$

  The correspondence between analytical model and simulation results can be seen in Fig. 3.14. The matching is good, since the only difference can be noticed in *dq* and *qd* axis at high frequencies, where the impedance magnitude is much lower compared to the *dd* and *qq* impedances.

  Typically, the output impedance of a current controlled converter is very high at low frequencies because of the integral term of the controller. However,

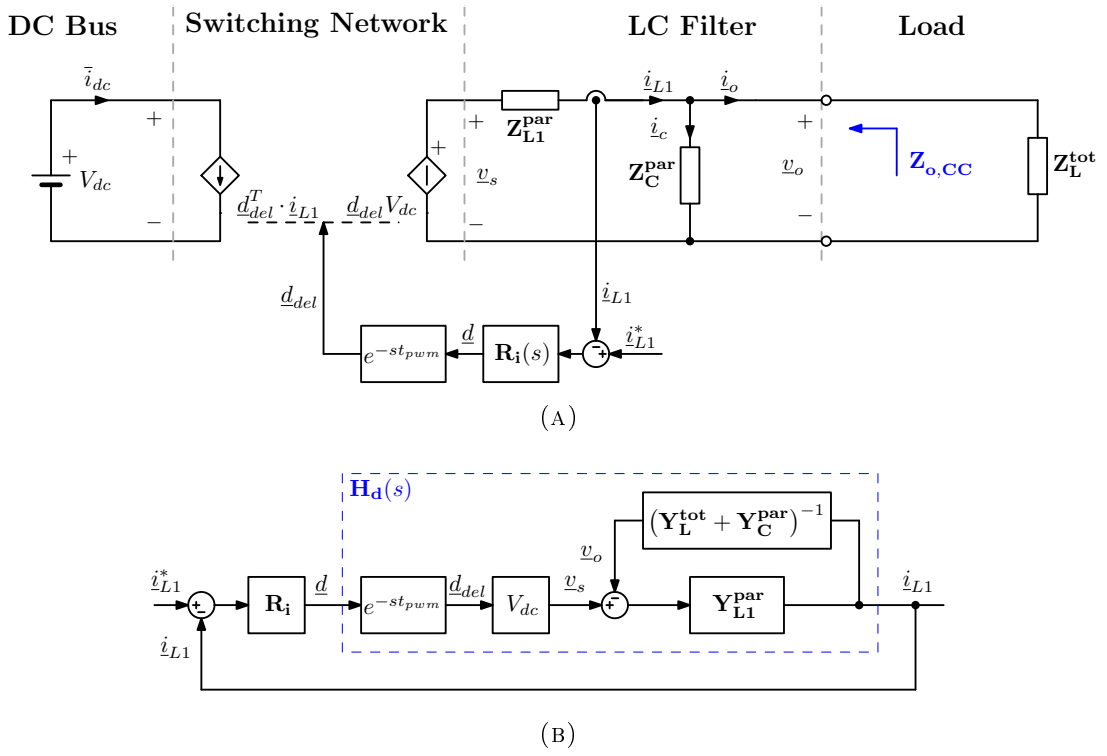

FIGURE 3.12: Direct Control: average model for the three-phase voltage source inverter (VSI) in dq-frame and control scheme.

in this case the impedance is constant because only a proportional controller has been used.

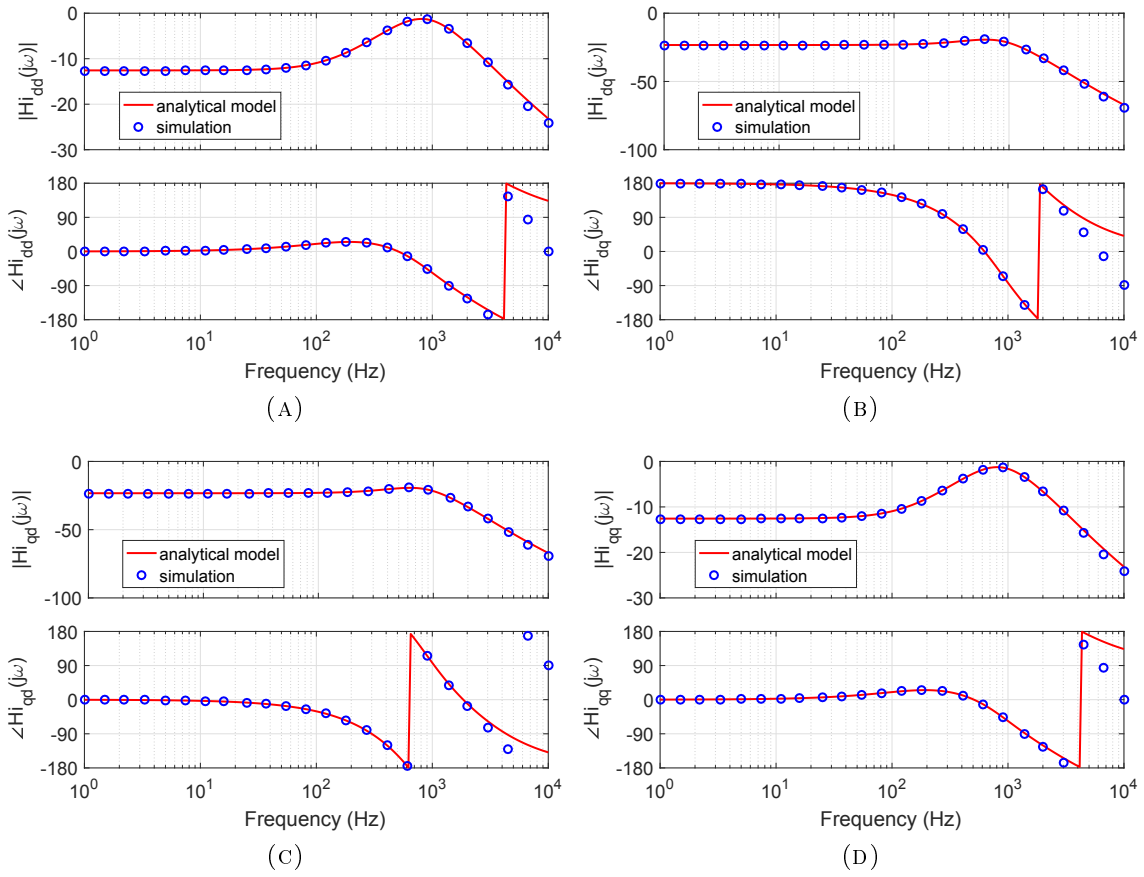

FIGURE 3.13: Current Control: closed loop $\mathbf{H_i}$ ($\hat{i}^*_{L1}$ to $\hat{i}_{L1}$) transfer functions in dq-frame.

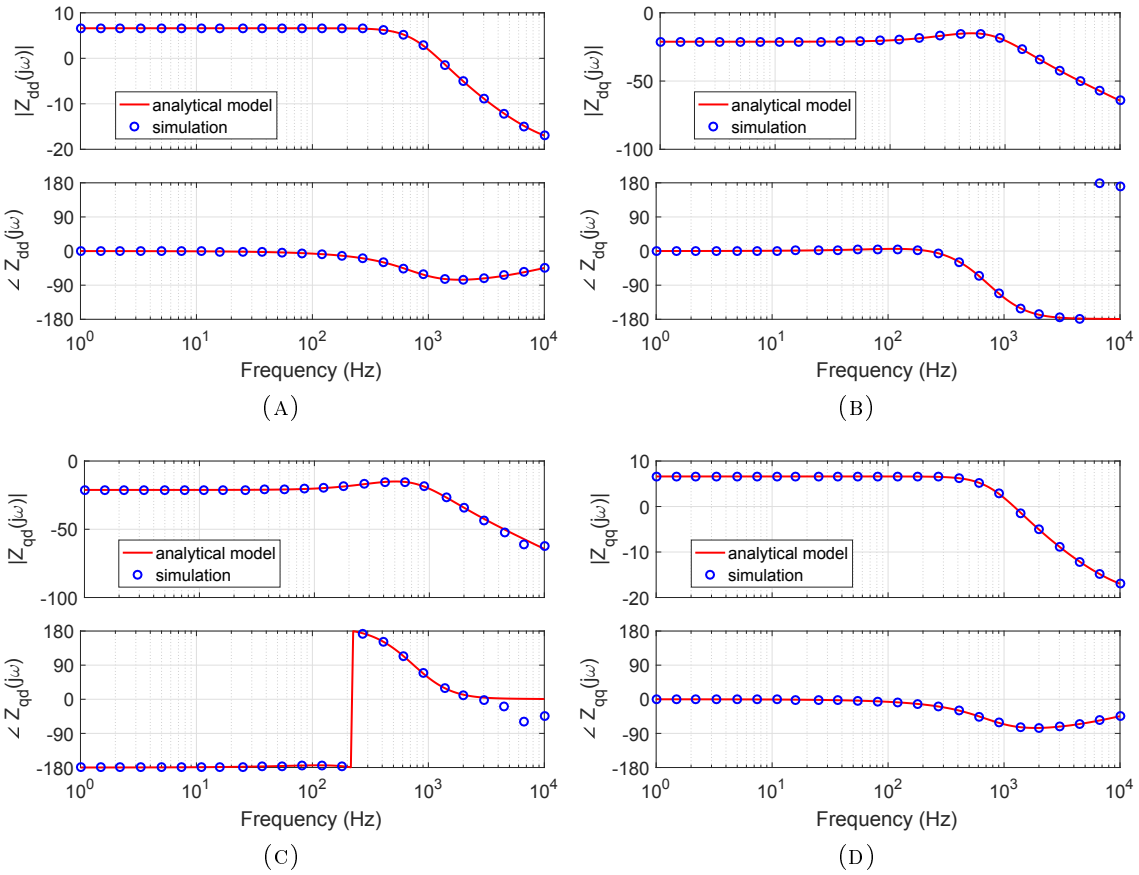

FIGURE 3.14: Current Control: output impedances $\mathbf{Z_{o,CC}}$ in dq-frame.

3.7.3 Voltage Control

The voltage control is applied in cascade to the current control, in order to realize a voltage source inverter (VSI). The regulator $\mathbf{R_v}$ includes proportional k_{pv} and integral k_{iv} terms and the calculation delay t_{calc}:

$$\mathbf{R_v}(s) = \begin{bmatrix} \left(k_{pv} + \frac{k_{iv}}{s}\right) e^{-st_{calc}} & 0 \\ 0 & \left(k_{pv} + \frac{k_{iv}}{s}\right) e^{-st_{calc}} \end{bmatrix} \tag{3.73}$$

where the proportional coefficients are equal for both axes and the calculation delay is included and it is equal to the switching period T_{sw}, as in Tab.3.2.

The main transfer functions and the output impedance for the current controlled configuration are determined hereafter:

- the transfer function matrix between $\underline{v}_o^*$ and $\underline{v}_o$:

$$\underline{v}_o = \mathbf{H_v} \cdot \underline{v}_o^* \tag{3.74}$$

  can be easily calculated considering the block scheme in Fig. 3.15b:

$$\mathbf{H_v} = \left[\mathbf{I} + \left(\mathbf{Y_L^{tot}} + \mathbf{Y_C^{par}}\right)^{-1} \cdot \mathbf{H_i} \cdot \mathbf{R_v}\right]^{-1} \cdot \left(\mathbf{Y_L^{tot}} + \mathbf{Y_C^{par}}\right)^{-1} \cdot \mathbf{H_i} \cdot \mathbf{R_v} \tag{3.75}$$

  The correspondence between analytical model and simulation results can be seen in Fig. 3.16. Once again, the difference becomes consistent at high frequencies, where the delay approximation is no longer acceptable.

- the output impedance can be easily determined considering firstly the effect of both the current and the voltage controls on the inverter side inductance

$$\mathbf{Z_{L1,VC}^{par}} = \left[\mathbf{I} + V_{dc} e^{-st_{pwm}} \mathbf{R_v} \cdot \mathbf{R_i}\right]^{-1} \cdot \mathbf{Z_{L1}^{par}} \cdot \left[\mathbf{I} + V_{dc} e^{-st_{pwm}} \mathbf{Y_{L1}^{par}} \cdot \mathbf{R_i}\right] \tag{3.76}$$

  where the impedance is multiplied on the left by the inverse of the voltage loop gain and on the right by the current loop gain. Therefore, the voltage control acts in the expected way decreasing the output impedance, as in single-phase systems where the impedance is divided for $(1 + T_v)$, where T_v is the current open loop gain. Considering both the control loops in single-phase:

$$Z_{L1,VC} = Z_{L1} \cdot \frac{1 + T_i}{1 + T_v} \tag{3.77}$$

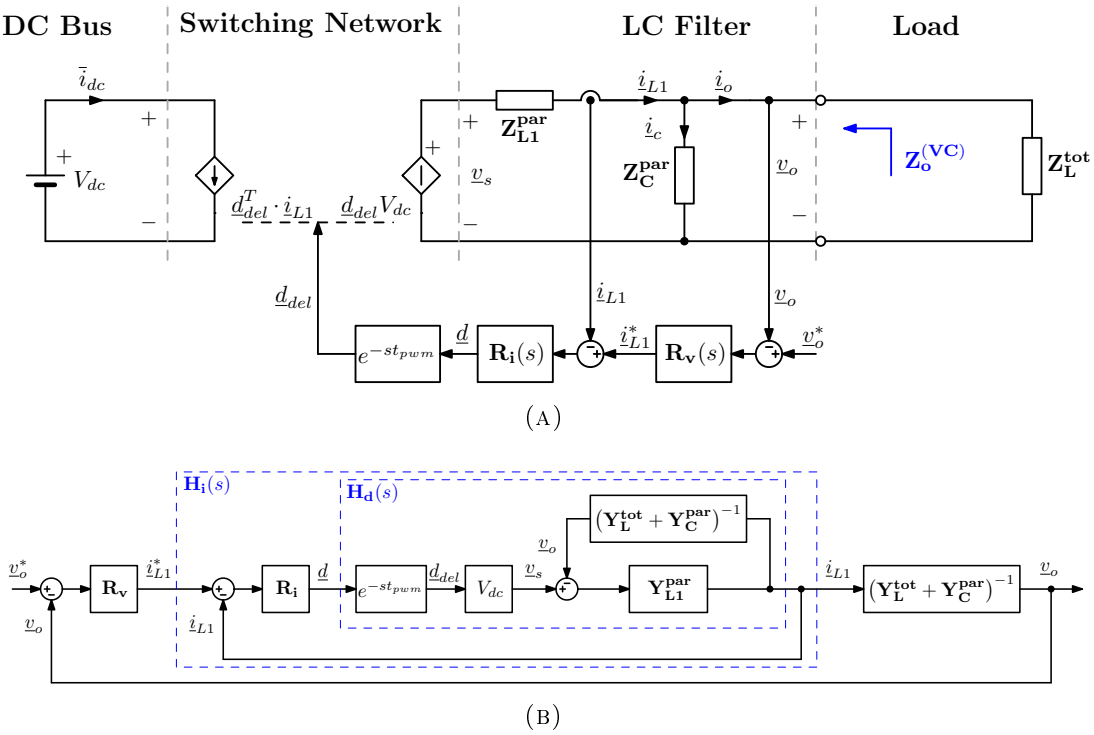

FIGURE 3.15: Voltage Control: average model for the three-phase voltage source inverter (VSI) in dq-frame and control scheme.

Hence, the output impedance is determined as the parallel of $\mathbf{Z_{L1,VC}^{par}}$ with the filter capacitor $\mathbf{Z_C^{par}}$:

$$\mathbf{Z_{o,VC}^{par}} = \left[\mathbf{Y_{L1,VC}^{par}} + \mathbf{Y_C^{par}}\right]^{-1} \tag{3.78}$$

The correspondence between analytical model and simulation results can be seen in Fig. 3.17. The matching is good, since the only difference can be noticed in the dq and the qd components at high frequencies, where the impedance magnitude is much lower compared to the dd and qq impedances.

As expected, the output impedance of a voltage controlled converter is very low at low frequencies, thanks to the proportional-integral control.

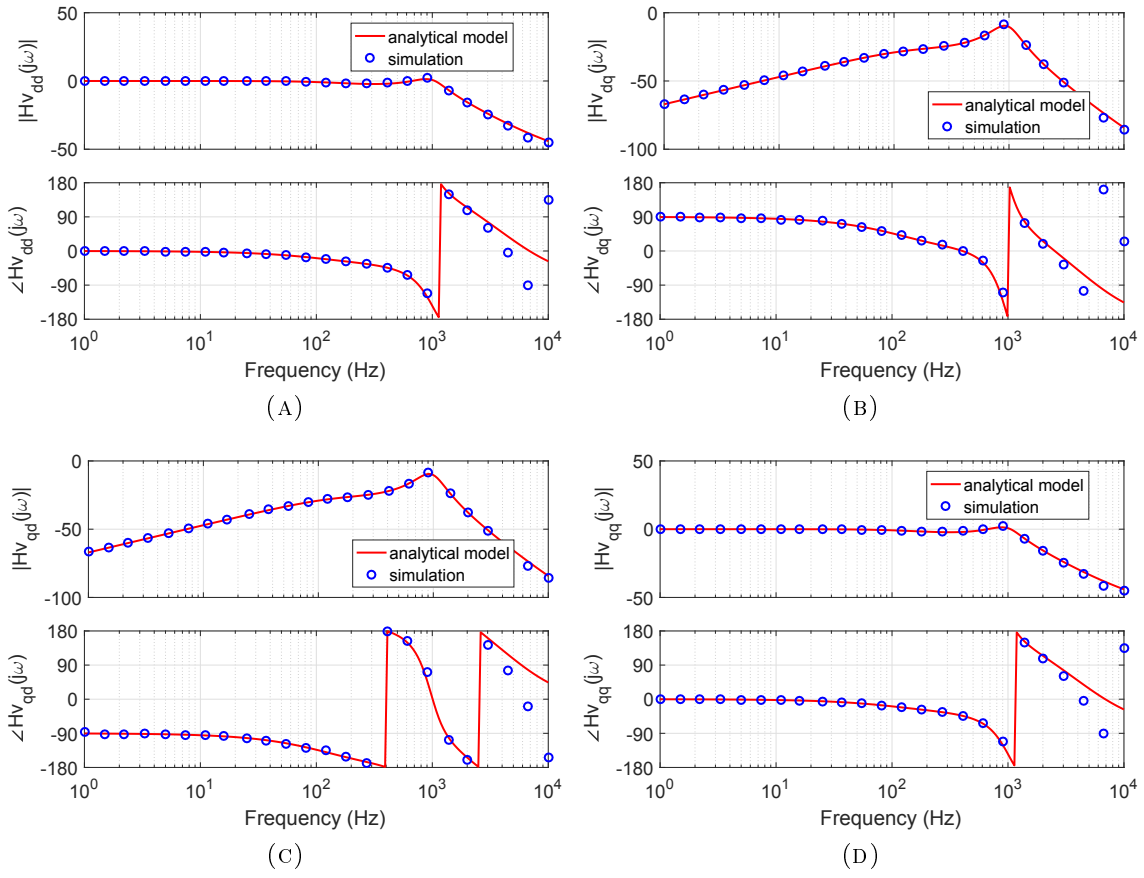

FIGURE 3.16: Voltage Control: closed loop $\mathbf{H_v}$ ($\underline{\hat{v}}_o^*$ to $\underline{\hat{v}}_o$) transfer functions in dq-frame.

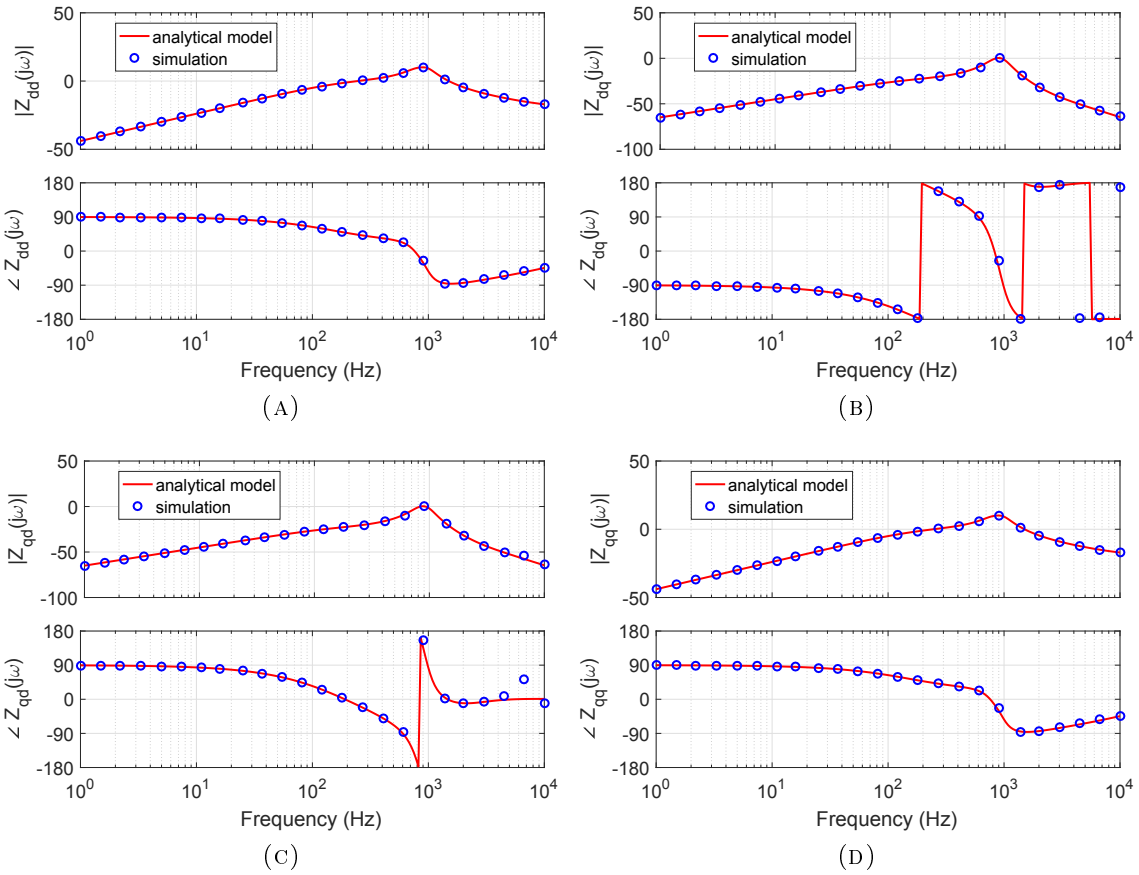

FIGURE 3.17: Voltage Control: output impedances $\mathbf{Z_{o,VC}}$ in dq-frame.

3.8 Black-box converter modeling

It is possible to model any voltage source converter by considering the no-load transfer functions $\mathbf{H_{v0}}$ and the output impedances $\mathbf{Z_{o,VC}}$.

Starting from the duty-cycle to inductance current transfer function in (3.65) and considering a null load impedance $\mathbf{Z_L^{tot}} = \mathbf{0}$:

$$\begin{aligned}\mathbf{H_{d0}} = \mathbf{H_d}\big|_{\mathbf{Z_L^{tot}=0}} &= V_{dc}e^{-st_{pwm}}\left[\mathbf{I} + \mathbf{Y_{L1}^{par}} \cdot \mathbf{Z_C^{par}}\right]^{-1} \cdot \mathbf{Y_{L1}^{par}} \\ &= V_{dc}e^{-st_{pwm}}\left[\mathbf{Z_{L1}^{par}} + \mathbf{Z_C^{par}}\right]^{-1}\end{aligned} \tag{3.79}$$

then passing to

$$\mathbf{H_{i0}} = \mathbf{H_i}|_{\mathbf{Z_L^{tot}=0}} = \left[\mathbf{I} + \mathbf{H_{d0}} \cdot \mathbf{R_i}\right]^{-1} \cdot \mathbf{H_{d0}} \cdot \mathbf{R_i} \tag{3.80}$$

and finally obtaining the no-load transfer function $\underline{\hat{v}}_{o,0} = \mathbf{H_{v0}} \cdot \underline{\hat{v}}_o^*$:

$$\mathbf{H_{v0}} = \mathbf{H_v}\big|_{\mathbf{Z_L^{tot}=0}} = \left[\mathbf{I} + \mathbf{Z_C^{par}} \cdot \mathbf{H_{i0}} \cdot \mathbf{R_v}\right]^{-1} \cdot \mathbf{Z_C^{par}} \cdot \mathbf{H_{i0}} \cdot \mathbf{R_v} \tag{3.81}$$

Hence, as in Fig. 3.19, combining $\mathbf{H_{v0}}$ and $\mathbf{Z_{o,VC}}$ it is possible to describe the dynamic behavior of the converter with an equivalent converter.

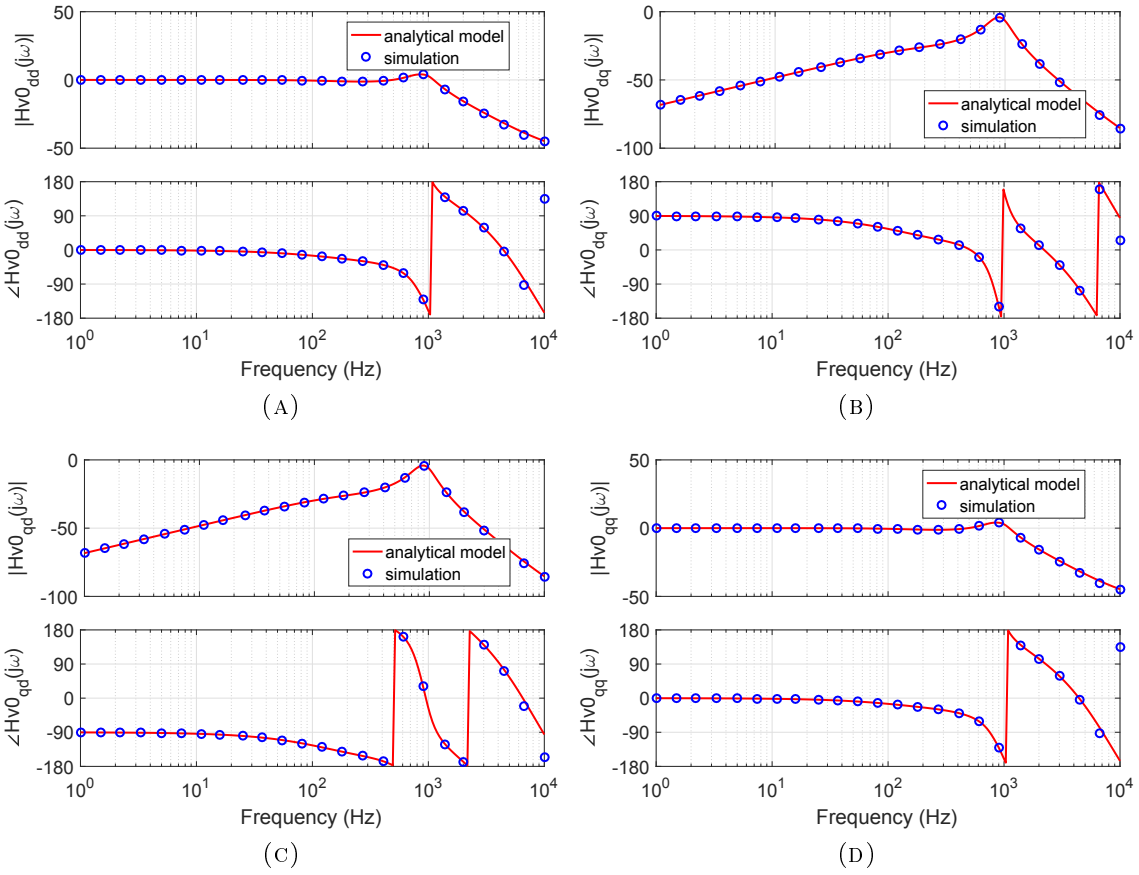

FIGURE 3.18: Voltage Control: closed loop $\mathbf{H_{v0}}$ transfer functions in dq-frame in no-load condition.

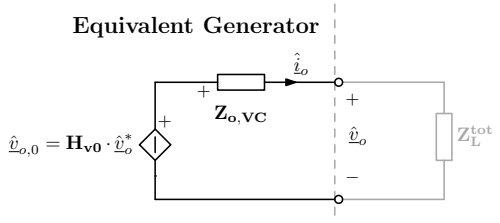

FIGURE 3.19: Equivalent generator modeling for the voltage source inverter.

3.9 Experimental Results

Firstly, a brief introduction to the impedance measurement unit (IMU) is hereafter provided, in order to understand the basic functioning.

3.9.1 Impedance Measurement Unit

The IMU shown in Fig. 3.21 consists of a controlled converter which can inject current or voltage perturbations into the three-phase system under test [77–81]. The current perturbation is introduced in the system as a shunt injection, while the voltage perturbation is performed with a series injection, as can be noticed in Fig. 3.21. The shunt injection gives better results for source impedances, typically low impedances if the source is voltage controlled, and series injection for load impedances, typically high impedances.

Both the injection and the measurements need a synchronization which is a critical aspect of this unit to inject/read properly. This issue is crucial since the system works in the *dq*-frame, which needs a proper synchronization. It is implemented with a phase locked loop (PLL), which dynamics can influence the final measurements and have to be considered [82]. The system in *dq* coordinates is shown in Fig. 3.20, where a shunt injection is performed.

The perturbation strategy can vary, starting from the basic frequency-by-frequency sinusoidal injection to faster and more elaborated solutions [83], e.g. chirp injection [84]. The goal of the IMU is to measure both the source and load side *dq* impedances, in order to address the stability of a three-phase system in the synchronous reference frame, according to the GNC [35,36] as shown in [15, 27, 31].

Defining the system as in the patent [85], one can obtain frequency-by-frequency the measurement of the source impedance as:

$$Z_{Sdq} = \left(\begin{bmatrix} i_{Sdd} & i_{Sdq} \\ i_{Sqd} & i_{Sqq} \end{bmatrix}^T \cdot \begin{bmatrix} i_{Sdd} & i_{Sdq} \\ i_{Sqd} & i_{Sqq} \end{bmatrix} \right)^{-1} \cdot \begin{bmatrix} i_{Sdd} & i_{Sdq} \\ i_{Sqd} & i_{Sqq} \end{bmatrix}^T \cdot \begin{bmatrix} v_{Sdd} & v_{Sdq} \\ v_{Sqd} & v_{Sqq} \end{bmatrix} \quad (3.82)$$

and equivalently for the load impedance

$$Z_{Ldq} = \left(\begin{bmatrix} i_{Ldd} & i_{Ldq} \\ i_{Lqd} & i_{Lqq} \end{bmatrix}^T \cdot \begin{bmatrix} i_{Ldd} & i_{Ldq} \\ i_{Lqd} & i_{Lqq} \end{bmatrix} \right)^{-1} \cdot \begin{bmatrix} i_{Ldd} & i_{Ldq} \\ i_{Lqd} & i_{Lqq} \end{bmatrix}^T \cdot \begin{bmatrix} v_{Ldd} & v_{Ldq} \\ v_{Lqd} & v_{Lqq} \end{bmatrix} \quad (3.83)$$

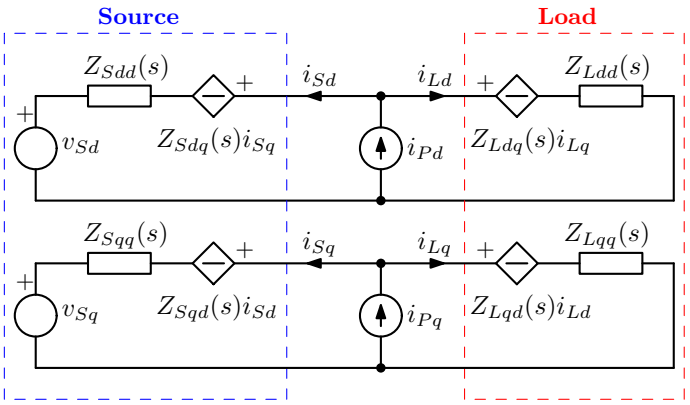

FIGURE 3.20: System in dq coordinates with shunt injection.

3.9.2 Measurement of the DER Output Impedance

In the analyzed configurations, the current control is always the same, while two configurations are considered for the voltage control, as shown in Tab. 3.3. The output impedance estimated through the analytical model is compared with the experimental results. In Fig. 3.22 the case Voltage-Controlled #1 and in Fig. 3.23 the case Voltage-Controlled #2 are shown, accordingly with Tab. 3.3. The experimental results are matching well the analytical model when the impedance presents a high magnitude, while there are some mismatches when the magnitude is low, due to the system precision.

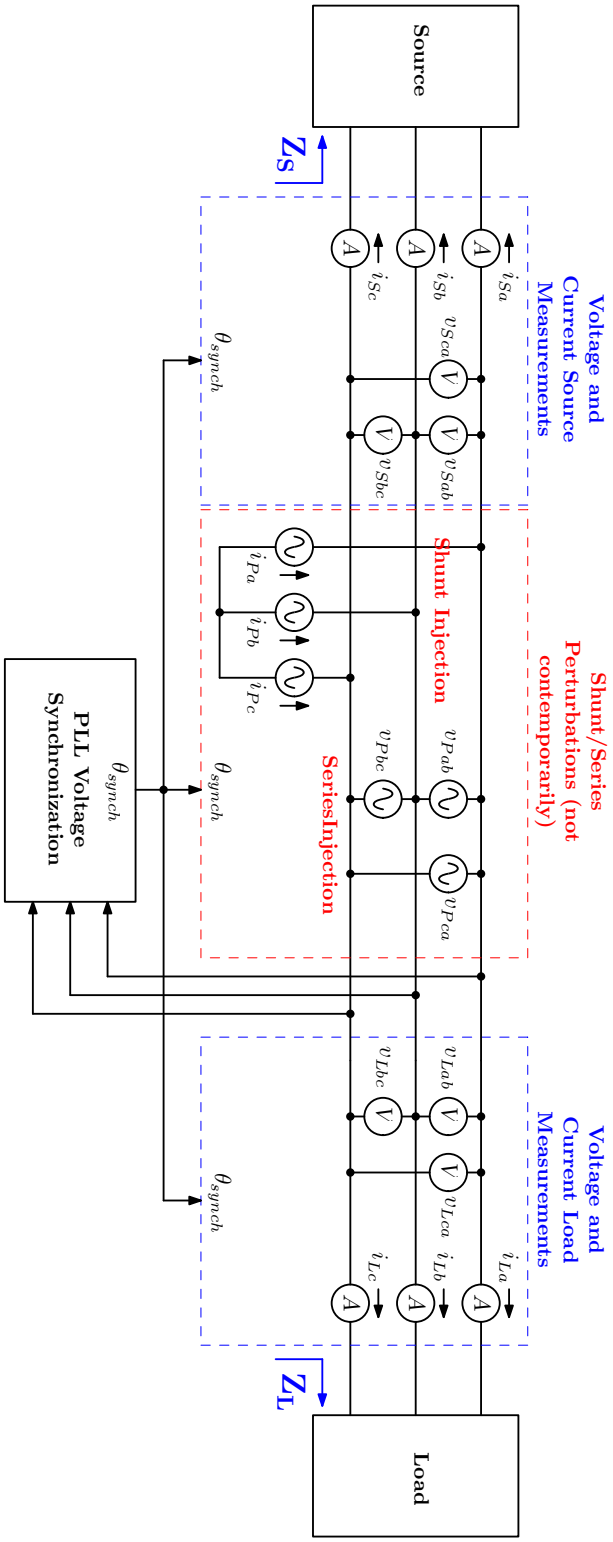

FIGURE 3.21: Basic electrical scheme of the impedance measurement unit (IMU).

		VSI Bandwidth and Coefficients				References				Load	AC Bus	
		f_c	ϕ_M	k_p	k_i	V_d^*	V_q^*	I_d^*	I_q^*	R_L	V	I
#	Configuration	[Hz]	[deg]			[V]	[V]	[A]	[A]	[Ω]	[Vrms]	[Arms]
1	Current-Controlled	1000	93	0.0104	0			52.5	52.5	10.0	68.9	7.34
2	Voltage-Controlled # 1	600	65	0.6421	1012.8	85.0	85.0			15.0	70.0	7.0
3	Voltage-Controlled # 2	300	60	0.3304	968.4	85.0	85.0			15.0	66.7	4.53

TABLE 3.3: Experimental for the characterization of the inverter in current- and voltage-controlled configurations.

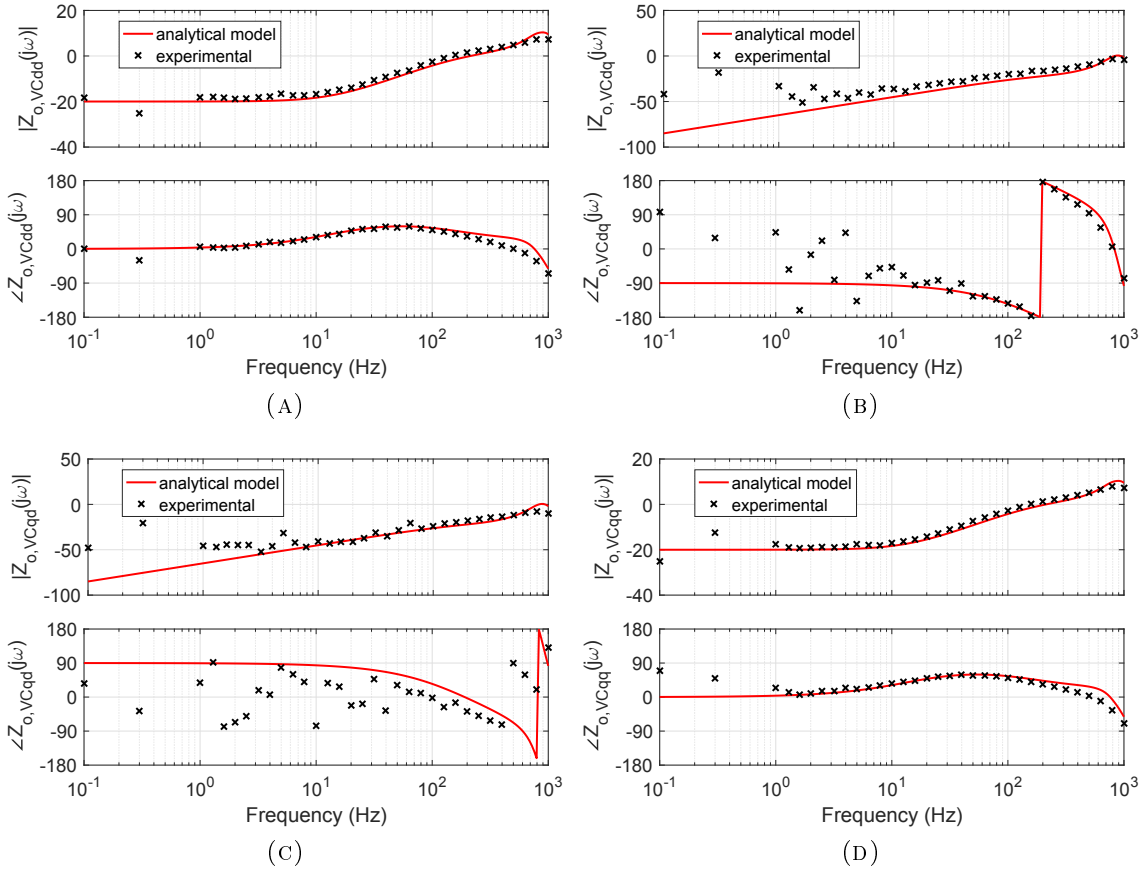

FIGURE 3.22: Voltage Control: output impedances $\mathbf{Z_{o,VC}}$ in dq-frame compared with experimental results for 60 deg @700Hz.

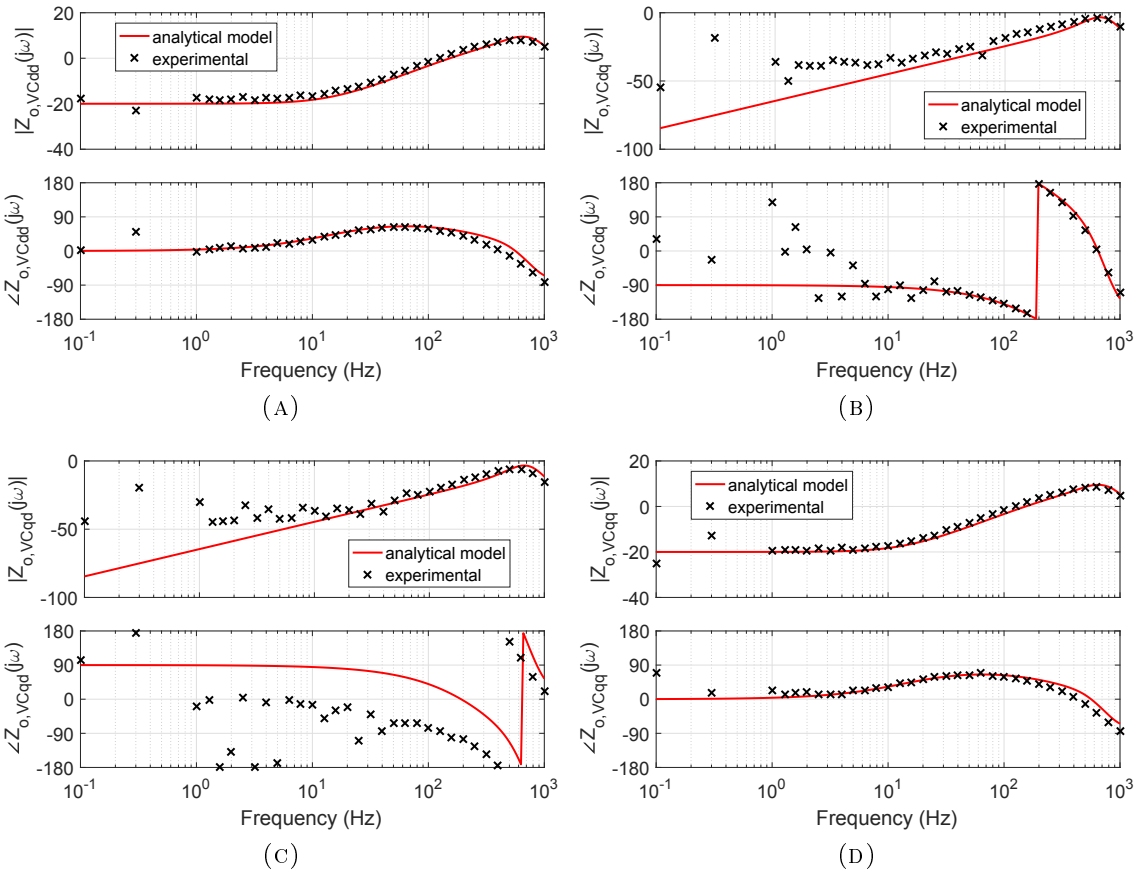

FIGURE 3.23: Voltage Control: output impedances $\mathbf{Z_{o,VC}}$ in dq-frame compared with experimental results for 60 deg @300Hz.

Chapter 4

Hybrid-Grid Modeling

Microgrids are emerging as an important component of large-scale smart grids [86–91]. The renewables are spreading in many applications, both in on-grid and off-grid systems. The latter, typically consists of a mini-grid with diesel generators, where the energy produced by the renewables allows to reduce the fuel consumption. However, the main disadvantage comes from the intermittent nature of these sources, where the PV works only during daytime and WG is not constant and sometimes unpredictable. In general, four main applications where battery energy storage systems (BESSs) are deployed to increase the share of variable renewable energy and improve electricity reliability are [92]:

- island and off-grid/rural electrification with renewable energy deployment;
- households with solar photovoltaic (PV);
- variable renewable energy smoothing and energy supply shift;
- fast, short-term electricity balancing in ancillary markets.

Hence, BESSs are usually deployed in order to store the *surplus* of energy produced by PV and WG and release it during night.

In general, three different types of electrical equipment can be defined according to the inner characteristics/control strategies as defined in [93]:

- *grid-forming*, when the equipment generates the grid voltage, and is typically represented by an ideal voltage generator (e.g. voltage-controlled inverter);
- *grid-feeding*, when the equipment, thanks to a PLL, synchronizes with the grid voltage and injects a current (e.g. PV inverter), hence it is represented with an ideal current generator;
- *grid-supporting*, when the equipment is capable of both creating the grid voltage and injecting current into the grid (e.g. droop-controlled inverter). It is modeled as a voltage generator with an output impedance.

Moreover, the power sharing control can be structured in four layers [94], from the fastest to the slowest:

- *Zero control*: it consists on the inner loops for the current and voltage regulation of the inverter.
- *Primary control*: it refers to the possibility of the inverters to change frequency and voltage in order to immediately satisfy the power request of the load, according to the P/f and Q/V droop laws. It represents the fastest control.
- *Secondary control*: voltage and frequency are kept at precise values, so this control provides the chance to reach these reference values shifting the droop curves.
- *Tertiary control*: it consists of the variation of the power set points of the equipments connected to the grid.

The hybrid-grid modeled hereafter has two important requirements, which have to be respected:

1. provide the possibility to connect/disconnect the diesel generator for maintenance or for backup functioning;
2. reduce the fuel consumption of the diesel generator.

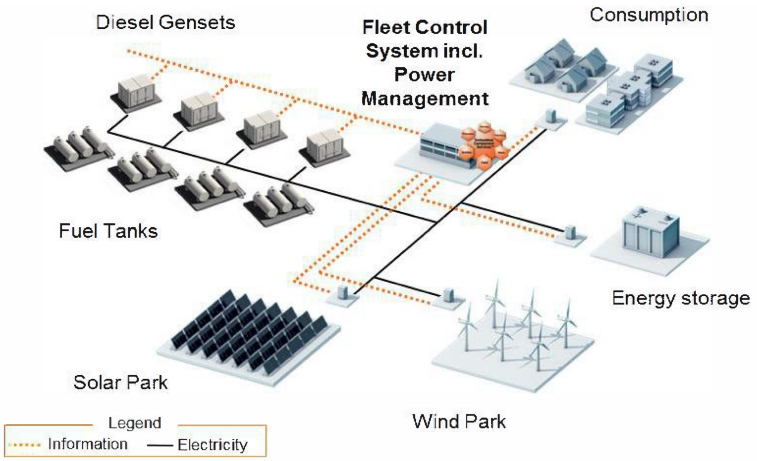

FIGURE 4.1: From [86]: generic hybrid-grid.

These two requirements give the first constraints to the control strategy, since the inverters must be capable of sustaining the grid voltage when the diesel generator is disconnected: the inverters must be controlled as *grid-supporting* equipments, where the droop-control is suitable for this purpose.

The control described in [95] provides *primary* and *secondary controls*. Moreover, during connection and disconnection the instant current is absorbed by the inverter, while the diesel generator results less influenced. Hence, it has been adopted in this work.

This part is divided in the following main parts:

1. Firstly, the hybrid-grid and the related instability issue is presented.
2. Then a literature review concerning control techniques for DERs showing the beneficial features of synchronous generators is discussed. The Diesel Generator is presented (virtual synchronous machine (VSG) and emulation).
3. In the third section the theoretical background necessary to model the diesel generator is presented with the diesel engine and the synchronous generator and the other parts involved. A simulation model is compared with the experimental results for a load step.
4. In the fourth section the PCS is described and the simulation results in the grid-connected mode are compared to the experimental results, with perturbations of the simulation model for the most significant transfer functions.
5. The fifth section analyzes the hybrid-grid, where the PCS is connected in parallel to the diesel generator, through the simulation model implemented

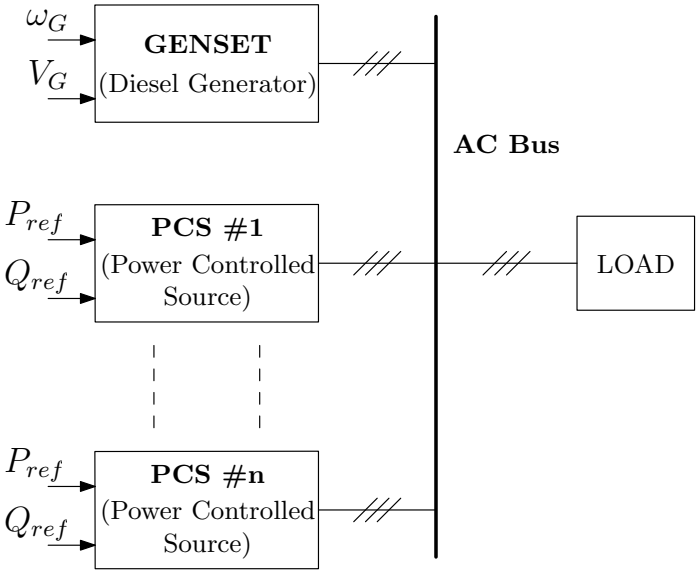

FIGURE 4.2: Hybrid-grid under investigation.

in MATLAB/Simulink: perturbations and step responses can be found, where the simulation results are compared with the experimental tests.

4.1 System Description and Instability Issue

The system under investigation is depicted in Fig.4.2. The grid consists of:

- a Genset (Diesel Generator) which imposes the frequency (*isochronous mode*) and the voltage to the grid;
- a certain number of PCS (Power Controlled Source), which are *droop controlled* inverters as in [95];
- a resistive load;
- the AC bus where all the parts included are connected.

Some of the existing applications in the hybrid-grids work with the conventional control for photovoltaic inverters, where the current reference is synchronized to the grid voltage thanks to a phase-locked loop (PLL) and the inverter can be considered as a current generator (grid-feeding). However, with this control strategy the PCS is not able to do the grid forming when the GenSet is disconnected because the grid voltage is not set by any generator.

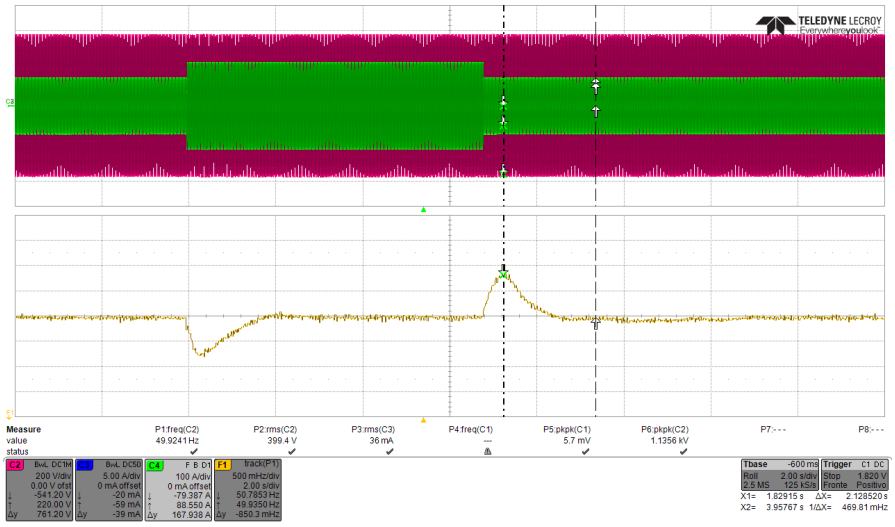

(A) Genset: load step $50kW \rightarrow 80kW \rightarrow 50kW$ (2s/*div*)

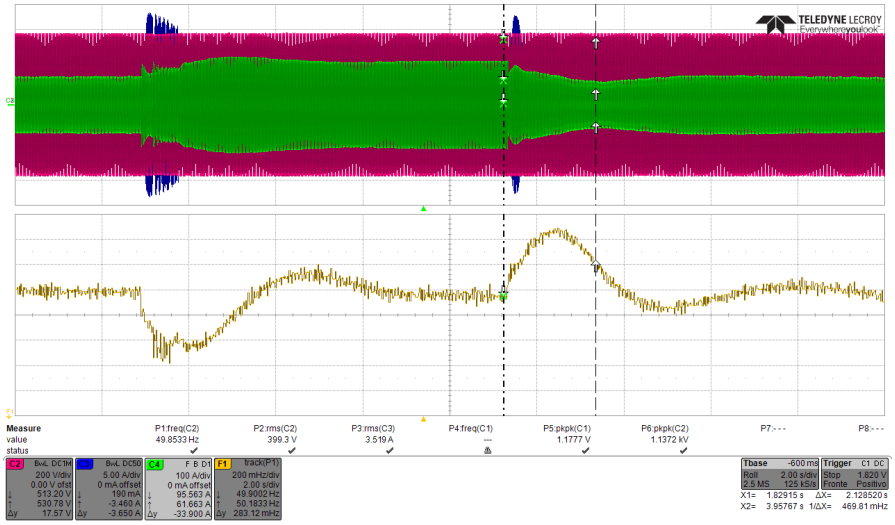

(B) Genset and PCS: load step $50kW \rightarrow 80kW \rightarrow 50kW$ (5s/*div*)

FIGURE 4.3: Comparison of the load steps of the Genset without and with a PCS connected in parallel (in *magenta* the AC bus voltage, in *green* the GenSet current, in *blue* the PCS current, the waveform in *yellow* in the lower part represents the frequency of the waveforms): the current becomes oscillating when a load step is applied.

The desired scenario is to have a grid where the GenSet can be disconnected and for this reason the inverter must be *droop controlled*, in order to sustain the grid voltage also when the GenSet is disconnected.

Using the control scheme implemented in [95], where an outer loop is considered in order to have a correct power tracking, the system exhibits a low stability margin when the PCS is connected in parallel to the GenSet.

In Fig.4.3 the experimental tests can be seen for the case without, in Fig.4.3a, and with, in Fig.4.3b, the PCS connected to the GenSet when the load power

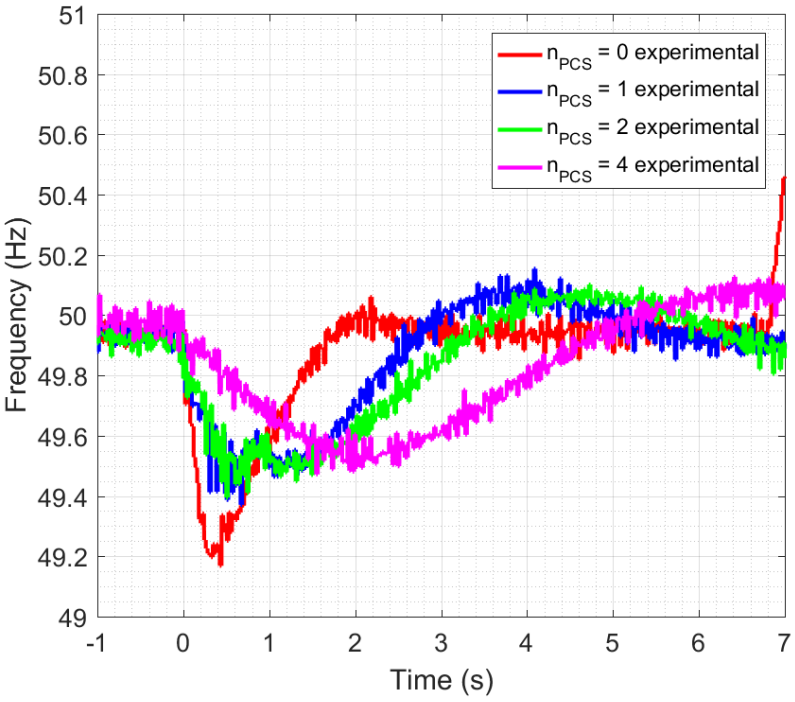

FIGURE 4.4: Load step comparison of the GenSet with an increasing number of parallel PCSs (experimental data) for a load step of $P_L = 50\text{kW} \rightarrow 80\text{kW} \rightarrow 50\text{kW}$ and with a reference power of the PCSs of $p_{ref} = 0\text{kW}$.

changes as: $P_L = 50\text{kW} \rightarrow 80\text{kW} \rightarrow 50\text{kW}$. The first transient regards the load connection and the frequency decreases, while in the second transient the load is disconnected causing a frequency increase. While in the case without PCS connected the transient resolves as a first order system, in the case with PCS the transient exhibits some second order system oscillations.

In Fig.4.4 the experimental currents and frequencies during the load disconnection are compared for an increasing number of connected PCSs with a power reference of $P_{ref} = 0\text{kW}$. The case without PCSs ($n_{PCS} = 0$) has a minimum frequency of about $f_{0PCS,max} = 50.8\text{Hz}$ with a settling time is of about $t_{set,0PCS} = 1.5\text{s}$. In the other cases the settling time increases up to $t_{set,6PCS} = 15\text{s}$ even if the maximum frequency is $f_{6PCS,max} = 50.3\text{Hz}$ for the case of 6 PCSs connected ($n_{PCS} = 6$).

This undesired oscillation increases with the number of PCSs connected to the GenSet and it is reflected to the currents as well. The current oscillation can be critical and a limitation by the PCSs protections could occur. In Fig.4.4 can be seen that, even if the power reference is $P_{ref} = 0\text{kW}$, the PCSs reach a high maximum current. The case with 6 PCSs reaches the highest current value because the load applied is the same and the load current is divided by the number of connected PCSs.

4.2 Literature Review

In this section the state of the art concerning the hybrid-grids with Diesel Generator is presented. Firstly, an overview on the hybrid-grid state of the art is presented.

Reference [96] analyzes the possible scenarios that can be found in an isolated hybrid-grid and gives a wide description of the problems that can be found and the control strategies already used. As stated in [96]: IEA PVPS (International Energy Agency, Photovoltaic Power System Programme) in Task 11 explores various design, control, and operational aspects of remote power generation and delivery systems (hybrid mini-grids) that include multiple energy sources to supply community-type loads. The immediate applications are for electrification of non-integrated areas and geographical islands based on renewable energy sources (RES). Traditionally, remote communities worldwide have been supplied electricity by diesel engine-generator sets (gensets). The use of RES can reduce the environmental impact of power generation, displacing diesel fuel and reducing the overall electricity price. When there is high penetration of RES, the inherent fluctuating and intermittent power characteristics of RES and the highly variable load profile of remote communities create significant challenges for the grid forming (master) unit(s) that regulate voltage and frequency. These challenges can be addressed with suitable control strategies which should at one level, (primary control) maintain grid stability by balancing generation and consumption of power and, at the other level, (secondary, or supervisory, control) optimize the generation of all sources and operation of the energy storage units.

The main information collected in [96] are the following:

- The *multi-master rotating machine dominated mini-grid*, which is a typical configuration for a diesel mini-grid, has multiple ac sources (fossil fuel gensets, PV inverters, and other RES) connected to the mini-grid and simultaneously supplying power. The gensets do the grid forming and the other sources follow the mini-grid voltage and frequency. In a typical instance of this architecture, the grid is formed by a diesel power plant consisting of two or more diesel units, with at least one of them operating continuously. Interruptible diesel operation is possible in the presence of adequate amounts of renewable energy sources (RES) and energy storage capacity. Power quality and system stability depend on the ability of the gensets to respond to changes in power balance and other disturbances. Conventional diesel gensets are not designed to operate for extended periods at loads under

about 30% of their rating. Other steps to maximize RES energy contribution include:

  - resizing the gensets in the diesel plant and adopting a genset cycling strategy so that a lower power genset operates when load demand is low and/or RES contribution is high
  - ensuring that the gensets are equipped with modern controllers that allow rapid, automatic response to changing load conditions
  - upgrading the supervisory control system to manage the RES contribution,
  - increasing RES capabilities, in terms of control and communications, including short term storage
  - adding an automated demand management system that sheds or adds dispatchable loads (e.g. water pumping, cooling/heating, etc.) as needed

- The *single switched master mini-grid* architecture has multiple ac sources connected to the mini-grid (typically battery and PV inverters and a fossil fuel genset), but the grid forming control is switched between the genset and the battery inverter(s). This allows the genset to be turned off. This architecture has evolved from smaller PV hybrid systems for solar home applications. Developments in inverter and system technology have resulted in systems that can support village mini-grids. These advances include:

  - introduction of new PV battery charge controllers that incorporate PV maximum power point tracking (MPPT), temperature compensated multi-stage battery charging algorithms, and means to coordinate with the inverter/charger to manage the battery charging process. These MPPT charge controllers may be integrated into the inverter/charger, or remain as separate devices that communicate with the inverter/charger over a data network.
  - Introduction of higher power capability for larger systems. This is achieved either through higher capacity inverter/chargers, or by modular systems that allow inverter/chargers to be connected in parallel to increase capacity.
  - Introduction of data networks that interconnect system elements (e.g. PV charge controllers, inverter/chargers, generator controls, human interface) to enable system control, energy management, and monitoring.

  - Development of control techniques that allow true, bidirectional four quadrant operation of the inverter/charger (rectifier) and fast, smooth transition of the inverter from a voltage source (grid former) to a current source (grid follower). This allows implementation of new operating modes that support both genset operation and interconnection to the central utility grid.

  In this system, the bidirectional inverter/chargers exercise supervisory control over the system and manage the transitions among operating modes. The operating modes are:

  - autonomous operation with inverter/charger as the grid forming master. Multiple inverters can be paralleled to increase output power capability but their operation is controlled by a master unit to synchronize their ac output waveforms and to share output power.
  - Autonomous operation with genset master. The inverter/chargers can be configured to operate as battery chargers which absorb power from the mini-grid only, or they can be configured to provide generator support also, by delivering power to the ac mini-grid under high demand conditions.

  Over the past decade this technology has advanced substantially, allowing the SSM system to remain competitive with newer approaches for small mini-grid applications. Key advances include the development of control techniques that allow fast, smooth transition of the inverter from a voltage source to a current source.

- The *multi-master inverter dominated mini-grid* also has multiple ac sources (fossil fuel gensets, PV inverters, battery inverters, other RES) connected to the minigrid and simultaneously supplying power, but in this case certain inverters participate in the grid forming along with the gensets. This architecture is aimed at decentralized mini-grid applications where new generation sources can be added at locations throughout the mini-grid. A decentralized control structure that does not need high speed communication links is required. In such a case, the droop methods that are widely used for paralleling synchronous generators in conventional power systems have an advantage since they do not require a separate communication channel. For paralleling grid forming inverters, the frequency and magnitude of the reference voltage of each inverter can be made a function of their active and reactive powers with the classical droop functions.

The sizing of the diesel generator is a key point in the hybrid-grid design. In general, the optimal unit sizing of a diesel power plant requires careful consideration of several factors including detailed analysis of daily and seasonal load fluctuations, annual load growth, and incorporation of practical constraints for feasible and reliable diesel operation [96, 97].

As stated in [98, 99], a Battery Energy Storage System (BESS) has the potential to reduce the fuel consumption and the maintenance costs of diesel hybrid mini-grids with high penetration of Renewable Energy Sources (RESs). For that, it should be able to support the grid forming genset or diesel power plant, by balancing the load and supplying/absorbing average active power so that the diesel genset(s) can operate in a high efficiency region. Besides, it should be able to allow the shut-down of the genset(s) and form the grid when the favorable conditions arise. The control system presented is capable to perform all this tasks as demonstrated by simulation [98]. The main aspects of this paper are the actual configuration of the control circuit using per-phase *dq* control and the approach for controlling the active power absorbed/supplied by the BESS to force the genset to operate in a desired region supplying balanced currents. Also, the operation of the BESS in the grid forming mode, providing balanced voltages while supplying active power in two phases and absorbing in one. In [99] the BESS is tested for genset support mode, grid forming mode and while changing the mode from one to another. From the results presented, throughout this paper, it is concluded that this BESS control strategy is high effective for genset support mode, grid forming mode and during the transients.

Other references such as [100, 101] perform the simulation of a hybrid-grids with diesel genset and RES. In particularly, in reference [100] the simulations are performed in DigSilent. To allow the parallel operation of diesel generators, a droop control is simulated. The grid under investigation is reported in Fig.4.5a, where a primary-secondary control is applied:

- the primary control, which is regulated by the governors of diesel generators and the frequency controller of the BESS, adapts the output power of the power sources in order to balance the active power of the grid again;
- the secondary control is the supplementary control, which reacts to the frequency deviation and brings it back again to the nominal value; it is much slower than the reaction of the primary control in order to avoid the interaction with the transient values of frequency deviations shortly after the load changes. Therefore, the secondary control regulates in terms of seconds to minutes.

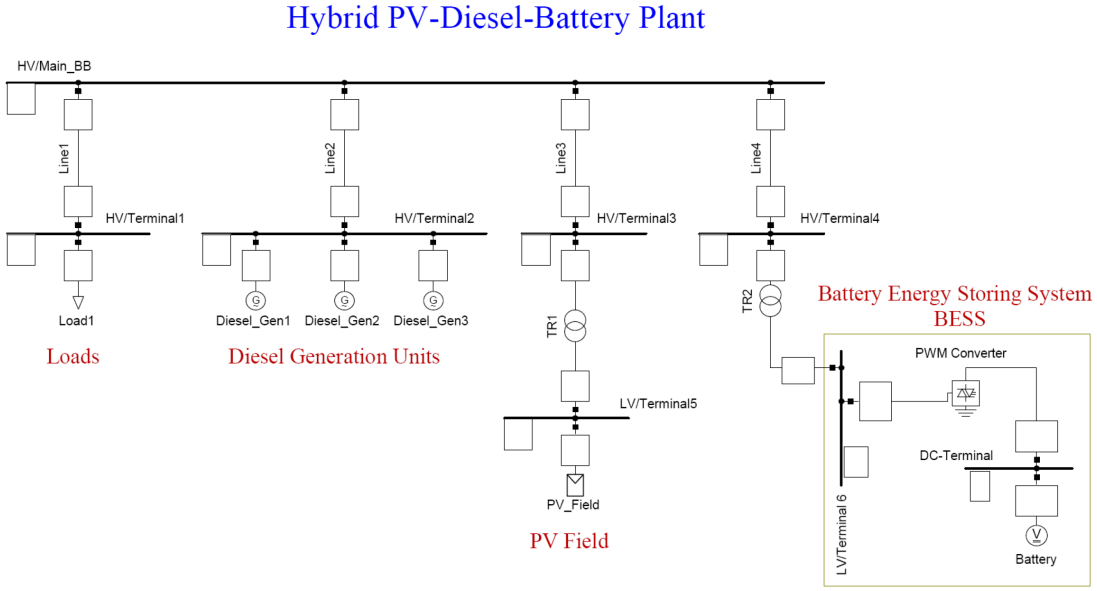

(A)

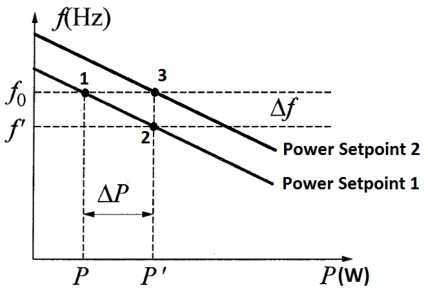

(B)

FIGURE 4.5: From [100]: (a) hybrid-grid under investigation and (b) mechanism of secondary control with drooping power source.

as in Fig.4.5b, where: at point (1) the frequency of the grid is at the nominal value (f_0), at point (2) the load increased and the frequency decreased according to droop control and finally at point (3) the set point of the power source is increased in order to retrieve the frequency. In [100] several simulation results are presented, from the fuel consumption to the frequency and powers, and two control strategies are presented:

- the first control strategy represents the operation of the plant when the primary control is provided by the diesel generators and the BESS in parallel, and the secondary control is provided by the BESS;
- the second control strategy represents the operation of the plant when the primary control is provided by the diesel generators and the BESS in parallel, and the secondary control is provided by the diesel generator and the BESS in parallel.

A load step of the 10% of the total power is applied to the system with the first control. The result of the simulation is shown in 4.6a: the frequency drops directly after the load increase, and then it retrieves the nominal value after about 75 seconds. The output power of the diesel generators increases shortly after the load increase according to the primary control, but it drops again after a short time according to secondary control. On the other hand, the output power of the BESS increases instantaneously as the load increase according to primary control, and then it increases again to cover all the extra demanded power by the load in order to restore the frequency to the nominal value.

A load step of the 10% of the total power is applied to the system with the second control. The result of the simulation is shown in 4.6b: the frequency drops directly after the load increase, and then it retrieves the nominal value after about 50 seconds. The settlement time is shorter, because more power sources contribute to the secondary control. The output power of the diesel generators increases shortly after the load increase according to primary control, and then it stabilizes at a higher value than the initial output power according to secondary control. On the other hand, the output power of the BESS increases instantaneously as the load increases according to primary control, and then it decreases slightly until it reaches the steady state value according to secondary control.

In reference [102] the stability analysis of a hybrid-grid is performed. The stability droop controlled inverter is evaluated in grid-connected condition, with a parallel inverter and finally with a diesel generator as in Fig.4.7a. The coupling impedance of the droop control in Fig.4.7b determines the stability of the system, and the stability regions are reported. The main considerations are:

- the droop coefficients k_P and k_Q are already determined by the used frequency and voltage range of an island grid;
- the remaining degrees of freedom are the time constants and the ohmic-inductive impedance of the coupled voltage sources;
- high impedance leads to more stability of the droop controlled inverter(s) and the diesel genset;
- high time constants of the droop lead to more stability but also to a longer settling time;
- high inertia constant of diesel genset together with a small time constant of the inverter droop leads to an overshoot of active power step response of the

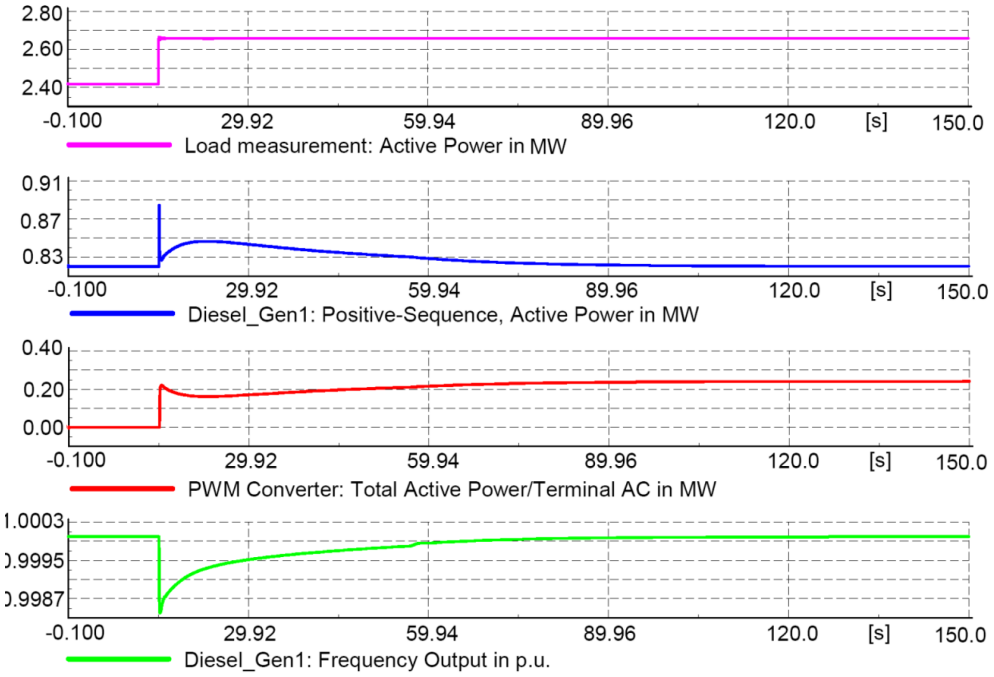

(A)

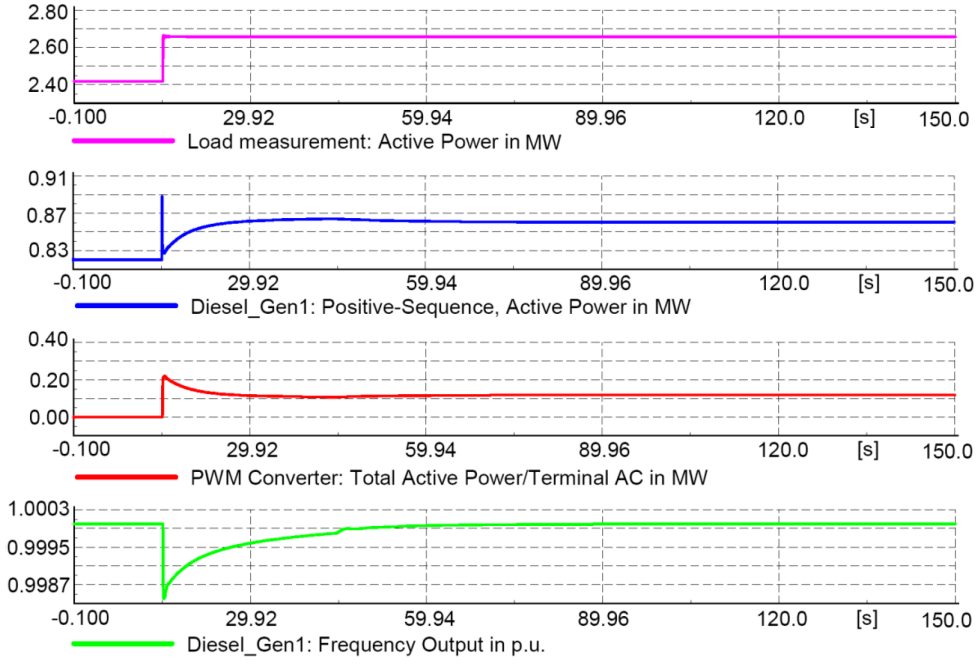

(B)

FIGURE 4.6: From [100]: (a) first control strategy (b) second control strategy.

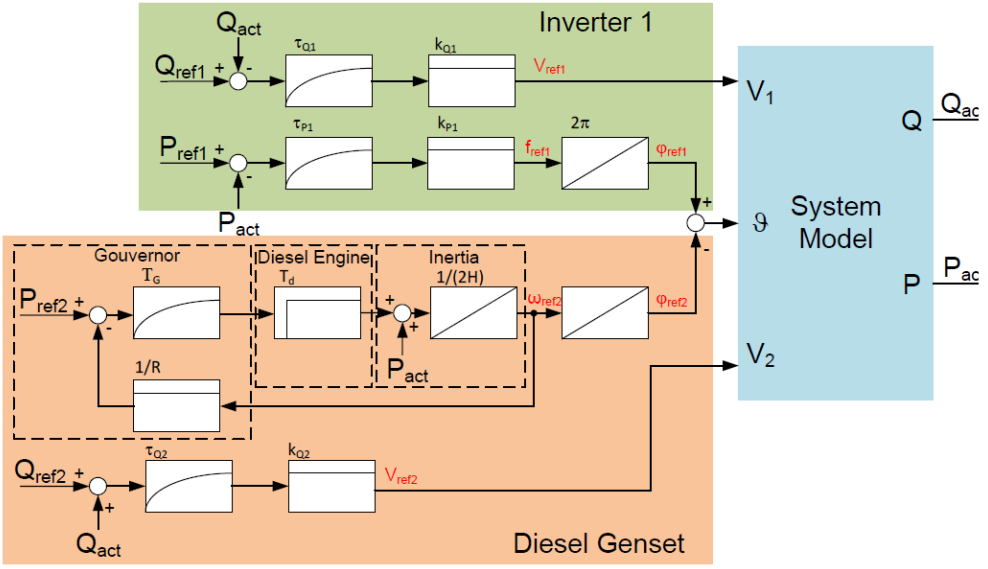

(A)

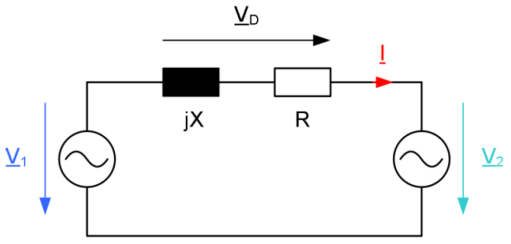

(B)

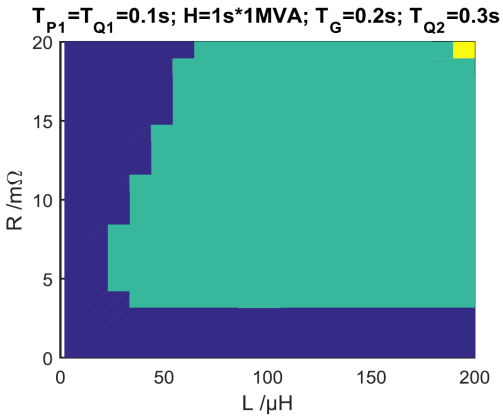

(C)

FIGURE 4.7: From [100]: (a) system model and (b) hybrid-grid and (c) stability region for the coupling impedance.

inverter. To avoid this behavior a bigger time constant of the inverter droop can be chosen.

Many simulation results are presented in the previous papers, but without any accurate analyses.

In [103] the stability analysis is performed. In recent researches on inverter-based distributed generator, disadvantages of traditional grid-connected current control, such as no grid-forming ability and lack of inertia, have been pointed out. In [103]:

- dynamic characteristics of both control methods (VSG [104, 105] and Droop Control [106]) are studied;

- the analysis is done in both stand-alone mode and synchronous-generator-connected mode, to understand the differences caused by swing equation (implemented in VSG and not in the droop control);
- small-signal models are built to compare transient responses of frequency during a small loading transition, and state-space models are built to analyze oscillation of output active power;
- effects of delays in both controls are also studied, and an inertial droop control method is proposed based on the comparison, then the results are verified by simulations and experimental tests;
- it is suggested that VSG control and proposed inertial droop control inherits the advantages of droop control, and in addition, provides inertia support for the system;
- an additional low pass filter is added in the active power loop of the droop control in order to emulate the synchronous generator inertia.

Here we want to understand the difference of the adopted control scheme in Fig.4.25 that will be adopted, with respect to the control scheme proposed in the literature to emulate a virtual synchronous generator on the basis of swing equation implementation [103].

The swing equation used to implement a virtual synchronous generator is:

$$p_0 - \frac{1}{k_p}(\omega_m - \omega_0) - p_{OUT} = J\omega_m \frac{d\omega_m}{dt} + D(\omega_m - \omega_g) \ , \tag{4.1}$$

where:

- p_0 is the set value of active power
- k_p is the droop coefficient
- ω_g is the measured grid frequency (at the point where the voltage sensor is installed)
- ω_0 is the nominal grid frequency (which is a constant value)
- ω_m is the rotation frequency of the virtual machine
- p_{OUT} is the generator output power
- J is the virtual inertia

- D is the virtual damping factor

To find a small-signal model of (4.1), it is necessary to linearize the term $\omega_m \frac{d\omega_m}{dt}$. To this purpose, we observe that during desired steady-state operating conditions, the system operates at constant frequency Ω. By applying small-signal perturbations to the system, it is possible to write $\omega_m = \Omega_m + \hat{\omega}_m$, where $|\hat{\omega}_m| << |\Omega_m|$. Then:

$$\omega_m \frac{d\omega_m}{dt} = (\Omega_m + \hat{\omega}_m) \frac{d(\Omega_m + \hat{\omega}_m)}{dt} = \Omega_m \frac{d\hat{\omega}_m}{t} + \hat{\omega}_m \frac{d\hat{\omega}_m}{dt} \xrightarrow{(\hat{\omega}_m/\Omega_m)\to 0} \Omega_m \frac{d\hat{\omega}_m}{dt} \tag{4.2}$$

By using (4.2) in (4.1) we find the following small-signal model:

$$\hat{\omega}_m = \frac{k_p}{1+Dk_p} \frac{1}{1+s\frac{J\Omega k_p}{1+Dk_p}} (\hat{p}_0 - \hat{p}_{out}) + \frac{1}{1+Dk_p} \frac{1}{1+s\frac{J\omega k_p}{1+Dk_p}} \hat{\omega}_0 + \frac{Dk_p}{1+Dk_p} \frac{1}{1+s\frac{J\Omega k_p}{1+Dk_p}} \hat{\omega}_g \,. \tag{4.3}$$

We are here interested in the stability effect of implementing the control equation (4.1) in the droop control loop relevant to the control of ω_m on the basis of the measured output power p_{OUT}. By focusing on the relation between $\hat{\omega}_m$ and $\hat{p}_{OUT}$ and assuming $D = 0$, it results:

$$\hat{\omega}_m = -k_p \frac{1}{1+sJ\Omega k_p} \hat{p}_{out} \,. \tag{4.4}$$

This shows that the implementation of the virtual inertia J by means of the swing equation gives a $\hat{\omega}_m/\hat{p}_{OUT}$ transfer function that is equivalent to the one in Fig.4.25. In particular, in our control scheme, virtual inertia emulation is obtained by a proper choice of the cut-off frequency of the adopted low-pass power filter.

4.3 Diesel Generator Modeling

The diesel generator (GenSet) is a rotating electrical generator, usually a synchronous generator, driven by a diesel engine [107], as in Fig.4.9a. As reported in [107,108], the diesel generator, or Genset, consists of five subsystems, see Fig.4.9:

1. diesel engine (DE);
2. synchronous machine (SM);
3. coupling shaft;
4. speed governor;
5. automatic voltage regulator (AVR).

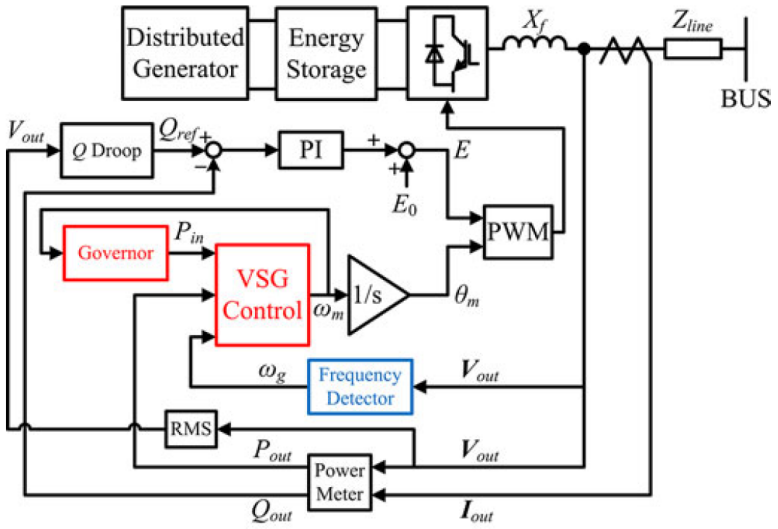

(A)

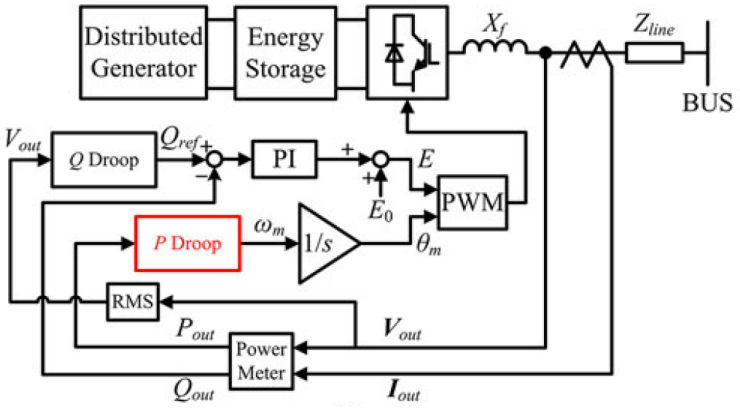

(B)

FIGURE 4.8: From [103]: basic control systems of (a) VSG and (b) droop control.

4.3.1 Diesel Engine

The Diesel Engine is modeled with several degree of precision. In [109–112] accurate studies are presented. For instance, in [111] three dynamic models with different complexity of the single-cylinder are compared through numerical simulations:

1. Model I is a detailed dynamic model, analytically linking the engine indicated pressure with speed. The model includes instantaneous friction, viscosity variations with temperature, inertia variations and a dynamometer model.

2. Model II is similar to the previous model, but, in an effort to reduce the execution time and, thus increase the suitability for real-time applications, it

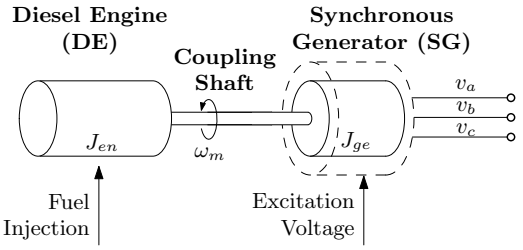

(A) Diesel Engine coupled with the Synchronous Generator

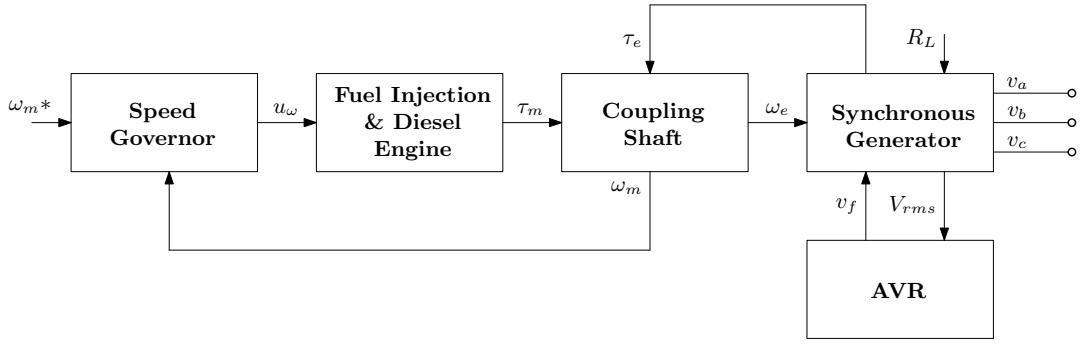

(B) Diesel Generator subsystems as in [107]

FIGURE 4.9: Representations of the Diesel GenSet.

does not use an instantaneous friction model and instead it models the mean friction components, only. Furthermore, the inertia variations are excluded, because of their limited influence on engine dynamics over a wide range of operational states.

3. Model III is entirely constructed from experimental data and identification procedures (black box).

The single-cylinder model is reported in Fig.4.10a and the comparison between the experimental and simulation results of the models described above of the engine speed as function of the crankshaft angle is shown in Fig.4.10b, Fig.4.10c and Fig.4.10d. Model III is less accurate, but exhibits a good matching.

In [112, 113] multi-cylinder diesel engine are modeled and the simulation results are compared with the experimental results.

In [102, 107, 108, 114, 115] the diesel engine models for the stability analysis in power systems have in common three main parts:

1. fuel injection system, which is modeled with a first order transfer function and its time constant t_e is related to the speed of the injection variation;

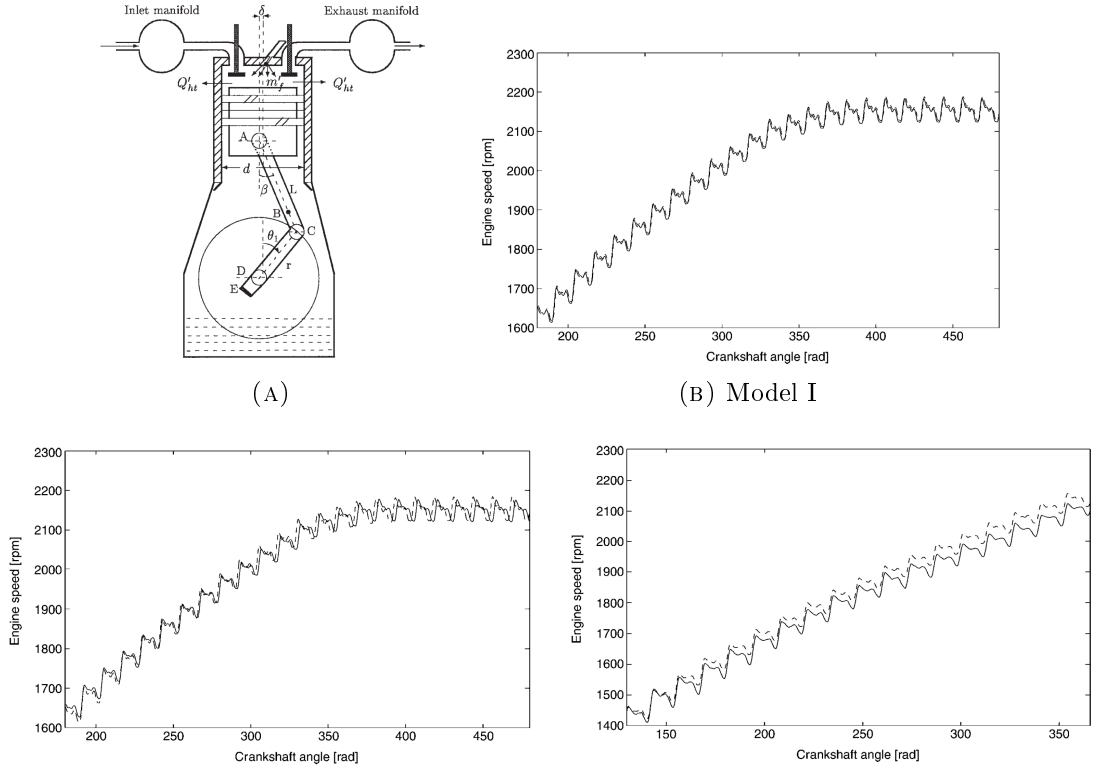

(A) (B) Model I

(C) Model II (D) Model III

FIGURE 4.10: Single-cylinder diesel engine (a) and comparison between the three models (b-d) described in [111].

2. dead time t_d of the diesel engine that comprises three delays: the time elapsed until the actuator output actually injects fuel in the cylinder, fuel burning time to produce torque, and time until all cylinders produce torque at engine shaft [115];

3. inertia of the internal rotating parts of the engine and flywheel, which is considered in the coupling shaft subsystem.

Hence, the model for stability studies can be represented as in Fig.4.11, where the maximum torque k_e is added, since u_ω gives a normalized output. The maximum torque is usually indicated in the datasheet of the diesel engine and is related to the maximum power and the mechanical frequency of the diesel engine:

$$k_e = \frac{P_{n,DE}}{\omega_m} \tag{4.5}$$

The considered transfer function for the diesel engine, as in [102, 107, 108, 115], is:

$$G_{DE} = \frac{\tau_m(s)}{u_\omega(s)} = k_e \cdot \frac{e^{-s \cdot t_d}}{1 + s \cdot t_e}. \tag{4.6}$$

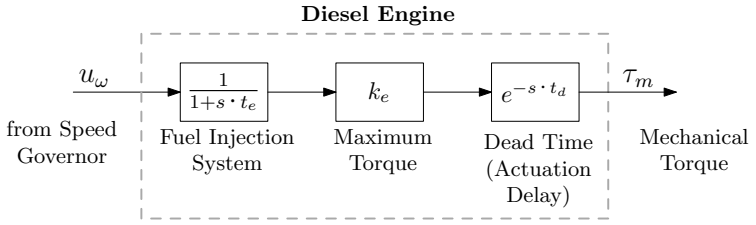

FIGURE 4.11: Diesel Engine model for stability studies.

4.3.2 Coupling Shaft

In [107, 108], the coupling shaft is modeled as two rotational masses coupled by a linear flexible shaft as in Fig.4.12, which can be described by these equations:

$$\begin{aligned} J_{en}\frac{d\omega_{en}}{dt} &= -k_{fens}\omega_{en} + k_{fs}\omega_{ge} - \tau_{ss} + \tau_m \\ J_{ge}\frac{d\omega_{ge}}{dt} &= k_{fs}\omega_{en} - k_{fges}\omega_{ge} + \tau_{ss} - \tau_e \\ \frac{d\tau_{ss}}{dt} &= k_{ss}\omega_{en} - k_{ss}\omega_{ge} \end{aligned} \tag{4.7}$$

The inputs are:

- τ_m: mechanical torque supplied by the engine;
- τ_e: electromagnetic torque due to electric load.

The state variables are:

- ω_{en}: rotational speed of the prime mover;
- ω_{ge}: rotational speed of the electrical generator;

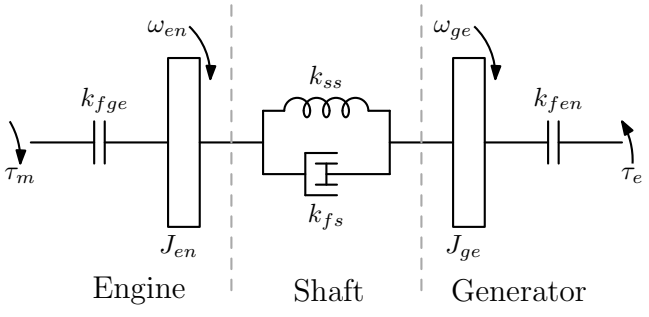

FIGURE 4.12: Two-mass model of the coupling shaft.

- τ_{ss}: torque transmitted through the spring element.

The parameters used are:

- J_{en}, J_{ge}: moments of inertia;
- k_{fen}, k_{fge}: frictional losses coefficients of the engine and electrical generator;
- k_{fs}, k_{ss}: torsional damping and stiffness coefficients of the shaft;

To simplify the notation $k_{fens} = k_{fen} + k_{fs}$ and $k_{fges} = k_{fge} + k_{fs}$.

The system can be described as:

$$\begin{bmatrix} \omega_{en}(s) \\ \omega_{ge}(s) \end{bmatrix} = \begin{bmatrix} h_{sh11}(s) & h_{sh12}(s) \\ h_{sh21}(s) & h_{sh22}(s) \end{bmatrix} \cdot \begin{bmatrix} \tau_m(s) \\ \tau_e(s) \end{bmatrix} \tag{4.8}$$

The transfer function of interest is $h_{sh11}(s) = \omega_m(s)/\tau_m(s)$ and has a complex expression as [107]:

$$h_{sh11}(s) = \frac{\omega_m(s)}{\tau_m(s)} = \\ = \frac{J_{ge}s^2 + k_{fges}s + k_{ss}}{J_{ge}J_{en}s^3 + (J_{ge}k_{fens} + J_{en}k_{fges})s^2 + \left[k_{ss}(J_{ge} + J_{en}) + k_{fens}k_{fges} - k_{fs}^2\right]s + k_{ss}(k_{fen} + k_{fge})} \tag{4.9}$$

A typical transfer function can be seen in Fig.4.13, where a resonance around 100rad/s appears. However, for this study, the dynamics of interest are at lower frequencies, so that resonance can be neglected and the equivalent transfer function becomes:

$$h_{eq}(s) = \frac{\omega_m(s)}{\tau_m(s)} = \frac{1}{J_{eq}s + k_{feq}} \tag{4.10}$$

which is indicated in Fig.4.13 as well. ω_{eq} is the equivalent moment of inertia of the diesel engine-electrical generator set, $J_{eq} = J_{en} + J_{ge}$ is the equivalent moment of inertia and $k_{feq} = k_{fen} + k_{fge}$ is the equivalent frictional losses coefficient. Moreover, for the purpose of this analysis, also the frictional losses dynamics can be neglected, so we can consider only the dynamic related to the inertia in the model:

$$h'_{eq}(s) = \frac{\omega_m(s)}{\tau_m(s)} = \frac{1}{J_{eq}s} \tag{4.11}$$

Finally, the complete model of the Diesel Generator can be found in Fig.4.14.

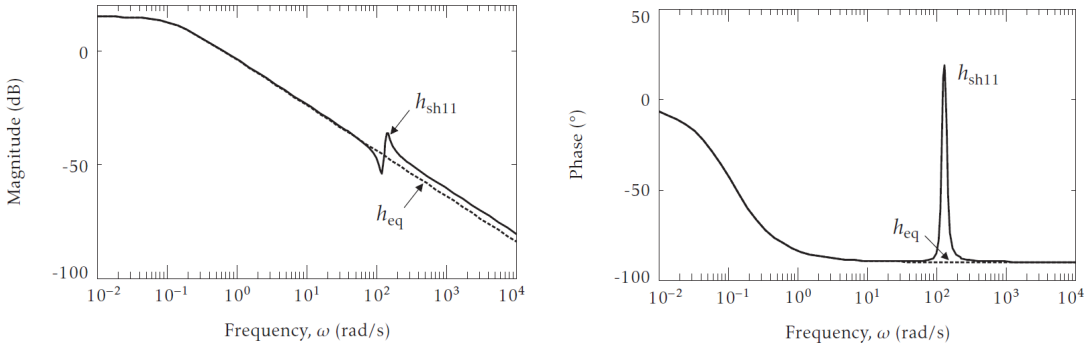

(A) Magnitude (B) Phase

FIGURE 4.13: From [107]: bode plot of the transfer function $h_{sh11}(s) = \omega_m(s)/\tau_m(s)$.

4.3.3 Synchronous Machine

The synchronous machine has been widely investigated in literature as in [115–119] and this section provides the basic equations and the modeling for power system stability analyses are reported. Hereafter the formulations for the case with dampers is reported as in [117], and the model without dampers is presented in Sec. 4.3.3.4.

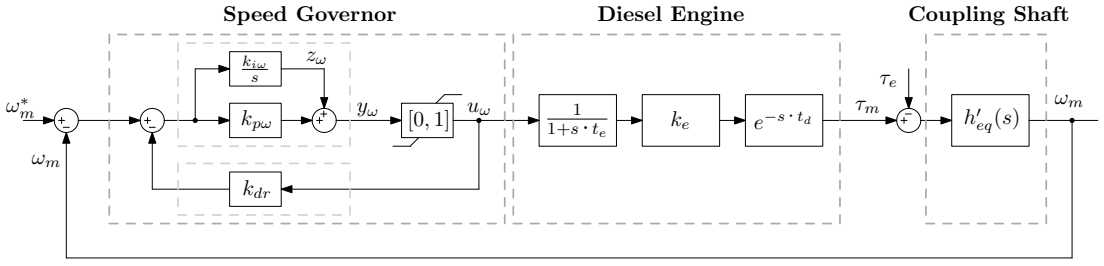

FIGURE 4.14: Complete model of the Diesel Generator.

4.3.3.1 Basic equations

The model with damper windings on the d-axis and the q-axis is considered. The flux linkage equations in the stator and in the rotor are given by:

$$\begin{cases} \psi_d = -L_d i_d + m_{sf} i_f + m_{sD} i_D \\ \psi_q = -L_q i_q + m_{sQ} i_Q \\ \psi_f = L_f i_f + m_{fD} i_D - m_{sf} i_d \\ \psi_D = L_D i_D + m_{fD} i_f - m_{sD} i_d \\ \psi_Q = L_Q i_Q - m_{sQ} i_q \end{cases} \tag{4.12}$$

and the voltage equations in the stator and in the rotor:

$$\begin{cases} v_d = -r_s i_d - \omega_e \psi_q + \frac{d\psi_d}{dt} \\ v_q = -r_s i_q + \omega_e \psi_d + \frac{d\psi_q}{dt} \\ v_f = r_f i_f + \frac{d\psi_f}{dt} \\ 0 = r_D i_D + \frac{d\psi_D}{dt} \\ 0 = r_Q i_Q + \frac{d\psi_Q}{dt} \end{cases} \tag{4.13}$$

Combining the flux linkages and the voltage equations:

$$\begin{cases} v_d = -r_s i_d + L_q \omega_e i_q - m_{sQ} \omega_e i_Q - L_d \frac{di_d}{dt} + m_{sf} \frac{di_f}{dt} + m_{sD} \frac{di_D}{dt} \\ v_q = -r_s i_q - L_d \omega_e i_d + m_{sf} \omega_e i_f - m_{sD} \omega_e i_D - L_q \frac{di_q}{dt} + m_{sQ} \frac{di_Q}{dt} \\ v_f = r_f i_f + L_f \frac{di_f}{dt} - m_{sf} \frac{di_d}{dt} + m_{fD} \frac{di_D}{dt} \\ 0 = r_D i_D + L_D \frac{di_D}{dt} + m_{fD} \frac{di_f}{dt} - m_{sD} \frac{di_d}{dt} \\ 0 = r_Q i_Q + L_Q \frac{di_Q}{dt} - m_{sQ} \frac{di_q}{dt} \end{cases} \tag{4.14}$$

where:

- L_D, L_Q: inductances of the direct and quadrature damper windings.
- L_f: inductance of the main field winding.
- L_d, L_q: inductances of the d-axis stator winding and q-axis stator winding.
- m_{sf}: mutual inductance between the field winding and the d-axis stator winding.
- m_{sD}: mutual inductance between the d-axis stator winding and the d-axis damper winding.

- m_{sQ}: mutual inductance between the q-axis stator winding and the q-axis damper winding.
- m_{fD}: mutual inductance between the field winding and the d-axis damper winding.

4.3.3.2 Synchronous Machine for Stability Studies

In the datasheet of a generic synchronous machine the explicit values of the standard parameters are not reported. However, the operational parameters are indicated, as:

- X_d, X_q: d-axis and q-axis synchronous reactances unsaturated;
- X'_d, X'_q: d-axis and q-axis transient reactances saturated;
- X''_d, X''_q: d-axis and q-axis subtransient reactances saturated;
- T'_d, T'_q: transient short-circuit time constants;
- T''_d, T''_q: subtransient short-circuit time constants;
- T'_{d0}, T'_{q0}: transient open-circuit time constants;
- T''_{d0}, T''_{q0}: subtransient open-circuit time constants.

In this section these operational parameters are related to the standard parameters considered in the previous section. In fact, a convenient method of identifying the machine electrical characteristics is in terms of operational parameters relating the armature and field terminal quantities [117], according to the IEEE Std. 115 [120]. The main tests of the procedure are discussed in [121]. The relationship between the incremental values of terminal quantities may be expressed in the operational form as follows:

$$\begin{cases} \Delta\psi_d(s) = G(s)\Delta v_f(s) - L_d(s)\Delta i_d(s) \\ \Delta\psi_q(s) = -L_q(s)\Delta i_q(s) \end{cases} \tag{4.15}$$

where the operator Δ denotes incremental or perturbed values, and:

- $G(s)$ is the stator to field transfer function;
- $L_d(s)$ is the d-axis operational inductance;

- $L_q(s)$ is the q-axis operational inductance.

The orders of the numerator and denominator polynomials of $L_d(s)$ and $L_q(s)$ are equal to the number of rotor circuits assumed in the respective axes, and $G(s)$ has the same denominator as $L_d(s)$, but a different numerator of order one less than the denominator [117]. This model structure is generally considered adequate for stability studies and is widely used in large scale stability programs [117].

In the incremental model, the flux linkages for the d-axis in the operational form become:

$$\begin{aligned}\psi_d(s) &= -L_d i_d(s) + m_{sf} i_f(s) + m_{sD} i_D(s)\\ \psi_f(s) &= -m_{sf} i_d(s) + L_f i_f(s) + m_{fD} i_D(s)\\ \psi_D(s) &= -m_{sD} i_d(s) + m_{fD} i_f(s) + L_D i_D(s)\end{aligned} \tag{4.16}$$

The operational form for rotor voltages in the d-axis are:

$$\begin{aligned}v_f(s) &= r_f i_f(s) + (s\psi_f(s) - \psi_f(0))\\ 0 &= r_D i_D(s) + (s\psi_D(s) - \psi_D(0))\end{aligned} \tag{4.17}$$

where $\mathscr{L}\{\frac{d\psi}{dt}\} = s\psi(s) - \psi(0)$ and $\psi_d(0)$, $\psi_f(0)$ and $\psi_D(0)$ denote initial values of the flux linkages [117]. In order to cancel the initial values, we express these equations in terms of incremental values (under steady-state condition are zero). Substituting the flux linkages in terms of the currents, the rotor voltages equations in incremental form become:

$$\begin{aligned}\Delta v_f(s) &= r_f \Delta i_f(s) + s\Delta\psi_f(s) =\\ &= -sm_{sf}\Delta i_d(s) + (r_f + sL_f)\Delta i_f(s) + sm_{fD}\Delta i_D(s)\end{aligned} \tag{4.18}$$

$$\begin{aligned}0 &= r_D \Delta i_D(s) + s\Delta\psi_D(s) =\\ &= -sm_{sD}\Delta i_d(s) + sm_{fD}\Delta i_f(s) + (r_D + sL_D)\Delta i_D(s)\end{aligned} \tag{4.19}$$

To express the d-axis equations as in (4.15) and assuming all equal mutual inductances $m = m_{sf} = m_{sD} = m_{fD}$:

$$\begin{aligned}\Delta i_f(s) &= \frac{1}{D(s)}\left[(r_D + sL_D)\Delta v_f(s) + sm(r_D + sL_{DD})\Delta i_d(s)\right]\\ \Delta i_D(s) &= \frac{1}{D(s)}\left[-sm\Delta v_f(s) + sm(r_f + sL_f)\Delta i_d(s)\right]\end{aligned} \tag{4.20}$$

where

$$D(s) = s^2\left(L_{DD}L_{ff} - m^2\right) + s\left(L_{DD}r_f + L_{ff}r_D\right) + r_D r_f \tag{4.21}$$

Given that [117]:

$$\begin{aligned} L_d &= m + L_l \\ L_{ff} &= m + L_f \\ L_{DD} &= m + L_D \end{aligned} \tag{4.22}$$

Considering the incremental form of the first equation in (4.16), all equal mutual inductances and substituting as in (4.42):

$$\begin{aligned} \Delta\psi_d(s) &= -L_d\Delta i_d(s) + m\Delta i_f(s) + m\Delta i_D(s) = \\ &= G(s)\Delta v_f(s) - L_d(s)\Delta i_d(s) \end{aligned} \tag{4.23}$$

The expressions for the d-axis operational parameters are given by:

$$L_d(s) = L_d\frac{1 + (T_4 + T_5)s + T_4T_6s^2}{1 + (T_1 + T_2)s + T_1T_3s^2} \tag{4.24}$$

$$G(s) = G_0\frac{(1 + sT_{kd})}{1 + (T_1 + T_2)s + T_1T_3s^2} \tag{4.25}$$

where

$$\begin{aligned} G_0 = \frac{m}{r_f} \quad &, \quad T_{kd} = \frac{L_D}{r_D} \\ T_1 = \frac{m + L_f}{r_f} \quad &, \quad T_2 = \frac{m + L_D}{r_D} \\ T_3 = \frac{1}{r_D}\left(L_D + \frac{mL_f}{m + L_f}\right) \quad &, \quad T_4 = \frac{1}{r_f}\left(L_f + \frac{mL_l}{m + L_l}\right) \\ T_5 = \frac{1}{r_D}\left(L_D + \frac{mL_l}{m + L_l}\right) \quad &, \quad T_6 = \frac{1}{r_D}\left(L_D + \frac{mL_fL_l}{mL_l + mL_f + L_fL_l}\right) \end{aligned} \tag{4.26}$$

The final expression is the form:

$$L_d(s) = L_d\frac{(1 + sT'_d)(1 + sT''_d)}{(1 + sT'_{d0})(1 + sT''_{d0})} \tag{4.27}$$

$$G(s) = G_0\frac{(1 + sT_{kd})}{(1 + sT'_{d0})(1 + sT''_{d0})} \tag{4.28}$$

A similar procedure can be done also for the q-axis, where:

$$L_q(s) = L_q\frac{(1 + sT'_q)(1 + sT''_q)}{(1 + sT'_{q0})(1 + sT''_{q0})} \tag{4.29}$$

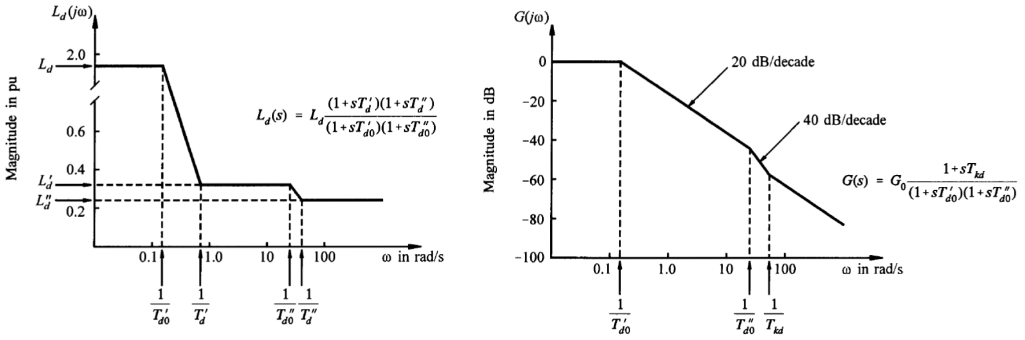

(A) (B)

FIGURE 4.15: Transfer functions of (a) $L_d(s)$ and (b) $G(s)$ as in [117].

Tipically:

$$X_d \geq X_q > X'_q \geq X'_d > X''_q \geq X''_d, \tag{4.30}$$

$$T'_{d0} > T'_d > T'_{d0} > T''_d > T_{kd}, \tag{4.31}$$

$$T'_{q0} > T'_q > T'_{q0} > T''_q. \tag{4.32}$$

The time constants associated with the expressions of $L_d(s)$,$L_q(s)$ and $G(s)$ in the factored form represent important machine parameters. The magnitude of $L_d(s)$ and $G(s)$ can be seen in Fig.4.15.

4.3.3.3 Standard Parameters

It is possible to relate the operational parameters to the time constants in (4.26), considering (4.24) and (4.27):

$$1 + (T_4 + T_5)s + T_4T_6s^2 = (1 + sT'_d)(1 + sT''_d) \tag{4.33}$$

$$1 + (T_1 + T_2)s + T_1T_3s^2 = (1 + sT'_{d0})(1 + sT''_{d0}) \tag{4.34}$$

The standard parameters can be determined with the classical expressions, where considering that $r_d \gg r_f$:

$$T_2, T_3 \ll T_1 \quad , \quad T_5, T_6 \ll T_4 \tag{4.35}$$

or through the accurate expressions, without any simplification. The expressions for both cases are reported in Tab.4.1.

Parameter	Classical Expression	Accurate Expression
T'_{d0}	T_1	$T_1 + T_2$
T'_d	T_4	$T_4 + T_5$
T''_{d0}	T_3	$T_3[T_1/(T_1 + T_2)]$
T''_d	T_6	$T_6[T_4/(T_4 + T_5)]$
L'_d	$L_d(T_4/T_1)$	$L_d(T_4 + T_5)/(T_1 + T_2)$
L''_d	$L_d(T_4T_6)/(T_1T_3)$	$L_d(T_4T_6)/(T_1T_3)$

TABLE 4.1: Expressions for Standard Parameters of Synchronous Machine for the d-axis.

4.3.3.4 Model without dampers

Here the model neglecting the damper windings. The expressions of this model will be used to estimate the machine parameters, instead of using the previous detailed method. The flux linkage equations in the stator and in the rotor are given by:

$$\begin{cases} \psi_d = -L_d i_d + m_{sf} i_f \\ \psi_q = -L_q i_q \\ \psi_f = L_f i_f - m_{sf} i_d \end{cases} \tag{4.36}$$

and the voltage equations in the stator and in the rotor:

$$\begin{cases} v_d = -r_s i_d - \omega_e \psi_q + \frac{d\psi_d}{dt} \\ v_q = -r_s i_q + \omega_e \psi_d + \frac{d\psi_q}{dt} \\ v_f = r_f i_f + \frac{d\psi_f}{dt} \end{cases} \tag{4.37}$$

Combining the flux linkages and the voltage equations:

$$\begin{cases} v_d = -r_s i_d + L_q \omega_e i_q - L_d \frac{di_d}{dt} + m_{sf} \frac{di_f}{dt} \\ v_q = -r_s i_q - L_d \omega_e i_d + m_{sf} \omega_e i_f - L_q \frac{di_q}{dt} \\ v_f = r_f i_f + L_f \frac{di_f}{dt} - m_{sf} \frac{di_d}{dt} \end{cases} \tag{4.38}$$

The incremental model is calculated for d-axis and q-axis separately, as for the previous model with damper windings. The flux linkages for the d-axis in the operational form become:

$$\begin{aligned} \psi_d(s) &= -L_d i_d(s) + m_{sf} i_f(s) \\ \psi_f(s) &= -m_{sf} i_d(s) + L_f i_f(s) \end{aligned} \tag{4.39}$$

The operational form for rotor voltages in the d-axis are:

$$v_f(s) = r_f i_f(s) + (s\psi_f(s) - \psi_f(0)) \tag{4.40}$$

where $\mathscr{L}\{\frac{d\psi_f}{dt}\} = s\psi_f(s) - \psi_f(0)$ and $\psi_f(0)$ denote initial value of the flux linkage [117]. In order to cancel the initial values, we express these equations in terms of incremental values (under steady-state condition are zero). Substituting the flux linkages in terms of the currents, the rotor voltages equations in incremental form become:

$$\begin{aligned} \Delta v_f(s) &= r_f \Delta i_f(s) + s\Delta\psi_f(s) = \\ &= -sm_{sf}\Delta i_d(s) + (r_f + sL_f)\Delta i_f(s) \end{aligned} \tag{4.41}$$

To express the d-axis equations as in (4.15):

$$\Delta i_f(s) = \frac{1}{r_f + sL_f}\left[\Delta v_f(s) + sm_{sf}\Delta i_d(s)\right] \tag{4.42}$$

Considering the incremental form of the first equation in (4.16), all equal mutual inductances and substituting as in (4.42):

$$\begin{aligned} \Delta\psi_d(s) &= -L_d\Delta i_d(s) + m_{sf}\Delta i_f(s) = \\ &= G(s)\Delta v_f(s) - L_d(s)\Delta i_d(s) \end{aligned} \tag{4.43}$$

The expressions for the d-axis operational parameters are given by:

$$L_d(s) = L_d\frac{1 + sT'_d}{1 + sT'_{d0}} \tag{4.44}$$

$$G(s) = G_0\frac{1}{1 + sT'_{d0}} \tag{4.45}$$

where

$$G_0 = \frac{m_{sf}}{r_f} \quad , \quad T'_d = \frac{1}{r_f}\left(L_f - \frac{m_{sf}^2}{L_d}\right) \quad , \quad T'_{d0} = \frac{L_f}{r_f} \tag{4.46}$$

Given the operational parameters X_d, X'_d, T'_d, T'_{d0}, T_a and assuming that $m = m_{sf} = 2/3L_d$, it is possible to determine the parameters of the simplified machine starting from :

$$\begin{aligned} L_d &= \frac{X_d}{2\pi} \quad , \quad L'_d = L_d\frac{T'_d}{T'_{d0}} = L_d - \frac{m_{sf}^2}{L_f} \\ T'_d &\simeq \frac{L_f L'_d}{r_f L_d} \quad , \quad T_a \simeq \frac{2L'_d L_q}{r_s(L'_d + L_q)} \end{aligned} \tag{4.47}$$

where T_a is the armature time constant and gives the rate of decay of the unidirectional component (low frequency offset) of armature phase currents following a three-phase short-circuit at the terminals.

The flux linkage for the q-axis in the operational form become:

$$\psi_q(s) = -L_q i_q(s) \tag{4.48}$$

The incremental form can be expressed as:

$$\Delta\psi_q(s) = -L_q(s)\Delta i_q(s) \tag{4.49}$$

where $L_q(s) = L_q = X_q/(2\pi)$.

4.3.4 Speed Governor

The purpose of the speed governor is to control the fuel injection to the engine cylinders so as to control the speed of the unit, holding the speed constant for all conditions of load imposed on the generator conditions of load imposed on the generator being driven by the engine. In order to maintain the frequency of the generator output, the engine speed must be held constant. The basic governor includes:

- speed setting element (reference);
- speed sensing element;
- error sensing/correcting element;
- power element sufficient to manage engine fuel controls;
- compensation/resetting/stabilizing element;
- possibility of determining the method of operation (droop or isochronous mode)

The speed governor has typically the structure of a PI controller with a droop function [107, 115, 117] which can be implemented by the feedback of the controller output. There are also some standards or reports [122, 123] concerning this important part of the diesel generator. For parallel operation of multiple generators, which is the case in most systems, these governors typically use a droop behavior [102].

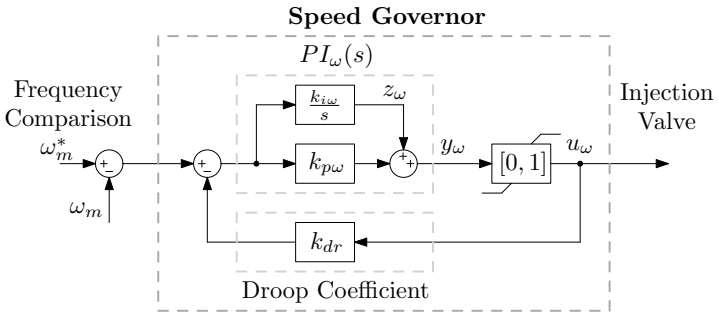

FIGURE 4.16: Diesel Engine model for stability studies.

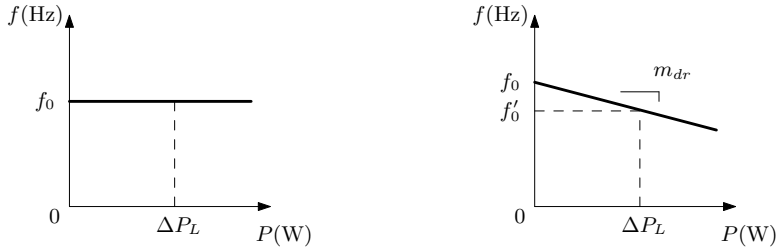

(A) isochronous ($k_{dr} = 0$) (B) droop ($k_{dr} > 0$)

FIGURE 4.17: $P - f$ static curves for (a) the isochronous and (b) the droop controls.

The block diagram of the governor considered [107] in this analysis is shown in Fig. 4.16:

$$R_\omega(s) = \frac{PI_\omega(s)}{1 + k_{dr} PI_\omega(s)} \tag{4.50}$$

where

$$PI_\omega(s) = k_{p\omega} + \frac{k_{i\omega}}{s} \tag{4.51}$$

The speed droop grain is defined as $k_{dr} = m_{dr}\Omega_m$, where m_{dr} is the static droop slope, and Ω_m is the prime mover nominal speed.

4.3.5 Automatic Voltage Regulator

The automatic voltage regulator (AVR) provides, through an exciter, the direct current of the synchronous machine rotor windings in order to give the desired voltage at the output terminal of the Diesel Generator [117]. This regulator has to comply with the standard IEEE Std. 421.5 [124]. Three distinctive types of excitation systems are identified on the basis of excitation power source [124]:

- *type DC excitation systems*, which utilize a direct current generator with a commutator as the source of excitation system power;

- *type AC excitation systems*, which use an alternator and either stationary or rotating rectifiers to produce the direct current needed for the synchronous machine field;
- *type ST excitation systems*, in which excitation power is supplied through transformers or auxiliary generator windings and rectifiers.

In Fig.4.19 the AVR is described with the main subsystems [117, 124]:

- *Exciter*: provides DC power to the synchronous machine field winding, constituting the power stage of the excitation system;
- *Regulator (AVR)*: processes and amplifies input control signals to a level and form appropriate for the control of the exciter (with regulating and excitation system system transfer functions);
- *Terminal voltage transducer and load compensator*: senses generator terminal voltage with an additional filtering, and in addition load compensation may be provided;
- *Power System Stabilizer*: provides an additional input signal to the regulator to damp the power system oscillations;
- *Limiter and Protective Circuits*: include a wide array of control and protective functions which ensure the capability limits of the exciter and synchronous generator are not exceeded.

In [107, 108] the model used is the one depicted in Fig.4.18a where the *regulator*, the *exciter* and the *limiter* dynamics are considered. The *terminal voltage transducer* and the *power system stabilizer* have been neglected.

In this work, also the dynamic of the *exciter* is neglected. This assumption is not critical for the $P - f$ (active power and frequency) responses, since the influence of this loop is mainly on the reactive power $(Q - V)$.

The *limiter* allows a normalized field voltage in the range $[0, V_{fault}]$. Once determined the short-circuit current $I_{cc} = 4 \cdot I_n$, the fault voltage is:

$$V_{fault} = \left| \frac{E_n + jI_{cc}X_dZ_b}{E_n} \right| \tag{4.52}$$

where E_n is the line-to-neutral rms nominal voltage, X_d is the normalized synchronous reactance of the d-axis, Z_b is the base impedance.

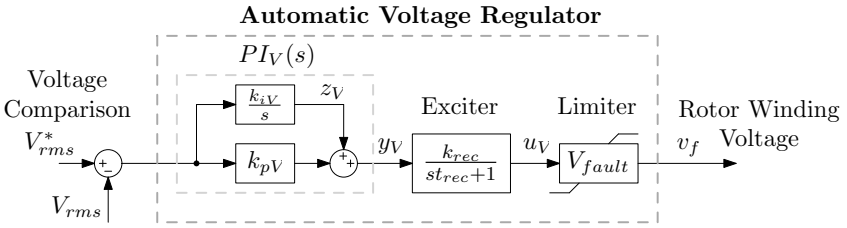

(A) AVR as in [107]

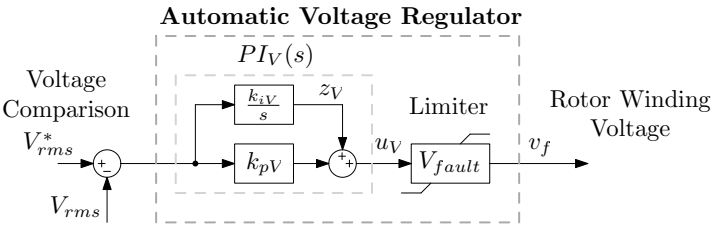

(B) AVR considered

FIGURE 4.18: Representations of the Automatic Voltage Regulator.

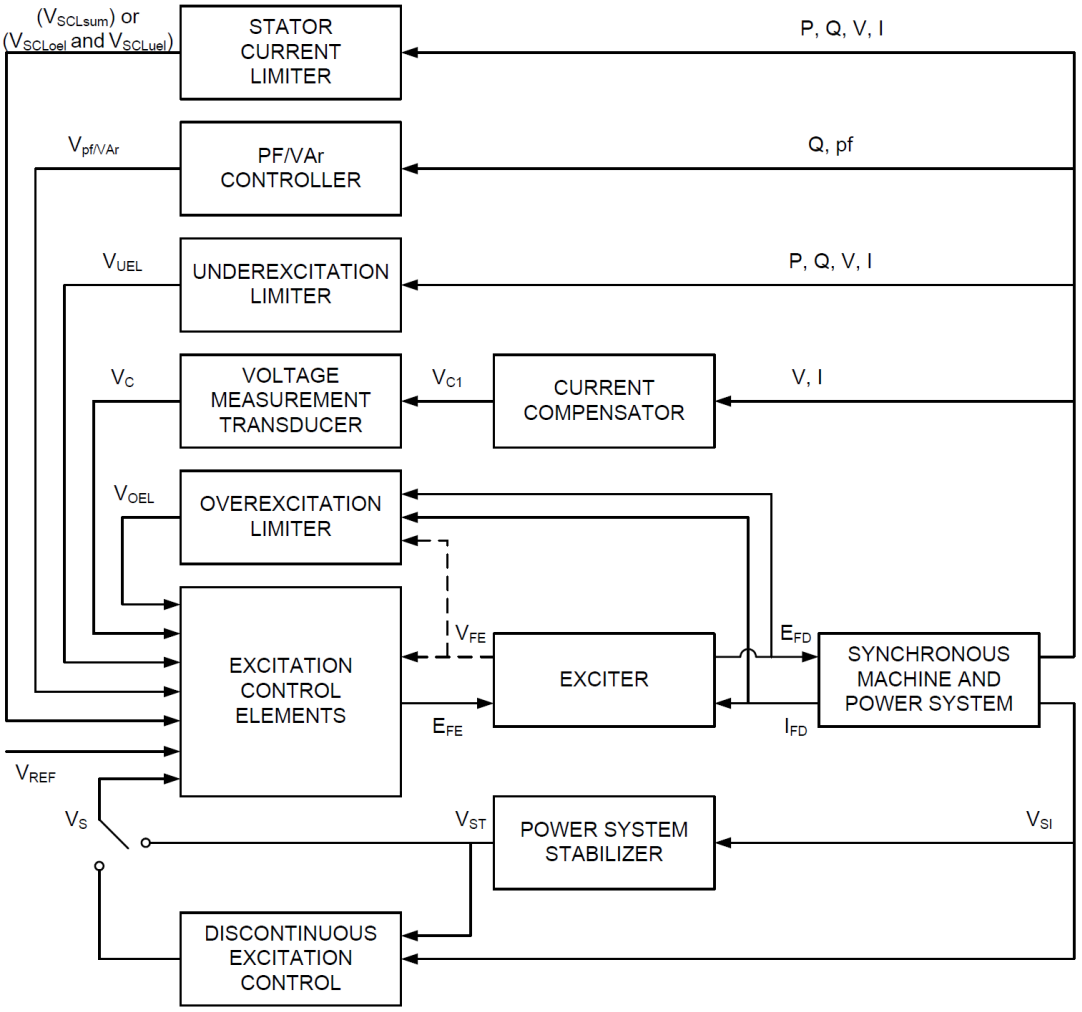

FIGURE 4.19: Functional block diagram of a synchronous generator excitation system [124].

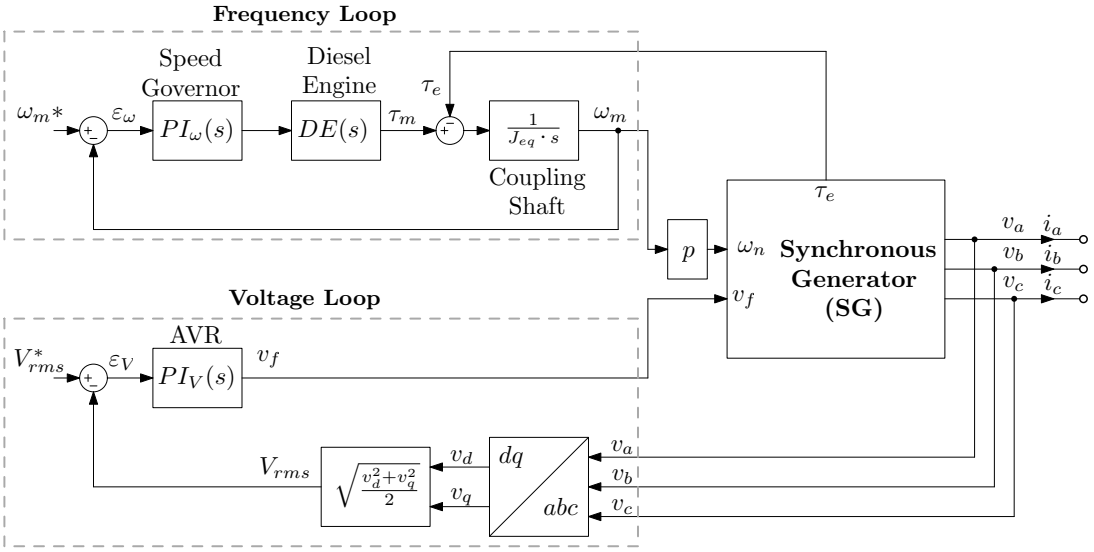

FIGURE 4.20: Whole control scheme of the Diesel Generator.

Parameter	Symbol	Value	Unit
Maximum Power	P_{en}	356	kW
Maximum Torque	k_e	2330	$\mathrm{N}\cdot\mathrm{m}$
Engine Inertia	J_{en}	3.43	$\mathrm{kg}\cdot\mathrm{m}^2$
Fuel Injection Time Constant*	t_e	35	ms
Engine Delay†	t_d	22	ms

TABLE 4.2: Parameters of interest from Volvo TAD1343GE datasheet (*found in a datasheet of a comparable power diesel engine, †given in [107]).

4.3.6 Simulation Model

In Fig.4.20 the control scheme of the Diesel Generator is shown. The speed governor and the AVR regulators are included in the frequency loop and in the voltage loop, respectively.

The resistive case is here considered the benchmark for the Diesel Generator SDMO V410C2 (see the attached datasheet), which uses:

- diesel engine Volvo TAD1343GE;
- synchronous machine Leroy Somer LSA 47.2 VS4;

The values considered in this analysis are found in the datasheets and are reported in Tab.4.2 and in Tab.4.3 for the diesel engine and the synchronous machine, respectively.

(A) (B)

FIGURE 4.21: Pictures of the Diesel Generator SDMO V410C2.

Parameter	Symbol	Value	Unit
Nominal Power	P_n	410	kVA
Nominal Voltage	V_n	400	Vrms
Nominal Frequency	f_n	50	Hz
Pole Pairs	p	2	–
Synchronous Reactance (d-axis)	X_d	3.220	$p.u.$
Transient Reactance (d-axis)	X'_d	0.173	$p.u.$
Subtransient Reactance (d-axis)	X''_d	0.121	$p.u.$
Synchronous Reactance (q-axis)	X_d	1.930	$p.u.$
Subtransient Reactance (q-axis)	X_d	0.163	$p.u.$
Leakage Reactance†	X_l	0.060	$p.u.$
Short-circuit Time Constant (d-axis)	T_d	100	ms
Subtransient Time Constant (d-axis)	T''_d	10	ms
Subtransient Time Constant (q-axis)	T''_q	10	ms
Armature Time Constant	T_a	15	ms
Generator Inertia	J_{ge}	6.9	$\mathrm{kg \cdot m^2}$

TABLE 4.3: Parameters of interest from Leroy Somer LSA 47.2 VS4 datasheet (†typical value) used in the synchronous machine model given in the *SimPowerSystems* library of MATLAB/Simulink.

4.3.6.1 Step Response

Once collect all the parameters of interest for the analysis, the experimental load step response of the Diesel Generator is compared to the results of the simulation [125]. The regulators have been tuned to obtain a good matching with the experimental data, where the speed governor and the AVR controllers are given by

$$PI_\omega(s) = k_{p\omega} + \frac{k_{i\omega}}{s} \quad , \quad PI_V(s) = k_{pV} + \frac{k_{iV}}{s} \tag{4.53}$$

Parameter	Value	Unit
$f_{c\omega}$	0.9	Hz
ϕ_{ω}	55	deg
$k_{p\omega}$	0.02448	–
$k_{i\omega}$	0.04147	–
f_{cV}	0.5	Hz
ϕ_{V}	55	deg
k_{pV}	0.01140	–
k_{iV}	0.02976	–

TABLE 4.4: Regulators of the Diesel Generator.

and the uncompensated loops in no-load condition are, respectively

$$T_{\omega 0}(s) = DE(s) \cdot h'_{eq}(s) = k_e \frac{e^{-s \cdot t_d}}{1 + s \cdot t_e} \cdot \frac{1}{s \cdot J_{eq}} \quad , \quad T_{V0}(s) = \frac{V_n}{1 + s\frac{L_f}{R_f}} \tag{4.54}$$

The comparison between the two responses can be seen in Fig.4.22a, considering the parameters in Tab.4.4. The load connection 50kW → 80kW and disconnection 80kW → 50kW are applied, where a reference frequency of 49.95Hz is considered. During the load connection, the minimum frequency is 49.2Hz and during the disconnection the maximum frequency is 50.8Hz. The recovery time is around 2s, which is comparable to the values reported in the datasheet. The matching of the step response is enough accurate, especially on the load disconnection.

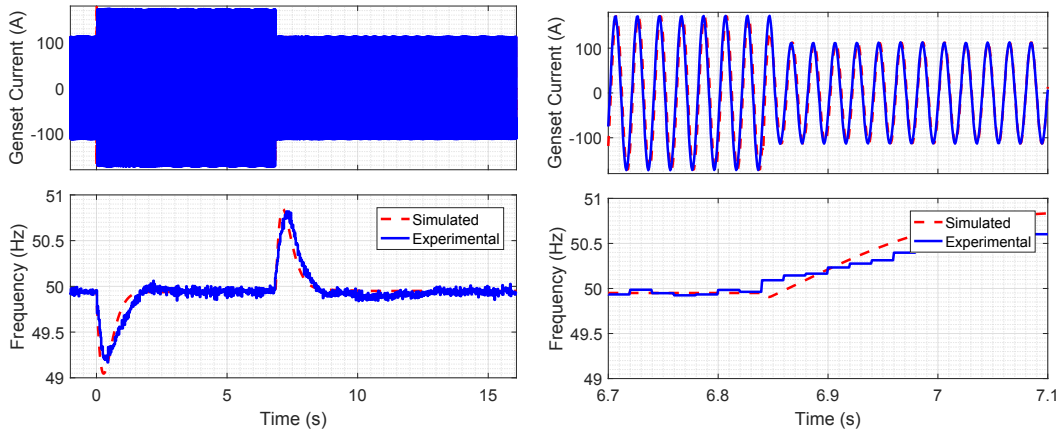

(A) Load connection and disconnection

(B) Detail

FIGURE 4.22: Load step 50kW → 80kW applied to the Diesel Generator. The settling time is around 1.5s.

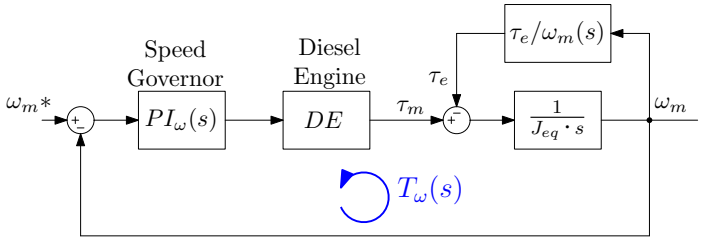

FIGURE 4.23: Frequency loop in the Diesel Generator. The transfer functions of interest are $\tau_e/\omega_m(s)$, $\omega_m/\tau_m(s)$ and $T_\omega(s)$

4.3.6.2 Perturbations

The simulation model is now close to the real one, and the frequency loop of the Diesel Generator can be perturbed to find the most significant frequency responses.

Electrical Torque/Mechanical Frequency The transfer function $\tau_e/\omega_m(s)$ can be found in Fig.4.24a. Within the bandwidth of the AVR, the transfer function can be calculated as follows:

$$\tau_e(\omega_m, p_e) = T_e + \hat{\tau}_e = \frac{p_e}{\omega_m}\bigg|_Q + \hat{p_e}\frac{\partial \tau_e(\omega_m, p_e)}{\partial p_e}\bigg|_Q + \hat{\omega_m}\frac{\partial \tau_e(\omega_m, p_e)}{\partial \omega_m}\bigg|_Q \tag{4.55}$$

and

$$T_e = \frac{P_e}{\Omega_m} \quad , \quad \hat{\tau}_e = \hat{p_e}\frac{1}{\Omega_m} - \hat{\omega_m}\frac{P_e}{\Omega_m^2} \tag{4.56}$$

where $p_e = P_e + \hat{p_e}$ is the load power connected to the output of the Diesel Generator and $Q = (P_e, \Omega_m)$ is the operating point. Hence, in the bandwidth of the AVR regulator:

$$\frac{\tau_e}{\omega_m}(s) \overset{f \ll f_{cV}}{=} -\frac{P_e}{\Omega_m^2} \tag{4.57}$$

the phase is equal to -180^o.

At higher frequencies, where the AVR regulation has no remarkable effects, the voltage is related to the rotational speed and can be expressed as:

$$v_0 = V_0\frac{\omega_m}{\Omega_m} \tag{4.58}$$

The electrical torque is:

$$\tau_e = \frac{p_e}{\omega_m} = \frac{v_0^2}{R_{load}}\frac{1}{\omega_m} = \frac{V_0^2}{R_{load}}\frac{\omega_m^2}{\Omega_m^2}\frac{1}{\omega_m} = \frac{P_e}{\Omega_m^2}\omega_m \tag{4.59}$$

and

$$T_e = \frac{P_e}{\Omega_m^2} \quad , \quad \hat{\tau_e} = \hat{p_e}\frac{1}{\Omega_m} + \hat{\omega_m}\frac{P_e}{\Omega_m^2} \tag{4.60}$$

Hence, the $\frac{\tau_e}{\omega_m}(s)$ results in:

$$\frac{\tau_e}{\omega_m}(s) \overset{f \gg f_{cV}}{=} \frac{P_e}{\Omega_m} \tag{4.61}$$

with a phase equal to 0^o, that is the opposite of (4.57). These considerations can be seen in Fig.4.24a.

Mechanical Frequency/Mechanical Torque The transfer function $\omega_m/\tau_m(s)$ consists of the feedback between the coupling shaft transfer function $h'_{eq}(s)$ and $\tau_e/\omega_m(s)$:

$$\frac{\omega_m}{\tau_m}(s) = \frac{h'_{eq}(s)}{1 + \tau_e/\omega_m(s)h'_{eq}(s)} \tag{4.62}$$

this transfer function can be observed in Fig.4.24b.

Speed Governor Loop The transfer function $T_\omega(s)$ of the speed governor loop comprises the transfer function $\omega_m/\tau_m(s)$, the diesel engine $DE(s)$ and the speed governor $PI_\omega(s)$. The result of the perturbations of the simulation model are reported in Fig.4.24c. The crossing frequency goes from 0.6Hz under heavy-load condition to 1Hz under light-load condition, so there are no significant changing in the step responses when a resistive load is applied.

4.4 Inverter Modeling

The power controlled source (PCS) is modeled in this section. For the purpose of this analysis, the inner current and voltage loops of the PCS are neglected. This assumption is done because the dynamics of interests are slow (with a frequency below 1Hz) compared to the typical bandwidth of these two loops, usually around hundreds of Hz. This helps also to speed up the simulations that, in case of parallel PCSs, become very long.

In Fig.4.25 the control scheme, where the Power Controlled Source (PCS) is a voltage-controlled inverter with the external power loops for the power reference tracking, as presented in [95]. The parts indicated in the scheme are:

- p_{ref}, q_{ref}: inverter active and reactive power references;

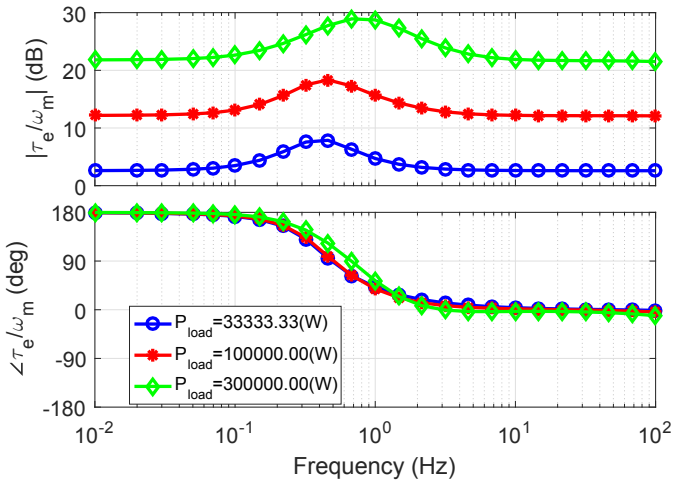

(A) $\tau_e/\omega_m(s)$

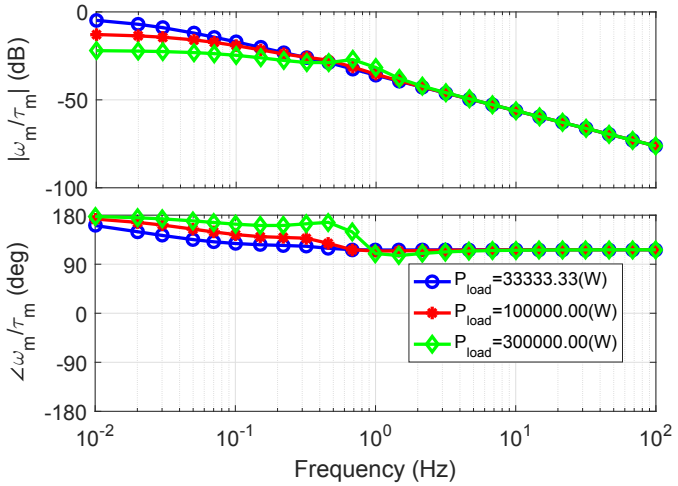

(B) $\omega_m/\tau_m(s)$

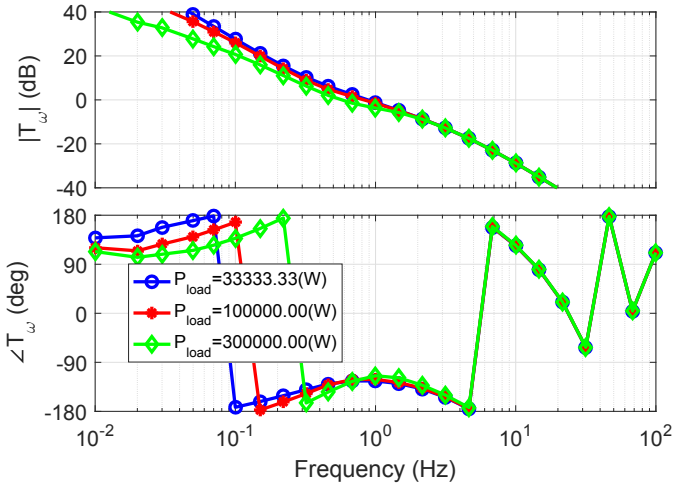

(C) $T_\omega(s)$

FIGURE 4.24: Genset transfer functions of the resistive case with parametric variations of the load of the power.

Description	Parameter	Value	Unit
Nominal Power	S_{nom}	40	kVA
Virtual Inductance	L_{series}	1.516	mH
Active Power External Coefficient	$k_{iref,p}$	6	–
Reactive Power External Coefficient	$k_{iref,q}$	87.5	–
Active Power Saturation	P_{sat}	210	kW
Rective Power Saturation	Q_{sat}	50	kVAR
Active Power Internal Coefficient	k_p	$7.368 \cdot 10^{-6}$	Hz/W
Reactive Power Internal Coefficient	k_q	$5 \cdot 10^{-4}$	VAR/Vrms
Powers Cutoff Frequency	ω_c	39.27	rad/s

TABLE 4.5: Parameters of the PCS.

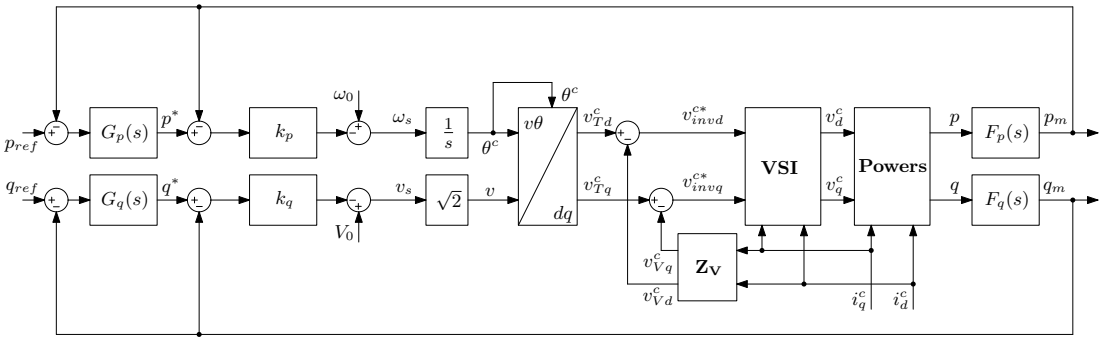

FIGURE 4.25: Control loops of the PCS.

- p^*, q^*: inverter active and reactive power references after the external regulators for the correct power tracking;

- $G_p(s), G_q(s)$: external controller of the active and the reactive power loop, where

$$G_p(s) = \frac{k_{iref,p}}{s} \quad , \quad G_q(s) = \frac{k_{iref,q}}{s} \tag{4.63}$$

  and the saturations are determined as in [95];

- k_p, k_q: internal controller of the active and reactive power loop, which represent the classical droop coefficients, note that k_p is multiplied by 2π because it is inserted in the angular frequency loop and k_q is divided by n_{trafo} because of the presence of the output transformer;

- $F_p(s), F_q(s)$: power filters, where

$$F_p(s) = F_q(s) = \frac{1}{s/\omega_c + 1}. \tag{4.64}$$

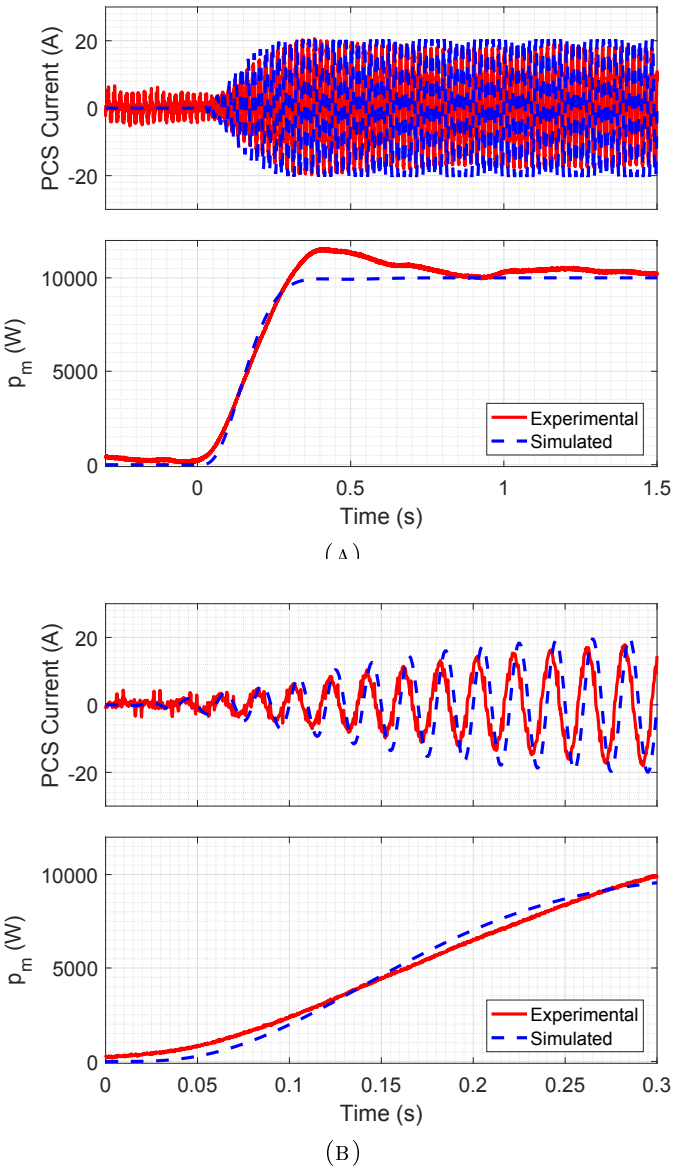

FIGURE 4.26: (a) Power reference step response of the PCS grid-connected and (b) detail.

4.4.1 Grid-Connected Case

The grid-connected application is considered as a benchmark for the PCS. The step response to the power reference $p_{ref} = 0 \rightarrow 10$kW is shown in Fig.4.26. The simulated response is more stable and reaches the set point in 300ms, while the experimental waveform exhibits an overshoot and reaches the set point in 1s. The detail of the transient is reported in Fig.4.26b. The difference between the two responses is mainly due to the assumption done on the inner voltage and current loops. As described in the following chapters, this mismatch is not critical when the PCS is connected to the Diesel Generator, since its dynamics are slower.

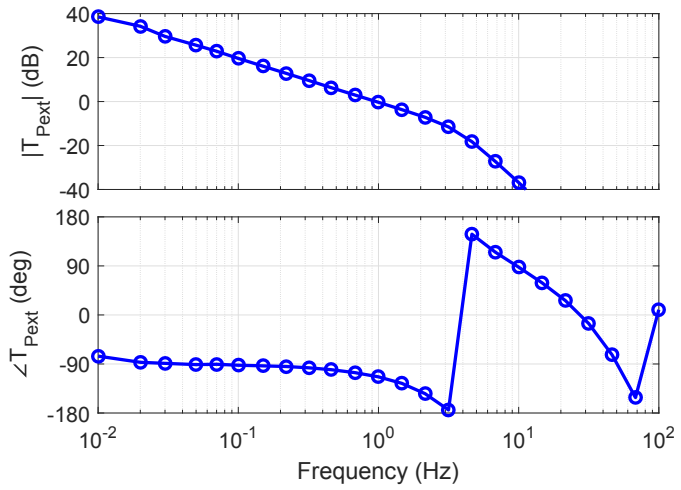

(A) $T_{Pext}(s)$

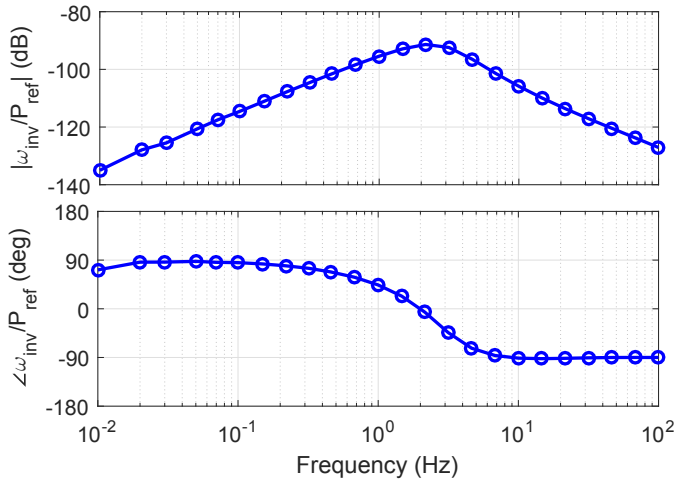

(B) $\omega_{inv}/p_{ref}(s)$

FIGURE 4.27: Transfer functions of the (a) active power loop $T_{Pext}(s)$ and of the (b) $\omega_{inv}/p_{ref}(s)$ functions in grid-connected condition.

In Fig.4.27 the results of the perturbations in the external active power loop $T_{Pext}(s)$ and the $\omega_{inv}/p_{ref}(s)$ are shown. The crossing frequency of the loop is 1Hz with a phase margin of 60^o. The peak of the $\omega_{inv}/p_{ref}(s)$ transfer function is around 2Hz and the damping factor of the system determines the slope of the phase around the resonance frequency.

4.5 Hybrid-Grid

The stability issue in the hybrid-grid under investigation can be considered both from the Diesel Generator and from the PCS perspectives. The models considered have been described in the previous chapters and they are here combined in order to simulate the system under investigation in Fig.4.28:

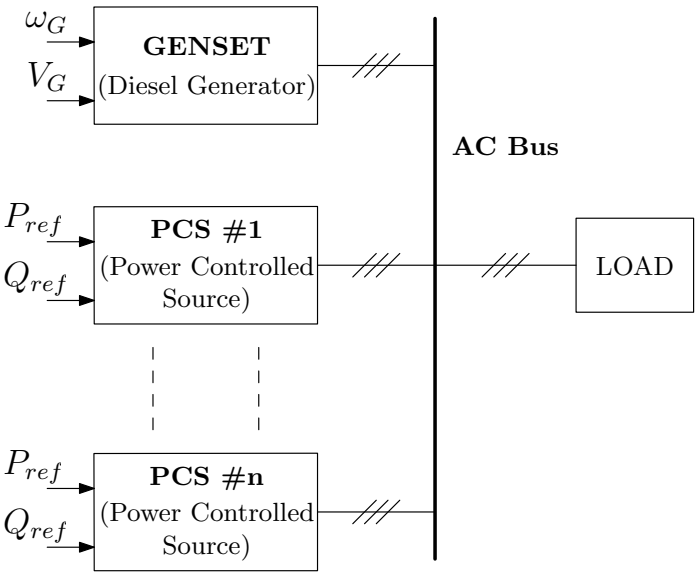

FIGURE 4.28: The considered hybrid-grid.

- the Diesel Generator SDMO V410C2 is controlled in isochronous mode, with reference frequency of $f_{ref} = 50$Hz and reference voltage $V_n = 400$V;
- the PCS is droop controlled with the control structure reported in the previous chapter.

This chapter aims to give an insight on the phenomenon that takes place in the system when one or more PCS are connected and in case of variations of some important parameters. This study is performed:

- from the Diesel Generator perspective, where only the frequency loop in Fig.4.29 is considered, this because the instability issue is between the active power and the frequency $P - f$, and the voltage loop is not crucial. The transfer functions $\tau_e/\omega_m(s)$, $\omega_m/\tau_m(s)$ and $T_\omega(s)$ are shown.
- from the PCS perspective, where the transfer functions of interest are $T_{Pext}(s)$, $\omega_{inv}/p_{ref}(s)$. Also the transfer function $T_{Qext}(s)$ is considered.

4.5.1 Diesel Generator perspective

In Fig.4.30 the comparison between the experimental and the simulated waveforms of the current and the frequency of the Diesel Generator to a load steps 50kW $\rightarrow$ 80kW when a single PCS is connected. The response is oscillating and the settling time is around 5s, twice compared to the resistive case.

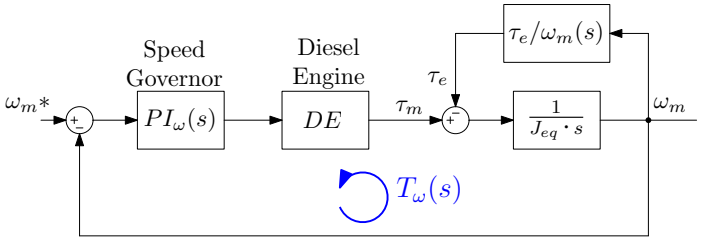

FIGURE 4.29: Control loops of the PCS.

The transfer function of interest are:

- *Electrical Torque/Mechanical Frequency*: the transfer function $\tau_e/\omega_m(s)$ in Fig.4.32a is compared to the resistive load case, and can be seen that the magnitude of the transfer function is much higher than the previous one, reaching 50dB around 1Hz.
- *Mechanical Frequency/Mechanical Torque*: the transfer function $\omega_m/\tau_m(s)$ in Fig.4.32b results in a lower magnitude, decreasing of about 40dB in some points.
- *Speed Governor Loop*: the transfer function $T_\omega(s)$ of the speed loop can be seen in Fig.4.32c. It is clear from the magnitude that the PCS is reducing the performance of the speed loop. The crossing frequency passes from 1Hz in the resistive case, to 0.2Hz when the PCS is connected: the PCS control is critical for the system.

Neglecting the synchronous machine dynamics, it is possible to have a good match between the the frequency response resulting from the perturbations and the transfer functions at low frequencies, within the bandwidth of the droop control.

The equations of the inverter power loops are ($\omega_e = \omega_{inv}$):

$$\begin{aligned} \omega_s &= \omega_0 - k_p \cdot [(p_{ref} - p_{inv} \cdot F_p) \cdot G_p - p_{inv} \cdot F_p] \\ v_s &= V_0 - k_q \cdot [(q_{ref} - q_{inv} \cdot F_q) \cdot G_q - q_{inv} \cdot F_q] \end{aligned} \tag{4.65}$$

where $\omega_e = \omega_{inv}$ is the angular frequency of the inverter, p_{inv} and q_{inv} are the active and reactive powers of the inverter, $G_p = k_{irefp}/s$ and $G_q = k_{irefq}/s$ are the external regulators. The filters of the powers are $F_p = F_q = 1/(s/\omega_c + 1)$.

Since the transfer function has to be expressed in terms of $\tau_e/\omega_m(s)$, it is worth to substitute the electrical frequency with the mechanical frequency, considering

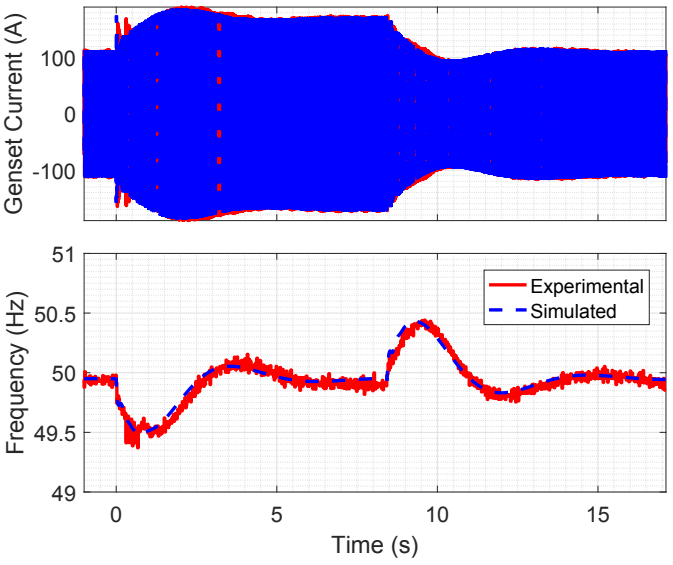

(A) Connection and disconnection

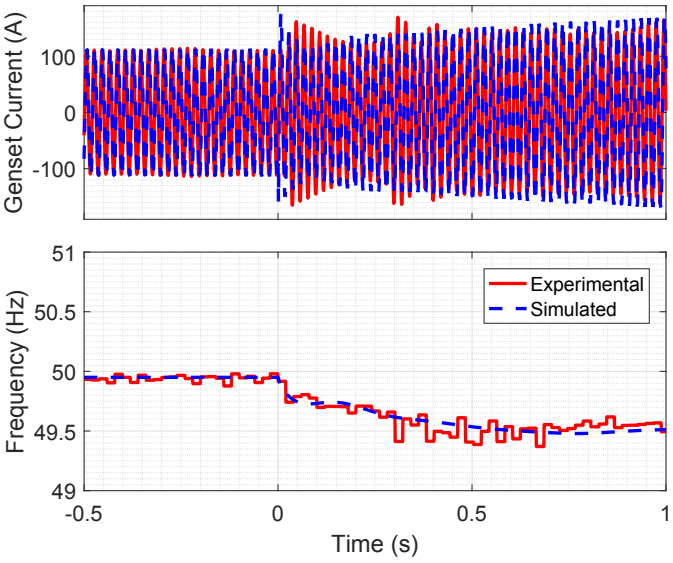

(B) Connection

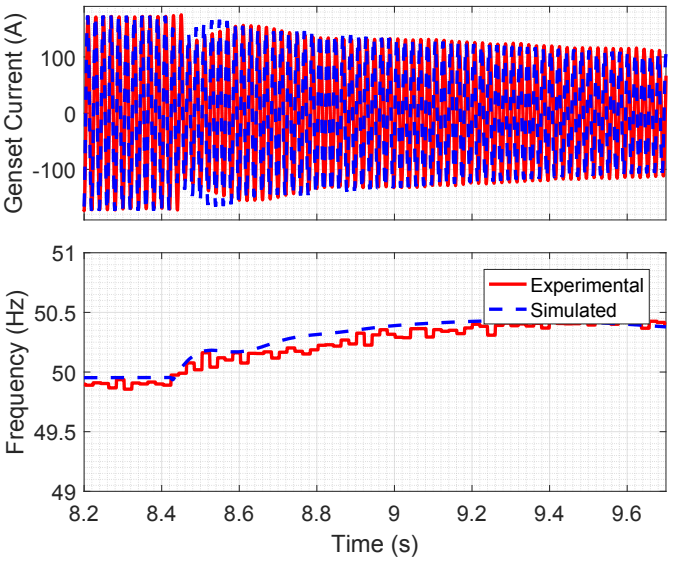

(C) Disconnection

FIGURE 4.30: Response of the Diesel Generator to the load variation 50kW → 80kW when the PCS is connected.

the pole pairs in the synchronous machine p_p:

$$\omega_e = p_p \cdot \omega_m \tag{4.66}$$

The active power determines the torque and can be expressed using (4.65) as:

$$p_{inv} = \left(\frac{p_p \omega_m - \omega_0}{k_p} + p_{ref} G_p(s) \right) \cdot \frac{1}{F_p(s) \cdot (1 + G_p(s))} \tag{4.67}$$

Considering a system with a load with power p_L and an inverter with power p_{inv}, the total electrical power is:

$$p_e = p_L + p_{inv} = p_L + \left(\frac{p_p \omega_m - \omega_0}{k_p} + p_{ref} G_p(s) \right) \cdot \frac{1}{F_p(s) \cdot (1 + G_p(s))} \tag{4.68}$$

In this last equation four quantities can be perturbed:

- the electrical torque: $\tau_e = T_e + \hat{\tau}_e$
- the mechanical frequency: $\omega_m = \Omega_m + \hat{\omega}_m$
- the load power: $p_L = P_L + \hat{p}_L$
- the inverter power reference: $p_{ref} = P_{ref} + \hat{p}_{ref}$

and the electrical torque can be expressed as follows

$$\tau_e = \underbrace{\left. \frac{p_e}{\omega_m} \right|_Q}_{T_e} + \underbrace{\hat{p}_L \cdot \left. \frac{\partial \tau_e}{\partial p_L} \right|_Q + \hat{p}_{ref} \cdot \left. \frac{\partial \tau_e}{\partial p_{ref}} \right|_Q + \hat{\omega}_m \cdot \left. \frac{\partial \tau_e}{\partial \omega_m} \right|_Q}_{\hat{\tau}_e} \tag{4.69}$$

where the operating point is given as $Q = (P_L, P_{ref}, \Omega_m)$ and $\Omega_m = \omega_0 / p_p$. The steady-state quantity is given by:

$$T_e = \left. \frac{p_e}{\omega_m} \right|_Q = \frac{1}{\Omega_m} \cdot \left[P_L + P_{ref} \cdot \frac{G_p}{F_p \cdot (1 + G_p)} \right] \tag{4.70}$$

while the transfer functions related to the perturbation are

$$\begin{aligned}
\left. \frac{\partial \tau_e}{\partial p_L} \right|_Q &= \frac{1}{\Omega_m} \\
\left. \frac{\partial \tau_e}{\partial p_{ref}} \right|_Q &= \frac{1}{\Omega_m} \cdot \frac{G_p}{F_p \cdot (1 + G_p)} \\
\left. \frac{\partial \tau_e}{\partial \omega_m} \right|_Q &= -\frac{P_L}{\Omega_m^2} - \frac{P_{ref} G_p(s)}{\Omega_m^2 F_p(s) \cdot (1 + G_p(s))} + \frac{p_p}{k_p \Omega_m F_p(s) \cdot (1 + G_p(s))}
\end{aligned} \tag{4.71}$$

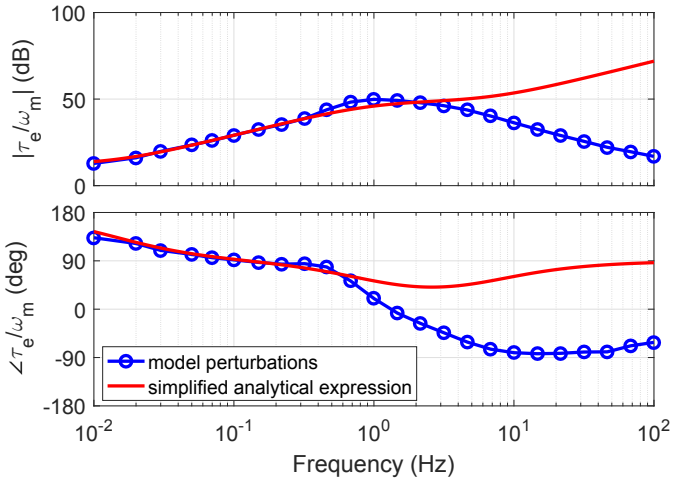

FIGURE 4.31: Comparison of the result from the perturbed simulation model and the simplified analytical expression.

The comparison between the result of the perturbations in the simulation model and the simplified analytical expression with the inverter can be seen in Fig.4.31. Magnitude and phase overlap below 1Hz. For higher frequencies there is a mismatch because the synchronous machine dynamics and the output impedances have been neglected. This simplified analytical expression can prove the increase in magnitude of the $\tau_e/\omega_m(s)$ transfer function in the frequency range of interest. The second term of the $\partial\tau_e/\partial\omega_m|_Q$ is related to the active power of the inverter P_{ref}, but the magnitude of the transfer function is negligible compared to the other two contributions when P_{ref} is in the power limits given for the single inverter module. Hence, it is possible to say that the $\tau_e/\omega_m(s)$ transfer function is independent from the inverter power.

In Fig.4.32a the $\tau_e/\omega_m(s)$ functions in the resistive and in the inverter case are compared. The connection of the inverter results in a high increase in the magnitude, and this causes also a decrease of the function $\omega_m/\tau_m(s)$ of the same quantity. This decrease is reflected also in the open loop transfer function $T_\omega(s)$, where the crossing frequency passes from 1Hz to 0.22Hz with a decrease also in the phase margin: the resulting system is slower and less stable, and this causes the undesired oscillations which occur. Moreover, the stability margin of the system is not enough to guarantee a good performance, since this oscillating phenomenon appears when a single PCS of a power of $P_{PCS} = 40$kW is only the $\simeq 10\%$ of $P_{GEN} = 410$kVA.

The simulation model predicts the behavior in case of multiple connected PCSs as shown in Fig.4.33b for the cases with 2, 4 PCSs connected. For example, when 6 PCSs ($\simeq 60\%$ of P_{GEN}) are connected to the Diesel Generator, the system needs a settling time of almost ten times with respect to the resistive case, and increases

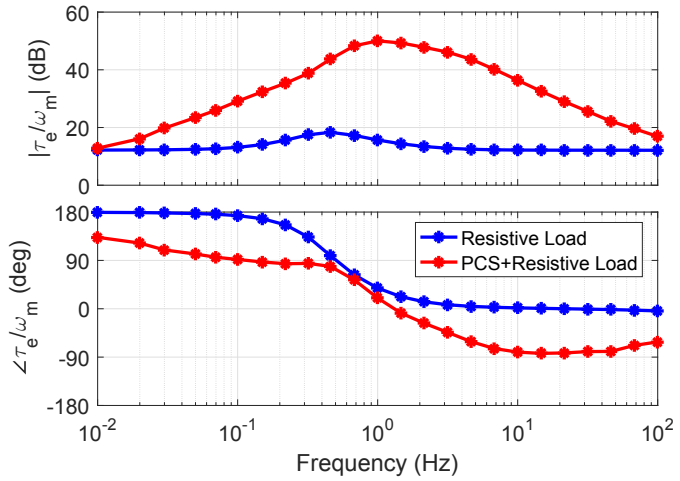

(A) $\tau_e/\omega_m(s)$

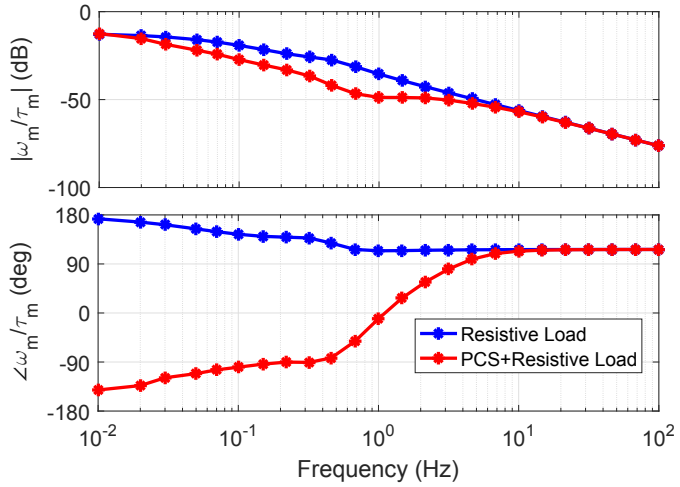

(B) $\omega_m/\tau_m(s)$

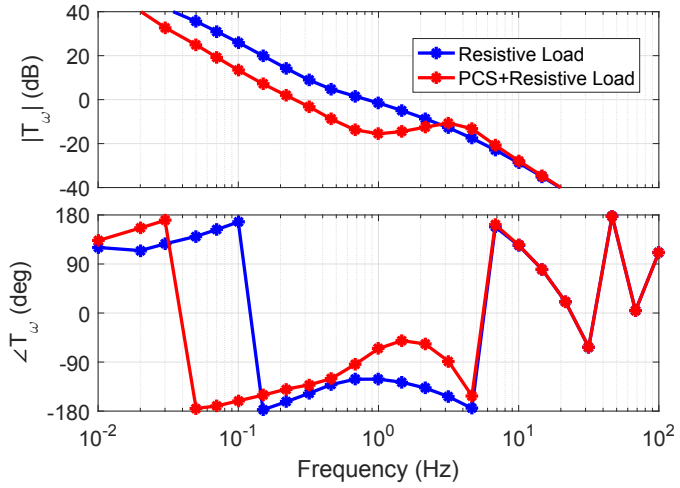

(C) $T_\omega(s)$

FIGURE 4.32: Comparison of the perturbations in the resistive case and in the case with PCS.

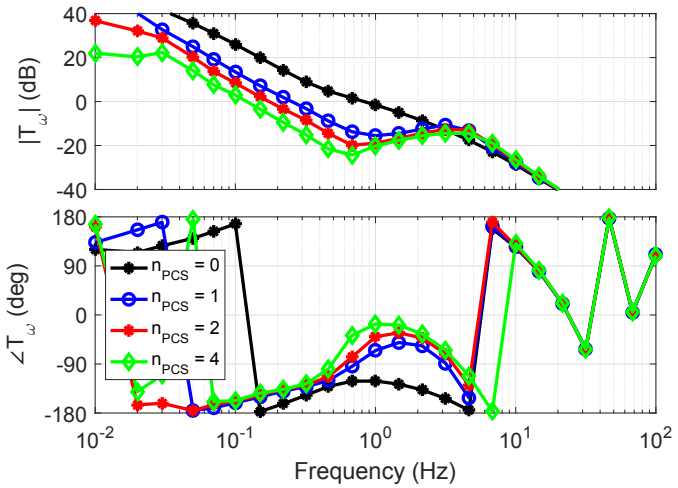

(A) Speed Loop $T_\omega(s)$

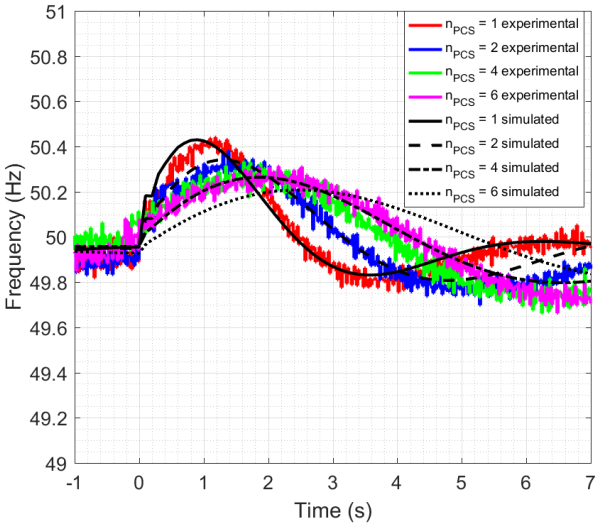

(B) Disconnection

FIGURE 4.33: (a) speed loop transfer function and (b) step responses for an increasing number of PCSs connected to the Diesel Generator.

with the number of connected PCSs. This more unstable behavior can be seen also in the frequency domain thanks to the result of the perturbations shown in Fig.4.33a, where the crossing frequencies and the phase margins decreases as in Tab.4.6. Hence, the higher the number of parallel PCSs, the lower the stability margin and the crossing frequency, that results in a longer settling time.

4.5.2 Inverter perspective

It is possible to analyze the system also from the PCS perspective. In Fig.4.34a the response of the inverter measured power p_m is shown for a power reference step p_{ref} = 0kW $\rightarrow$ 10kW and good matching can be observed. In Fig.4.34b a

$\#PCS$	Crossing Frequency $f_{c\omega}$(Hz)	Phase Margin $\phi_{PM\omega}(^o)$
0	1	60
1	0.22	40
2	0.16	35
4	0.13	25

TABLE 4.6: Crossing frequencies and phase margins of $T_\omega(s)$ with an increasing number of parallel PCSs.

detail of the connection is shown. In Fig.4.34c the comparison between the grid-connected and the genset-connected cases is presented, where the genset-connected case shows a larger settling time.

This changes in the settling time can be seen also looking at the perturbations in the external active power loop $T_{Pext}(s)$ in Fig.4.35a, where the crossing frequency and the pase margin decrease as in Tab.4.7. Moreover, in the $\omega/p_{ref}(s)$ transfer function the resonance peak moves to a lower frequency, as in Fig.4.35b. The increase in magnitude results in a bigger drop in frequency for the same load increase.

Case	Crossing Frequency $f_{c\omega}$(Hz)	Phase Margin $\phi_{PM\omega}(^o)$
Grid-connected	1	60
Genset-connected	0.22	45

TABLE 4.7: Crossing frequencies and phase margins of $T_{Pext}(s)$ in grid-connected and genset-connected cases.

4.5.3 Parametric Variations

In Fig.4.36 is shown the comparison for the variations of the PCS active power loop coefficients, and the simulated results are compared to the experimental tests:

- in Fig.4.36a the external coefficient is changed: the simulation model matches with the experimental results;
- in Fig.4.36b the internal coefficient is changed: the simulation model matches with the experimental results.

To better understand how the transfer functions change depending on these parameters:

- external regulator coefficients $k_{iref,p}$, $k_{iref,q}$;
- internal regulator coefficients k_p, k_q;
- coupling output inductance L_{series};
- frequency of the power filter ω_c;
- load power P_{load};
- number of inverters n_{inv} (or n_{PCS}).

The transfer functions analyzed are:

- $\tau_e/\omega_m(s)$ in Fig.4.37: the internal and external regulators of the active power loop cause a variation in the frequency response, while the parameters in the reactive power loop do not. A load power increase causes a higher magnitude at low frequencies, since the transfer function for resistive load condition increases and is added to the transfer function associated to the PCS. Once again, the power filter cutoff frequency does not change this transfer function significantly. The output inductance causes a variation only for frequencies above 1Hz. The increasing number of PCSs causes a significant variation of the frequency response for all the frequencies.
- $\omega_m/\tau_m(s)$ in Fig.4.38: the internal and external regulators of the active power loop cause a variation in the frequency response, while the parameters in the reactive power loop do not. A load power increase causes a lower magnitude at low frequencies. As mentioned in the previous point, the power filter cutoff frequency does not change this transfer function significantly. The output inductance causes a variation only for frequencies above 1Hz. The increasing number of PCSs causes a significant variation of the frequency response for the low frequencies.
- $T_\omega(s)$ in Fig.4.39: the internal and external regulators of the active power loop cause a variation in the frequency response, while the parameters in the reactive power loop do not, as expected. A load power increase causes a lower phase margin at the crossing frequency. As mentioned in the previous point, the power filter cutoff frequency does not change this transfer function significantly. The output inductance causes a resonance around 2Hz. The increasing number of PCSs causes a significant variation of the frequency response at low frequencies.

- $T_{Pext}(s)$ in Fig.4.40: the internal and external regulators of the active power loop cause a variation in the frequency response, while the parameters in the reactive power loop do not, as expected. A load power increase does not changes significantly this transfer function. The power filter cutoff frequency changes the response above 1Hz. The output inductance increase causes a drop of the frequency response around 3Hz. The increasing number of PCSs causes a significant variation of the frequency response at low frequencies.

- $T_{Qext}(s)$ in Fig.4.41: the internal and external regulators of the reactive power loop cause a variation in the frequency response, while the parameters in the active power loop do not, as expected. A load power increase does not changes this transfer function. The power filter cutoff frequency changes the response above 1Hz. The output inductance increase causes a drop of the frequency response around for all the frequencies analyzed. The increasing number of PCSs does not vary this transfer function.

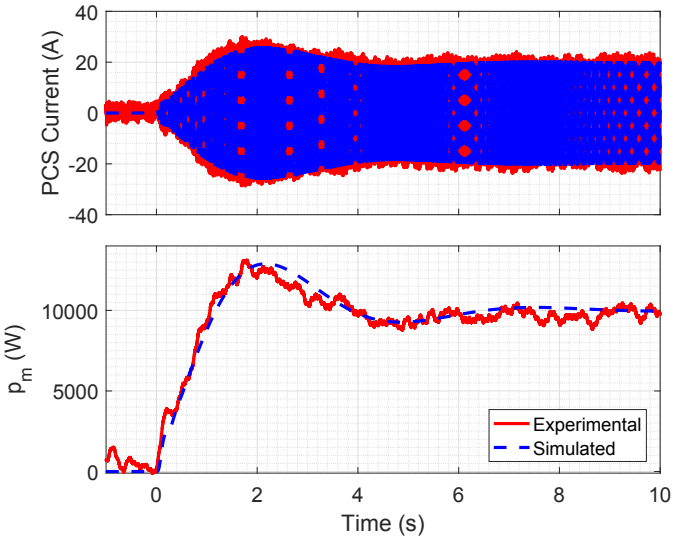

(A) Whole step response

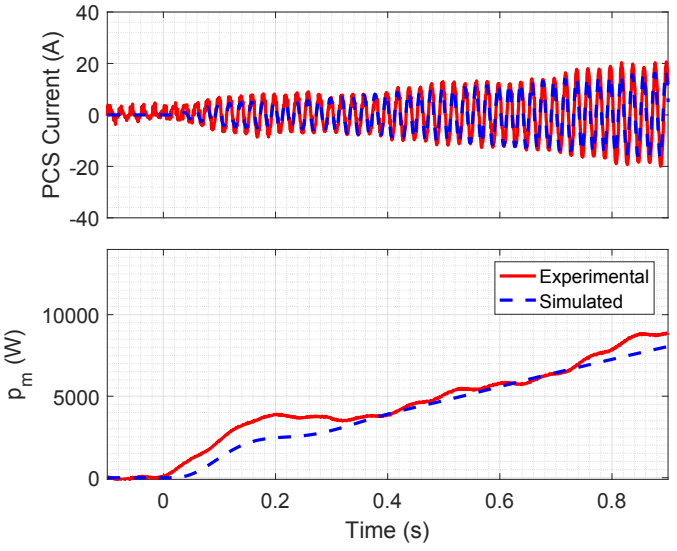

(B) Detail

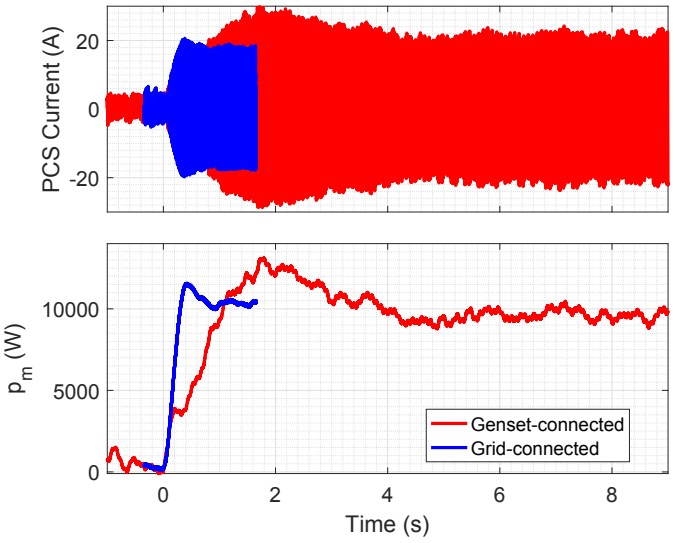

(C) Comparison

FIGURE 4.34: Power reference p_{ref}: (a) whole step response, (b) detail and (c) comparison with the grid-connected step response.

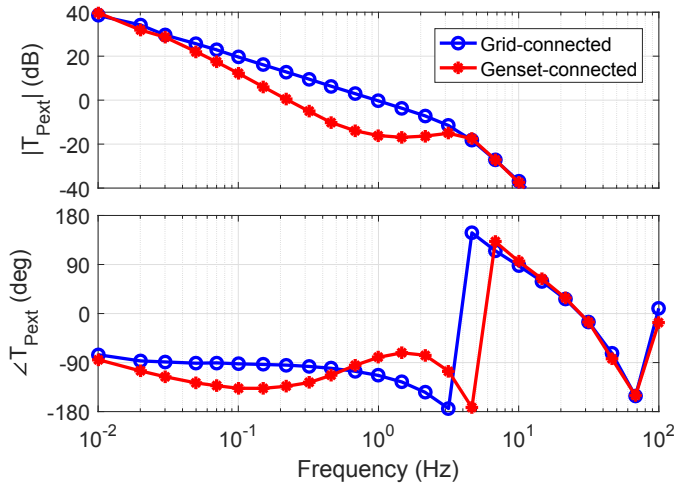

(A) $T_{Pext}(s)$

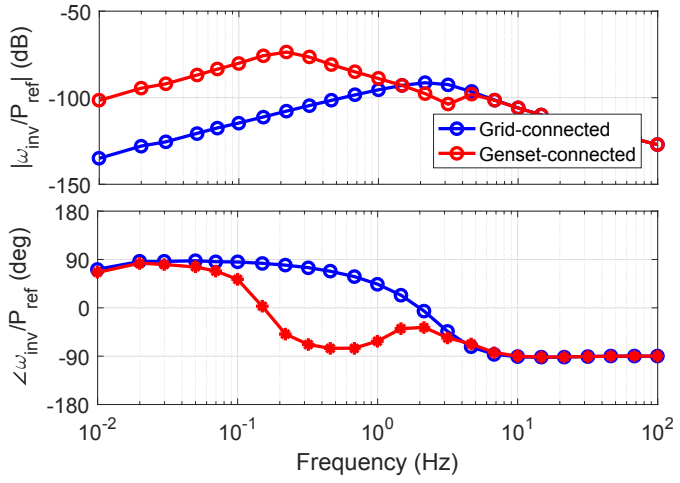

(B) $\omega/p_{ref}(s)$

FIGURE 4.35: Comparison between the grid-connected case and the Genset connected case for (a) $T_{Pext}(s)$ and (b) $\omega/p_{ref}(s)$.

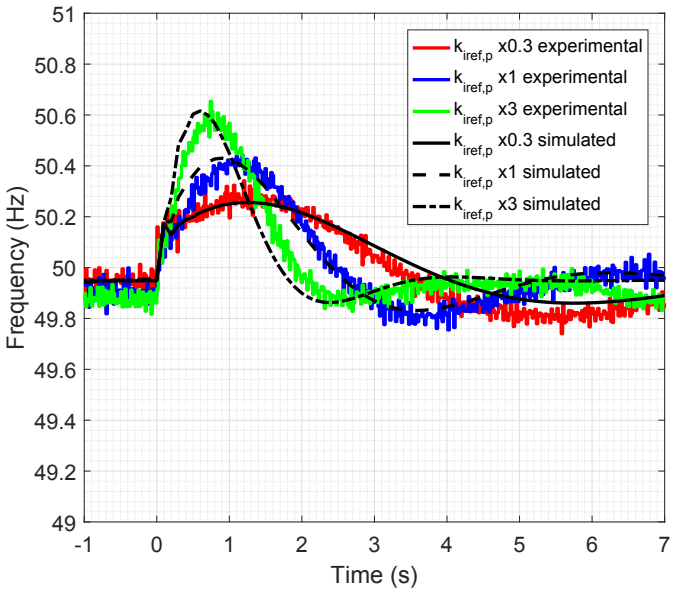

(A) $k_{iref,p}$

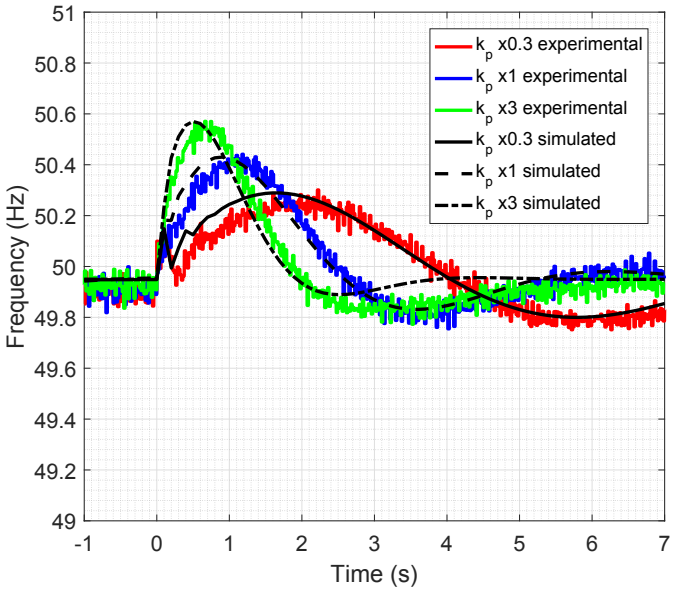

(B) n_{inv}

FIGURE 4.36: Transfer function $T_{Pext}(s)$ with parametric variations.

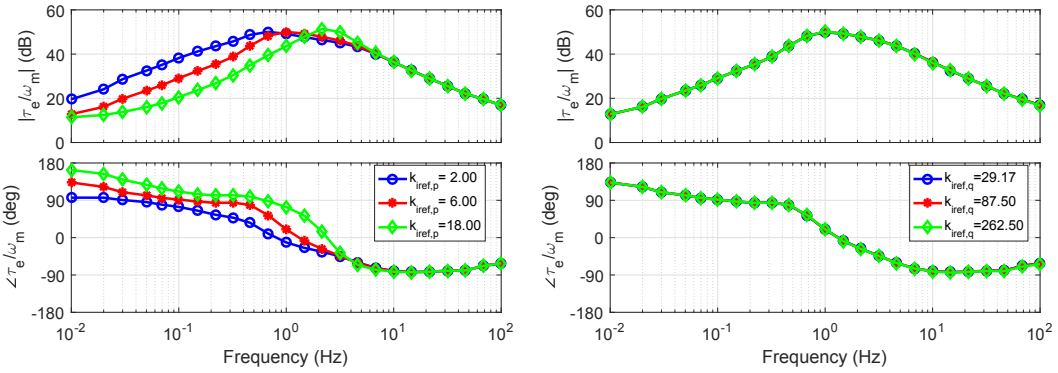

(A) $k_{iref,p}$

(B) $k_{iref,q}$

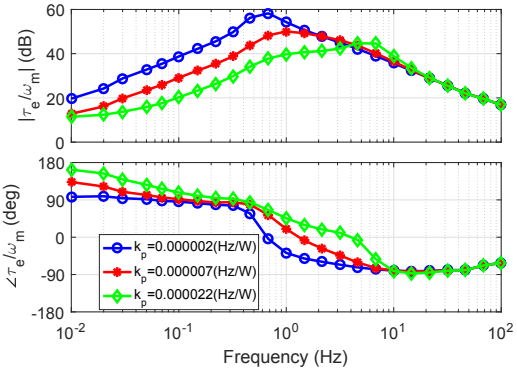

(C) k_p

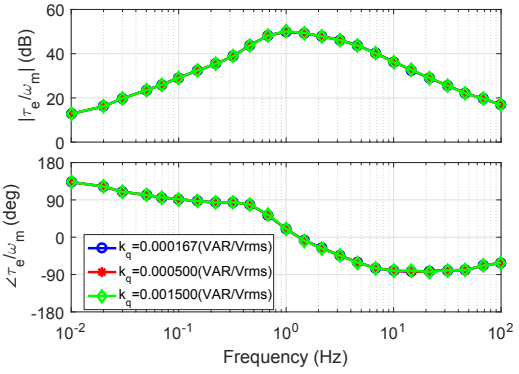

(D) k_q

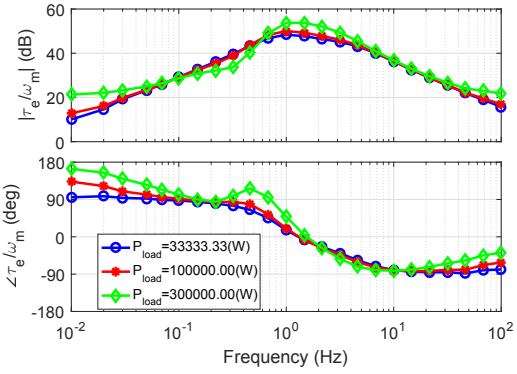

(E) P_{load}

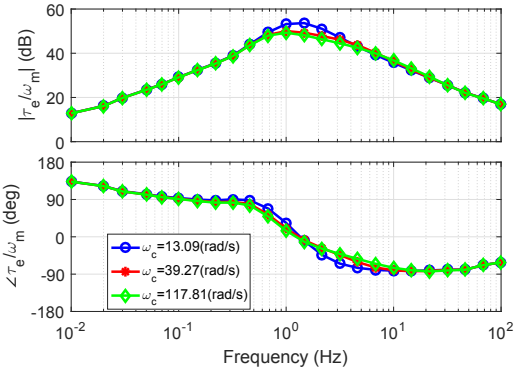

(F) ω_c

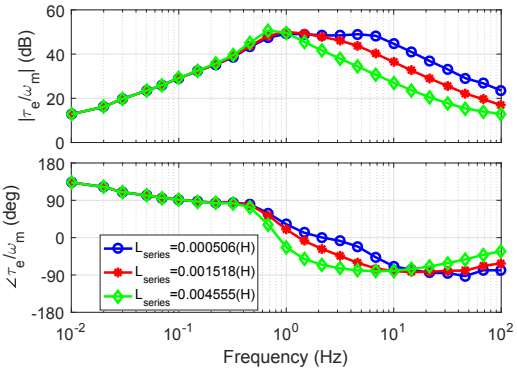

(G) L_{series}

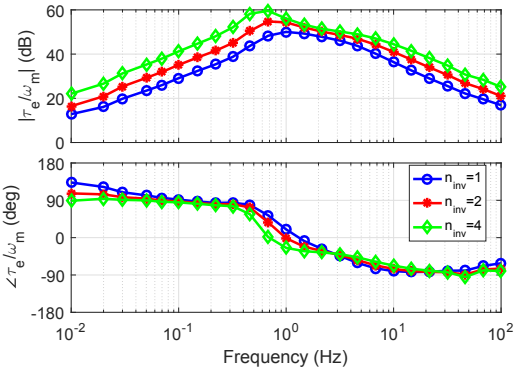

(H) n_{inv}

FIGURE 4.37: Transfer function $\tau_e/\omega_m(s)$ with parametric variations.

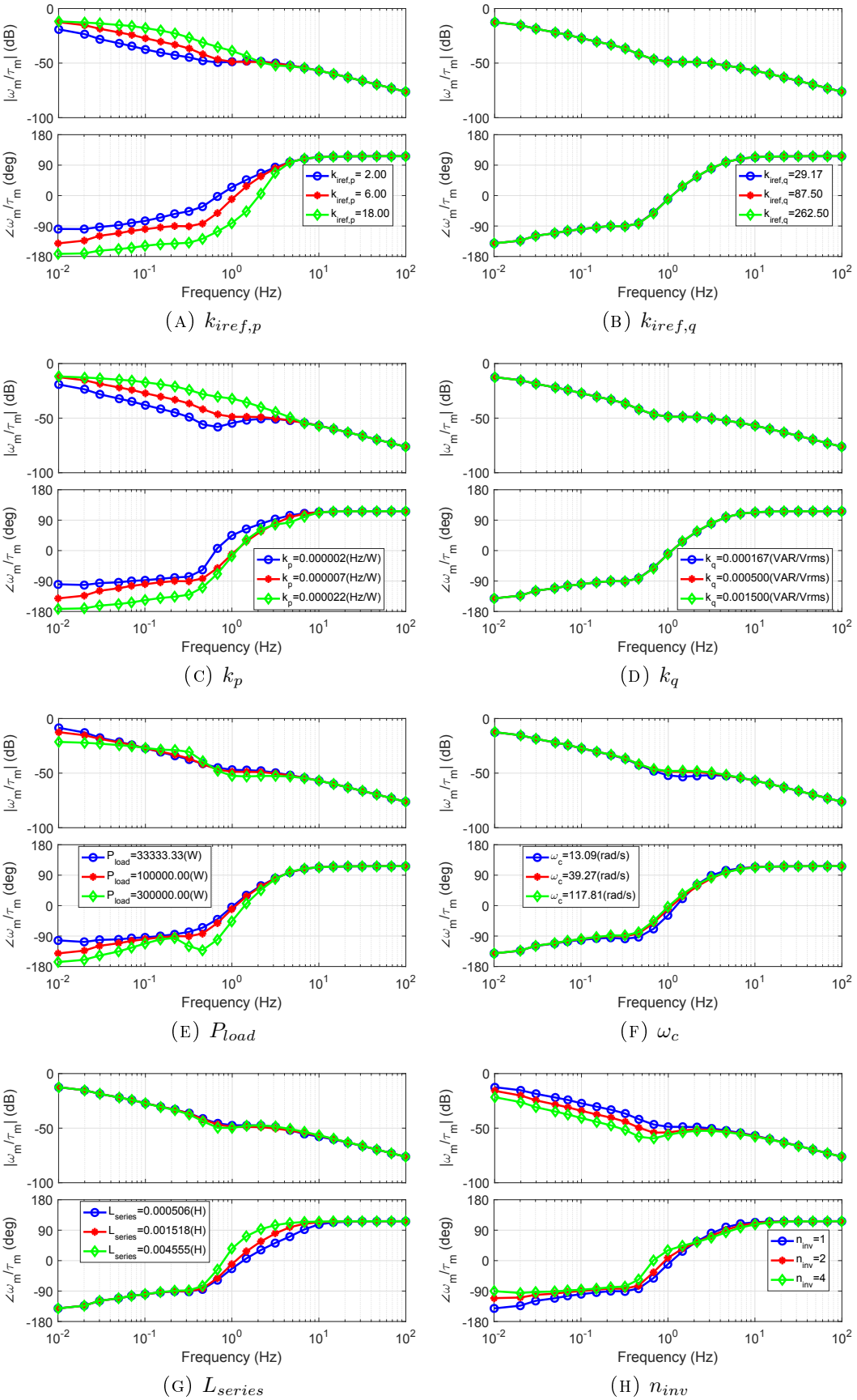

(A) $k_{iref,p}$ (B) $k_{iref,q}$

(C) k_p (D) k_q

(E) P_{load} (F) ω_c

(G) L_{series} (H) n_{inv}

FIGURE 4.38: Transfer function $\omega_m/\tau_m(s)$ with parametric variations.

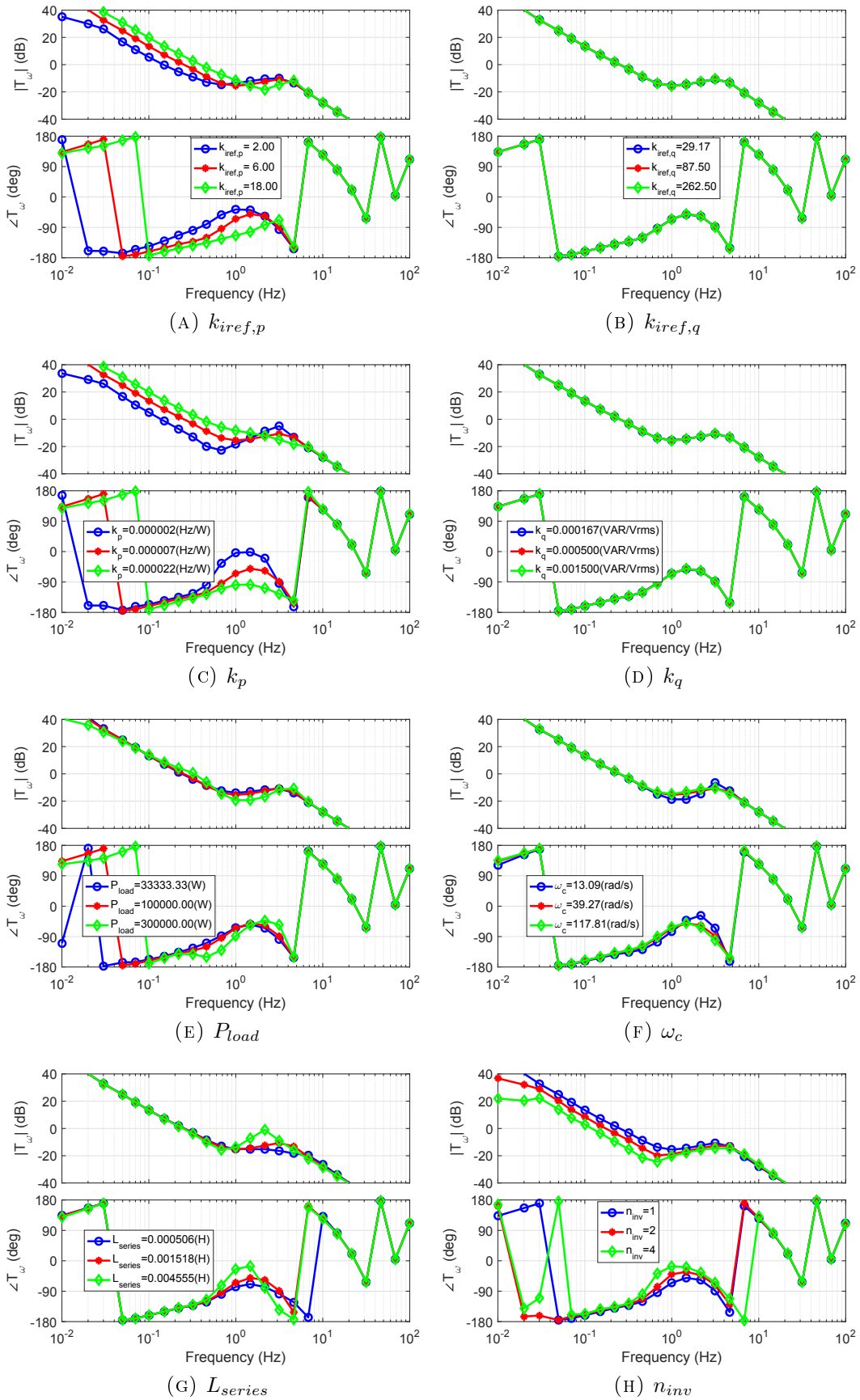

(A) $k_{iref,p}$ (B) $k_{iref,q}$

(C) k_p (D) k_q

(E) P_{load} (F) ω_c

(G) L_{series} (H) n_{inv}

FIGURE 4.39: Transfer function $T_\omega(s)$ with parametric variations.

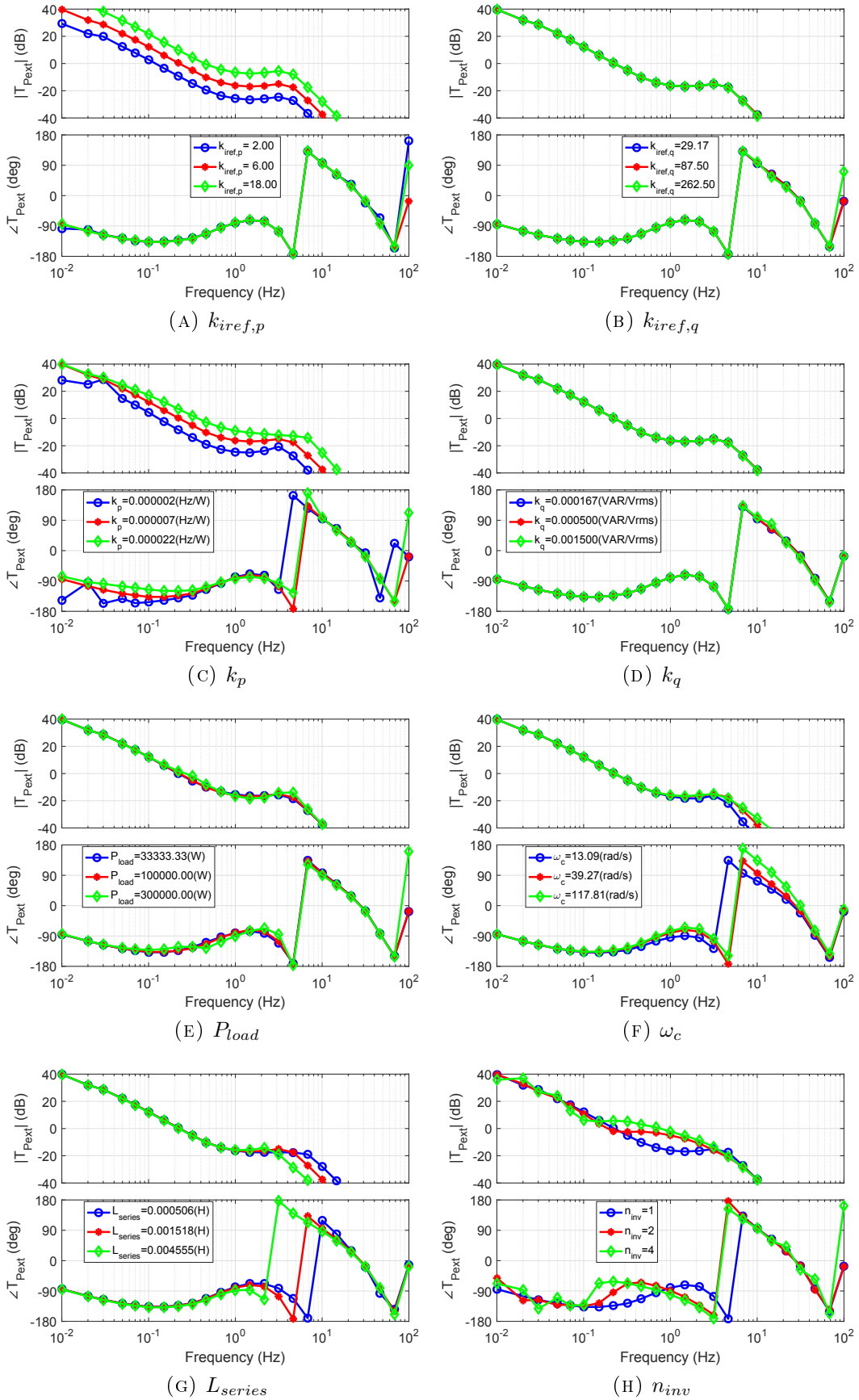

(A) $k_{iref,p}$ (B) $k_{iref,q}$

(C) k_p (D) k_q

(E) P_{load} (F) ω_c

(G) L_{series} (H) n_{inv}

FIGURE 4.40: Transfer function $T_{Pext}(s)$ with parametric variations.

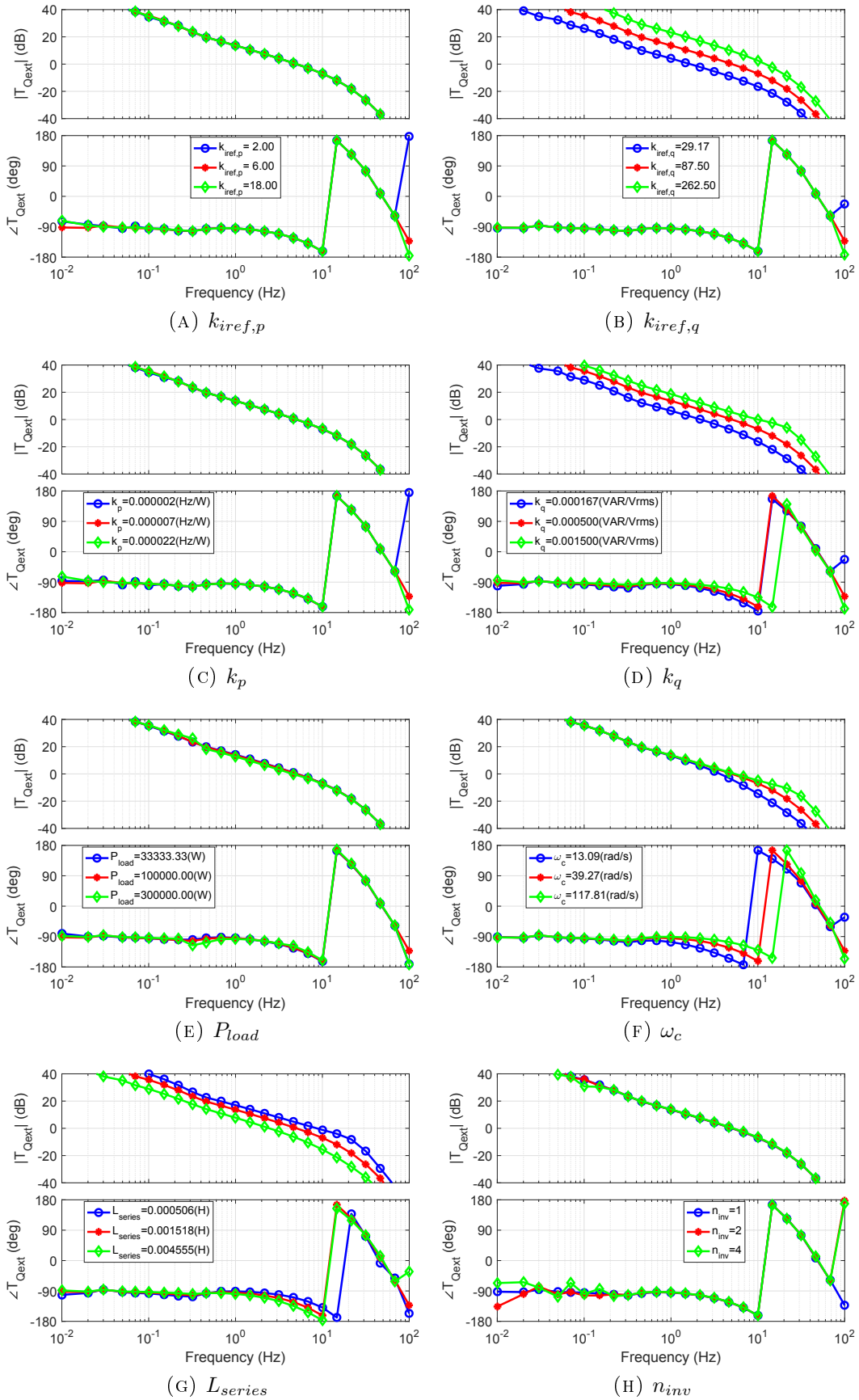

(A) $k_{iref,p}$ (B) $k_{iref,q}$

(C) k_p (D) k_q

(E) P_{load} (F) ω_c

(G) L_{series} (H) n_{inv}

FIGURE 4.41: Transfer function $T_{Qext}(s)$ with parametric variations.

Chapter 5

Output Impedance of the Droop Controlled Inverter

In Sec. 4.4 the simulation model of the droop control strategy introduced in [95] is applied. This control strategy provides an additional external loop with respect to the basic droop control in [94, 126], in order to have an exact tracking of the power references when the PCS is connected to the grid.

The goal of this chapter is to provide the analytical expressions to derive the output impedance of the droop-controlled inverter with the basic configuration shown in [94]. Firstly, the standard for interconnecting DRs is introduced in Sec. 5.1, then the generic case of a system with different dq-frames is presented in Sec. 5.2.

The dq impedance measurement is considered ideal in this chapter, since the injection in simulation is performed through ideal generators. Moreover, for the synchronization with the three-phase system to obtain the phase does not need any PLL, since an identical steady-state model is generated and executed concurrently in the same MATLAB/Simulink simulation model to have the angle in the steady-state condition. This allows the complete separation between the sub-model necessary to align the phase with the three-phase voltage and the sub-model

subject to the perturbations, and so avoid the need of a PLL and consequently neglect its influence in the system.

5.1 Standard for Interconnecting DRs with Electric Power Systems

In order to model the droop-controlled inverter, it is worth to provide the parameters as indicated in the standards. In this section, the part of interest of the standard IEEE 1547 [127], which describes the interconnection for distributed resources (DRs) in off-grid condition, is shown. The frequency and voltage ranges allowed for by the standards for the DRs are shown in Tab. 5.1 and Tab. 5.2, respectively.

For the frequency range, the DRs are divided by size. The clearing time for DRs of bigger size is longer. The frequency considered is 60Hz. The range for DRs $\leq$ 30kVA is [59.3Hz, 60.5Hz], while for $>$ 30kVA is [57.0Hz, 60.5Hz].

For the voltage range, the range considered is the percentage of the base voltage: [88%, 120%]. Hence, the whole range is about 22% of the base voltage.

DR size [kVA]	Frequency range [Hz]	Clearing time [s]
≤ 30	> 60.5	0.16
	< 59.3	0.16
> 30	> 60.5	0.16
	$< \{59.8 - 57.0\}$	$\{0.16 - 300\}$
	< 57.0	0.16

TABLE 5.1: Frequency range and clearing time for DRs in IEEE 1547.

Voltage range [% of base voltage]	Clearing time [s]
$V > 50$	0.16
$50 \leq V < 88$	2.00
$110 \leq V < 120$	1.00
$V \geq 120$	0.16

TABLE 5.2: Voltage range and clearing time for DRs in IEEE 1547.

Therefore, the angular frequency and voltage ranges are:

$$\begin{aligned} \Delta\omega &= \quad 7.54 \quad [\text{rad/s}] \\ \Delta V &= 0.22 \cdot V_n \quad [\text{V}] \end{aligned} \tag{5.1}$$

and these ranges will be used for the determination of the droop control coefficients k_p and k_q for the P/f and Q/V laws.

5.2 System and Controller dq-frames

In Fig. 5.1a the droop-controlled inverter is connected to a resistive-inductive load. In between the inverter and the load, the impedance measurement unit (IMU) is placed, in order to measure the source and the load impedances in dq-frame, $\mathbf{Z_S}$ and $\mathbf{Z_L}$ respectively.

The IMU is aligned to the terminal output voltage, and the resulting dq-frame is indicated as *system frame* ($d^s q^s$ axes). If the IMU is not injecting any perturbations, the *controller frame* ($d^c q^c$ axes), which is used by the internal control of the droop-controlled inverter, is stable and presents in general a phase-shift ϕ. This is due to the internal decoupling impedance, virtual or physical, if present.

In Fig. 5.1b the IMU starts to perturb the system in order to measure the output impedance. The current and voltage perturbations result in power perturbations and finally in an angle perturbations of the inner *controller frame*, as can be observed in the control scheme in Fig. 5.2a.

5.3 Control Scheme

The main control scheme for the droop-controlled inverter is depicted in Fig. 5.2a. Since the system has dimension 2×2, it is possible to define the vectors and the matrices and provide a more compact notation as in Fig. 5.2b. The vectors definitions are presented hereafter, together with the steady-state and the perturbed quantities:

- power references vector, active and reactive powers:

$$\underline{s}^* = \begin{bmatrix} p^* \\ q^* \end{bmatrix} \qquad \simeq \underline{S}^* + \hat{\underline{s}}^* = \begin{bmatrix} P^* \\ P^* \end{bmatrix} + \begin{bmatrix} \hat{p}^* \\ \hat{q}^* \end{bmatrix}; \tag{5.2}$$

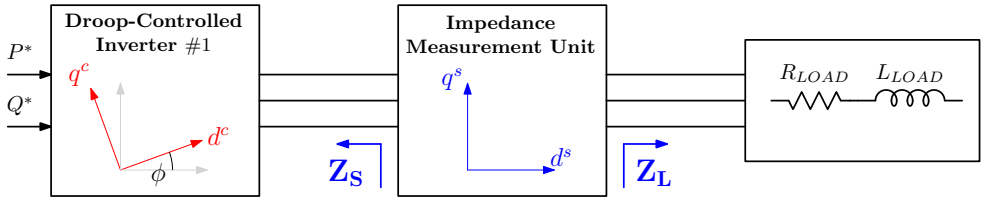

(A) No injection

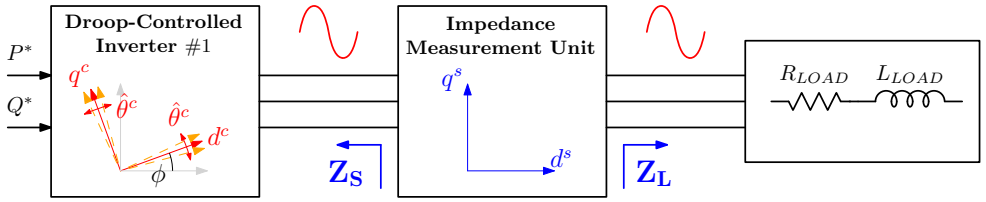

(B) Injection from the IMU

FIGURE 5.1: Representation of the system and the controller dq-frames: (a) before perturbing the system the controller dq-frame is stable and phase-shifted (if an internal decoupling inductance is included). (b) When the IMU starts perturbing, the controller dq-frame exhibits an oscillation due to the current or voltage perturbation.

- operating point reference, reference frequency and voltage:

$$\underline{X}_0 = \begin{bmatrix} \omega_0 \\ V_0 \end{bmatrix}; \tag{5.3}$$

- operating point vector, system frequency and voltage (from P/f and Q/V droop regulations):

$$\underline{x} = \begin{bmatrix} \omega_s \\ v_s \end{bmatrix} \quad \simeq \underline{X} + \hat{\underline{x}} = \begin{bmatrix} \Omega_s \\ V_s \end{bmatrix} + \begin{bmatrix} \hat{\omega}_s \\ \hat{v}_s \end{bmatrix}; \tag{5.4}$$

- angle and amplitude vector:

$$\underline{r}^c = \begin{bmatrix} \theta^c \\ v \end{bmatrix} \quad \simeq \underline{R}^c + \hat{\underline{r}}^c = \begin{bmatrix} \Omega_s \cdot t \\ V \end{bmatrix} + \begin{bmatrix} \hat{\theta}^c \\ \hat{v} \end{bmatrix}; \tag{5.5}$$

- the vector of the references resulting from the Park's transformation (controller frame)

$$\underline{v}_T^c = \begin{bmatrix} v_{Td}^c \\ v_{Tq}^c \end{bmatrix} \quad \simeq \underline{V}_T^c + \hat{\underline{v}}_T^c = \begin{bmatrix} V_{Td}^c \\ V_{Tq}^c \end{bmatrix} + \begin{bmatrix} \hat{v}_{Td}^c \\ \hat{v}_{Tq}^c \end{bmatrix}; \tag{5.6}$$

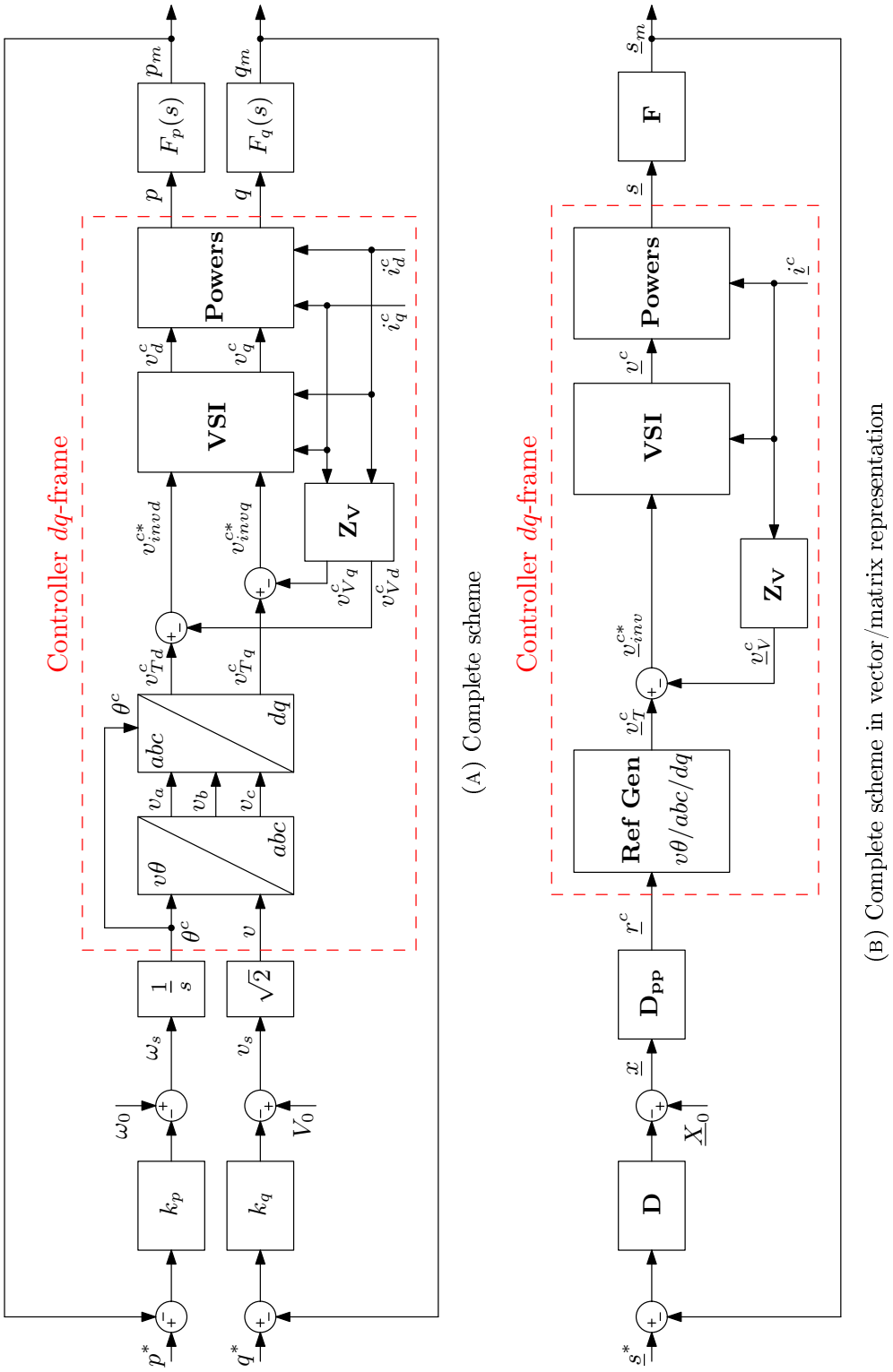

(A) Complete scheme

(B) Complete scheme in vector/matrix representation

FIGURE 5.2: Droop Control.

- the vector of the feedback term due to the virtual inductance (controller frame):

$$\underline{v}_V^c = \begin{bmatrix} v_{Vd}^c \\ v_{Vq}^c \end{bmatrix} \simeq \underline{V}_V^c + \hat{\underline{v}}_V^c = \begin{bmatrix} V_{Vd}^c \\ V_{Vq}^c \end{bmatrix} + \begin{bmatrix} \hat{v}_{Vd}^c \\ \hat{v}_{Vq}^c \end{bmatrix}; \tag{5.7}$$

- VSI references vector (controller frame):

$$\underline{v}_{inv}^{c*} = \begin{bmatrix} v_{invd}^{c*} \\ v_{invq}^{c*} \end{bmatrix} \simeq \underline{V}_{inv}^{c*} + \hat{\underline{v}}_{inv}^{c*} + \begin{bmatrix} V_{invd}^{c*} \\ V_{invq}^{c*} \end{bmatrix} + \begin{bmatrix} \hat{v}_{invd}^{c*} \\ \hat{v}_{invq}^{c*} \end{bmatrix}; \tag{5.8}$$

- output voltages vector (controller frame):

$$\underline{v}^c = \begin{bmatrix} v_d^c \\ v_q^c \end{bmatrix} \simeq \underline{V}^c + \hat{\underline{v}}^c = \begin{bmatrix} V_d^c \\ V_q^c \end{bmatrix} + \begin{bmatrix} \hat{v}_d^c \\ \hat{v}_q^c \end{bmatrix}; \tag{5.9}$$

- outcoming output currents vector (controller frame):

$$\underline{i}^c = \begin{bmatrix} i_d^c \\ i_q^c \end{bmatrix} \simeq \underline{I}^c + \hat{\underline{i}}^c = \begin{bmatrix} I_d^c \\ I_q^c \end{bmatrix} + \begin{bmatrix} \hat{i}_d^c \\ \hat{i}_q^c \end{bmatrix}; \tag{5.10}$$

- instant powers vector:

$$\underline{s} = \begin{bmatrix} p \\ q \end{bmatrix} \simeq \underline{S} + \hat{\underline{s}} = \begin{bmatrix} P \\ Q \end{bmatrix} + \begin{bmatrix} \hat{p} \\ \hat{q} \end{bmatrix}; \tag{5.11}$$

- filtered powers vector:

$$\underline{s}_m = \begin{bmatrix} p_m \\ q_m \end{bmatrix} \simeq \underline{S}_m + \hat{\underline{s}}_m = \begin{bmatrix} P \\ Q \end{bmatrix} + \begin{bmatrix} \hat{p}_m \\ \hat{q}_m \end{bmatrix}. \tag{5.12}$$

Some matrices are described:

- droop coefficient matrix:

$$\mathbf{D} = \begin{bmatrix} k_p & 0 \\ 0 & k_q \end{bmatrix}; \tag{5.13}$$

- the phase-peak matrix gives the angle θ^c from the angular frequency ω_s and the peak voltage from v:

$$\mathbf{D_{pp}} = \begin{bmatrix} \frac{1}{s} & 0 \\ 0 & \sqrt{2} \end{bmatrix}; \tag{5.14}$$

- the virtual impedance, if implementing a virtual inductance, can be expressed in the controller frame as:

$$\mathbf{Z_V^c} = \begin{bmatrix} sL_V & -\omega_s L_V \\ \omega_s L_V & sL_V \end{bmatrix}. \tag{5.15}$$

and the virtual impedance in steady-state condition is defined as:

$$\mathbf{Z_{V0}^c} = \begin{bmatrix} 0 & -\omega_s L_V \\ \omega_s L_V & 0 \end{bmatrix}; \tag{5.16}$$

- the power filters can be written in matrix form as:

$$\mathbf{F} = \begin{bmatrix} F_p(s) & 0 \\ 0 & F_q(s) \end{bmatrix}, \tag{5.17}$$

where the power filters are low pass filters in the form:

$$F_p(s) = F_q(s) = \frac{1}{\frac{s}{\omega_f} + 1} \quad . \tag{5.18}$$

In Appendix A the calculations to pass from angle and amplitude, to *abc*-frame and finally to *dq*-frame are performed. The final expressions in (A.7), considering a balanced system, can be expressed as in (A.11):

$$\begin{aligned} v_d(t) &= v(t)\sqrt{\frac{3}{2}} \cdot \cos\Big(\theta_S(t) - \theta_T(t)\Big) \\ v_q(t) &= v(t)\sqrt{\frac{3}{2}} \cdot \sin\Big(\theta_S(t) - \theta_T(t)\Big) \end{aligned} \tag{5.19}$$

5.4 Steady-State Analysis

The operating point is necessary to determine the *dq* output impedance of the droop-controlled inverter. The dependence on the operating point is verified when the impedance expressions exhibit steady-state voltages or currents or, in this case, also the system frequency. However, it is worth to precise that, in first approximation, not all the *dq*-impedances are operating point dependent. This is true for resistances, inductances or capacitances, where the operating point does not appear in the expressions and does not change the resulting small-signal impedance.

The reference scheme is reported in Fig. 5.3a. It is possible to determine the inductive-resistive load starting from the desired output powers, or vice versa. The voltage V_s and the angular frequency ω_s due to the droop control can be calculated from the active P and the reactive Q load powers as:

$$\begin{aligned} \underline{X} &= \underline{X}_0 - \mathbf{D} \cdot (\underline{S}^* - \underline{S}) = \\ \begin{bmatrix} \omega_s \\ V_s \end{bmatrix} &= \begin{bmatrix} \omega_0 \\ V_0 \end{bmatrix} - \begin{bmatrix} k_p & 0 \\ 0 & k_q \end{bmatrix} \cdot \left(\begin{bmatrix} P^* \\ Q^* \end{bmatrix} - \begin{bmatrix} P \\ Q \end{bmatrix} \right) \end{aligned} \tag{5.20}$$

where $\underline{S}^*$ indicates the power references, $\underline{S}$ indicates the steady-state active and reactive load powers. The current vector $\underline{I}^c$ can be easily determined by:

$$\underline{I}^c = (\mathbf{Z_{RL}} + \mathbf{Z_{LL}})^{-1} \cdot \underline{V}^c \tag{5.21}$$

The series load impedance is defined in the system frame as:

$$\mathbf{Z^s_{Ltot}}(s) = \mathbf{Z^s_{RL}}(s) + \mathbf{Z^s_{LL}}(s) = \begin{bmatrix} R_L + sL_L & -\omega_s L_L \\ \omega_s L_L & R_L + sL_L \end{bmatrix} \tag{5.22}$$

The steady-state condition in dq-frame results in $s = 0$, therefore:

$$\mathbf{Z^s_{Ltot}}(0) = \mathbf{Z^s_{Ltot}}(s)\big|_{s=0} = \begin{bmatrix} R_L & -\omega_s L_L \\ \omega_s L_L & R_L \end{bmatrix} \tag{5.23}$$

In steady-state condition, the system and the controller frame are only phase-shifted. As aforementioned, resistances and inductances do not depend on the operating point and:

$$\mathbf{Z^c_{Ltot}}(0) = \mathbf{Z^s_{Ltot}}(0) \tag{5.24}$$

Hence, the voltage vector $\underline{V}^c$ at the inverter terminals can be expressed as:

$$\underline{V}^c = \mathbf{Z^c_{Ltot}}(0) \cdot \left[\mathbf{Z^c_V}(0) + \mathbf{Z^c_{Ltot}}(0)\right]^{-1} \cdot \underline{V}^{c*}_{inv} \tag{5.25}$$

Can be found from Fig. 5.3a that $\underline{V}^{c*}_{inv} = \mathbf{f}(V_s)$, while $\underline{V}^c = [V^c_d, V^c_q]^T = \mathbf{f}(\omega_s, V_s, R_L, L_L)$. It is now possible to apply the expressions just determined in (5.25) for V^c_d and V^c_q in the following expression to determine the power:

$$\underline{S} = \begin{bmatrix} V^c_d & V^c_q \\ V^c_q & -V^c_d \end{bmatrix} \cdot \underline{I}^c = \begin{bmatrix} V^c_d & V^c_q \\ V^c_q & -V^c_d \end{bmatrix} \cdot (\mathbf{Z_{Ltot}(0)})^{-1} \cdot \begin{bmatrix} V^c_d \\ V^c_q \end{bmatrix} \tag{5.26}$$

Finally, isolating the terms R_L and L_L from this last system of equations, it is possible to get the final values:

$$\begin{aligned} R_L &= -\frac{3PV_s^2 \cdot [\omega_s^2 L_V^2 (P^2+Q^2) - 9V_s^4]}{(P^2+Q^2) \cdot [\omega_s^2 L_V^2 (P^2+Q^2) - 6\omega_s L_V Q V_s^2 + 9V_s^4]} \\ L_L &= -\frac{[\omega_s L_V (P^2+Q^2) - 3QV_s^2] \cdot [\omega_s^2 L_V^2 (P^2+Q^2) - 9V_s^4]}{\omega_s \cdot (P^2+Q^2) \cdot [\omega_s^2 L_V^2 (P^2+Q^2) - 6\omega_s L_V Q V_s^2 + 9V_s^4]} \end{aligned} \tag{5.27}$$

Applying these resistance and inductance in the simulation model it is then possible to obtain the desired active and reactive power levels, which result in specific system frequency, voltages and currents calculated in the following section.

5.4.1 Steady-state voltages and currents

In this section, the steady-state operating point is determined neglecting the inner dynamics of the VSI, since for steady-state condition the reference-to-output voltage transfer function is unitary for both d- and q-axes, while the output impedance is negligible. A generic virtual decoupling impedance $\mathbf{Z_V^c} \neq \mathbf{0}$ is considered. Once determined the steady-state voltage amplitude V_s from the droop control, it is possible to write the voltage vector after the transformation:

$$\underline{V}_T^c = \mathbf{T^c} \cdot \mathbf{D_{pp}} \cdot \underline{X} = \begin{bmatrix} \sqrt{3}V_s \\ 0 \end{bmatrix} \tag{5.28}$$

where

$$\mathbf{T^c} = \sqrt{\frac{3}{2}} \begin{bmatrix} 0 & 1 \\ 0 & 0 \end{bmatrix} \tag{5.29}$$

To determine the voltage vector $\underline{V}_{inv}^{c*} = \underline{V}^c$ it is necessary to calculate first the current vector $\underline{I}^c$ and then consider the virtual impedance $\mathbf{Z_V^c}$:

$$\begin{aligned} \underline{I}^c &= (\mathbf{Z_V^c} + \mathbf{Z_{Ltot}^c})^{-1} \cdot \underline{V}_T^c \\ \underline{V}^c &= \mathbf{Z_{Ltot}^c} \cdot \underline{I}^c = \mathbf{Z_{Ltot}^c} \cdot (\mathbf{Z_V^c} + \mathbf{Z_{Ltot}^c})^{-1} \cdot \underline{V}_T^c \end{aligned} \tag{5.30}$$

where the vectors $\underline{V}^c$ and $\underline{I}^c$ are defined in (5.9) and (5.10), respectively. The operating point $(\underline{V}^c, \underline{I}^c)$ is determined and it can be used in the output impedance expressions.

5.4.2 Steady-state phase shift and rotational matrix

The exact value of the phase-shift is necessary, in order to perform the correct transformations in both steady-state and perturbed models. Hence, from the steady-state voltages and currents it is possible to determine the phase shift ϕ:

- for $\mathbf{Z_V^c = 0}$ the phase shift is zero: $\phi = 0$. The system and controller frames are superimposed before the IMU injection. When a perturbation is applied from the IMU, the controller frame d^c- and q^c-axes start to oscillate with a perturbation $\hat{\theta}$ around the system frame d^s- and q^s-axes with null constant phase shift;
- for $\mathbf{Z_V^c \neq 0}$ the phase shift is non null: $\phi \neq 0$. The alignment condition to a dq-frame is achieved when the q component of the voltage becomes zero. Therefore, the phase shift between system and controller frame can be determined from the steady-state voltages $\underline{V}^c$ in (5.30) as:

$$\phi = -\arctan \frac{V_q^c}{V_d^c} \tag{5.31}$$

Considering the phase-shift just calculated, it is then possible to define the rotational matrix as:

$$\mathbf{R} = \begin{bmatrix} \cos\phi & -\sin\phi \\ \sin\phi & \cos\phi \end{bmatrix} \quad , \quad \mathbf{R}^{-1} = \mathbf{R}^T = \begin{bmatrix} \cos\phi & \sin\phi \\ -\sin\phi & \cos\phi \end{bmatrix} \tag{5.32}$$

and finally perform the frame changing for the steady-state quantities as:

$$\begin{aligned} \underline{V}^s &= \mathbf{R} \cdot \underline{V}^c \quad , \quad \underline{I}^s = \mathbf{R} \cdot \underline{I}^c \\ \underline{V}^c &= \mathbf{R}^T \cdot \underline{V}^s \quad , \quad \underline{I}^c = \mathbf{R}^T \cdot \underline{I}^s \end{aligned} \tag{5.33}$$

The transformation is valid for all the steady-state voltages and the currents in the system.

5.5 Output Impedance $\mathbf{Z_{o,DC}^c}$ in the Controller Frame

The impedance calculation complexity can be very different in a frame with respect to another one. This essentially is due to the current and voltage transformations, due to the phase shift and the angle perturbation between the system and controller frames. In the case presented hereafter, it can be observed that

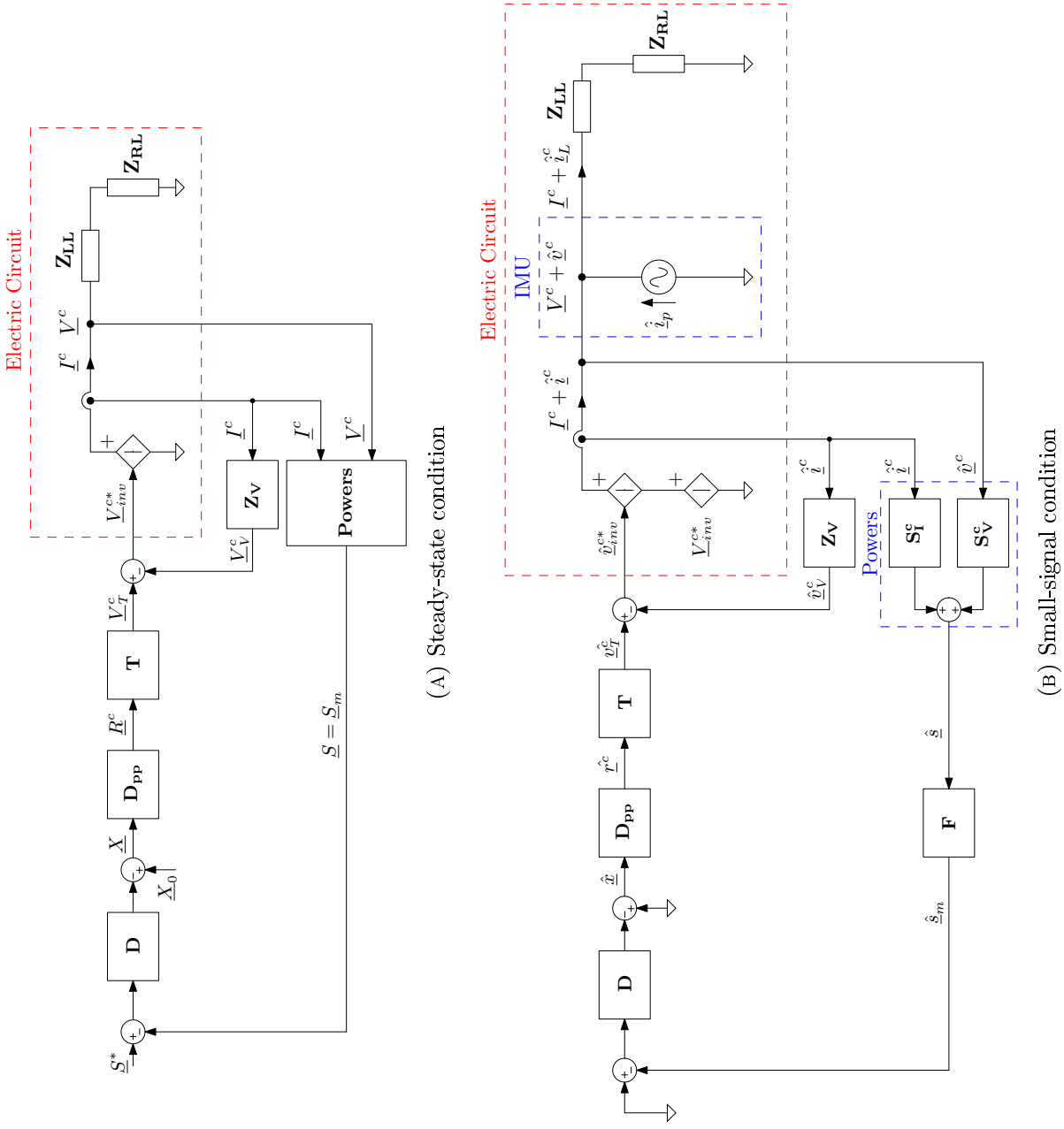

FIGURE 5.3: Electrical schemes with steady-state and small-signal controls applied.

the impedances calculated in the controller frame result less complicated compared to the same impedances expressed in the system frame. In order to perform the output impedance calculation in the controller all the missing matrices in the small-signal sense have to be determined:

- the transformation to obtain $\underline{v}_T^c$ from $\underline{r}^c$ is nonlinear due to the sine and cosine functions. Perturbing both the angle and the amplitude as in (A.18), it is possible to obtain the small-signal transfer function matrix between $\underline{v}_T^{c*}$ and $\underline{r}^c$:

$$\mathbf{T^c} = \sqrt{\frac{3}{2}} \begin{bmatrix} 0 & 1 \\ 0 & 0 \end{bmatrix} \tag{5.34}$$

  which is equal to the one used to determine the steady-state condition in (5.29);

- the powers can be expressed in a matrix form as:

$$\begin{aligned} \underline{s} = \underline{S} + \hat{\underline{s}} = \begin{bmatrix} P \\ Q \end{bmatrix} + \begin{bmatrix} \hat{p} \\ \hat{e} \end{bmatrix} = \\ = \begin{bmatrix} V_d^c & V_q^c \\ V_q^c & -V_d^c \end{bmatrix} \cdot \begin{bmatrix} I_d^c \\ I_q^c \end{bmatrix} + \begin{bmatrix} V_d^c & V_q^c \\ V_q^c & -V_d^c \end{bmatrix} \cdot \begin{bmatrix} \hat{i}_d^c \\ \hat{i}_q^c \end{bmatrix} + \begin{bmatrix} I_d^c & I_q^c \\ -I_q^c & I_d^c \end{bmatrix} \cdot \begin{bmatrix} \hat{v}_d^c \\ \hat{v}_q^c \end{bmatrix} \end{aligned} \tag{5.35}$$

  The steady-state powers can be expressed from the controller frame as:

$$\underline{S} = \begin{bmatrix} V_d^c & V_q^c \\ V_q^c & -V_d^c \end{bmatrix} \cdot \begin{bmatrix} I_d^c \\ I_q^c \end{bmatrix} \tag{5.36}$$

  and the perturbed powers

$$\hat{\underline{s}} = \underbrace{\begin{bmatrix} V_d^c & V_q^c \\ V_q^c & -V_d^c \end{bmatrix}}_{\mathbf{S_I^c}} \cdot \begin{bmatrix} \hat{i}_d^c \\ \hat{i}_q^c \end{bmatrix} + \underbrace{\begin{bmatrix} I_d^c & I_q^c \\ -I_q^c & I_d^c \end{bmatrix}}_{\mathbf{S_V^c}} \cdot \begin{bmatrix} \hat{v}_d^c \\ \hat{v}_q^c \end{bmatrix} \tag{5.37}$$

  are expressed in terms of voltage and current perturbations. The matrices $\mathbf{S_V^c}$ and $\mathbf{S_I^c}$ provide the operating point.

In Fig. 5.4a the representation of the small-signal control scheme in the controller frame is shown. The goal is to represent the system in order to determine the output impedance from the voltage $\hat{\underline{v}}^c$ and current $\hat{\underline{i}}^c$ perturbations. In Fig. 5.4b the control scheme is oriented in order to easily calculate the output impedance, giving as input the current perturbations and the voltage perturbations as output.

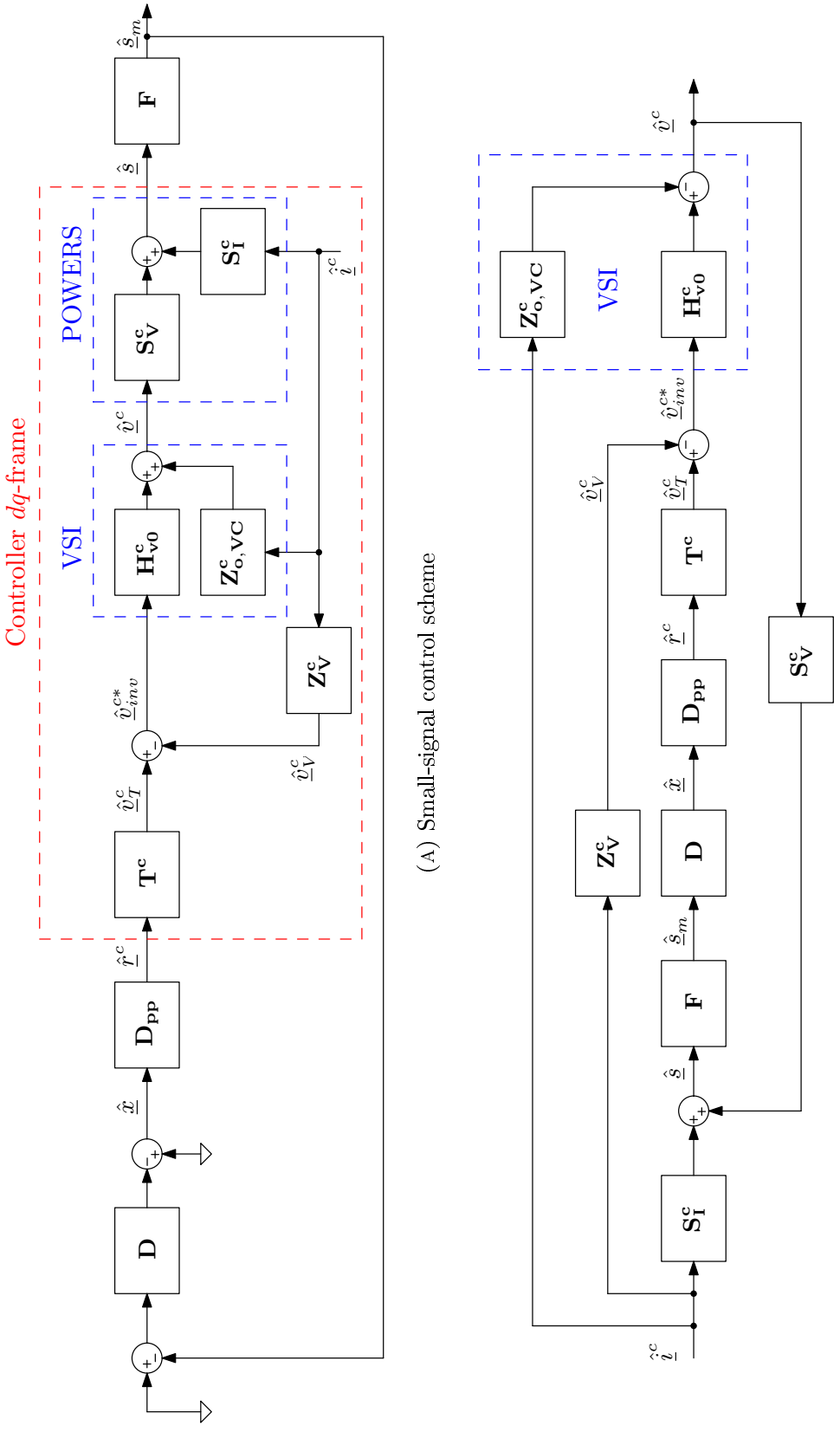

(A) Small-signal control scheme

(B) Revised scheme for controller frame

FIGURE 5.4: Small-signal equivalent scheme of the Droop Control.

The output impedance of the droop-controlled inverter in the controller dq-frame is then defined as:

$$\underline{\hat{v}}^c = \mathbf{Z^c_{o,DC}} \cdot \underline{\hat{i}}^c \tag{5.38}$$

Considering an ideal inverter ($\mathbf{H_{v0}} = \mathbf{1}$, $\mathbf{Z_{o,VC}} = \mathbf{0}$), the output impedance of the droop-controlled (DC) inverter in the controller frame can be calculated as:

$$\mathbf{Z^c_{o,DC}} = -\left[\mathbf{I} - \mathbf{L^c} \cdot \mathbf{S^c_V}\right]^{-1} \cdot \left[\mathbf{L^c} \cdot \mathbf{S^c_I} - \mathbf{Z^c_V}\right] \tag{5.39}$$

where $\mathbf{L^c} = \mathbf{T^c} \cdot \mathbf{D_{pp}} \cdot \mathbf{D} \cdot \mathbf{F}$ and the negative sign is added, since the currents $\underline{\hat{i}}^c$ are considered as outcoming currents.

Considering a non ideal inverter ($\mathbf{H_{v0}} \neq \mathbf{1}$, $\mathbf{Z_{o,VC}} \neq \mathbf{0}$), the output impedance of the droop-controlled (DC) inverter in the controller frame can be calculated as:

$$\mathbf{Z^c_{o,DC}} = -\left[\mathbf{I} - \mathbf{H^c_{v0}} \cdot \mathbf{L^c} \cdot \mathbf{S^c_V}\right]^{-1} \cdot \left[\mathbf{H^c_{v0}} \cdot \left(\mathbf{L^c} \cdot \mathbf{S^c_I} - \mathbf{Z^c_V}\right) - \mathbf{Z^c_{o,VC}}\right] \tag{5.40}$$

where the minus sign is considered, since the currents $\underline{\hat{i}}^c$ are outcoming currents. The main problem is that the determination of $\mathbf{H^c_{v0}}$ and $\mathbf{Z^c_{o,VC}}$ is difficult to determine.

5.5.1 Null virtual impedance $\mathbf{Z^c_V} = \mathbf{0}$ with ideal inverter

In this section, the virtual impedance $\mathbf{Z^c_V}$ generated by the inverter control is considered null, and it results in a null phase shift angle $\phi = 0$. An ideal inverter is considered ($\mathbf{H_{v0}} = \mathbf{1}$, $\mathbf{Z_{o,VC}} = \mathbf{0}$). One can derive the ouptut impedance as:

$$\mathbf{Z^c_{o,DC}} = \frac{\sqrt{3} k_q \omega_f}{s + \omega_f \left(1 + \sqrt{3} I^c_q k_q\right)} \cdot \begin{bmatrix} -V^c_q & V^c_d \\ 0 & 0 \end{bmatrix} \tag{5.41}$$

In Fig. 5.3a it is clear that, for $\mathbf{Z_V} = \mathbf{0}$, the system frame used by the IMU and the controller frame used by the inverter are aligned. This means that the two frames, in steady-state condition, are equivalent and superimposed. The IMU synchronization results in a null q component of the voltage, hence:

$$V^s_q \overset{\phi=0}{=} V^c_q = 0 \tag{5.42}$$

which forces the term in the dd-channel in (5.41) to be zero as

$$\mathbf{Z^c_{o,DC}} = \frac{\sqrt{3} k_q \omega_f}{s + \omega_f \left(1 + \sqrt{3} I^c_q k_q\right)} \cdot \begin{bmatrix} 0 & V^c_d \\ 0 & 0 \end{bmatrix} \tag{5.43}$$

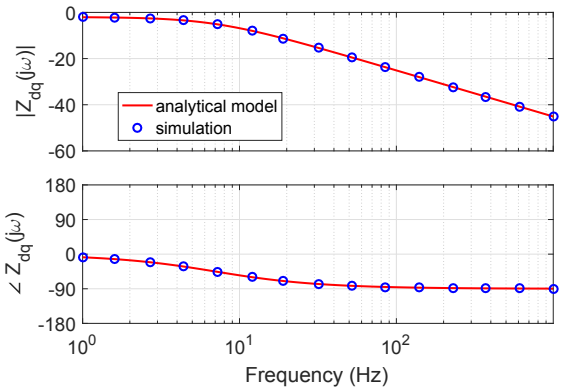

FIGURE 5.5: Droop Control: output impedances $\mathbf{Z^c_{o,DC}}$ in the controller dq-frame with $\mathbf{Z^c_V} = \mathbf{0}$.

Therefore, the output impedances of the droop-controlled inverter determined in the controller dq-frame are all zero except for the dq-channel component. The simulation results can be observed in Fig. 5.5. There is a good matching between the analytical model of the Z_{dq} component and the simulation results. The other impedances in the matrix are zero, as expected.

The final expression of this impedance presents a very simple transfer function, consisting on a first order low pass filter. The cutoff frequency of this transfer function is related to the power filter bandwidth ω_f, while the current I^c_q and the Q/V droop coefficient contribution is almost negligible.

5.5.2 Non null virtual impedance $\mathbf{Z^c_V} \neq \mathbf{0}$ with ideal inverter

The virtual impedance is defined in the controller frame as:

$$\mathbf{Z^c_V} = \begin{bmatrix} \frac{sL_V}{\frac{s}{\omega_V}+1} & -\omega_s L_V \\ \omega_s L_V & \frac{sL_V}{\frac{s}{\omega_V}+1} \end{bmatrix} \tag{5.44}$$

where L_V is the inductance value, ω_V is the bandwidth of the first order low pass filter to limit the derivative effect and ω_s is the system frequency. Therefore the virtual impedance $\mathbf{Z^c_V}$ is emulating an inductive behavior, which provides the power loops decoupling and allows the droop control to work properly even when the load is not inductive.

The final expression of the droop-controlled output impedance with $\mathbf{Z_V^c} \neq \mathbf{0}$ can be determined as:

$$\begin{aligned}
Z^c_{o,DC_{dd}} &= \frac{(\omega_V L_V)\, s^2 + \left(\omega_f \omega_V L_V \left(1 + \sqrt{3} I_d^c k_q \omega_s\right)\right) s + \left(\sqrt{3} I_d^c k_q \omega_s \omega_f \omega_V L_V\right)}{s^2 + \left(\omega_V + \omega_f \left(1 + \sqrt{3} I_q^c k_q\right)\right) s + \left(\omega_V \omega_f \left(1 + \sqrt{3} I_q^c k_q\right)\right)} \\
Z^c_{o,DC_{dq}} &= \frac{(-\omega_s L_V)\, s^2 + \left(\sqrt{3} V_d^c k_q \omega_f - \omega_V \omega_f \omega_s L_V (\omega_f - \omega_V)\right) s + \left(-\omega_V \omega_f (L_V \omega_s + \sqrt{3} V_d^c k_q)\right)}{s^2 + \left(\omega_V + \omega_f \left(1 + \sqrt{3} I_q^c k_q\right)\right) s + \left(\omega_V \omega_f \left(1 + \sqrt{3} I_q^c k_q\right)\right)} \\
Z^c_{o,DC_{qd}} &= \omega_s L_V \\
Z^c_{o,DC_{qq}} &= \frac{(L_V)\, s}{\frac{s}{\omega_V} + 1}
\end{aligned} \tag{5.45}$$

where $V_q^c = V_q^s = 0$ because of the IMU alignment.

The *dd* and *dq* impedances have the same denominator which can be simplified, since $k_q \ll 1$, to:

$$s^2 + (\omega_V + \omega_f)\, s + (\omega_V \omega_f) \tag{5.46}$$

where the cutoff frequency and the damping factor are both determined by ω_f and ω_V.

The *qd* and *qq* impedances are the same components of the virtual impedance $\mathbf{Z_V^c}$ defined in (5.44). Analytical model and simulation results are compared in Fig. 5.6, where a good match is achieved for all the impedances.

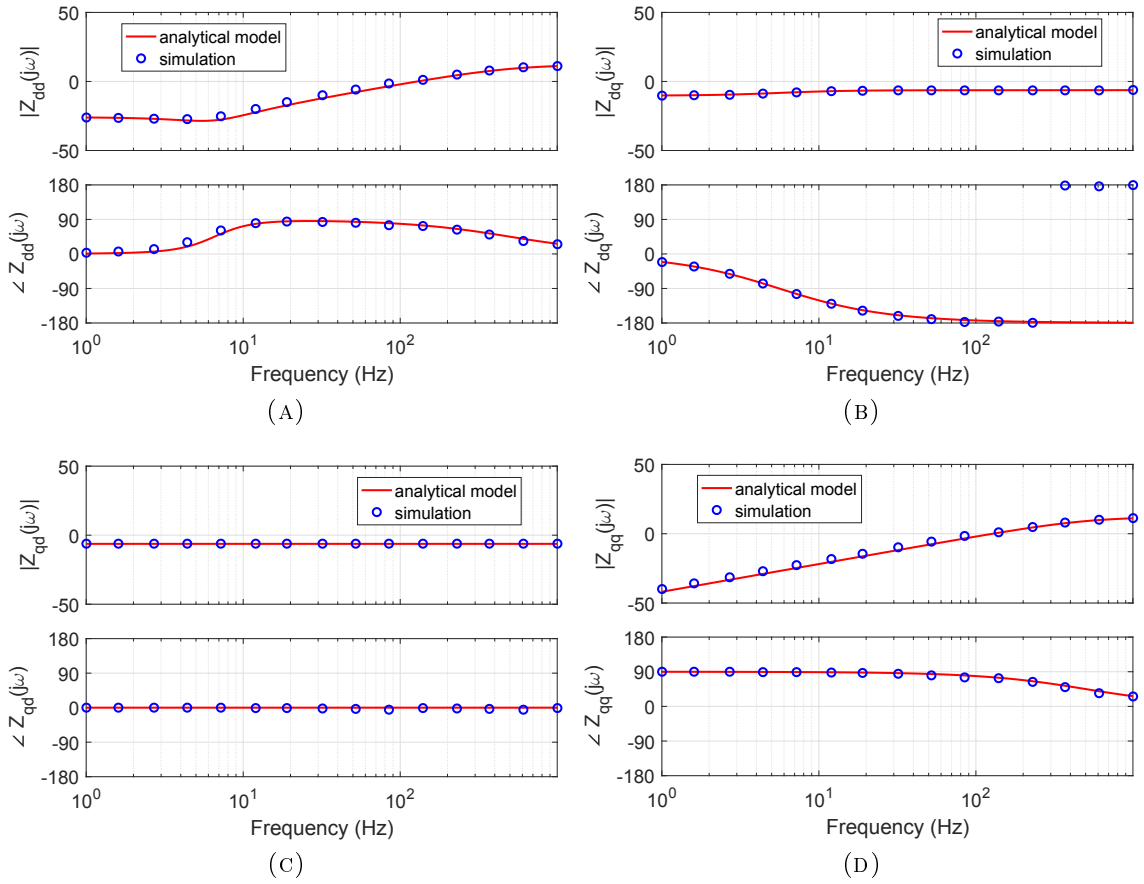

FIGURE 5.6: Droop Control: output impedances $\mathbf{Z^c_{o,DC}}$ in the controller dq-frame with $\mathbf{Z_V} \neq \mathbf{0}$.

5.6 Output Impedance $\mathbf{Z^s_{o,DC}}$ in the System Frame

It is possible to determine the output impedance in the system frame considering that only some of the terms are changing in the final expression. In fact, all the matrices where there is a manipulation of the power perturbations are not going to vary. This is essentially because the powers do not depend on the chosen frame. The matrices in the small-signal sense for the system frame are:

- the transformation to obtain $\underline{v}^s_T$ from $\underline{r}^s = [\theta^s, v]^T$ is nonlinear due to the sine and cosine functions. Perturbing both the angle and the amplitude as in (A.16), it is possible to obtain the small-signal transfer function matrix between $\underline{v}^{s*}_T$ and $\underline{r}^s$:

$$\mathbf{T^s} = \sqrt{\frac{3}{2}} \begin{bmatrix} -\sqrt{2}V_s \sin(\phi) & \cos(\phi) \\ \sqrt{2}V_s \cos(\phi) & \sin(\phi) \end{bmatrix} \tag{5.47}$$

  where $V = \sqrt{2}V_s$. For $\mathbf{Z_V} = \mathbf{0}$, $\phi = 0$ and:

$$\mathbf{T^s}\big|_{\phi=0} = \sqrt{\frac{3}{2}} \begin{bmatrix} 0 & 1 \\ \sqrt{2}V_s & 0 \end{bmatrix} \tag{5.48}$$

- as reported in (5.35) for the controller frame, the powers can be expressed in a matrix form in the system frame as:

$$\begin{aligned} \underline{s} = \underline{S} + \hat{\underline{s}} = \begin{bmatrix} P \\ Q \end{bmatrix} + \begin{bmatrix} \hat{p} \\ \hat{e} \end{bmatrix} = \\ = \begin{bmatrix} V^s_d & V^s_q \\ V^s_q & -V^s_d \end{bmatrix} \cdot \begin{bmatrix} I^s_d \\ I^s_q \end{bmatrix} + \begin{bmatrix} V^s_d & V^s_q \\ V^s_q & -V^s_d \end{bmatrix} \cdot \begin{bmatrix} \hat{i}^s_d \\ \hat{i}^s_q \end{bmatrix} + \begin{bmatrix} I^s_d & I^s_q \\ -I^s_q & I^s_d \end{bmatrix} \cdot \begin{bmatrix} \hat{v}^s_d \\ \hat{v}^s_q \end{bmatrix} \end{aligned} \tag{5.49}$$

  The steady-state powers can be expressed from the system frame as:

$$\underline{S} = \begin{bmatrix} V^s_d & V^s_q \\ V^s_q & -V^s_d \end{bmatrix} \cdot \begin{bmatrix} I^s_d \\ I^s_q \end{bmatrix} \tag{5.50}$$

  and the perturbed powers as

$$\hat{\underline{s}} = \underbrace{\begin{bmatrix} V^s_d & V^s_q \\ V^s_q & -V^s_d \end{bmatrix}}_{\mathbf{S^s_I}} \cdot \begin{bmatrix} \hat{i}^s_d \\ \hat{i}^s_q \end{bmatrix} + \underbrace{\begin{bmatrix} I^s_d & I^s_q \\ -I^s_q & I^s_d \end{bmatrix}}_{\mathbf{S^s_V}} \cdot \begin{bmatrix} \hat{v}^s_d \\ \hat{v}^s_q \end{bmatrix} \tag{5.51}$$

are expressed in terms of voltage and current perturbations. The matrices $\mathbf{S^s_V}$ and $\mathbf{S^s_I}$ provide the operating point.

Instead of the virtual decoupling impedance $\mathbf{Z^c_V}$ defined in (5.44), the decoupling effect is provided by a physical impedance $\mathbf{Z^s_D}$, whose expression is:

$$\mathbf{Z^s_D} = \begin{bmatrix} sL_D & -\omega_s L_D \\ \omega_s L_D & sL_D \end{bmatrix} \tag{5.52}$$

The output impedance of the droop-controlled inverter in the controller *dq*-frame is defined as:

$$\underline{\hat{v}}^s = \mathbf{Z^s_{o,DC}} \cdot \underline{\hat{i}}^s \tag{5.53}$$

Considering an ideal inverter ($\mathbf{H^s_{v0}} = \mathbf{1}$, $\mathbf{Z^s_{o,VC}} = \mathbf{0}$), the output impedance of the droop-controlled (DC) inverter in the system frame can be calculated from Fig. 5.8 as:

$$\mathbf{Z^s_{o,DC}} = -\left[\mathbf{I} - \mathbf{L^s} \cdot \mathbf{S^s_V}\right]^{-1} \cdot \left[\mathbf{L^s} \cdot \mathbf{S^s_I} - \mathbf{Z^s_D}\right] \tag{5.54}$$

where $\mathbf{L^s} = \mathbf{T^s} \cdot \mathbf{D_{pp}} \cdot \mathbf{D} \cdot \mathbf{F}$ and the negative sign is considered, since the currents $\underline{\hat{i}}^s$ are considered as outcoming currents.

Considering a non ideal inverter ($\mathbf{H^s_{v0}} \neq \mathbf{1}$, $\mathbf{Z^s_{o,VC}} \neq \mathbf{0}$), the output impedance of the droop-controlled (DC) inverter in the system frame can be calculated from Fig. 5.8 as:

$$\mathbf{Z^s_{o,DC}} = -\left[\mathbf{I} - \mathbf{H_{v0}} \cdot \mathbf{L^s} \cdot \mathbf{S^s_V}\right]^{-1} \cdot \left[\mathbf{H_{v0}} \cdot \left(\mathbf{L^s} \cdot \mathbf{S^s_I}\right) - \mathbf{Z_{o,VC}}\right] \tag{5.55}$$

where the minus sign is considered, since the currents $\underline{\hat{i}}^s$ are outcoming currents.

5.6.1 Null physical decoupling impedance $\mathbf{Z^s_D} = \mathbf{0}$ with ideal inverter

From (5.54) it is possible to compute the calculations to get the expression of the output impedance $\mathbf{Z^s_{o,DC}}$ in the system frame:

$$\mathbf{Z^s_{o,DC}} = -\left[\mathbf{I} - \mathbf{L^s} \cdot \mathbf{S^s_V}\right]^{-1} \cdot \left[\mathbf{L^s} \cdot \mathbf{S^s_I}\right]$$

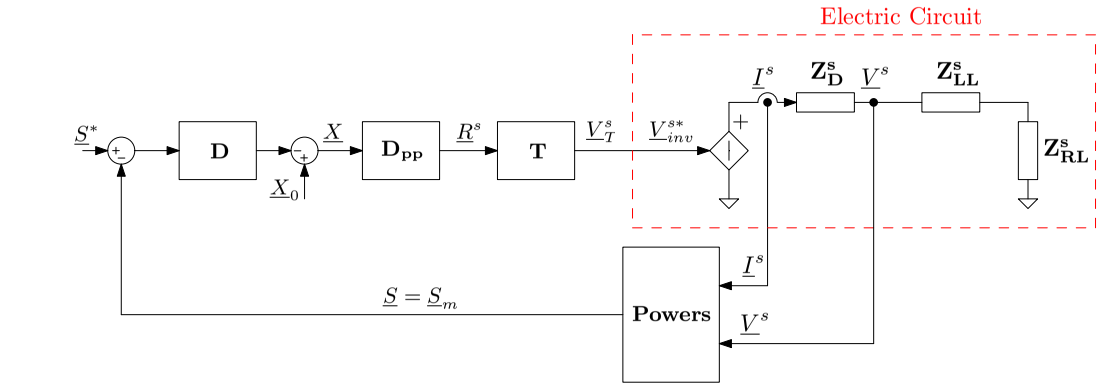

(A) Steady-state condition

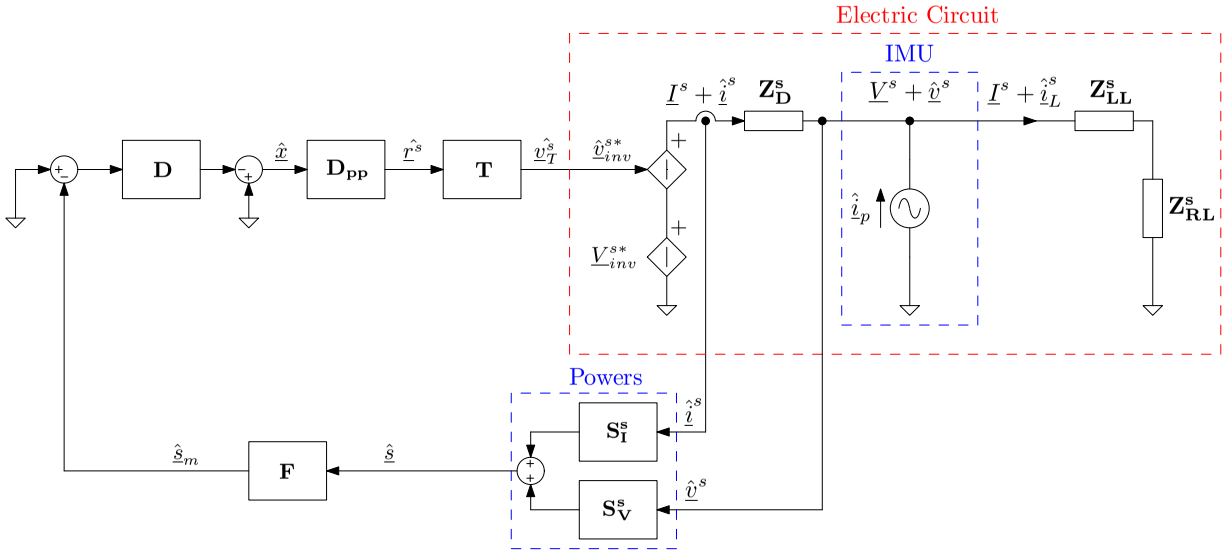

(B) Small-signal condition

FIGURE 5.7: Electrical schemes with steady-state and small-signal representations for the droop-controlled inverter. The physical decoupling inductance $\mathbf{Z_D^s}$ is applied in series with the inverter.

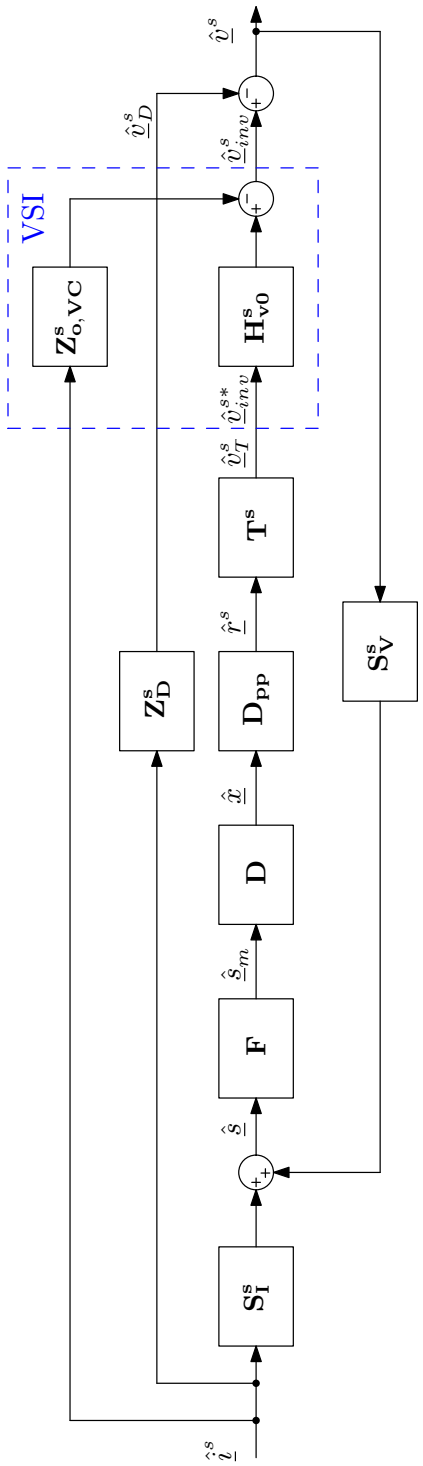

FIGURE 5.8: Small-signal equivalent scheme of the Droop Control in the system frame.

and elaborating the expressions, one can get:

$$
\begin{aligned}
Z^s_{o,DC\,dd} &= k_{dd}\frac{1}{\left(-\frac{1}{b_{dd}}\right)s^3+\left(\frac{-\omega_f(2+\sqrt{3}Iq_sk_q)}{b_{dd}}\right)s^2+\left(\frac{\sqrt{3}I^s_q\omega_f(k_pV_s-k_q\omega_f)-\omega_f^2}{b_{dd}}\right)s+1}\\
Z^s_{o,DC\,dq} &= k_{dq}\frac{\left(\frac{-\sqrt{3}V^s_dk_q\omega_f}{a_{dq}}\right)s^2+\left(\frac{-\sqrt{3}V^s_dk_q\omega_f^2}{a_{dq}}\right)s+1}{\left(-\frac{1}{b_{dd}}\right)s^3+\left(\frac{-\omega_f(2+\sqrt{3}Iq_sk_q)}{b_{dd}}\right)s^2+\left(\frac{\sqrt{3}I^s_q\omega_f(k_pV_s-k_q\omega_f)-\omega_f^2}{b_{dd}}\right)s+1}\\
Z^s_{o,DC\,qd} &= k_{qd}\frac{\left(\frac{\sqrt{3}V^s_dV_sk_p\omega_f}{a_{qd}}\right)s+1}{\left(-\frac{1}{b_{dd}}\right)s^3+\left(\frac{-\omega_f(2+\sqrt{3}Iq_sk_q)}{b_{dd}}\right)s^2+\left(\frac{\sqrt{3}I^s_q\omega_f(k_pV_s-k_q\omega_f)-\omega_f^2}{b_{dd}}\right)s+1}\\
Z^s_{o,DC\,qq} &= k_{qq}\frac{1}{\left(-\frac{1}{b_{dd}}\right)s^3+\left(\frac{-\omega_f(2+\sqrt{3}Iq_sk_q)}{b_{dd}}\right)s^2+\left(\frac{\sqrt{3}I^s_q\omega_f(k_pV_s-k_q\omega_f)-\omega_f^2}{b_{dd}}\right)s+1}
\end{aligned}
\tag{5.56}
$$

where

$$
\begin{aligned}
b_{dd} &= \sqrt{3}V_sk_p\omega_f^2\left[\sqrt{3}k_q(I_q^{s2}+I_q^{s2})+I_q^s\right]\\
a_{dd} &= a_{dq} = -a_{qq} = 3I^s_dV^s_dV_sk_pk_q\omega_f^2\\
a_{qd} &= \sqrt{3}V^s_dV_sk_p\omega_f^2(1+\sqrt{3}I^s_qk_q)
\end{aligned}
\tag{5.57}
$$

and

$$
\begin{aligned}
k_{dd} = k_{dq} = -k_{qq} &= \frac{a_{dd}}{b_{dd}} = \frac{\sqrt{3}I^s_dV^s_dk_q}{\sqrt{3}k_q(I_q^{s2}+I_q^{s2})+I_q^s}\\
k_{qd} &= \frac{a_{qd}}{b_{dd}} = \frac{V^s_d(1+\sqrt{3}I^s_qk_q)}{\sqrt{3}k_q(I_q^{s2}+I_q^{s2})+I_q^s} \overset{k_q\ll 1}{\simeq} \frac{V^s_d}{\sqrt{3}k_q(I_q^{s2}+I_q^{s2})+I_q^s}
\end{aligned}
\tag{5.58}
$$

Can be noticed that gains depend on the current and voltage steady-state values.

Considering that the droop coefficients are very small values, $k_p \ll 1$ and $k_q \ll 1$, the expressions can be simplified as:

$$\begin{aligned}
Z^s_{o,DC_{dd}} &\overset{k_p\ll1,k_q\ll1}{=} k_{dd}\frac{1}{\left(-\frac{1}{b_{dd}}\right)s^3+\left(\frac{-2\omega_f}{b_{dd}}\right)s^2+\left(\frac{-\omega_f^2}{b_{dd}}\right)s+1}\\
Z^s_{o,DC_{dq}} &\overset{k_p\ll1,k_q\ll1}{=} k_{dq}\frac{\left(\frac{-\sqrt{3}V_d^s k_q\omega_f}{a_{dq}}\right)s^2+\left(\frac{-\sqrt{3}V_d^s k_q\omega_f^2}{a_{dq}}\right)s+1}{\left(-\frac{1}{b_{dd}}\right)s^3+\left(\frac{-2\omega_f}{b_{dd}}\right)s^2+\left(\frac{-\omega_f^2}{b_{dd}}\right)s+1}\\
Z^s_{o,DC_{qd}} &\overset{k_p\ll1,k_q\ll1}{=} k_{qd}\frac{\left(\frac{1}{\omega_f}\right)s+1}{\left(-\frac{1}{b_{dd}}\right)s^3+\left(\frac{-2\omega_f}{b_{dd}}\right)s^2+\left(\frac{-\omega_f^2}{b_{dd}}\right)s+1}\\
Z^s_{o,DC_{qq}} &\overset{k_p\ll1,k_q\ll1}{=} k_{qq}\frac{1}{\left(-\frac{1}{b_{dd}}\right)s^3+\left(\frac{-2\omega_f}{b_{dd}}\right)s^2+\left(\frac{-\omega_f^2}{b_{dd}}\right)s+1}
\end{aligned} \tag{5.59}$$

From these simplified expression is then possible to determine in an easier way the poles of the system:

$$\begin{aligned}
\omega_{p1} &= \sqrt{3}V_s k_p\left[\sqrt{3}k_q(I_q^{s2}+I_q^{s2})+I_q^s\right]\\
\omega_{p2} &\simeq \omega_f
\end{aligned} \tag{5.60}$$

and the denominator can be expressed as:

$$d(s)=\left(-\frac{1}{b_{dd}}\right)s^3+\left(\frac{-2\omega_f}{b_{dd}}\right)s^2+\left(\frac{-\omega_f^2}{b_{dd}}\right)s+1=(s+\omega_{p1})(s+\omega_{p2})^2 \tag{5.61}$$

Hence, all the impedances in Fig.5.9, present a low frequency pole due to the operating point, the droop coefficients and the power filter cutoff frequency. Moreover, a double pole around ω_f is found.

To complete the analysis with poles and zeros, the zeros of the impedances $Z^s_{o,DC_{dq}}$

$$\begin{aligned}
\omega_{z1,dq} &\simeq -I_q^s V_s k_p\\
\omega_{z2,dq} &\simeq \omega_f
\end{aligned} \tag{5.62}$$

and $Z^s_{o,DC_{qd}}$

$$\omega_{z1,qd}=\omega_f \tag{5.63}$$

are determined. Finally, after canceling out the zero-pole couples in the dq-channel and in the qd-channel impedance, the expressions of the impedances can be collected in the following table:

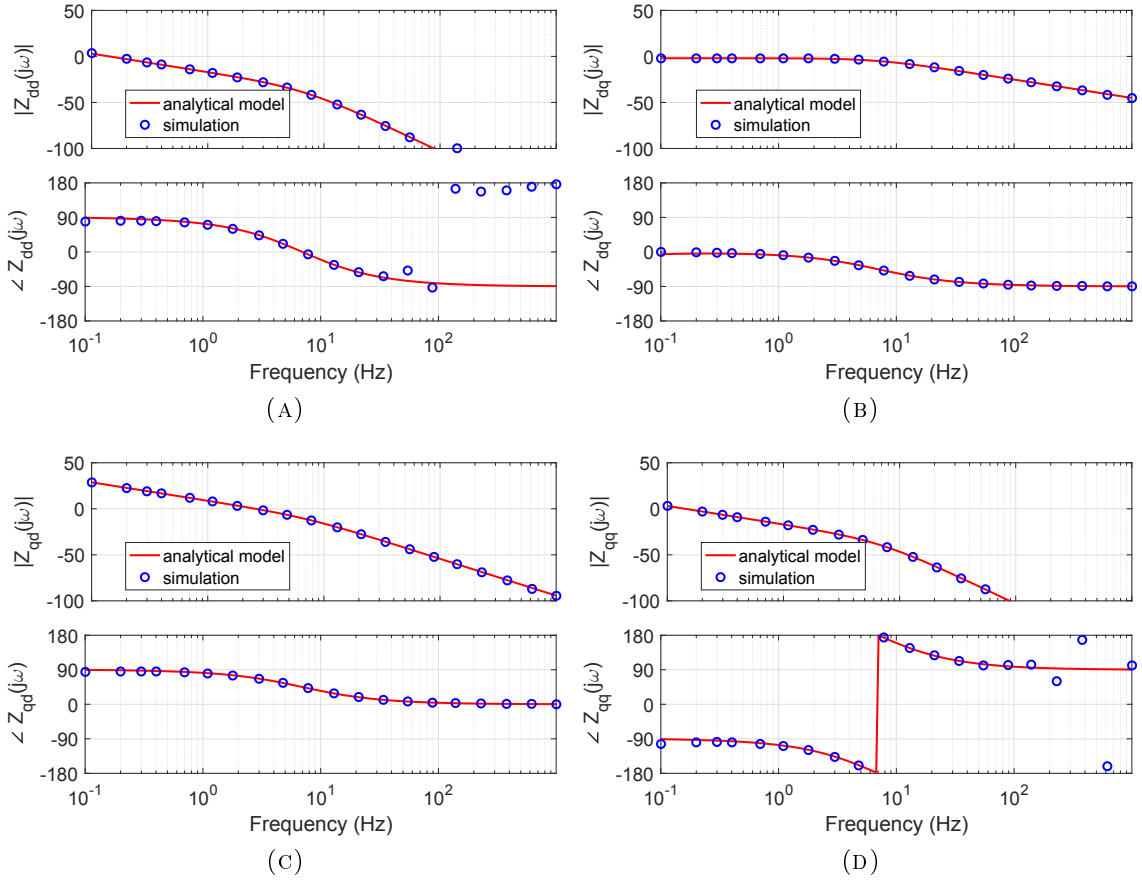

FIGURE 5.9: Droop Control: output impedances $\mathbf{Z^s_{o,DC}}$ in the system dq-frame with null decoupling impedance.

It is then clear that the cross-coupling impedances are of the second order, while the diagonal impedances are of the third order. Moreover, the dd and qq impedances have the same magnitude but the opposite sign, since $k_{dd} = -k_{qq}$.

Can be observed from Fig. 5.9 that the simulation results exhibit a very good matching with the analytical model. Moreover, can be noticed that the dominant impedance at low frequencies is the one in the qd-channel in Fig. 5.9c.

$Z^s_{o,DC_{dd}} \overset{k_p \ll 1, k_q \ll 1}{=} k_{dd} \dfrac{1}{\left(\frac{s}{\omega_{p1}}+1\right)\left(\frac{s}{\omega_{p2}}+1\right)^2}$	$Z^s_{o,DC_{dq}} \overset{k_p \ll 1, k_q \ll 1}{=} k_{dq} \dfrac{\left(\frac{s}{\omega_{z1,dq}}+1\right)}{\left(\frac{s}{\omega_{p1}}+1\right)\left(\frac{s}{\omega_{p2}}+1\right)}$
$Z^s_{o,DC_{qd}} \overset{k_p \ll 1, k_q \ll 1}{=} k_{qd} \dfrac{1}{\left(\frac{s}{\omega_{p1}}+1\right)\left(\frac{s}{\omega_{p2}}+1\right)}$	$Z^s_{o,DC_{qq}} \overset{k_p \ll 1, k_q \ll 1}{=} k_{qq} \dfrac{1}{\left(\frac{s}{\omega_{p1}}+1\right)\left(\frac{s}{\omega_{p2}}+1\right)^2}$

TABLE 5.3: Output impedance expressions of $\mathbf{Z^s_{o,DC}}$ for null decoupling impedance and for $k_p \ll 1$ and $k_q \ll 1$.

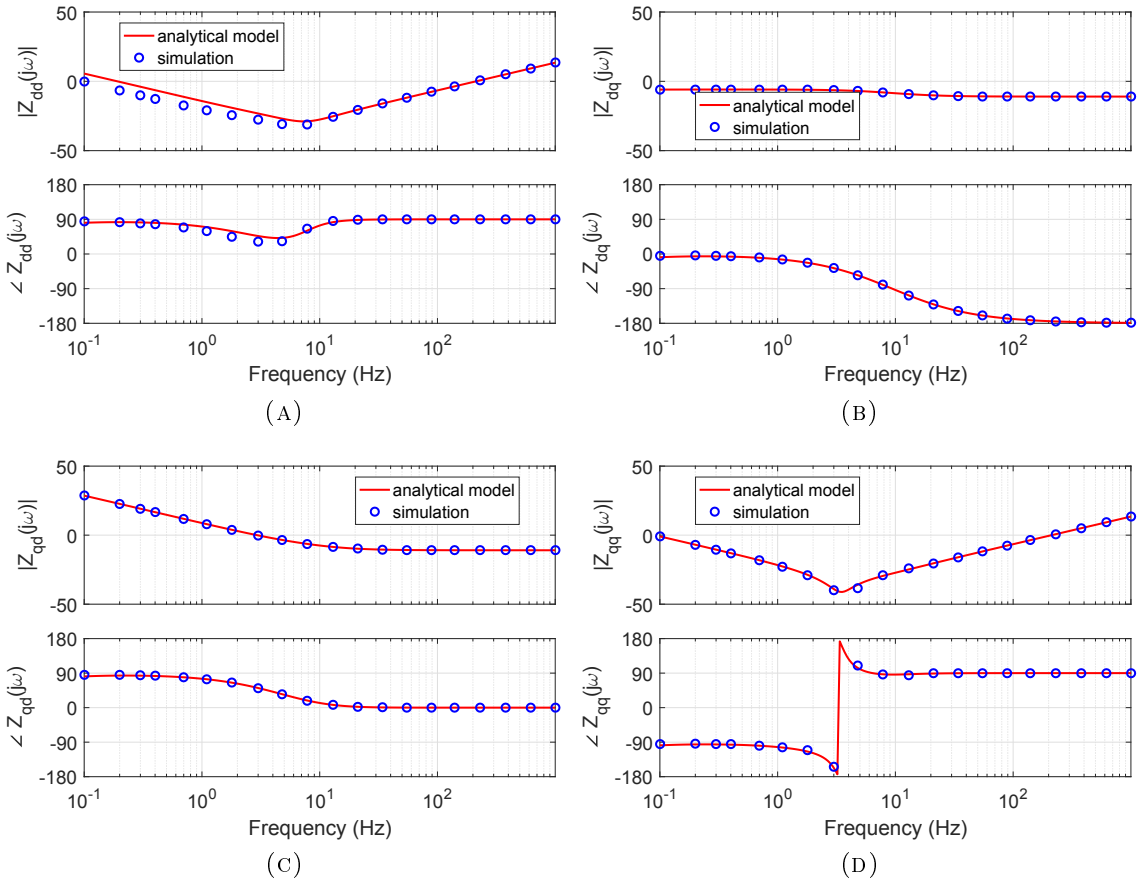

FIGURE 5.10: Droop Control: output impedances $\mathbf{Z^s_{o,DC}}$ in the system dq-frame with decoupling impedance $\mathbf{Z^s_D \neq 0}$.

5.6.2 Non null physical impedance $\mathbf{Z^s_D \neq 0}$ with ideal inverter

Referring to (5.54), it is possible to determine the expressions of the impedances for the case with physical decoupling inductance.

Firstly, it has been verified that the denominator does not change in this condition, hence the denominator refers to the expression in (5.61). It means that the additional decoupling impedance does not change the poles of the system.

As can be noticed, the output impedances present a high frequency behavior that is compatible with an inductive impedance. This means that the droop control is acting up to $10Hz$ and its effect becomes less influent into the overall output impedances because of the power filters. In fact, the higher the filtering effect, the lower the angle perturbation applied to the controller frame.

$$
\begin{aligned}
Z^s_{o,DC,dd} &= k_{dd}\frac{n_{dd}(s)}{\left(-\frac{1}{b_{dd}}\right)s^3+\left(\frac{-2\omega_f}{b_{dd}}\right)s^2+\left(\frac{-\omega_f^2}{b_{dd}}\right)s+1}\\
Z^s_{o,DC,dq} &= k_{dq}\frac{n_{dq}(s)}{\left(-\frac{1}{b_{dd}}\right)s^3+\left(\frac{-2\omega_f}{b_{dd}}\right)s^2+\left(\frac{-\omega_f^2}{b_{dd}}\right)s+1}\\
Z^s_{o,DC,qd} &= k_{qd}\frac{n_{qd}(s)}{\left(-\frac{1}{b_{dd}}\right)s^3+\left(\frac{-2\omega_f}{b_{dd}}\right)s^2+\left(\frac{-\omega_f^2}{b_{dd}}\right)s+1}\\
Z^s_{o,DC,qq} &= k_{qq}\frac{n_{qq}(s)}{\left(-\frac{1}{b_{dd}}\right)s^3+\left(\frac{-2\omega_f}{b_{dd}}\right)s^2+\left(\frac{-\omega_f^2}{b_{dd}}\right)s+1}
\end{aligned}
\tag{5.64}
$$

where

$$
\begin{aligned}
n_{dd}(s) = &\left(-\frac{L_D}{a_{dd}}\right)s^4+\left(\frac{-2L_D\omega_f}{a_{dd}}\right)s^3+\ldots\\
&\left(\frac{\sqrt{3}L_D\omega_f\left(I^s_qV_sk_p-I^s_dk_q\omega_s\right)-L_D\omega_f^2}{a_{dd}}\right)s^2+\ldots\\
&\left(\frac{\sqrt{3}L_D\omega_f^2\left(I^s_qV_sk_p-I^s_dk_q\omega_s\right)}{a_{dd}}\right)s+1
\end{aligned}
\tag{5.65}
$$

$$
\begin{aligned}
n_{dq}(s) = &\left(\frac{\omega_sL_D-\sqrt{3}I^s_dL_Dk_q\omega_f}{a'_{dq}}\right)s^3+\ldots\\
&\left(\frac{2\omega_f\omega_sL_D-\sqrt{3}k_q\omega_f(V^s_d+I^s_dL_D\omega_f)}{a'_{dq}}\right)s^2+\ldots\\
&\left(\frac{\omega_f^2\omega_sL_d-\sqrt{3}\omega_f\left(V^s_dk_q\omega_f-I^s_qV_sk_p\omega_sL_D\right)}{a'_{dq}}\right)s+1
\end{aligned}
\tag{5.66}
$$

$$
\begin{aligned}
n_{dq}(s) = &\left(\frac{-\omega_sL_D}{a_{qd}}\right)s^3+\ldots\\
&\left(\frac{-2\omega_f\omega_sL_D-\sqrt{3}L_D\omega_f\left(I^s_dV_sk_p+I^s_q\omega_sk_q\right)}{a_{qd}}\right)s^2+\ldots\\
&\left(\frac{-\omega_f^s\omega_sL_D+\sqrt{3}\omega_f\left(V^s_dV_sk_p-I^s_qk_q\omega_f\omega_sL_D-I^s_dV_sk_p\omega_fL_D\right)}{a_{qd}}\right)s+1
\end{aligned}
\tag{5.67}
$$

$$
\begin{aligned}
n_{qq}(s) = &\left(-\frac{L_D}{a_{dd}}\right) s^4 + \left(\frac{-2L_D\omega_f - \sqrt{3}I_q^s L_D k_q \omega_f}{a_{dd}}\right) s^3 + \dots \\
&\left(\frac{-\omega_f^2 L_D - \sqrt{3}I_q^s L_D k_q \omega_f^2}{a_{dd}}\right) s^2 + \dots \\
&\left(\frac{\sqrt{3}I_d^s V_s k_p \omega_f \omega_s L_D}{a_{dd}}\right) s + 1
\end{aligned}
\tag{5.68}
$$

and

$$
\begin{aligned}
a'_{dq} &= \sqrt{3}I_q^s V_s k_p \omega_f^2 \left(\sqrt{3}V_d^s k_q - \omega_s L_D\right) \\
a'_{qq} &= \sqrt{3}I_d^s V_s k_p \omega_f^2 \left(\omega_s L_D - \sqrt{3}V_d^s k_q\right)
\end{aligned}
\tag{5.69}
$$

The numerators of the dd and qq components, in (5.65) and (5.68) respectively, presents a fourth order polynomial, introduced by the inductive term. The numerators of the cross-coupling terms, in (5.66) and (5.67) respectively, present a third order polynomial, and so the same order of the denominator. The high frequency term is constant because of the inductive term, which dominates at high frequencies.

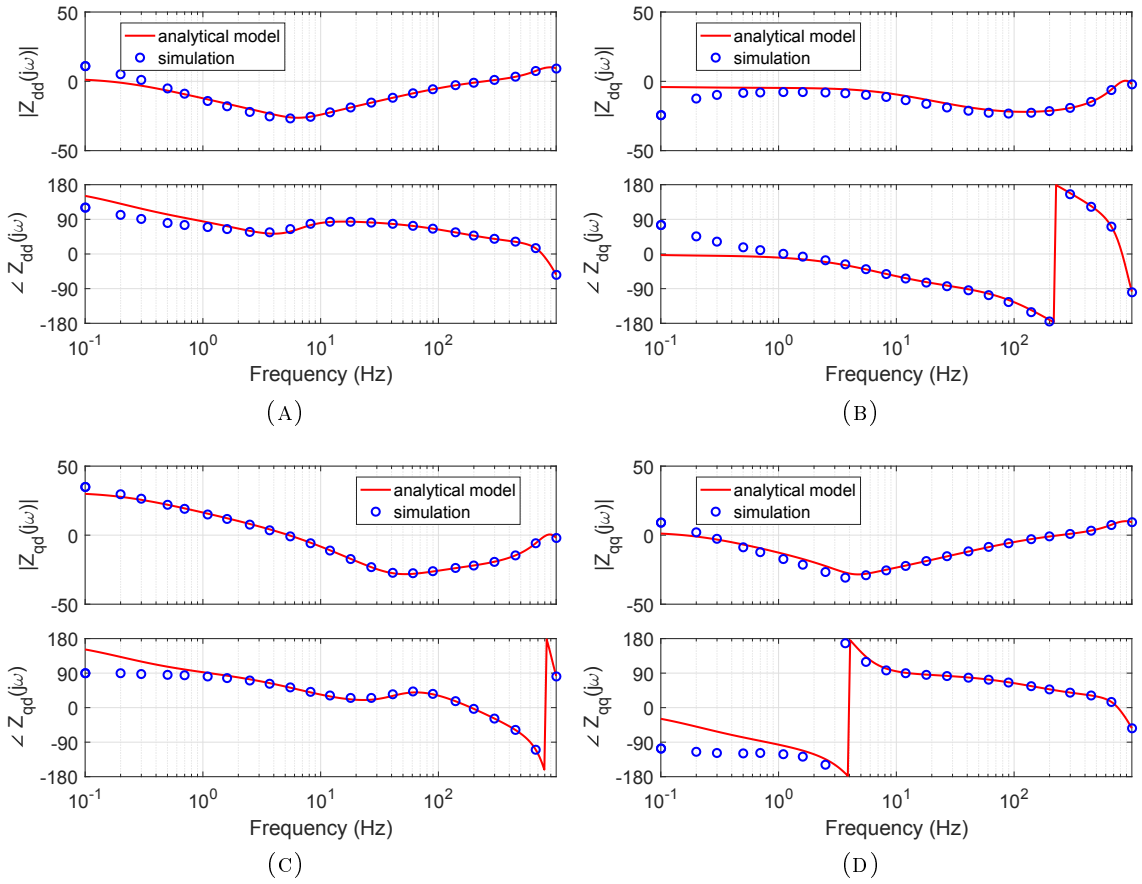

FIGURE 5.11: Droop Control: output impedances $\mathbf{Z^s_{o,DC}}$ in the system dq-frame with $\mathbf{Z^s_V} = \mathbf{0}$ and inverter dynamics considered.

5.7 Null decoupling impedance with inverter inner dynamics

Finally, in Fig. 5.11 the inverter contributions are included as in (5.55). The output impedance depends mainly on the droop control at low frequencies, while the output impedance of the inverter dominates at high frequencies. Moreover, it can be observed that an inductive behavior is provided by the inverter itself, without any additional external decoupling inductance.

The impedance $Z^s_{o,DCqd}$ dominates at low frequencies, since its amplitude is higher than the other impedances.

Chapter 6

Impedance Frame Changing

Systems with different *dq*-frames can be found, i.e. a common reference frame (system frame) and the converters individual frames (controller frames), where a conversion to the same frame becomes mandatory in order to perform a stability analysis. In some cases, accordingly to the selected frame, it is possible to obtain impedance expressions easily, while in other cases the calculations become more complex.

In [128] the problem of the impedance conversion between different frames is addressed. The subsystems which exhibit the mirror frequency decoupling (MFD) [129] are shown to be invariant from the selected frame, as for inductors and capacitors. A conversion tool which included the conversion between two different phase-shifted *dq* frames is derived.

In [130] the conversion between *dq*-frames with different frequencies is considered for the harmonic compensations. In particular the harmonic synchronous reference frames (HSRFs) are shown and the efficient multiple-reference-frame (EMRF) is derived in order to reduce the number of computations.

In a droop-controlled inverter, the power perturbations, induced by the voltage and current perturbations, cause an angle perturbation $\hat{\theta}$. The peculiarity of the conversion hereafter presented is this angle perturbation, which results in a more

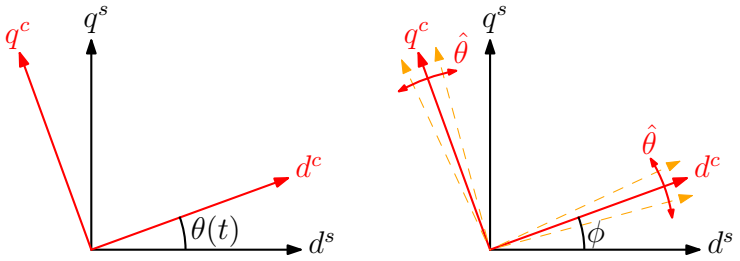

(A) Generic $\theta(t)$ (B) Perturbed angle

FIGURE 6.1: System and controller dq-frames.

complex transformation between the frames. For completeness, both the direct and the inverse transformations are derived.

6.1 Conversion of Voltage and Current Perturbations

The conversion of voltage and current small-signal perturbations has already been discussed in [131], where the stability of an autonomous operation of inverter-based microgrid is analyzed. The system is modeled with n different frames, which are phase-shifted and angle perturbations are considered, from which the need to perform the transformation.

In Fig. 6.1 the system frame with d^sq^s-axes and controller frame with d^cq^c-axes are shown. The system frame is considered as the main reference frame. The controller frame is phase shifted of an angle ϕ and subject to the angle perturbation $\hat{\theta}$.

Let $\underline{x}^s$ be the vector of a current or voltage signal in the system d^sq^s-frame. It can be converted in the controller d^cq^c-frame as $\underline{x}^c$ considering the rotational matrix

$$\mathbf{R}_{\theta(t)} = \begin{bmatrix} \cos\theta(t) & -\sin\theta(t) \\ \sin\theta(t) & \cos\theta(t) \end{bmatrix} \tag{6.1}$$

where the angle $\theta(t)$. Hence, it is possible to apply the rotational matrix to the vector $\underline{x}^s$ in order to get $\underline{x}^c$ as:

$$\underline{x}^c = \mathbf{R}_{\theta(t)} \cdot \underline{x}^s \tag{6.2}$$

Considering small-signal perturbations, it is possible to rewrite the expressions taking into account that:

$$\theta(t) = \phi + \hat{\theta} \tag{6.3}$$

where ϕ is a constant angle, $\hat{\theta}$ represents the small-signal perturbation, and

$$\begin{aligned} \underline{x}^s &= \underline{X}^s + \underline{\hat{x}}^s \\ \underline{x}^c &= \underline{X}^c + \underline{\hat{x}}^c \end{aligned} \tag{6.4}$$

where $\underline{X}^s = \left[X_d^s, X_q^s\right]^T$, $\underline{X}^c = \left[X_d^c, X_q^c\right]^T$ represent the steady-state values and $\underline{\hat{x}}^s = \left[\hat{x}_d^s, \hat{x}_q^s\right]^T$, $\underline{\hat{x}}^c = \left[\hat{x}_d^c, \hat{x}_q^c\right]^T$ represent the perturbations in the system and controller frames, respectively.

From (6.1), (6.2) and considering (6.3) and (6.4), one can write:

$$\underline{X}^c + \underline{\hat{x}}^c = \begin{bmatrix} \cos(\phi+\hat{\theta}) & -\sin(\phi+\hat{\theta}) \\ \sin(\phi+\hat{\theta}) & \cos(\phi+\hat{\theta}) \end{bmatrix} \cdot (\underline{X}^s + \underline{\hat{x}}^s) \tag{6.5}$$

which gives the expressions for the steady-state and perturbed quantities:

$$\begin{aligned} \underline{X}^c &= \mathbf{R}_\phi \cdot \underline{X}^s \\ \underline{\hat{x}}^c &= \mathbf{R}_\phi \cdot \underline{\hat{x}}^s + \mathbf{Q}_\mathbf{X}^\mathbf{c}\hat{\theta} \end{aligned} \tag{6.6}$$

where $\mathbf{Q}_\mathbf{X}^\mathbf{c} = \left[X_q^c, -X_d^c\right]^T$. Moreover, the inverse transformation can be derived as:

$$\begin{aligned} \underline{X}^s &= \mathbf{R}_\phi^T \cdot \underline{X}^c \\ \underline{\hat{x}}^s &= \mathbf{R}_\phi^T \cdot \underline{\hat{x}}^c - \mathbf{Q}_\mathbf{X}^\mathbf{s}\hat{\theta} \end{aligned} \tag{6.7}$$

where $\mathbf{R}_\phi^T = \mathbf{R}_\phi^{-1}$ and $\mathbf{Q}_\mathbf{X}^\mathbf{s} = \left[X_q^s, -X_d^s\right]^T$.

Hence, the expressions in (6.6) and (6.7) are valid for both voltage and current perturbations, where the letters x, X will be replaced according to the quantity considered.

6.2 Impedance Conversion

Expressing the angle perturbation $\hat{\theta}$ with current and voltage perturbations becomes necessary in order to perform the impedance conversion. Therefore:

$$\hat{\theta} = f\left(\underline{\hat{v}}^s, \underline{\hat{i}}^s\right) = f\left(\underline{\hat{v}}^c, \underline{\hat{i}}^c\right) \tag{6.8}$$

and, more in detail, one can say:

$$\hat{\theta} = \mathbf{W}_\mathbf{V}^\mathbf{s} \cdot \underline{\hat{v}}^s + \mathbf{W}_\mathbf{I}^\mathbf{s} \cdot \underline{\hat{i}}^s = \mathbf{W}_\mathbf{V}^\mathbf{c} \cdot \underline{\hat{v}}^c + \mathbf{W}_\mathbf{I}^\mathbf{c} \cdot \underline{\hat{i}}^c \tag{6.9}$$

where $\mathbf{W_V^s}$, $\mathbf{W_I^s}$, $\mathbf{W_V^c}$ and $\mathbf{W_I^c}$ are transfer functions coming from the control implemented in the converter. Depending on the chosen conversion, it is then possible to express the angle perturbation in the system or in the controller *dq*-frame.

6.2.1 System-to-Controller Frame Conversion

The impedance definition in the system frame is:

$$\underline{\hat{v}}^s = \mathbf{Z^s} \cdot \underline{\hat{i}}^s \tag{6.10}$$

where incoming currents are considered, also for steady-state values. Applying the transformation in (6.7) for voltages and currents, one can notice that the angle perturbation remains in the expression:

$$\left(\mathbf{R}_\phi^T \cdot \underline{\hat{v}}^c - \mathbf{Q_V^s}\hat{\theta}\right) = \mathbf{Z^s} \cdot \left(\mathbf{R}_\phi^T \cdot \underline{\hat{i}}^c - \mathbf{Q_I^s}\hat{\theta}\right) \tag{6.11}$$

In (6.11) the perturbations have all to be expressed in the controller frame as indicated in (6.9), hence:

$$\left[\mathbf{R}_\phi^T \cdot \underline{\hat{v}}^c - \mathbf{Q_V^s}\left(\mathbf{W_V^c} \cdot \underline{\hat{v}}^c + \mathbf{W_I^c} \cdot \underline{\hat{i}}^c\right)\right] = \mathbf{Z^s} \cdot \left[\mathbf{R}_\phi^T \cdot \underline{\hat{i}}^c - \mathbf{Q_I^s}\left(\mathbf{W_V^c} \cdot \underline{\hat{v}}^c + \mathbf{W_I^c} \cdot \underline{\hat{i}}^c\right)\right]$$

Multiplying the voltage $\underline{\hat{v}}^c$ and the current $\underline{\hat{i}}^c$ terms, one can get:

$$\underline{\hat{v}}^c = \left[\mathbf{R}_\phi^T + (\mathbf{Z^s} \cdot \mathbf{Q_I^s} - \mathbf{Q_V^s}) \cdot \mathbf{W_V^c}\right]^{-1} \cdot \left[\mathbf{Z^s} \cdot \mathbf{R}_\phi^T + (\mathbf{Q_V^s} - \mathbf{Z^s} \cdot \mathbf{Q_I^s}) \cdot \mathbf{W_I^c}\right] \cdot \underline{\hat{i}}^c$$

Therefore the expression of the impedance $\mathbf{Z^c}$ in the controller *dq*-frame is:

$$\mathbf{Z^c} = \left[\mathbf{R}_\phi^T + (\mathbf{Z^s} \cdot \mathbf{Q_I^s} - \mathbf{Q_V^s}) \cdot \mathbf{W_V^c}\right]^{-1} \cdot \left[\mathbf{Z^s} \cdot \mathbf{R}_\phi^T + (\mathbf{Q_V^s} - \mathbf{Z^s} \cdot \mathbf{Q_I^s}) \cdot \mathbf{W_I^c}\right] \tag{6.12}$$

Moreover, it is possible to represent the transformation through block scheme, as in Fig. 6.2. It can be noticed that, when the angle perturbation $\hat{\theta} = 0$:

$$\mathbf{Z^c} = \mathbf{R}_\phi \cdot \mathbf{Z^s} \cdot \mathbf{R}_\phi^T \tag{6.13}$$

6.2.2 Controller-to-System Frame Conversion

The same procedure done for the system-to-controller frame conversion can be implemented for the inverse transformation. The impedance definition in the

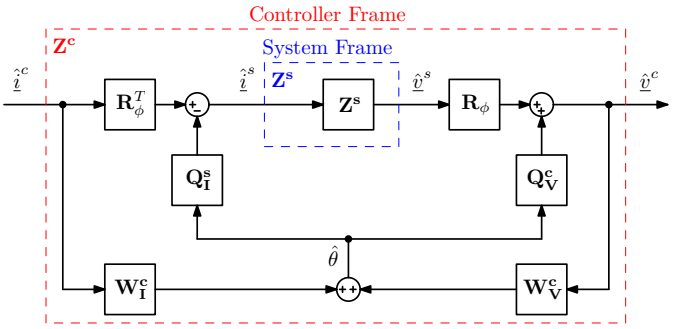

FIGURE 6.2: Block scheme representation for the system-to-controller frame transformation.

system frame is:

$$\hat{\underline{v}}^c = \mathbf{Z^c} \cdot \hat{\underline{i}}^c \tag{6.14}$$

where incoming currents are considered, also for steady-state values. Applying the transformation in (6.6) for voltages and currents, one can notice that the angle perturbation remains in the expression:

$$\left(\mathbf{R}_\phi \cdot \hat{\underline{v}}^s + \mathbf{Q_V^c}\hat{\theta}\right) = \mathbf{Z^c} \cdot \left(\mathbf{R}_\phi \cdot \hat{\underline{i}}^s + \mathbf{Q_I^c}\hat{\theta}\right) \tag{6.15}$$

In (6.15) the perturbations have all to be expressed in the system frame as indicated in (6.9), hence:

$$\left[\mathbf{R}_\phi \cdot \hat{\underline{v}}^s + \mathbf{Q_V^c}\left(\mathbf{W_V^s} \cdot \hat{\underline{v}}^s + \mathbf{W_I^s} \cdot \hat{\underline{i}}^s\right)\right] = \mathbf{Z^c} \cdot \left[\mathbf{R}_\phi \cdot \hat{\underline{i}}^s + \mathbf{Q_I^c}\left(\mathbf{W_V^s} \cdot \hat{\underline{v}}^s + \mathbf{W_I^s} \cdot \hat{\underline{i}}^s\right)\right]$$

Collecting the terms multiplying the voltage $\hat{\underline{v}}^s$ and the current $\hat{\underline{i}}^s$ terms, one can get:

$$\hat{\underline{v}}^s = \left[\mathbf{R}_\phi + \left(\mathbf{Z^c} \cdot \mathbf{Q_I^c} - \mathbf{Q_V^c}\right) \cdot \mathbf{W_V^s}\right]^{-1} \cdot \left[\mathbf{Z^c} \cdot \mathbf{R}_\phi + \left(\mathbf{Q_V^c} - \mathbf{Z^c} \cdot \mathbf{Q_I^c}\right) \cdot \mathbf{W_I^s}\right] \cdot \hat{\underline{i}}^s$$

Therefore the expression of the impedance $\mathbf{Z^s}$ in the controller dq-frame is:

$$\mathbf{Z^s} = \left[\mathbf{R}_\phi + \left(\mathbf{Z^c} \cdot \mathbf{Q_I^c} - \mathbf{Q_V^c}\right) \cdot \mathbf{W_V^s}\right]^{-1} \cdot \left[\mathbf{Z^c} \cdot \mathbf{R}_\phi + \left(\mathbf{Q_V^c} - \mathbf{Z^c} \cdot \mathbf{Q_I^c}\right) \cdot \mathbf{W_I^s}\right] \tag{6.16}$$

Moreover, it is possible to represent the transformation through block scheme, as in Fig. 6.3. It can be noticed that, when the angle perturbation $\hat{\theta} = 0$:

$$\mathbf{Z^s} = \mathbf{R}_\phi^T \cdot \mathbf{Z^c} \cdot \mathbf{R}_\phi \tag{6.17}$$

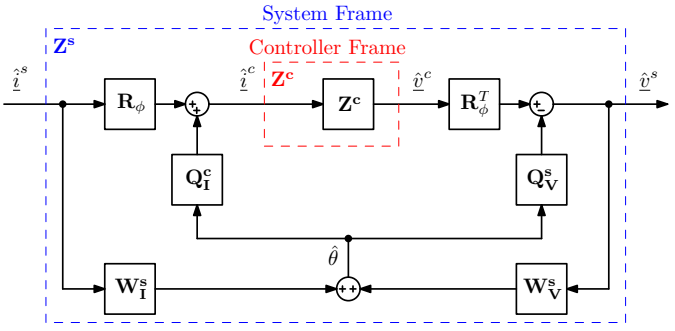

FIGURE 6.3: Block scheme representation for the controller-to-system frame transformation.

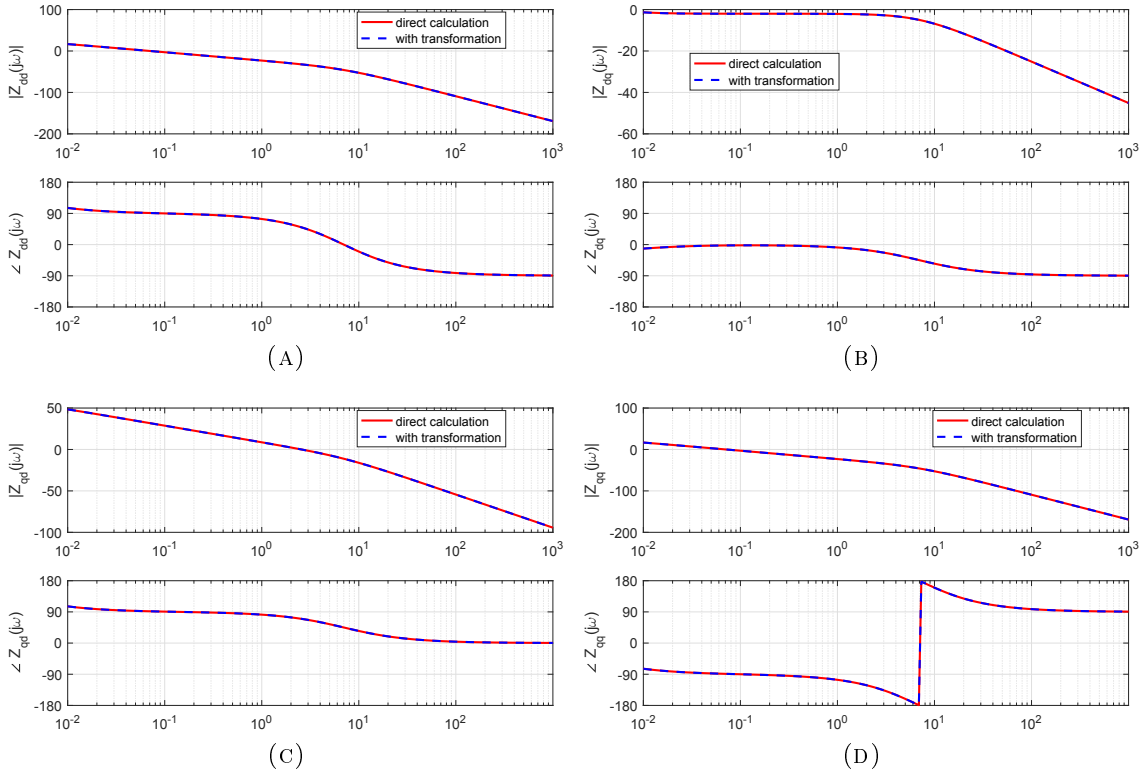

FIGURE 6.4: Output impedance $\mathbf{Z^s_{o,DC}}$ of the droop controlled inverter in the system *dq*-frame (without virtual or physical decoupling inductance): comparison between direct calculation in the system frame and controller-to-system frame transformation of $\mathbf{Z^c_{o,DC}}$.

6.3 Impedance Frame Conversion for the Droop-Controlled Inverter

The tool derived in the previous sections can be used for the droop controlled inverter case. For example, in Fig. 6.4 it is possible to observe that the output impedance $\mathbf{Z^s_{o,DC}}$ (with $\mathbf{Z^s_D} = \mathbf{0}$) can be calculated equivalently from (5.54) or applying the transformation in (6.16) to the output impedance in the controller frame calculated in (5.39).

Firstly, to perform such transformation it is necessary to determined the angle perturbation $\hat{\theta}$. Since it appears in the vector $\underline{\hat{r}}^s$, it is worth to explicit in function

of the current $\hat{\underline{i}}$ and voltage $\hat{\underline{v}}$ perturbations:

$$\begin{aligned}\hat{\underline{r}}^s = \begin{bmatrix}\hat{\theta}\\ \hat{v}\end{bmatrix} &= \mathbf{D_{pp}}\cdot\mathbf{D}\cdot\mathbf{F}\cdot\mathbf{S_I^s}\cdot\hat{\underline{i}}^s + \mathbf{D_{pp}}\cdot\mathbf{D}\cdot\mathbf{F}\cdot\mathbf{S_V^s}\cdot\hat{\underline{v}}^s = \\ &= \begin{bmatrix}\frac{k_p\omega_f V_d^s}{s(s+\omega_f)} & \frac{k_p\omega_f V_q^s}{s(s+\omega_f)}\\ \frac{\sqrt{2}k_q\omega_f V_q^s}{s+\omega_f} & -\frac{\sqrt{2}k_q\omega_f V_d^s}{s+\omega_f}\end{bmatrix}\cdot\hat{\underline{i}}^s + \begin{bmatrix}\frac{k_p\omega_f I_d^s}{s(s+\omega_f)} & \frac{k_p\omega_f I_q^s}{s(s+\omega_f)}\\ -\frac{\sqrt{2}k_q\omega_f I_q^s}{s+\omega_f} & \frac{\sqrt{2}k_q\omega_f I_d^s}{s+\omega_f}\end{bmatrix}\cdot\hat{\underline{v}}^s\end{aligned} \tag{6.18}$$

accordingly to the matrix definitions provided in the previous chapter.

The first rows of the two matrices will be part of the matrices $\mathbf{W_V^s}$ and $\mathbf{W_I^s}$. To be considered that, since the currents I_d^s and I_q^s are considered as outcoming currents in the previous chapter, a minus sign must be applied in order to provide the correct final transformation:

$$\mathbf{W_I^s} = \begin{bmatrix}\frac{k_p\omega_f V_d^s}{s(s+\omega_f)} & \frac{k_p\omega_f V_q^s}{s(s+\omega_f)}\end{bmatrix} \tag{6.19}$$

and

$$\mathbf{W_V^s} = \begin{bmatrix}-\frac{k_p\omega_f I_d^s}{s(s+\omega_f)} & -\frac{k_p\omega_f I_q^s}{s(s+\omega_f)}\end{bmatrix} \tag{6.20}$$

In the missing terms for the final transformation reported in (6.16), the operating points defined as $\mathbf{Q_V^c}$ and $\mathbf{Q_I^c}$ are:

$$\mathbf{Q_V^c} = \begin{bmatrix}V_q^c\\ -V_d^c\end{bmatrix} \tag{6.21}$$

and

$$\mathbf{Q_I^c} = \begin{bmatrix}-I_q^c\\ I_d^c\end{bmatrix} \tag{6.22}$$

where the sign of the currents of $\mathbf{Q_I^c}$ has been already changed, once again because the currents indicated in the previous chapter have been considered outcoming. Using the phase shift angle ϕ defined in (5.31), it is possible to determined the rotational matrix $\mathbf{R}_\phi$.

Finally, the impedance $\mathbf{Z_{o,DC}^c}$ from the controller frame can be transformed into the impedance $\mathbf{Z_{o,DC}^s}$ thanks to the transformation in (6.2.2), and the matching between the transformed and the calculated impedances can be found in Fig. 6.4.

Chapter 7

Conclusions and Future Work

The impedance-based approach has been widely used in DC systems for years, to investigate the converters interactions and predicting the stability also in case of multiple paralleled converters, often using criteria to limit the interactions and guarantee a stable configuration. Then, the method has been extended to single-phase and three-phase AC system, where the multi-input multi-output configuration needs the generalized Nyquist criterion (GNC) for the stability assessment.

The first case presented in this work was a grid-connected large photovoltaic (PV) farm. The inverters control is provided in *abc*-frame, and considering a balanced and symmetrical system the equivalent single-phase inverter is considered in this analysis. The stability is addressed according to the impedance-based approach and two sets of poles are distinguished: *internal* and *external poles*. Thanks to this approach, the *external poles* are found to be related to the interaction between the inverters and the grid and so the impedance ratio, while the *internal poles* come from the equivalent current generator used to model the inverter. The *impedance multiplication effect* has been formalized also for the case of different parallel inverters, which case can be managed thanks to the impedance-based approach. The influence of the line impedance and of the power rating of the inverter is considered, and the multiplied impedance is shown to exhibit some resonances

in correspondence of the unstable frequency. The outcome of the study is an approach featuring both accurate stability analysis, as in multi-input multi-output based approaches, and modularity, as in impedance-based approaches. Moreover, the analysis is validated through simulation and experimental results with three 5kVA inverters.

Recently, the interest on the hybrid-grids with diesel generators and battery energy storage systems (BESSs) are gaining higher attention because nearly one in five people in the world live without access to electricity. This off-grid solution is then able to provide a continuous generation and also integrate the renewables in the same system. The second part of the thesis focuses on the modeling of a three-phase hybrid-grid, and the experimental results of a system with a 400kVA diesel generator and up to around 300kVA coming from droop-controlled inverters are included. The analysis has led to the full reproduction of the interaction between the diesel generator and an increasing number of connected inverters, where the total inertia of the system changes and a $\simeq 0.2$Hz oscillating behavior appears.

However, in literature there is no stability analysis accurate enough to analyze such a complex system and predict instabilities. The modularity of the impedance-based stability analysis can then provide a subdivision of this complexity, and so is a suitable approach. In the last part of this thesis, the output impedance of a droop-controlled inverter is determined, in order to determine a first essential part of the grid, widely used in off-grid applications. Firstly, the system frequency and voltage for a droop-controlled inverter depend on the load, hence the steady-state operating point is determined. Then, the analytical model of the output impedance is derived in both controller and system frame, including the effect of the virtual or physical decoupling impedance. The inverter dynamics are finally introduced into the model. All the results are compared with simulation results, considering the inverter models developed for the previous hybrid-grid case.

Finally, since the main issue for the stability analysis lies on the fact that such system presents more than one phase shifted and perturbed dq-frames, a generic mathematical tool to convert impedances from a synchronous reference frame to another one is derived and applied to the droop-controlled inverter case. The dq-impedance is transformed for the case with the ideal inverter and null decoupling impedance, and exhibits a good matching with the correspondent directly calculated impedance. Therefore, the stability analysis of grids with droop-controlled inverters can now be addressed with the impedance-based approach.

Appendix A

Transformation $v\theta, abc, dq$

Let $\omega_T(t)$ be the angular frequency for the Park's transformation and:

$$\theta_T(t) = \int_t \omega_T(\tau) \cdot \mathrm{d}\tau \tag{A.1}$$

be the angle of the rotating dq-frame considered. Hence, the Park transformation matrix can be written as:

$$\mathbf{T_{park}}(t) = \sqrt{\frac{2}{3}} \cdot \begin{bmatrix} \cos\left(\theta_T(t)\right) & \cos\left(\theta_T(t) - \frac{2\pi}{3}\right) & \cos\left(\theta_T(t) - \frac{4\pi}{3}\right) \\ -\sin\left(\theta_T(t)\right) & -\sin\left(\theta_T(t) - \frac{2\pi}{3}\right) & -\sin\left(\theta_T(t) - \frac{4\pi}{3}\right) \\ \frac{1}{\sqrt{2}} & \frac{1}{\sqrt{2}} & \frac{1}{\sqrt{2}} \end{bmatrix} \tag{A.2}$$

Let $\theta_S(t)$ be the source angle, given by the integration of the angular frequency of the system $\omega_s(t)$:

$$\theta_S(t) = \int_t \omega_s(\tau)\, \mathrm{d}\tau \tag{A.3}$$

where $\omega_s(t)$ is the source time-varying angular frequency.

Let $v_a(t)$, $v_b(t)$ and $v_c(t)$ be the phase voltages in a three-phase sinusoidal, symmetrical and balanced system:

$$\begin{aligned} v_a(t) &= v(t) \cdot \cos\left(\theta_S(t)\right) \\ v_b(t) &= v(t) \cdot \cos\left(\theta_S(t) - \frac{2\pi}{3}\right) \\ v_c(t) &= v(t) \cdot \cos\left(\theta_S(t) - \frac{4\pi}{3}\right) \end{aligned} \tag{A.4}$$

where $v(t)$ and $\theta_S(t)$ are time-varying voltage and angle of the source, respectively. According to the fact that the system is balanced, one can write:

$$v_a(t) + v_b(t) + v_c(t) = 0 \tag{A.5}$$

Applying the Park transformation to the abc voltages expressions in (A.4), one can get:

$$\begin{bmatrix} v_d(t) \\ v_q(t) \\ v_0(t) \end{bmatrix} = \mathbf{T_{park}}(t) \cdot \begin{bmatrix} v_a(t) \\ v_b(t) \\ v_c(t) \end{bmatrix} \tag{A.6}$$

and the following relations can be found

$$\begin{aligned} v_d(t) &= \sqrt{\frac{3}{2}} \cdot v(t) \cdot \left[\cos\Big(\theta_S(t)\Big) \cos\Big(\theta_T(t)\Big) + \sin\Big(\theta_S(t)\Big) \sin\Big(\theta_T(t)\Big) \right] \\ v_q(t) &= \sqrt{\frac{3}{2}} \cdot v(t) \cdot \left[\cos\Big(\theta_S(t)\Big) \sin\Big(\theta_T(t)\Big) - \sin\Big(\theta_S(t)\Big) \cos\Big(\theta_T(t)\Big) \right] \\ v_0(t) &= \sqrt{\frac{1}{2}} \cdot v(t) \cdot \left[\cos\Big(\theta_S(t)\Big) + \cos\left(\theta_S(t) - \frac{2\pi}{3}\right) + \cos\left(\theta_S(t) - \frac{4\pi}{3}\right) \right] = 0 \end{aligned} \tag{A.7}$$

where $v_0(t) = 0$ from the definition in (A.5).

Considering the trigonometrical identities:

$$\begin{aligned} \cos\Big(\theta_S(t)\Big) \cdot \cos\Big(\theta_T(t)\Big) &= \frac{1}{2} \cdot \big[a + b\big] \\ \sin\Big(\theta_S(t)\Big) \cdot \sin\Big(\theta_T(t)\Big) &= \frac{1}{2} \cdot \big[a - b\big] \end{aligned} \tag{A.8}$$

$$\begin{aligned} \cos\Big(\theta_S(t)\Big) \cdot \sin\Big(\theta_T(t)\Big) &= \frac{1}{2} \cdot \big[c - d\big] \\ \sin\Big(\theta_S(t)\Big) \cdot \cos\Big(\theta_T(t)\Big) &= \frac{1}{2} \cdot \big[c + d\big] \end{aligned} \tag{A.9}$$

and

$$\begin{aligned} a &= \cos\Big(\theta_S(t) - \theta_T(t)\Big) \quad , \qquad b = \cos\Big(\theta_S(t) + \theta_T(t)\Big) \\ c &= \sin\Big(\theta_S(t) + \theta_T(t)\Big) \quad , \qquad d = \sin\Big(\theta_S(t) - \theta_T(t)\Big) \end{aligned} \tag{A.10}$$

the final expressions in (A.7), considering a balanced system, can be expressed as:

$$\begin{aligned} v_d(t) &= v(t)\sqrt{\frac{3}{2}} \cdot \cos\Big(\theta_S(t) - \theta_T(t)\Big) \\ v_q(t) &= v(t)\sqrt{\frac{3}{2}} \cdot \sin\Big(\theta_S(t) - \theta_T(t)\Big) \end{aligned} \tag{A.11}$$

A.1 To system frame

The source $\theta_S(t)$ and the transformation $\theta_T(t)$ angle, considering to move to the system dq-frame rotating with angle $\theta^s = \Omega_s t$ at constant speed, will be expressed as:

$$\theta_S(t) = \theta^c(t) = \theta^s(t) + \phi + \hat{\theta}(t) \quad , \quad \theta_T(t) = \theta^s(t)$$

where ϕ is a constant phase shift and $\hat{\theta}(t)$ is a perturbation. Using the relations in (5.19), the output voltages of the transformation are given by:

$$\begin{aligned} v_d(t) &= v(t)\sqrt{\frac{3}{2}} \cdot \cos\Big(\phi + \hat{\theta}(t)\Big) \\ v_q(t) &= v(t)\sqrt{\frac{3}{2}} \cdot \sin\Big(\phi + \hat{\theta}(t)\Big) \end{aligned} \tag{A.12}$$

Considering the angle transformation identities:

$$\begin{aligned} v_d(t) &= v(t)\sqrt{\frac{3}{2}} \cdot \Big[\cos(\phi)\cos(\hat{\theta}(t)) - \sin(\phi)\sin(\hat{\theta}(t))\Big] \\ v_q(t) &= v(t)\sqrt{\frac{3}{2}} \cdot \Big[\sin(\phi)\cos(\hat{\theta}(t)) + \cos(\phi)\sin(\hat{\theta}(t))\Big] \end{aligned} \tag{A.13}$$

and finally considering that $v(t) = V + \hat{v}(t)$ (where $V = \sqrt{2}V_s$ will be the voltage resulting from the Q/V droop control) and $\hat{\theta}(t) \simeq 0$ ($\sin\hat{\theta}(t) \simeq \hat{\theta}(t)$, $\cos\hat{\theta}(t) \simeq 1$)

$$\begin{aligned} v_d(t) &\simeq (V + \hat{v}(t))\sqrt{\frac{3}{2}} \cdot \Big[\cos(\phi) - \sin(\phi)\hat{\theta}(t)\Big] \\ v_q(t) &\simeq (V + \hat{v}(t))\sqrt{\frac{3}{2}} \cdot \Big[\sin(\phi) + \cos(\phi)\hat{\theta}(t)\Big] \end{aligned} \tag{A.14}$$

Therefore, expressing all the terms and neglecting the product of perturbations:

$$\begin{aligned} v_d(t) &\simeq \sqrt{\frac{3}{2}}V\cos(\phi) + \sqrt{\frac{3}{2}}\cos(\phi)\hat{v}(t) - \sqrt{\frac{3}{2}}V\sin(\phi)\hat{\theta}(t) \\ v_q(t) &\simeq \sqrt{\frac{3}{2}}V\sin(\phi) + \sqrt{\frac{3}{2}}\sin(\phi)\hat{v}(t) + \sqrt{\frac{3}{2}}V\cos(\phi)\hat{\theta}(t) \end{aligned} \tag{A.15}$$

This last expression can be considered in matrix form, where the

$$\begin{bmatrix} \hat{v}_d^s \\ \hat{v}_q^s \end{bmatrix} = \underbrace{\sqrt{\frac{3}{2}} \begin{bmatrix} -V\sin(\phi) & \cos(\phi) \\ V\cos(\phi) & \sin(\phi) \end{bmatrix}}_{\mathbf{T^s}} \cdot \begin{bmatrix} \hat{\theta} \\ \hat{v} \end{bmatrix} \tag{A.16}$$

A.2 To controller frame

The angles $\theta_S(t) = \theta_T(t) = \theta^c(t)$, hence from (A.11)

$$\begin{aligned} v_d(t) &= \sqrt{\frac{3}{2}} v(t) \\ v_q(t) &= 0 \end{aligned} \tag{A.17}$$

Both from the previous expression and from (A.16), considering a null relative phase shift $\phi = 0$ and perturbation $\hat{\theta}(t) = 0$, it is possible to obtain the desired matrix:

$$\begin{bmatrix} \hat{v}_d^c \\ \hat{v}_q^c \end{bmatrix} = \underbrace{\sqrt{\frac{3}{2}} \begin{bmatrix} 0 & 1 \\ 0 & 0 \end{bmatrix}}_{\mathbf{T^c}} \cdot \begin{bmatrix} \hat{\theta} \\ \hat{v} \end{bmatrix} \tag{A.18}$$

In this last expression can be noticed that only the amplitude variation $\hat{v}(t)$ induces a variation on the output voltages: the system is insensitive to angle variation, since source and transformation angles are equal.

Bibliography

[1] R. E. P. N. for the 21st Century, "Renewables 2016 - global status report," Tech. Rep. [Online]. Available: http://www.ren21.net/wp-content/uploads/2016/06/GSR_2016_Full_Report.pdf

[2] A. Jäger-Waldau, "PV Status Report 2016," JRC Science for Policy Report, Tech. Rep., 2016. [Online]. Available: http://publications.jrc.ec.europa.eu/repository/bitstream/JRC103426/ldna28159enn.pdf

[3] PwC global power & utilities, "Electricity beyond the grid - Accelerating access to sustainable power for all," Tech. Rep., 2016. [Online]. Available: https://www.pwc.com/gx/en/energy-utilities-mining/pdf/electricity-beyond-grid.pdf

[4] IFC and ESMAP, "Energy Storage Trends and Opportunities in Emerging Markets," Tech. Rep., 2017. [Online]. Available: https://www.ifc.org/wps/wcm/connect/ed6f9f7f-f197-4915-8ab6-56b92d50865d/7151-IFC-EnergyStorage-report.pdf?MOD=AJPERES

[5] R. E. Thomas, "The stability of aircraft d-c power systems with inverter loads," *Transactions of the American Institute of Electrical Engineers, Part II: Applications and Industry*, vol. 76, no. 4, pp. 183–188, Sept 1957.

[6] ——, "Stability of aircraft d-c systems," *Electrical Engineering*, vol. 76, no. 10, pp. 859–859, Oct 1957.

[7] W. E. Corporation, "Computer Analysis of Shipboard Electrical Power Distribution Systems with Static Line Voltage Regulators," for U. S. Navy Marine Engineering Laboratory, Tech. Rep. No 67-1000, March 1967.

[8] A. Emadi, A. Khaligh, C. H. Rivetta, and G. A. Williamson, "Constant power loads and negative impedance instability in automotive systems: definition, modeling, stability, and control of power electronic converters and motor drives," *IEEE Transactions on Vehicular Technology*, vol. 55, no. 4, pp. 1112–1125, July 2006.

[9] S. D. Sudhoff, K. A. Corzine, S. F. Glover, H. J. Hegner, and H. N. Robey, "DC link stabilized field oriented control of electric propulsion systems," *IEEE Transactions on Energy Conversion*, vol. 13, no. 1, pp. 27–33, Mar 1998.

[10] G. Sulligoi, D. Bosich, G. Giadrossi, L. Zhu, M. Cupelli, and A. Monti, "Multiconverter Medium Voltage DC Power Systems on Ships: Constant-Power Loads Instability Solution Using Linearization via State Feedback Control," *IEEE Transactions on Smart Grid*, vol. 5, no. 5, pp. 2543–2552, Sept 2014.

[11] U. Javaid, F. D. Freijedo, D. Dujic, and W. van der Merwe, "Dynamic Assessment of Source-Load Interactions in Marine MVDC Distribution," *IEEE Transactions on Industrial Electronics*, vol. 64, no. 6, pp. 4372–4381, June 2017.

[12] I. Lazbin and B. R. Needham, "Analysis of the stability margins of the Space Station Freedom Electrical Power System," in *Power Electronics Specialists Conference, 1993. PESC 1993 Record., 24th Annual IEEE*, Jun 1993, pp. 839–845.

[13] T. C. Wang and J. B. Raley, "Electrical power system stability assurance for the International Space Station," in *IECEC-97 Proceedings of the Thirty-Second Intersociety Energy Conversion Engineering Conference (Cat. No.97CH6203)*, vol. 1, Jul 1997, pp. 246–252 vol.1.

[14] K. J. Karimi, A. J. Booker, A. C. Mong, and B. Manners, "Verification of Space Station secondary power system stability using design of experiment," in *IECEC-97 Proceedings of the Thirty-Second Intersociety Energy Conversion Engineering Conference (Cat. No.97CH6203)*, vol. 1, Jul 1997, pp. 526–531 vol.1.

[15] B. Wen, "Stability Analysis of Three-Phase AC Power Systems Based on Measured D-Q Frame Impedances," Ph.D. dissertation, Virginia Tech, 2015. [Online]. Available: http://hdl.handle.net/10919/51202

[16] K. N. Areerak, S. V. Bozhko, G. M. Asher, L. D. Lillo, and D. W. P. Thomas, "Stability study for a hybrid ac-dc more-electric aircraft power system," *IEEE Transactions on Aerospace and Electronic Systems*, vol. 48, no. 1, pp. 329–347, Jan 2012.

[17] Y. Panov and M. M. Jovanovic, "Stability and dynamic performance of current-sharing control for paralleled voltage regulator modules," *IEEE Transactions on Power Electronics*, vol. 17, no. 2, pp. 172–179, Mar 2002.

[18] J. Morroni, R. Zane, and D. Maksimovic, "An online stability margin monitor for digitally controlled switched-mode power supplies," *IEEE Transactions on Power Electronics*, vol. 24, no. 11, pp. 2639–2648, Nov 2009.

[19] A. Khodamoradi, G. Liu, P. Mattavelli, T. Caldognetto, and P. Magnone, "On-line stability monitoring for power converters in dc microgrids," in *2017 IEEE Second International Conference on DC Microgrids (ICDCM)*, June 2017, pp. 302–308.

[20] R. D. MIDDLEBROOK, "Measurement of loop gain in feedback systems," vol. 38, pp. 485–512, 04 1975.

[21] J. Castello and J. M. Espi, "Dsp implementation for measuring the loop gain frequency response of digitally controlled power converters," *IEEE Transactions on Power Electronics*, vol. 27, no. 9, pp. 4113–4121, Sept 2012.

[22] R. Middlebrook, "Input Filter Considerations in Design and Application of Switching Regulators," *IEEE Industry Applications Society Annual Meeting*, pp. 366–382, 1976.

[23] C. M. Wildrick, F. C. Lee, B. H. Cho, and B. Choi, "A method of defining the load impedance specification for a stable distributed power system," *IEEE Transactions on Power Electronics*, vol. 10, no. 3, pp. 280–285, May 1995.

[24] S. D. Sudhoff, S. F. Glover, P. T. Lamm, D. H. Schmucker, and D. E. Delisle, "Admittance space stability analysis of power electronic systems," *IEEE Transactions on Aerospace and Electronic Systems*, vol. 36, no. 3, pp. 965–973, Jul 2000.

[25] X. Feng, J. Liu, and F. C. Lee, "Impedance specifications for stable dc distributed power systems," *IEEE Transactions on Power Electronics*, vol. 17, no. 2, pp. 157–162, Mar 2002.

[26] S. Vesti, T. Suntio, J. A. Oliver, R. Prieto, and J. A. Cobos, "Impedance-based stability and transient-performance assessment applying maximum peak criteria," *IEEE Transactions on Power Electronics*, vol. 28, no. 5, pp. 2099–2104, May 2013.

[27] M. Belkhayat, "Stability Criteria for AC Power Systems with Regulated Loads," Ph.D. dissertation, Purdue University, 1997. [Online]. Available: http://docs.lib.purdue.edu/dissertations/AAI9821703/

[28] F. Gao, S. Bozhko, S. Yeoh, G. Asher, and P. Wheeler, "Stability of multi-source droop-controlled electrical power system for more-electric aircraft," in *2014 IEEE International Conference on Intelligent Energy and Power Systems (IEPS)*, June 2014, pp. 122–126.

[29] A. Riccobono, M. Cupelli, A. Monti, E. Santi, T. Roinila, H. Abdollahi, S. Arrua, and R. A. Dougal, "Stability of shipboard dc power distribution: Online impedance-based systems methods," *IEEE Electrification Magazine*, vol. 5, no. 3, pp. 55–67, Sept 2017.

[30] J. Sun, "Impedance-Based Stability Criterion for Grid-Connected Inverters," *IEEE Transactions on Power Electronics*, vol. 26, no. 11, pp. 3075–3078, Nov 2011.

[31] B. Wen, D. Boroyevich, R. Burgos, P. Mattavelli, and Z. Shen, "Analysis of d-q small-signal impedance of grid-tied inverters," *IEEE Transactions on Power Electronics*, vol. 31, no. 1, pp. 675–687, Jan 2016.

[32] J. Maciejowski, *Multivariable Feedback Design*, ser. Electronic systems engineering series. Addison-Wesley, 1989. [Online]. Available: https://books.google.it/books?id=dd5SAAAAMAAJ

[33] R. D. MIDDLEBROOK, "Measurement of loop gain in feedback systems," *International Journal of Electronics*, vol. 38, no. 4, pp. 485–512, 1975. [Online]. Available: http://dx.doi.org/10.1080/00207217508920421

[34] J. Liu, X. Feng, F. C. Lee, and D. Borojevich, "Stability margin monitoring for dc distributed power systems via perturbation approaches," *IEEE Transactions on Power Electronics*, vol. 18, no. 6, pp. 1254–1261, Nov 2003.

[35] A. G. J. Macfarlane and I. Postlethwaite, "Generalized nyquist stability criterion and multivariable root loci," *International Journal of Control*, vol. 25, no. 1, pp. 81–127, 1977. [Online]. Available: http://www.tandfonline.com/doi/pdf/10.1080/00207177708922217

[36] I. POSTLETHWAITE, "A generalized inverse Nyquist stability criterion," *International Journal of Control*, vol. 25, no. 1, pp. 81–127, 1977. [Online]. Available: http://www.tandfonline.com/doi/abs/10.1080/00207177708922313

[37] J. H. R. Enslin, W. T. J. Hulshorst, A. M. S. Atmadji, P. J. M. Heskes, A. Kotsopoulos, J. F. G. Cobben, and P. V. der Sluijs, "Harmonic interaction between large numbers of photovoltaic inverters and the distribution network," in *Power Tech Conference Proceedings, 2003 IEEE Bologna*, vol. 3, June 2003, pp. 6 pp. Vol.3–.

[38] C. Yoon, H. Bai, R. N. Beres, X. Wang, C. L. Bak, and F. Blaabjerg, "Harmonic stability assessment for multiparalleled, grid-connected inverters," *IEEE Transactions on Sustainable Energy*, vol. 7, no. 4, pp. 1388–1397, Oct 2016.

[39] F. Fuchs and A. Mertens, "Prediction and avoidance of grid-connected converter's instability caused by wind park typical, load-varying grid resonance," in *Energy Conversion Congress and Exposition (ECCE), 2014 IEEE*, Sept 2014, pp. 2633–2640.

[40] J. Xu, S. Xie, and T. Tang, "Evaluations of current control in weak grid case for grid-connected LCL-filtered inverter," *Power Electronics, IET*, vol. 6, no. 2, pp. 227–234, Feb 2013.

[41] J. Wang, Y. Song, and A. Monti, "A study of feedforward control on stability of grid-parallel inverter with various grid impedance," in *2014 IEEE 5th International Symposium on Power Electronics for Distributed Generation Systems (PEDG)*, June 2014, pp. 1–8.

[42] R. Teodorescu, M. Liserre, and P. Rodríguez, *Grid Converters for Photovoltaic and Wind Power Systems*. Wiley, 2011.

[43] A. Nagliero, R. Mastromauro, M. Liserre, and A. Dell'Aquila, "Monitoring and synchronization techniques for single-phase PV systems," in *2010 International Symposium on Power Electronics Electrical Drives Automation and Motion (SPEEDAM)*, June 2010, pp. 1404–1409.

[44] C. Zhang, X. Wang, F. Blaabjerg, W. Wang, and C. Liu, "The influence of phase-locked loop on the stability of single-phase grid-connected inverter," in *Energy Conversion Congress and Exposition (ECCE), 2015 IEEE*, Sept 2015, pp. 4737–4744.

[45] D. Dong, B. Wen, D. Boroyevich, P. Mattavelli, and Y. Xue, "Analysis of Phase-Locked Loop Low-Frequency Stability in Three-Phase Grid-Connected Power Converters Considering Impedance Interactions," *IEEE Transactions on Industrial Electronics*, vol. 62, no. 1, pp. 310–321, Jan 2015.

[46] J. Agorreta, M. Borrega, J. Lòpez, and L. Marroyo, "Modeling and Control of N-Paralleled Grid-Connected Inverters With LCL Filter Coupled Due to Grid Impedance in PV Plants," *IEEE Transactions on Power Electronics*, vol. 26, no. 3, pp. 770–785, March 2011.

[47] M. Lu, X. Wang, P. C. Loh, and F. Blaabjerg, "Interaction and aggregated modeling of multiple paralleled inverters with LCL filter," in *Energy Conversion Congress and Exposition (ECCE), 2015 IEEE*, Sept 2015, pp. 1954–1959.

[48] W. Choi, W. Lee, and B. Sarlioglu, "Effect of Grid Inductance on Grid Current Quality of Parallel Grid-Connected Inverter System with Output LCL Filter and Closed-Loop Control," *The Applied Power Electronics Conference and Exposition (APEC) 2016*, pp. 2679–2686, March 2016.

[49] F. Cavazzana, P. Mattavelli, M. Corradin, and I. Toigo, "Grid sensitivity considerations on multiple parallel inverters systems," in *2016 IEEE 8th International Power Electronics and Motion Control Conference (IPEMC-ECCE Asia)*, May 2016, pp. 993–999.

[50] Y. Wang, X. Wang, F. Blaabjerg, and Z. Chen, "Harmonic resonance assessment of multiple paralleled grid-connected inverters system," in *2017 IEEE 3rd International Future Energy Electronics Conference and ECCE Asia (IFEEC 2017 - ECCE Asia)*, June 2017, pp. 2070–2075.

[51] ——, "Frequency scanning-based stability analysis method for grid-connected inverter system," in *2017 IEEE 3rd International Future Energy Electronics Conference and ECCE Asia (IFEEC 2017 - ECCE Asia)*, June 2017, pp. 1575–1580.

[52] M. K. Bakhshizadeh, F. Blaabjerg, J. Hjerrild, X. Wang, L. Kocewiak, and C. L. Bak, "A numerical matrix-based method for stability and power quality studies based on harmonic transfer functions," *IEEE Journal of Emerging and Selected Topics in Power Electronics*, vol. PP, no. 99, pp. 1–1, 2017.

[53] M. Lu, X. Wang, P. C. Loh, and F. Blaabjerg, "Resonance interaction of multiparallel grid-connected inverters with lcl filter," *IEEE Transactions on Power Electronics*, vol. 32, no. 2, pp. 894–899, Feb 2017.

[54] J. Kwon, X. Wang, C. L. Bak, and F. Blaabjerg, "Harmonic interaction analysis in grid connected converter using harmonic state space (hss) modeling," in *2015 IEEE Applied Power Electronics Conference and Exposition (APEC)*, March 2015, pp. 1779–1786.

[55] E. Ebrahimzadeh, F. Blaabjerg, X. Wang, and C. L. Bak, "Dynamic resonance sensitivity analysis in wind farms," in *2017 IEEE 8th International Symposium on Power Electronics for Distributed Generation Systems (PEDG)*, April 2017, pp. 1–5.

[56] M. Cespedes and J. Sun, "Impedance Modeling and Analysis of Grid-Connected Voltage-Source Converters," *IEEE Transactions on Power Electronics*, vol. 29, no. 3, pp. 1254–1261, March 2014.

[57] J. Sun, "Ac power electronic systems: Stability and power quality," in *2008 11th Workshop on Control and Modeling for Power Electronics*, Aug 2008, pp. 1–10.

[58] T. Kato, K. Inoue, and H. Kawabata, "Stability analysis of a grid-connected inverter system," in *2012 IEEE 13th Workshop on Control and Modeling for Power Electronics (COMPEL)*, June 2012, pp. 1–5.

[59] C. Yoon, H. Bai, X. Wang, C. L. Bak, and F. Blaabjerg, "Regional modeling approach for analyzing harmonic stability in radial power electronics based power system," in *2015 IEEE 6th International Symposium on Power Electronics for Distributed Generation Systems (PEDG)*, June 2015, pp. 1–5.

[60] F. Cavazzana, P. Mattavelli, M. Corradin, and I. Toigo, "On the stability analysis of multiple parallel inverters using the impedance multiplication effect," in *8th IET International Conference on Power Electronics, Machines and Drives (PEMD 2016)*, April 2016, pp. 1–6.

[61] S. Buso and P. Mattavelli, *Digital Control in Power Electronics*, 2nd ed. Morgan & Claypool, 2015.

[62] J. Zhang and H. Xu, "Online identification of power system equivalent inertia constant," *IEEE Transactions on Industrial Electronics*, vol. 64, no. 10, pp. 8098–8107, Oct 2017.

[63] C. Yoon, X. Wang, C. L. Bak, and F. Blaabjerg, "Stabilization of multiple unstable modes for small-scale inverter-based power systems with impedance-based stability analysis," in *2015 IEEE Applied Power Electronics Conference and Exposition (APEC)*, March 2015, pp. 1202–1208.

[64] S. Skogestad and I. Postlethwaite, *Multivariable Feedback Control: Analysis and Design*. John Wiley & Sons, 2005.

[65] M. Liserre, R. Teodorescu, and F. Blaabjerg, "Stability of photovoltaic and wind turbine grid-connected inverters for a large set of grid impedance values," *IEEE Transactions on Power Electronics*, vol. 21, no. 1, pp. 263–272, Jan 2006.

[66] S. Hiti, "Modeling and control of three-phase PWM converters," Ph.D. dissertation, Virginia Tech, 1995. [Online]. Available: https://theses.lib.vt.edu/theses/available/etd-09192008-063200/

[67] V. Blasko and V. Kaura, "A new mathematical model and control of a three-phase ac-dc voltage source converter," *IEEE Transactions on Power Electronics*, vol. 12, no. 1, pp. 116–123, Jan 1997.

[68] F. Blaabjerg, M. Liserre, and K. Ma, "Power electronics converters for wind turbine systems," *IEEE Transactions on Industry Applications*, vol. 48, no. 2, pp. 708–719, March 2012.

[69] D. A. C. Luna, L. O. J. Legarda, and J. L. D. Gómez, "Experimental evaluation of a back-to-back power interface to grid integration of a wind turbine," in *2016 International Conference on Mechatronics, Electronics and Automotive Engineering (ICMEAE)*, Nov 2016, pp. 72–77.

[70] J. S. Lee, K. B. Lee, and F. Blaabjerg, "Open-switch fault detection method of a back-to-back converter using npc topology for wind turbine systems," *IEEE Transactions on Industry Applications*, vol. 51, no. 1, pp. 325–335, Jan 2015.

[71] J. Zhang, J. Chen, X. Chen, and C. Gong, "Modelling, analysis and design of droop-controlled parallel three phase voltage source inverter using dynamic phasors method," in *2014 IEEE Conference and Expo Transportation Electrification Asia-Pacific (ITEC Asia-Pacific)*, Aug 2014, pp. 1–6.

[72] J. C. Vasquez, J. M. Guerrero, M. Savaghebi, J. Eloy-Garcia, and R. Teodorescu, "Modeling, analysis, and design of stationary-reference-frame droop-controlled parallel three-phase voltage source inverters," *IEEE Transactions on Industrial Electronics*, vol. 60, no. 4, pp. 1271–1280, April 2013.

[73] Y. Jia and R. Wu, "Voltage source grid-connected pv inverters based on mppt and droop control," in *2016 IEEE 2nd Annual Southern Power Electronics Conference (SPEC)*, Dec 2016, pp. 1–6.

[74] X. Wang, F. Blaabjerg, and Z. Chen, "An improved design of virtual output impedance loop for droop-controlled parallel three-phase voltage

source inverters," in *2012 IEEE Energy Conversion Congress and Exposition (ECCE)*, Sept 2012, pp. 2466–2473.

[75] S. Hiti and D. Boroyevich, "Small-signal modeling of three-phase pwm modulators," in *PESC Record. 27th Annual IEEE Power Electronics Specialists Conference*, vol. 1, Jun 1996, pp. 550–555 vol.1.

[76] S. Hiti, D. Boroyevich, and C. Cuadros, "Small-signal modeling and control of three-phase pwm converters," in *Proceedings of 1994 IEEE Industry Applications Society Annual Meeting*, Oct 1994, pp. 1143–1150 vol.2.

[77] G. Francis, "An Algorithm and System for Measuring Impedance in D-Q Coordinates," Ph.D. dissertation, Virginia Tech, 2011. [Online]. Available: http://hdl.handle.net/10919/26462

[78] M. Jakšić, Z. Shen, I. Cvetković, D. Boroyevich, R. Burgos, C. DiMarino, and F. Chen, "Medium-voltage impedance measurement unit for assessing the system stability of electric ships," *IEEE Transactions on Energy Conversion*, vol. 32, no. 2, pp. 829–841, June 2017.

[79] K. Schoder, M. Steurer, F. Bogdan, J. Hauer, J. Langston, D. Boroyevich, R. Burgos, I. Cvetkovic, Z. Shen, and C. DiMarino, "Testing of a novel medium voltage impedance measurement unit," in *2015 IEEE 3rd Workshop on Wide Bandgap Power Devices and Applications (WiPDA)*, Nov 2015, pp. 287–290.

[80] Z. Shen, I. Cvetkovic, M. Jaksic, C. DiMarino, D. Boroyevich, R. Burgos, and F. Chen, "Design of a modular and scalable small-signal dq impedance measurement unit for grid applications utilizing 10 kv sic mosfets," in *2015 17th European Conference on Power Electronics and Applications (EPE'15 ECCE-Europe)*, Sept 2015, pp. 1–9.

[81] Z. Shen, M. Jaksic, P. Mattavelli, D. Boroyevich, J. Verhulst, and M. Belkhayat, "Design and implementation of three-phase ac impedance measurement unit (imu) with series and shunt injection," in *2013 Twenty-Eighth Annual IEEE Applied Power Electronics Conference and Exposition (APEC)*, March 2013, pp. 2674–2681.

[82] Z. Shen, M. Jaksic, B. Zhou, P. Mattavelli, D. Boroyevich, J. Verhulst, and M. Belkhayat, "Analysis of phase locked loop (pll) influence on dq impedance measurement in three-phase ac systems," in *2013 Twenty-Eighth Annual IEEE Applied Power Electronics Conference and Exposition (APEC)*, March 2013, pp. 939–945.

[83] M. Jaksic, "Identification of small-signal dq impedances of power electronics converters via single-phase wide-bandwidth injection," Ph.D. dissertation, Virginia Tech, 2014. [Online]. Available: http://hdl.handle.net/10919/51222

[84] Z. Shen, M. Jaksic, P. Mattavelli, D. Boroyevich, J. Verhulst, and M. Belkhayat, "Three-phase ac system impedance measurement unit (imu) using chirp signal injection," in *2013 Twenty-Eighth Annual IEEE Applied Power Electronics Conference and Exposition (APEC)*, March 2013, pp. 2666–2673.

[85] G. FRANCIS, R. Burgos, D. Boroyevich, F. Wang, Z. SHEN, P. Mattavelli, K. Karimi, and S. FU, "Algorithm and implementation system for measuring impedance in the d-q domain," Apr. 2013, uS Patent App. 13/618,513. [Online]. Available: https://www.google.com/patents/US20130099800

[86] G. Mondal, J. Bamberger, M. B. Buhl, and S. Nielebock, "Voltage source operation of parallel PV/wind inverters-stabilized hybrid power plants in Diesel Off-mode- an experimental verification," in *2017 IEEE 8th International Symposium on Power Electronics for Distributed Generation Systems (PEDG)*, April 2017, pp. 1–7.

[87] P. C. Sekhar, S. Mishra, and R. Sharma, "Data analytics based neuro-fuzzy controller for diesel-photovoltaic hybrid ac microgrid," *IET Generation, Transmission Distribution*, vol. 9, no. 2, pp. 193–207, 2015.

[88] S. Singh, M. Singh, S. Chanana, and D. Raveendhra, "Operation and control of a hybrid wind-diesel-battery energy system connected to micro-grid," in *2013 International Conference on Control, Automation, Robotics and Embedded Systems (CARE)*, Dec 2013, pp. 1–6.

[89] O. D. Mipoung, L. A. C. Lopes, and P. Pillay, "Frequency support from a fixed-pitch type-2 wind turbine in a diesel hybrid mini-grid," *IEEE Transactions on Sustainable Energy*, vol. 5, no. 1, pp. 110–118, Jan 2014.

[90] ——, "Potential of type-1 wind turbines for assisting with frequency support in storage-less diesel hybrid mini-grids," *IEEE Transactions on Industrial Electronics*, vol. 61, no. 5, pp. 2297–2306, May 2014.

[91] C. Guanglin, C. Rouyi, C. Jianbin, W. Ke, L. Yong, W. Liexin, and Z. Yongjun, "Research on simulations and model of the isolated wind-solar-diesel-battery hybrid micro-grid," in *2012 China International Conference on Electricity Distribution*, Sept 2012, pp. 1–4.

[92] IRENA, "Battery Storage for Renewables: Market Status and Technology Outlook," Tech. Rep., 2015. [Online]. Available: https://www.irena.org/documentdownloads/publications/irena_battery_storage_report_2015.pdf

[93] J. Rocabert, A. Luna, F. Blaabjerg, and P. Rodríguez, "Control of power converters in ac microgrids," *IEEE Transactions on Power Electronics*, vol. 27, no. 11, pp. 4734–4749, Nov 2012.

[94] J. M. Guerrero, J. C. Vasquez, J. Matas, L. G. de Vicuna, and M. Castilla, "Hierarchical Control of Droop-Controlled AC and DC Microgrids - A General Approach Toward Standardization," *IEEE Transactions on Industrial Electronics*, vol. 58, no. 1, pp. 158–172, Jan 2011.

[95] S. Lissandron and P. Mattavelli, "A controller for the smooth transition from grid-connected to autonomous operation mode," in *2014 IEEE Energy Conversion Congress and Exposition (ECCE)*, Sept 2014, pp. 4298–4305.

[96] L. A. C. Lopes, "PV Hybrid Mini-Grids: Applicable Control Methods for Various Situations," International Energy Agency (IEA), Tech. Rep., 2012. [Online]. Available: http://iea-pvps.org/index.php?id=227&eID=dam_frontend_push&docID=1127

[97] F. Katiraei and C. Abbey, "Diesel plant sizing and performance analysis of a remote wind-diesel microgrid," in *Power Engineering Society General Meeting, 2007. IEEE*, June 2007, pp. 1–8.

[98] N. A. Ninad and L. A. C. Lopes, "A BESS control system for reducing fuel-consumption and maintenance costs of diesel-hybrid mini-grids with high penetration of renewables," in *2013 IEEE ECCE Asia Downunder*, June 2013, pp. 409–415.

[99] M. Singh and L. A. C. Lopes, "Experimental assessment of a BESS control system for reducing fuel consumption and maintenance cost of diesel-hybrid mini-grids," in *7th IET International Conference on Power Electronics, Machines and Drives (PEMD 2014)*, April 2014, pp. 1–6.

[100] B. Idlbi, "Dynamic Simulation of a PV-Diesel-Battery Hybrid Plant for Off Grid Electricity Supply," Master's thesis, Faculty of Engineering, Cairo University, 2012. [Online]. Available: https://www.uni-kassel.de/eecs/fileadmin/datas/fb16/remena/theses/batch2/MasterThesis_Basem_Idlbi.pdf

[101] S. Chowdry, "Modelling, Simulation and Performance Analysis of PV-Diesel Generator Based Power Plant," Master's thesis, Department of Electrical Engineering, University of Cape Town, 2013. [Online]. Available: http://www.publishresearch.com/download/214

[102] S. Reichert and R. Singer, "Stability analysis of droop-control in diesel-hybrid systems," in *2016 IEEE 7th International Symposium on Power Electronics for Distributed Generation Systems (PEDG)*, June 2016, pp. 1–6.

[103] J. Liu, Y. Miura, and T. Ise, "Comparison of dynamic characteristics between virtual synchronous generator and droop control in inverter-based distributed generators," *IEEE Transactions on Power Electronics*, vol. 31, no. 5, pp. 3600–3611, May 2016.

[104] Q. C. Zhong and G. Weiss, "Synchronverters: Inverters that mimic synchronous generators," *IEEE Transactions on Industrial Electronics*, vol. 58, no. 4, pp. 1259–1267, April 2011.

[105] H. P. Beck and R. Hesse, "Virtual synchronous machine," in *2007 9th International Conference on Electrical Power Quality and Utilisation*, Oct 2007, pp. 1–6.

[106] J. M. Guerrero, L. G. de Vicuna, J. Matas, M. Castilla, and J. Miret, "A wireless controller to enhance dynamic performance of parallel inverters in distributed generation systems," *IEEE Transactions on Power Electronics*, vol. 19, no. 5, pp. 1205–1213, Sept 2004.

[107] M. A. T. Lépez, "Dynamic Frequency Control in Diesel-Hybrid Autonomous Power Systems using Virtual Synchronous Machines," May 2013. [Online]. Available: http://spectrum.library.concordia.ca/977316/

[108] M. Torres and L. Lopes, "Inverter-Based Diesel Generator Emulator for the Study of Frequency Variations in a Laboratory-Scale Autonomous Power System," *Energy and Power Engineering*, vol. 5 No. 3, pp. 274–283, 2013.

[109] J. F. W. Yahya H. Zweiri and L. D. Seneviratne, "Complete Analytical Model of a Single-Cylinder Diesel Engine for Non-linear Control and Estimation," p. 23, nov 1999.

[110] ——, "Detailed analytical model of a single-cylinder diesel engine in the crank angle domain," 2001.

[111] Y. Zweiri, J. Whidborne, L. Seneviratne, and K. Althoefer, "A Comparison of Dynamic Models of Various Complexity for Diesel Engines," *Mathematical*

and Computer Modelling of Dynamical Systems, vol. 8, no. 3, pp. 273–289, 2002. [Online]. Available: http://www.tandfonline.com/doi/abs/10.1076/mcmd.8.3.273.14100

[112] J. Asprion, "Optimal Control of Diesel Engines," Ph.D. dissertation, ETH (Zurich), 2013.

[113] P. Hillerborg, "Dynamic Model of a Diesel Engine for Diagnosis and Balancing," Master's thesis, KTH Signals Sensonrs and Systems, 2005.

[114] S. Roy, O. P. Malik, and G. S. Hope, "An adaptive control scheme for speed control of diesel driven power-plants," *IEEE Transactions on Energy Conversion*, vol. 6, no. 4, pp. 605–611, Dec 1991.

[115] I. Boldea, *Synchronous Generators, Second Edition*. CRC Press, 2015. [Online]. Available: https://books.google.it/books?id=VB-vCgAAQBAJ

[116] "IEEE Guide for Synchronous Generator Modeling Practices and Applications in Power System Stability Analyses," *IEEE Std 1110-2002*, pp. 1–72, 2003.

[117] P. Kundur, N. Balu, and M. Lauby, *Power system stability and control*, ser. EPRI power system engineering series. McGraw-Hill, 1994. [Online]. Available: https://books.google.it/books?id=wOlSAAAAMAAJ

[118] A. Barakat, S. Tnani, G. Champenois, and E. Mouni, "Analysis of synchronous machine modeling for simulation and industrial applications," *Simulation Modelling Practice and Theory*, vol. 18, no. 9, pp. 1382 – 1396, 2010. [Online]. Available: http://www.sciencedirect.com/science/article/pii/S1569190X1000119X

[119] C. Ong, *Dynamic Simulation of Electric Machinery: Using MATLAB/SIMULINK*. Prentice Hall PTR, 1998. [Online]. Available: https://books.google.it/books?id=_OweAQAAIAAJ

[120] "IEEE Guide for Test Procedures for Synchronous Machines, Part I: Acceptance and Performance Testing, Part II: Test Procedures and Parameter Determination for Dynamic Analysis," *IEEE Std 115-2009 (Revision of IEEE Std 115-1995)*, pp. 1–219, May 2010.

[121] *A guide for synchronous generator parameters determination using dynamic simulations based on IEEE standards*, 2010.

[122] "IEEE Recommended Specification for Speed Governing of Internal Combustion Engine-Generator Units," *IEEE Std 126-1959*, pp. 1–26, March 1959.

[123] T. force on Turbine-Governor Modeling, "Dynamic Models for Turbine-Governors in Power System Studies," IEEE, Tech. Rep., 2013.

[124] "IEEE Recommended Practice for Excitation System Models for Power System Stability Studies," *IEEE Std 421.5-2016 (Revision of IEEE Std 421.5-2005)*, pp. 1–207, Aug 2016.

[125] *BSI ISO 8528-5:2013 Reciprocating internal combustion engine driven alternating current generating sets Part 5: Generating sets*, Std.

[126] J. M. Guerrero, N. Berbel, J. Matas, J. L. Sosa, and L. G. de Vicuna, "Droop control method with virtual output impedance for parallel operation of uninterruptible power supply systems in a microgrid," in *APEC 07 - Twenty-Second Annual IEEE Applied Power Electronics Conference and Exposition*, Feb 2007, pp. 1126–1132.

[127] "Ieee standard for interconnecting distributed resources with electric power systems," *IEEE Std 1547-2003*, pp. 1–28, July 2003.

[128] A. Rygg, M. Molinas, E. Unamuno, C. Zhang, and X. Cai, "A simple method for shifting local dq impedance models to a global reference frame for stability analysis," 06 2017. [Online]. Available: https://www.researchgate.net/publication/317930684_A_simple_method_for_shifting_local_dq_impedance_models_to_a_global_reference_frame_for_stability_analysis

[129] A. Rygg, M. Molinas, C. Zhang, and X. Cai, "A modified sequence-domain impedance definition and its equivalence to the dq-domain impedance definition for the stability analysis of ac power electronic systems," *IEEE Journal of Emerging and Selected Topics in Power Electronics*, vol. 4, no. 4, pp. 1383–1396, Dec 2016.

[130] F. Shahnia, S. Rajakaruna, and A. Ghosh, *Static Compensators (STATCOMs) in Power Systems*, 2015.

[131] N. Pogaku, M. Prodanovic, and T. C. Green, "Modeling, analysis and testing of autonomous operation of an inverter-based microgrid," *IEEE Transactions on Power Electronics*, vol. 22, no. 2, pp. 613–625, March 2007.